This thesis aims to explore and improve the pneumatic powder delivery system for Laser Metal Deposition (LMD), an essential technology in additive manufacturing. The research is guided by three primary objectives: to analyze the structure of the system, investigate the effects of process parameters, and evaluate potential improvements, both in sustainability and capabilities.

A review of existing simulation models and experimental techniques was conducted to identify the most suitable methods for this study. Through a combination of multiphase simulations and high-speed imaging, the research delves into the flow phenomena within the system. Additionally, the powder delivery system of LMD was examined using both simulations and experimental validation.

The results reveal significant enhancements in our understanding of the system, offering key insights into the behavior of powder particles during the LMD process. Furthermore, the study identifies areas for sustainability improvements, aligning with the Sustainable Development Goals (SDGs). These findings contribute to the broader field of additive manufacturing by providing a robust framework for optimizing LMD processes and promoting sustainable practices.

CFD-DEM STUDY OF THE METALLIC POWDER FLOW IN LASER METAL DEPOSITION · Lorenzo Pedrolli

CFD-DEM study of the metallic powder flow in Laser Metal Deposition

Doctoral Thesis presented by Lorenzo Pedrolli

Deusto
Faculty of Engineering
Bilbao, 2024

This page is intentionally blank
and does not get printed

Abstract

This thesis aims to explore and improve the pneumatic powder delivery system for Laser Metal Deposition (LMD), an essential technology in additive manufacturing. The research is guided by three primary objectives: to analyze the structure of the system, investigate the effects of process parameters, and evaluate potential improvements, both in sustainability and capabilities.

A review of existing simulation models and experimental techniques was conducted to identify the most suitable methods for this study. Through a combination of multiphase simulations and high-speed imaging, the research delves into the flow phenomena within the system. Additionally, the powder delivery system of LMD was examined using both simulations and experimental validation.

The results reveal significant enhancements in our understanding of the system, offering key insights into the behavior of powder particles during the LMD process. Furthermore, the study identifies areas for sustainability improvements, aligning with the Sustainable Development Goals (SDGs). These findings contribute to the broader field of additive manufacturing by providing a robust framework for optimizing LMD processes and promoting sustainable practices.

Resumen

Esta tesis tiene como objetivo explorar y mejorar el sistema de entrega neumática de polvo para la Deposición de Metal por Láser (LMD), una tecnología esencial en la fabricación aditiva. La investigación se guía por tres objetivos principales: analizar la estructura del sistema, investigar los efectos de los parámetros del proceso y evaluar posibles mejoras, tanto en sostenibilidad como en capacidades.

Se realizó una revisión de los modelos de simulación existentes y de las técnicas experimentales para identificar los métodos más adecuados para este estudio. A través de una combinación de simulaciones multifásicas y de imágenes de alta velocidad, la investigación profundiza en los fenómenos de flujo dentro del sistema. Además, se examinó el sistema de transporte de polvo en los sistemas LMD usando simulaciónes y metodos experimentales.

Los resultados revelan mejoras significativas en nuestra comprensión del sistema, ofreciendo conocimientos clave sobre el comportamiento de las partículas de polvo durante el proceso de LMD. Además, el estudio identifica áreas para mejoras en sostenibilidad, alineándose con los Objetivos de Desarrollo Sostenible (SDGs). Estos hallazgos contribuyen al campo más amplio de la fabricación aditiva al proporcionar un marco sólido para optimizar los procesos de LMD y promover prácticas sostenibles.

CFD-DEM Study of the metallic powder flow in Laser Metal Deposition

Doctoral Thesis presented by Lorenzo Pedrolli
within the Doctoral Program in Engineering
for the Information Society and Sustainable Development.

Directed by Dr. Alejandro López and Dr. Beatriz Achiaga.

Deusto

Faculty of Engineering

Bilbao, 2024

CFD-DEM study of the metallic powder flow in Laser Metal Deposition

Author: Lorenzo Pedrolli

Advisor: Dr. Alejandro López

Advisor: Dr. Beatriz Achiaga

Text printed in Bilbao

First edition, November 2024

I would like to start by thanking my supervisors, Alejandro and Beatriz, for their invaluable guidance, encouragement, and expertise. Their insights have shaped my work and supported my growth as a researcher. I also extend my thanks to Inger, my supervisor in the first year of this project.

My heartfelt gratitude goes to my friends at DeustoTech, whose camaraderie and collaboration enriched my research experience. I also want to acknowledge the *Cofunders*, who shared this journey and offered friendship, encouragement, and inspiration along the way.

I am deeply thankful for my family, whose unwavering support from afar has been a source of strength, reminding me of home and motivating me to persevere. I am also grateful to my friends, both near and far, for their support and encouragement when I needed it most.

I wish to express my gratitude to my host institution, the University of Deusto, and the 6i-dirs MSCA cofund program for making this research possible. I also want to thank UPV/EHU for their support in the experimental investigation of the nozzle, as well as the host institutions abroad where I carried out my mobility, the Newcastle University and the University of Trento. In particular, I am grateful to Sadegh and Luigi, for their kindness and support.

Finally, I would like to express my gratitude to Nerea, who encouraged me to pursue this path. Without her, I would not have embarked on this journey.

Grazie,

Lorenzo Pedrolli

Table of Contents

List of Figures

List of Tables

Nomenclature

Roman Symbols

$\overline{v}$	Velocity vector
A	Area
a	Contact radius
C	Specific heat
d	Diameter or distance
F	Force
F_n	Normal force
F_t	Tangential force
k_n	Normal stiffness
M_r	Rolling resistance moment
nu	Poisson's ratio
O	Origin
P	Load or Power or Perimeter
p	Pressure
R	Radius
r_e	Effective radius
T	Temperature
t	time
U	Velocity component
U_E	Elastic energy
U_I	Internal energy
U_M	Mechanical energy
U_S	Strain energy
U_T	Thermal energy
V	Volume
y	Coordinate or variable

Greek Symbols

α	Angle or coefficient
α_s	Solid volume fraction
β	Damping ratio
Δ	Change or difference
δ	Displacement
δ_n	Normal displacement
δ_t	Tangential displacement
η_n	Normal damping coefficient

η_r	Rotational damping coefficient
η_t	Tangential damping coefficient
Γ	Adhesive energy
γ	Surface energy
λ	Rayleigh wave length
μ	Friction coefficient
μ_g	Dynamic viscosity of the gas
μ_r	Rolling friction coefficient
ν_g	Kinematic viscosity of the gas
ω	Angular velocity
$\overline{\delta}$	Mean displacement
ϕ	Angle or phase
π	Pi, a mathematical constant
ρ	Density
ρ_g	Density of the gas
ρ_p	Density of the particle
σ	Standard deviation or stress
σ_v	Standard deviation of velocity

Acronyms

AM	Additive Manufacturing
ANN	Artificial Neural Network
CAD	Computer Aided Design
CFD	Computational Fluid Dynamics
CGP	Coarse Grain Particle
CPU	Central Processing Unit
CSV	Comma-Separated Values (file format)
CT	Computerized Tomography
DED	Directed Energy Deposition
DEM	Discrete Element Modeling
DMAM	Direct Metal Additive Manufacturing
DPM	Discrete Phase Model
E-PBF	Electron Beam - Powder Bed Fusion
GD	Granular Dynamics
GPGPU	General-Purpose Graphical Processing Unit
GPU	Graphical Processing Unit
L-PBF	Laser - Powder Bed Fusion
LAP	Linear Assignment Problem
LMD	Laser Metal Deposition
MEMS	Micro Electro-Mechanical System
MP-PIC	MultiPhase - Particle In Cell

ODE	Ordinary Differential Equation
OF	OpenFOAM (a computational fluid dynamics software)
PDF	Probability Density Function
PISO	Pressure Implicit with Splitting of Operators
PSD	Particle Size Distribution
PT	Particle Tracking
PTV	Particle Tracking Velocimetry
RANS	Reynolds-Averaged Navier-Stokes
RMS	Root Mean Square
SIMPLE	Semi-Implicit Method for Pressure-Linked Equations
SST	Shear Stress Transport
STAR	Software for Thermal Analysis and Reaction
TFM	Two Fluid Model
WLAM	Wire and Laser based Additive Manufacturing

CHAPTER

1

Introduction

1.1 Motivation

In the 1960s, humanity began to deeply ponder its role in the universe, sparking a golden era of science-fiction literature. During this time, Soviet astrophysicist Nikolai Kardashev proposed a scale to classify a civilization's technological development based on its energy consumption, known as the Kardashev Scale [60]. The scale initially included three levels:

Type 1 (Planetary Civilization): Capable of harnessing all forms of energy available on its home planet.

Type 2 (Stellar Civilization): Capable of extracting and using all energy from its star.

Type 3 (Galactic Civilization): Able to utilize the energy output of its entire galaxy.

In order to give the scale a quantitative value, Carl Sagan [105] proposed a continuous function quantifying the Kardashev Scale with an index K:

$$K = \frac{logP - 6}{10} \tag{1.1}$$

where P is the total power consumption of the civilization. According to this, a type 2 civilization using one stellar output corresponds to $P = 10^{26}$ W, rounded from the Sun's power output of $P_{\odot} = 3.83 \times 10^{26}$ W [134]. Extrapolating these values, Sagan determined that a type 1 civilization has access to $P = 10^{16}$ W. In its current state, humanity stands at $K \sim 0.7276$ [14].

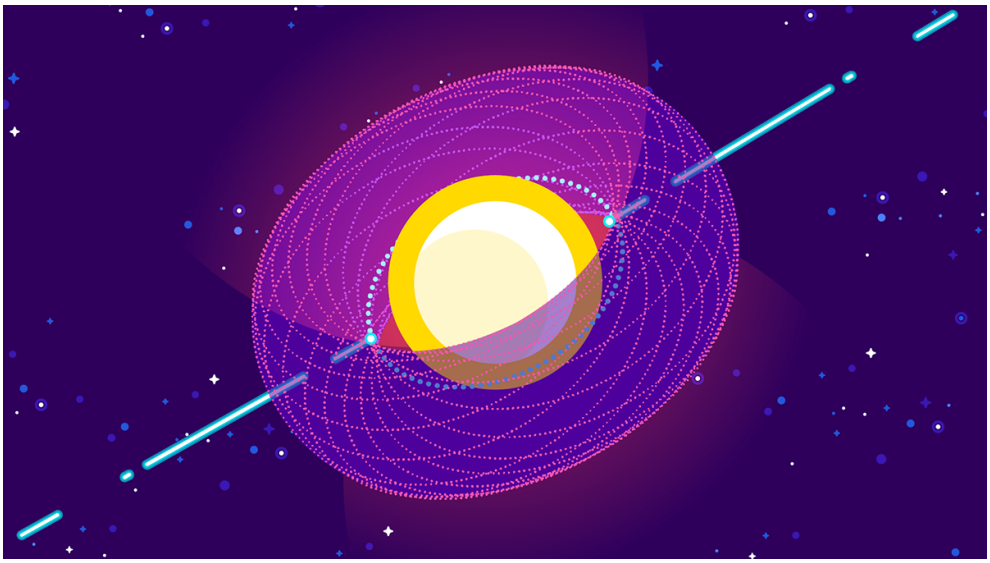

Figure 1.1: Artistic depiction of a Dyson sphere, formed by a swarm of individual satellites, partially surrounding the Sun. In this speculative work, the individual satellites would be manufactured on the surface of Mercury by automatic machines and sent into orbit with a linear accelerator. Even just 1% of the Sun's output is about 200 billion times the current energy consumption of humanity. Courtesy of Kurzgesagt.org.

Building on these visionary ideas, physicist and mathematician Freeman Dyson introduced the concept of the "Dyson sphere" in his 1960 paper "Search for Artificial Stellar Sources of Infra-Red Radiation" [28]. Dyson theorized that an advanced civilization would need to harvest energy directly from its star through a system of structures orbiting the star. This concept has been popularized in science fiction and visualized by contemporary media, such as the German studio Kurzgesagt.

The question remains: how can such grand potential, promised by fictional stories, be achieved? It is difficult to say, but it is an honor to contribute to the incremental advancements possible through the Scientific Method and the Scientific Community. One example of a plan is expressed by Smith [114]. The plan is broadly outlined, but it is pretty clear that to achieve such a structure, the fabrication needs to happen in space and harvest resources present locally. On September 24th, 2023, the probe OSIRIS-REx was able to return samples from the asteroid Bennu [88]. The main objectives of the mission include the retrieval

of the asteroid sample to study the early stages of the formation of Earth and the Moon. More relevant to this work, it outlines the ability to harvest and recover samples from a celestial body. A sample that in this case is granular in nature, and given the right composition (which is not necessarily the case for Bennu) could be harvested in order to build up structures in space. It is possible to speculate that similar materials could be used to build the elements that compose a Dyson sphere.

While these grand concepts provide a vision for humanity's potential technological future, achieving such ambitious goals requires incremental advancements in current technologies. Additive Manufacturing (AM) is an emerging technology that will surely be essential in the construction of structures in space, and is quickly reaching maturity, while remaining extremely attractive in a variety of applications here on Earth. AM is indicated as an essential technology in ESA's Technology Strategy document [129], including on-orbit/on-planet manufacturing and recycling (including the reconditioning of space debris for construction purposes). This work specifically analyzes Laser Metal Deposition, which is defined in Section 1.2.

The motivation behind this research is to contribute to the incremental advancements in manufacturing technologies that could one day support large-scale constructions in space, such as those envisioned by the Dyson sphere concept. More specifically, this work focuses on optimizing the Laser Metal Deposition (LMD) process—a key area of Additive Manufacturing that holds promise for both terrestrial and extraterrestrial applications.

By improving our understanding and control of particle behavior and mass flowrate in LMD, this research aims to enhance the quality and efficiency of the deposition process. This aligns with broader goals of technological innovation and sustainability, as outlined by the H2020 priorities and Sustainable Development Goals (SDGs), particularly SDG 9 (Industry, Innovation, and Infrastructure) and SDG 12 (Responsible Consumption and Production).

1.2 The Laser Metal Deposition process

Additive Manufacturing (AM), revolutionizes traditional manufacturing processes by directly fabricating three-dimensional objects from Computer Aided Design

(CAD) models. It reduces the need for elaborate process planning typically seen in other manufacturing techniques. AM simplifies the production of intricate 3D structures by relying on fundamental dimensional specifications and a basic understanding of the AM machine's operation and material properties. Commercialized AM machines primarily utilize a layer-based approach, differing in materials, layer creation methods, and layer bonding techniques. These differences influence crucial factors such as final part accuracy, material and mechanical properties, production speed, post-processing requirements, machine size, and overall cost of the AM process. By building parts layer by layer, each layer represents a thin cross-section derived from the original CAD data. These layers are stacked to approximate the desired 3D object. The thickness of each layer directly impacts the closeness of the final part to the original design [40]. One of the primary strengths of AM processes, such as laser-based systems, lies in their ability to create objects with intricate internal features, undercuts, and complex geometries that would be challenging or even impossible to achieve through traditional machining techniques. This capability to build complex structures in a single continuous process is a hallmark of AM, making it a valuable tool for industries ranging from aerospace to healthcare.

The ISO 17296-2:2015 norm and ISO/ASTM 52900 norms define seven AM categories:

- Vat photopolymerization
- Material jetting
- Binder jetting
- Powder bed fusion
- Material extrusion
- Directed energy deposition
- Sheet lamination

Of these, Figure 1.2 gives a more detailed overview of the five categories able to produce metal parts, or Direct Metal Additive Manufacturing (DMAM).

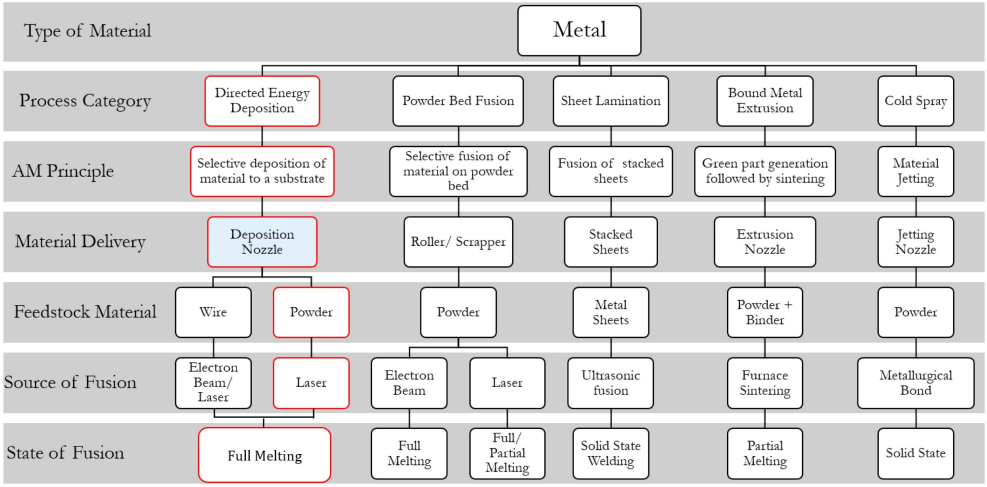

Figure 1.2: AM processes able to produce metal parts (DMAM); the highlighted part corresponds to LMD [113].

Directed Energy Deposition (DED) processes are a key subset within the realm of AM technology. DED is a category of additive manufacturing that leverages various energy sources, such as lasers or electron beams, to precisely bond material onto a substrate, forming intricate 3D structures. This technology is gaining traction in the world of multi-material and hybrid manufacturing. By combining different materials and deposition techniques, DED processes can produce components with tailored material properties, offering a level of customization and performance that traditional manufacturing methods struggle to match.

Apart from the ISO definitions, there are numerous names used to describe laser deposition welding. The common terms are Laser Metal Deposition (LMD), Direct(ed) Energy Deposition (DED), Direct(ed) Laser Deposition (DLD), Direct(ed) Metal Deposition (DMD). Other terms are Laser Assisted Metals Deposition (LAMD), Laser-Engineered Net Shaping (LENS), a proprietary term by the US company Optomec, and EHLA – Extrem Hochgeschwindigkeits LaserAuftragschweissen (Extreme High Speed Laser Material Deposition), used by Fraunhofer ILM [108]. Throughout this work, the technology is indicated as LMD, which has a strong usage in scientific works: it defines the source of energy as well as the type of material and Deposition, and distinguishes it clearly from a joining process.

In Laser Metal Deposition (LMD), highlighted in Figure 1.2, the material is

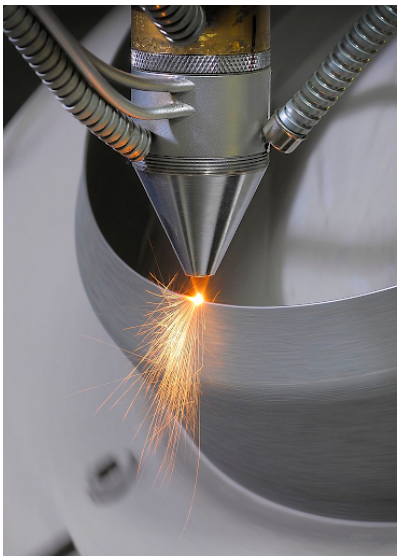

Figure 1.3: Example of a part being manufactured using LMD - source: `twi-global.com`

added in powder form and locally heated using a laser source to melt it onto the substrate. The process is represented in Figure 1.3, where a nozzle is depositing material on the thin metal structure being produced.

The laser head with powder feeding nozzle can move on arbitrary trajectories, showing great potential in repairing and re-manufacturing parts. Using powders as opposed to solid wires, employed in similar technologies like wire and laser based additive manufacturing (WLAM), there is no real limitation on the type of materials used or their combination and gradient through the structure, potentially allowing the fabrication of heterogeneous parts.

1.2.1 Powder delivery in LMD machines

This work has a strong focus on the part of the machine delivering the powder to the melting spot. The shielding and conveying gas used in most cases is Argon, which protects both the powder and the melt pool from oxidation. The whole powder delivery system is a continuous loop until the nozzle, where the powder needs to transverse a short distance without being constrained by pipes and conducts. Figure 1.5 is a schematic illustration on the generic pneumatic conveying in such machines. All the indicated units can have different working

principles, but in general they absolve the functions of the macro-systems reported in the figure.

A proper flow of powder is critical for a uniform and stable deposition, and consequently for all the quality indicators of the finished or repaired part, and for the reduction of waste. In this case, waste would be defined as anything that increments the use of any resource. Examples can be the lost powder that didn't adhere to the melt pool, or the additional manufacturing steps required to obtain full functionality.

This flow depends on the particles' geometry, collision and cohesion dynamics, carrier gas properties, and geometrical characteristics of the flow path. Once out of the nozzle, the environment and laser power have significant influence. A better understanding of the material's flow is critical to improve the reliability and applicability of the process for increasingly critical situations, and it will also allow to reduce the waste of resources, especially by reusing or reducing the amount of dispersed powder. Metallic powders used in LMD processes possess several characteristics that must be evaluated to accurately describe their behavior in a numerical simulation. The article from Nan et al. [87], clearly explains the methods used for the determination of such parameters for a different process, which can surely be used in this case. It is important to assess the stiffness, hardness, friction, restitution, and adhesion due to the surface energy. The same article describes the representation of particles using the clumped spheres method, based on the powder imaging using electron microscopy. In this way it is possible to account for particles that are elongated and adhered to one another in the production phase. It is an accurate representation for smooth particles such as metals, but if other types of crystalline powders (TiC in a matrix of Ti6Al4V [71]) are used, the sharp particle geometry will have a different impact on the fluid flow and the clumped-particle model might be inadequate [131].

Having characterized the particles, this information can be used to implement a numerical model of the flow inside a constrained pipe. Given that, the amount of carried particles will most likely result in alterations of the gas flow characteristics, which will be investigated using CFD-DEM coupling in different configurations of one, two, and four-way coupling.

Figure 1.4 reports a general phase diagram for horizontal flows [49]. Several

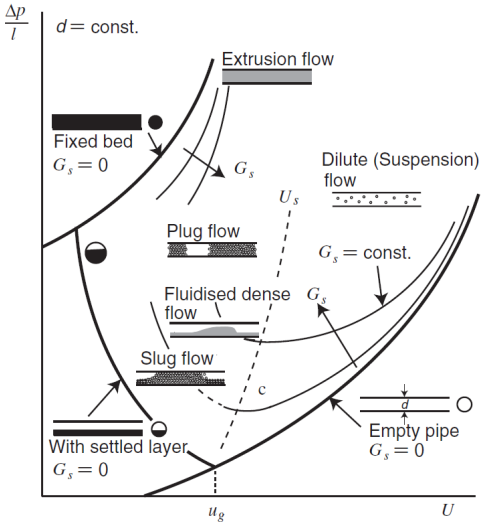

Figure 1.4: Phase diagram for pneumatic conveying of powders [49].

different regimes exist that can be grouped in "dense phase" regime, to differentiate them from the dilute flow. Flowrate irregularities are a known issue in Pneumatic Conveying even in dilute flows, as documented in the work by Yan and Rinoshika [137]. Most industrial cases, however, identify the dilute flow as a relatively homogeneous transport, and measure the flowrate on relatively long timescales [109, 69, 81, 63]. From the literature survey, no articles were found that analyzed the powder flowrate over time in the LMD technology, since it is delivered to the nozzle in dilute phase.

The simulation would be useful to find the effect of the conveying parameters on the flow characteristics and uniformity. The simulations would also be able to correctly predict the energy required to carry the particles and optimize the use of carrier gas. The information deriving from this analysis is also useful to assess the damage done to the internal channels of an LMD system, using an erosion model [73]. Adequate parameter optimization should result in a lower energy for the same powder output, while at the same time limiting the erosion, and avoiding the parameter combinations that could cause the powder delivery to be irregular.

The system indicated by *powder delivery and laser optics* is the final part of the system, where the nozzle shapes the flow of gas and powder in order to encounter the melt pool formed by the laser in the most optimal conditions. Pro-

cess control and monitoring, including feedback control, acts in this system. The deposition head is moved by the typical CNC systems, able to follow complex three-dimensional paths. The process tries to take advantage of all he movement categories applicable between three and six or more axes of movement. Cartesian systems represent the lower end of the spectrum, with what are called 2.5D movements that position the head in the plane and builds the object by superposition of flat layers. On the other end of the spectrum, deposition heads can be mounted on anthropomorphic robotic arms, with 6 degrees of freedom. The categorization of these movements is outside the scope of this work, but can be found in various specialized studies and reviews on CNC systems and robotic automation.

A simple gas supply provides the inert gas needed to protect the lens and shield the melt pool. In parallel, the powder conveyance unit provides the uniform and controlled flow of gas to convey the powder. The same gas used to pressurize the metering unit, is also used to convey the powder through a series of conducts. It is generally accepted that this occurs in what is known as dilute phase, where the air velocity is enough to suspend the particles. Figure 1.5 also represents a feedstock distributor, which ideally splits the multiphase flow (gas and particles) into a number of separate pipes that lead to the nozzle. In practice, this split is not always done using a dedicated component, but rather using generic pneumatic fittings.

The metering stage involves several mechanisms with the objective to provide a constant and uniform stream of powder, to be transported through to the nozzle. Singh et.al. [113] classify the delivery methods used in LMD in the chart reported in Figure 1.6. During the course of this doctorate, the investigation focused mostly on the pneumatic methods for powder conveying and gas-assisted delivery methods both in continuous and discrete coaxial nozzles.

1.2.2 **Flow Irregularities in Pneumatic Conveying for LMD**

The uniformity and stability of the powder flow in LMD processes are critical factors for achieving high-quality parts. However, the behavior of pneumatic conveying systems is often influenced by flow irregularities, which can introduce significant variability in the material deposition rate.

Flow irregularities in pneumatic conveying systems, particularly in dilute-

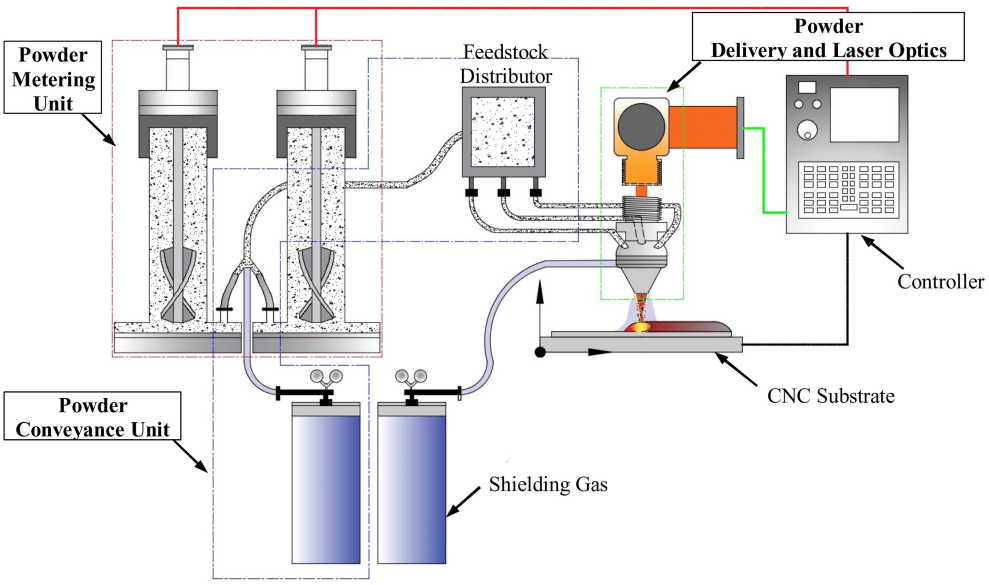

Figure 1.5: Schematic illustration of the powder delivery system in DED [113].

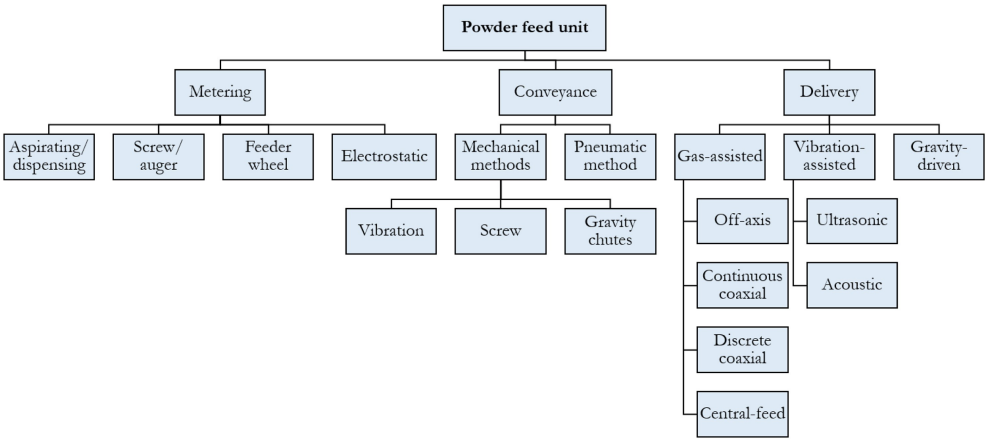

Figure 1.6: Powder feed mechanisms used in LMD, classified in a chart [113].

phase flows, are a well-documented phenomenon [137, 63, 21]. These irregularities are characterized by fluctuations in particle velocity and concentration, which can result in non-uniform material delivery to the LMD nozzle. While most industrial pneumatic conveying systems aim for steady flow, such fluctuations are inevitable due to particle-gas interactions and variations in system geometry, as discussed by Klinzing et al. [63].

In the context of LMD, these flow irregularities have a direct impact on the deposition process. Studies by Murer [86] and Zekovic [140] have analyzed time-averaged powder flows in LMD systems, but they did not consider the temporal variability of the mass flow rate. In contrast, the present work focuses on these short-term fluctuations and their potential effects on the quality of deposited layers.

Experimental and numerical studies on pneumatic conveying, such as the work by Zhou et al. [143], show that flow pulsations can be self-induced and regular, particularly in horizontal pipes. These pulsations, which were captured using CFD-DEM simulations, align with findings in the present study, where flowrate irregularities were observed in the powder feed system for LMD. Similarly, Alkassar et al. [5] experimentally demonstrated the presence of pressure pulsations in pneumatic conveying systems, highlighting their dependence on particle loading and system characteristics.

The results from this study, discussed in more detail in Chapter 5, demonstrate that flow irregularities in the powder delivery system are not only inevitable but can also lead to clustering of particles, which in turn causes fluctuations in the mass flow rate delivered to the LMD process. These fluctuations, although not always significant in terms of overall process efficiency, can impact the uniformity of the deposited material. Therefore, understanding and controlling these flow irregularities is one essential piece for improving the precision and reliability of LMD processes, particularly when dealing with complex geometries or fine-tuned material properties.

1.3 Aim of the Project and Research Questions

The key objectives of this study are the analysis and possible enhancement of a pneumatic conveying system for Laser Metal Deposition (LMD). These objectives

are designed to address various aspects of the LMD process, from understanding the system structure to assessing its sustainability implications.

Objective 1 Analyze the structure of a pneumatic conveying system for LMD and select the most appropriate simulation models, considering the material and geometric properties of the powders and their influence.

- Multiphase simulation in simple, confined domains of use-cases related to LMD.
- Survey of the existing simulation models and validation of their accuracy for LMD use-cases.
- Investigation of periodic and transient flow phenomena in pipelines and their possible effects on the LMD process.
- 3D characterization of fresh and recycled particles, assessing the modifications produced by previous use.
- Experimental investigation of flow phenomena using high-speed imaging techniques.
- Determination of the main DEM parameters for calibration.

Objective 2 Investigate the effects of process parameters on the LMD system performance, including material deposition rates, powder flow dynamics, and energy consumption.

- Determination of the harsh environment conditions during the LMD process.
- Identification of the key quality indicators (KQI) relevant to LMD and examine how they are influenced by the quantities which are possible to assess in simulation.
- Simulation of a relevant domain of the LMD process, investigating the change in flowability for new, recycled, and unusual powders.
- Experimental validation on the effect of varying contents of unusual or recycled powders on the KQIs.

Objective 3 Evaluate the sustainability improvement of LMD thanks to this work.

- Evaluate the increased capabilities (SDG 9) in terms of: flexibility, precision, manufacturing speed, accessibility, repair capabilities.
- Investigate the reduction of waste (SDG 12) through: better material and energy use, lees need of subsequent machining, different materials use, powder recycling, less gas use.

1.4 Alignment with H2020 Priorities and Sustainable Development Goals (SDGs)

Assessing the sustainability of AM requires a holistic approach because its advantages might not be evident on a first inspection. Important measures are the potential for energy saving, material saving, life extension, recycling, part consolidation, and process optimization. CM, including subtractive manufacturing, forming processes etc., are at a disadvantage when dealing with complex freeform shapes and heterogeneous structures, potentially requiring subsequent processes and generating a great deal of waste material. DMAM and, more specifically, LMD, also have a great potential for the repair and re-manufacture of complex components, allowing significant reductions in cost, lead times, and waste over CM [1].

Sustainability can be defined in terms of the Sustainable Development Goals (SDGs), a set of 17 interconnected global objectives aimed at addressing the world's most pressing challenges by 2030. These goals encompass a wide range of ambitions, from eradicating poverty and hunger to ensuring quality education, clean water, and sustainable cities.

The scope of this research is in clear alignment with the Horizon 2020 (H2020) agenda and the United Nations Sustainable Development Goals (SDGs). Specifically, our work is strategically positioned to contribute to the attainment of SDG goals 9 and 12.

SDG 9: Build Resilient Infrastructure, Promote Sustainable Industrialization, and Foster Innovation

SDG 9 highlights the importance of developing robust and sustainable infrastructure to support economic growth and enhance the well-being of communities.

This includes the creation of accessible and equitable infrastructure, sustainable industrialization, and technological innovation. The project aims to contribute to this goal through the development of advanced technologies and processes that improve industrial sustainability, resource efficiency, and infrastructure reliability.

9.1 Develop reliable, sustainable, resilient, and quality infrastructure, including regional and cross-border infrastructure, to support economic development and human well-being. Emphasis is placed on affordable and equitable access for all.

9.2 Promote inclusive and sustainable industrialization and significantly increase the contribution of industry to employment and gross domestic product by 2030, in alignment with national circumstances. This includes a twofold increase in least developed countries.

9.4 Modernize infrastructure and reconvert industries to be sustainable by 2030. This involves using resources more effectively and promoting the adoption of clean and environmentally sound industrial technologies and processes. All countries are encouraged to take measures within their respective capabilities.

SDG 12: Ensure Sustainable Consumption and Production Patterns

SDG 12 focuses on the need to achieve sustainable consumption and production patterns. This involves reducing waste generation through prevention, reduction, recycling, and reuse activities. The project aims to significantly contribute to this goal by exploring advanced technologies and processes that enable efficient resource usage, waste reduction, and sustainable production.

12.5 By 2030, significantly reduce waste generation through prevention, reduction, recycling, and reuse activities.

Alignment with H2020 Program Impacts and Key Action Lines

In line with H2020 program impacts, this research underscores the necessity to enhance the efficiency, quality, and reliability of manufactured components

while promoting the rational utilization of resources and raw materials. Such advancements present new business opportunities for Small and Medium Enterprises (SMEs) across Europe.

Key action lines indicated by the H2020 program include the development of new materials (DT-NMBP-19-2019), robust industrial processes (DT-FOF-04-2018), and high-precision measurement of large components (DT-FOF-10-2020). Regarding this work, it contributes to advancing process control in alignment with the H2020 program for quality assurance (DT-FOF-11-2020) through the digitization of associated production processes (DT-SPIRE-06-2019).

Potential Impact of the Research

This research leverages Technologies and Innovation Capacities (TICs) and advanced experimental media to enhance process performance and quality. The anticipated outcome is an improved industry competitiveness achieved by directing production processes towards sustainability in terms of energy and raw material consumption, while concurrently reducing waste disposal.

Furthermore, the research aligns with Europe's priorities by addressing job creation and tackling energy and resource efficiency challenges.

1.5 Chapters overview

This thesis investigates the Laser Metal Deposition (LMD) process, focusing on particle behavior, mass flowrate estimation, and the performance of a continuous coaxial nozzle. The document is organized as follows:

1.5.1 Chapter 1: Introduction

Chapter 1 provides an overview of the LMD process, discussing the fundamental principles and significance of the technology in modern manufacturing. It delves into the specifics of powder delivery systems in LMD machines, highlighting the challenges and innovations in this area. The chapter outlines the aims of the project and formulates key research questions that guide the study. Additionally, it highlights the alignment of this research with the H2020 priorities and Sustainable Development Goals (SDGs), particularly SDG 9 (Industry, Innovation, and Infrastructure) and SDG 12 (Responsible Consumption and Production).

1.5.2 **Chapter 2: Overall Methodology**

Chapter 2 describes the overall methodology employed in this research. It starts with an introduction to Discrete Element Modeling (DEM), explaining its relevance and application in simulating particle behavior in the LMD process. The chapter details how particle motion is simulated, including the principles of contact detection and interaction models. Various calibration methods are discussed to ensure the accuracy of the simulations. The chapter also introduces the coupled modeling framework that integrates Eulerian-Lagrangian forces, providing a comprehensive approach to capturing the complex interactions in LMD. This methodological foundation is crucial for the experimental and simulation studies presented in subsequent chapters.

1.5.3 **Chapter 3: Particle Contact Models**

Chapter 3 focuses on different particle contact models used in the simulations. It begins with Hertz's theory of contact of elastic bodies, providing the theoretical basis for understanding particle interactions. The chapter explores various Spring-Slider-Dashpot models, which are essential for simulating viscoelastic behavior. It also discusses adhesive elastic models, including the Tabor parameter, DMT model, and the M-D transition, which are critical for modeling adhesive forces between particles. The chapter further elaborates on the JKR elastic-adhesive contact model and its energetic balance, offering a detailed understanding of how these models are applied in the context of LMD.

1.5.4 **Chapter 4: The Kinetic Adhesion Test**

Chapter 4 introduces the Kinetic Adhesion Test (KAT), describing the test procedure and the theoretical basis for the calculations. It presents the results of the test, including validation using a DEM model and the strain-rate dependency of particle adhesion. The chapter provides a detailed description of the KAT device, including design files and hardware specifications. Additionally, it covers the determination of Particle Size Distribution (PSD) and other shape parameters through 2D particle characterization. This chapter highlights the importance of adhesion tests in understanding particle behavior and improving the accuracy of simulations.

1.5.5 **Chapter 5: Studies on Pneumatic Conveying**

Chapter 5 examines the pneumatic conveying of particles, a critical aspect of the LMD process. It compares different Eulerian-Lagrangian methods for modeling pipe flow, presenting the simulation models and configurations used. The chapter discusses the results of these simulations, including pressure profiles, particle velocity distributions, and solids flow rates, providing insights into the dynamics of particle transport. It also covers the experimental setup for pneumatic conveying, detailing the circuit, camera setup, and particle tracking methodologies. The chapter concludes with an analysis of the experimental results, including PSD, mass flowrate estimation, flow irregularities, and pressure measurements.

1.5.6 **Chapter 6: Study on the LMD Nozzle**

Chapter 6 presents an in-depth study of the LMD nozzle, both experimentally and through simulations. It begins by describing various nozzle configurations and reviewing previous studies, providing context for the current research. The chapter then details the experimental study of the continuous coaxial nozzle, including the parameters, camera setup, and particle tracking methods used. It presents the results of the experimental study, focusing on particle size distribution, locations, velocities, mass flowrate estimation, and flow irregularities. The chapter also covers the simulation of the continuous coaxial nozzle, discussing geometry and mesh generation, simulation setup, and boundary conditions.

1.5.7 **Chapter 7: Conclusions**

Chapter 7 summarizes the key findings from each of the previous chapters, discussing their implications for the LMD process. It highlights the contributions of this research to the field of additive manufacturing, emphasizing the advancements in understanding particle behavior, improving mass flowrate estimation, and optimizing nozzle design. The chapter also suggests directions for future work, identifying areas where further research could enhance the LMD process.

This structure offers a panoramic view the studies on the powder transport and delivery in the LMD process, from theoretical modeling and experimental validation to practical applications and future advancements. Each chapter builds on the previous ones, creating a cohesive narrative that advances the understanding

of powder delivery technology in LMD.

1.6 Chapter Summary

This introductory chapter establishes the groundwork for investigating advancements in Laser Metal Deposition (LMD) within the framework of additive manufacturing (AM). It begins by referencing the Kardashev Scale and the concept of the Dyson sphere to illustrate the long-term potential of AM harnessing technologies. These references highlight the importance of incremental technological progress in AM as a foundation for more complex future applications.

The chapter provides an overview of Additive Manufacturing, focusing on its significance in both current industrial practices and potential space applications. It introduces Laser Metal Deposition (LMD) as a key technique within Direct Metal Additive Manufacturing (DMAM), detailing its processes, benefits, and the essential role of powder delivery systems. Challenges related to pneumatic conveying in LMD, such as flow irregularities and their effects on deposition quality, are discussed to contextualize the research objectives.

Central to this work are the outlined objectives and research questions aimed at analyzing and improving pneumatic conveying systems for LMD. The chapter also explains how this research aligns with Horizon 2020 priorities and the United Nations Sustainable Development Goals (SDGs), specifically SDG 9 on Industry, Innovation, and Infrastructure, and SDG 12 on Responsible Consumption and Production. This alignment emphasizes the study's focus on enhancing sustainable industrial practices and fostering technological innovation.

Finally, the chapter outlines the structure of the thesis, providing a brief overview of the subsequent chapters that cover methodology, particle contact models, experimental studies, and simulations related to LMD. This organized approach ensures a thorough examination of powder transport and delivery in LMD, contributing to the optimization and sustainability of additive manufacturing processes.

CHAPTER

2

Overall methodology

Particulate systems are very common in natural and industrial processes. They are composed of a large number of individual grains or agglomerates, interacting with each other. Each element of the system can be relatively simple, obeying Newton's equations of motion and the solid interactions. The large number of degrees of freedom of the grains in the system results in a complex macroscale dynamics, behaving as a solid, liquid, or gas depending on factors such as material properties, compactness, and external loading or fluid flows. DEM (Discrete Element Method) is a modeling technique that aims to capture this emergent complex behavior, arising from the interaction of relatively simple discrete elements (see Figure 2.1).

Two fundamental perspectives delineate fluid motion: the Lagrangian and Eulerian specifications of the flow field.

Lagrangian Specification: In the Lagrangian specification, observers track individual fluid parcels as they traverse space and time. Plotting the position of a specific parcel over time generates a pathline, akin to drifting down a river while seated in a boat.

Eulerian Specification: Conversely, the Eulerian specification focuses on fixed locations in space, observing how the fluid flows through these points as time progresses. This can be envisioned as sitting on the bank of a river and observing the water pass at a fixed location.

These specifications, often denoted as the Lagrangian and Eulerian frames

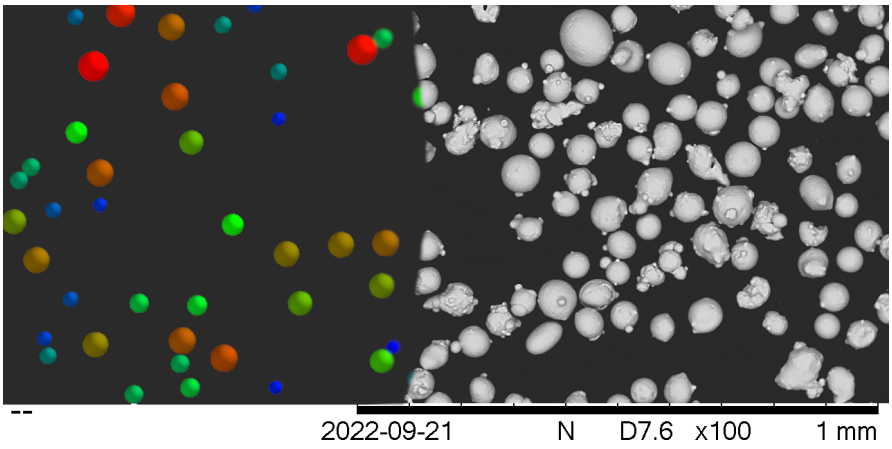

Figure 2.1: DEM aims to represent the behavior of real metallic powder particles (on the right, gas atomized 316L stainless steel powder, SEM image taken during the mobility at Newcastle University) using a simplified, computationally efficient representation (spheres on the left, colored by size, made with Altair EDEM).

of reference, are not strictly bound to any particular observer's perspective or coordinate system. They can be applied across diverse frames of reference and coordinate systems, rendering them versatile tools for fluid motion analysis.

In the domain of granular flows, these perspectives find reflection in simulation methodologies:

Lagrangian Simulations: also known as mesh-free simulations, they utilize simulation nodes that may move following the velocity field. This aligns with the Lagrangian perspective of tracking individual parcels, making it suitable for tracking each individual particle within the granular assembly.

Eulerian Simulations: employ a fixed mesh, emphasizing how the properties of large assemblies of particles evolve at specific grid points as time advances. This approach is particularly relevant when the motion of each granule can be effectively averaged over the larger assembly.

To accurately simulate the interactions between fine solid particles dispersed in a fluid domain, coupling methods such as CFD-DEM (Computational Fluid Dynamics - Discrete Element Method) are employed. CFD-DEM integrates the Eulerian approach for the fluid phase and the Lagrangian approach for the particle phase, providing a comprehensive analysis of multi-phase flows.

This method models the fluid phase using traditional CFD techniques, captur-

ing the macroscopic fluid behavior in an Eulerian framework. Simultaneously, the DEM tracks individual particles in a Lagrangian framework, calculating their trajectories based on Newton's equations of motion and accounting for inter-particle and particle-fluid interactions.

Given the scale of Laser Metal Deposition (LMD) systems and particles, CFD-DEM is the method of choice for this work. This approach is extensively used in various industrial and natural processes, such as pneumatic conveying, sediment transport, and fluidized beds. By coupling the detailed particle dynamics with the fluid flow, CFD-DEM provides insights into phenomena like particle agglomeration, collision dynamics, and the impact of particle shape and size on the overall flow behavior [117].

2.1 Discrete Element Modeling (DEM)

DEM simulations fall under the definition of Lagrangian simulations, encapsulating the precise tracking of individual particles in the granular assembly. The motion of each grain k in the system follows the behavior of a rigid body, according to Newton's equations of motion. These equations govern how objects in the system move, rotate, and interact under the influence of external forces. The motion of a grain can include translational and rotational aspects, both of which are determined based on its physical properties and the forces acting upon it. The dynamic behavior of granular materials in a DEM simulation is intricately linked to the interactions between particles, particularly during contacts or collisions. These interactions are depicted in detail in Figure 2.2. This figure provides a visual representation of the flow of information and computations between Newton's laws of motion and the contact mechanics that govern the forces and interactions at contact points between grains. In the simulation, the forces acting on each element (individual grains or particles) are determined by considering the mechanics of contact. These forces come into play during collisions or interactions between particles, where factors such as friction, hysteretic dissipation, and other material properties influence how the particles respond to the contact.

Understanding the contact behavior between discrete particles is pivotal in DEM. Chapter 3 focuses on the various contact models used to define contact distances and interaction forces between particles. Notable models include Hertz,

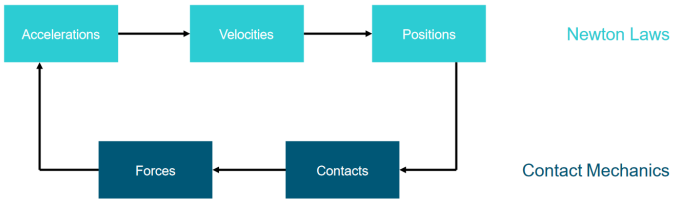

Figure 2.2: Flowchart depicting the relationship between Newton's laws and contact mechanics in DEM [Altair.com].

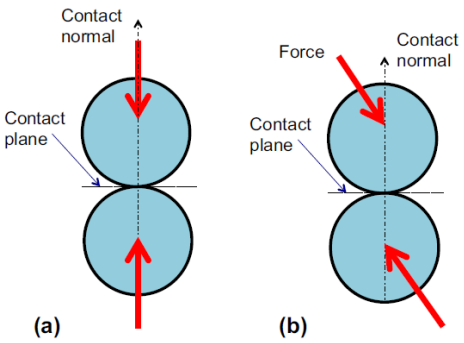

Figure 2.3: Illustration of normal (a) and oblique (b) interaction between two spheres [109].

Hertz-Mindlin, Spring-slider-dashpot, and adhesive models such as linear adhesion and JKR model. Elasto-plastic contact models are important to account the additional energy dissipation due to plastic deformation in high velocity impacts.

In DEM the particles can be either spherical, with relevant simplification in the contact calculation, or represented by more complex shape models (multisphere, rod-like, hyperquadric, polygonal, among others) [142][74]. When generating particle-shapes for DEM simulations, the multisphere method is gaining a lot of interest: the computation complexity of contact determination scales about linearly with the number of spheres per particle, which is a great advantage when matching the simulation detail with available computational resources. Angelidakis et.al. released two complementary pieces of software. SHAPE analyzes the 3D particle shape, for instance coming from a Computerized Tomography (CT) scan, to extract the single particles from the granular assembly, and provides a variety of standardized metrics on the particles (volume, surface area, sphericity, just to name a few) [8]. After this, CLUMP can be used to fill the 3D envelope

with a pre-determined number of spheres or desired precision: the same metrics are calculated and matched between the real representation determined experimentally, and the resulting multi-sphere clump [7].

Granular Dynamics (GD), or Discrete Particle Modeling (DPM), has been extensively used in previous studies on Laser Metal Deposition (LMD) and pneumatic conveying. These methods have proven effective for systems with very low particle loading. However, they are limited in their ability to accurately model more complex systems where particle-particle interactions play a significant role. For instance, GD and DPM treat particle interactions as instantaneous events and do not permit particle overlaps, which restricts their applicability to dilute flow regimes [80].

In contrast, the Discrete Element Method (DEM) provides a more general approach, capable of simulating systems ranging from very dilute to dense particulate flows. DEM allows for particle overlaps to represent deformation during contact, and explicitly models forces during particle-particle and particle-fluid interactions. This makes DEM a more suitable choice for a broader range of scenarios, including the study of multiphase flows where both dilute and dense regimes are present.

Previous work on LMD nozzles has used a variety of methods, including DPM [10], two-fluid models, and multiphase particle-in-cell (MP-PIC) approaches [86]. The flexibility of DEM, particularly when combined with computational fluid dynamics (CFD-DEM), allows for a more detailed and accurate analysis of particle behavior across different flow regimes. This capability is critical for applications such as LMD and pneumatic conveying, where particle dynamics are influenced by both fluid forces and inter-particle interactions.

By employing DEM in this study, a more comprehensive understanding of the system's behavior can be achieved, capturing both dilute and dense flow regimes with higher accuracy than would be possible using GD or DPM alone. The ability to model particle deformation and interaction forces provides a deeper insight into the physics of the system.

Solid Particles:

Thermal Effects:

Conduction of heat with solids or fluids.

Convection of heat with fluids.

Radiative heat transfer.

Chemical or physical Processes:

Dissolution in a fluid.

Coating.

Composition change.

Combustion processes.

Radioactive decay.

Mechanical and kinematic Behavior:

Deformation and contact behavior.

Contact forces and frictional interactions.

Failure and cracking of solid particles.

Adhesion and cohesion.

Hydro/Aero-dynamic forces acting on particles and relative reaction forces on the fluid.

Erosion and Wear:

Abrasion and wear of solid particles.

Erosion and material loss from the boundaries.

Particles Breakup:

Breakup of solid particles due to various forces and conditions.

Fluid Particles:

Thermal Effects:

Heat conduction with solids or fluids.

Heat convection with fluids.

Radiative heat transfer.

Chemical and physical Processes:

Dissolution in a fluid.

Chemical reactions occurring within fluid particles.

Changes in composition and properties of fluid particles due to chemical interactions.

Combustion processes.

Phase transitions (solid to liquid, liquid to gas, evaporation and condensation).

Hydrodynamic Behavior:

Fluid flow and pressure distribution within the particles.

Interaction forces among fluid particles.

Shear and turbulence effects within the fluid particles.

Breakup and Coalescence:

Modeling breakup of fluid particles due to mechanical or thermal stresses.

Coalescence of fluid particles leading to larger agglomerates.

2.1.1 **Particles' motion**

The six degrees of freedom in space of each object responds to the applied forces (translation) and moments (rotation):

$$\frac{d\vec{v_k}}{dt} = \frac{\sum \vec{F_k}}{m_k} \tag{2.1}$$

$$\frac{d\vec{\omega_k}}{dt} = \frac{\sum \vec{M_k}}{\hat{I}_k} \tag{2.2}$$

where forces $\vec{F}$ and moments $\vec{M}$ acting on the particle k change its linear velocity $\vec{v}$ and angular velocity $\vec{\omega}$ with respect to mass m and moment of inertia $\hat{I}$. The contact forces are determined by equations that describe the elastic behavior of the material, or contact models, which can encompass a variety of effects including strictly elastic Hertzian behavior, viscous dissipation, plastic deformation (and consequent energy dissipation), adhesion, as well as long-distance forces (electrostatic, magnetic). These forces can act in the direction of contact between the two elements or obliquely, as shown in Figure 2.3. Other forces include gravity and other external fields, such as those from a stationary or moving fluid. Forces can be further categorized into gravitational forces $F_{g,k}$, contact forces $F_{C,k}$ arising from interactions with other particles or walls and mediated by contact models, and non-contact forces $F_{NC,k}$ arising from interactions with non-contact fields such as electromagnetic effects or interactions with a stationary or moving fluid.

The motion of particles in space is tracked using Equations 2.1 and 2.2, which essentially form an Ordinary Differential Equation (ODE) problem. Numerical integration is a common technique for solving this class of mathematical problems. The Euler method, a simple forward first-order numerical procedure, is often used in DEM to integrate the equation of motion over a time step. This method provides a solution to ODEs based on an initial value. Considering the degrees of freedom of the particles, where positions and rotations are denoted by $\vec{x}(t)$, velocities and rotational velocities by $\vec{v}(t)$, and accelerations and angular accelerations by $\vec{a}(t)$, the evolution of an element in the system over time is determined using:

$$\vec{x}(t + \Delta t) = \vec{x}(t) + \vec{v}(t) \cdot \Delta t \vec{v}(t + \Delta t) = \vec{v}(t) + \vec{a}(t) \cdot \Delta t \tag{2.3}$$

where t is the time of the simulation, and Δt is the time-step. The evolution over time is represented in Figure 2.4.

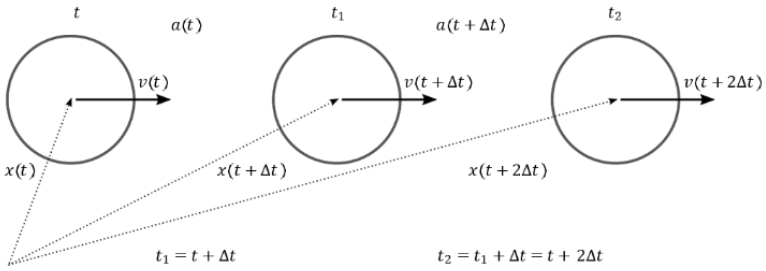

Figure 2.4: Integration of the motion of a single element in terms of accelerations $\vec{a}(t)$ and velocities $\vec{v}(t)$

The time-step Δt must be fine enough to avoid instability in integrating the particle's motion (see Figure 2.5). A finer time-step can prevent numerical instability in rapidly evolving systems, but each calculation comes at a computational cost. Thus, finding a suitable balance is crucial for efficient simulations. In general, Euler method of numerical integration is perfectly suited to solve the ODEs that describe the movement of each particle. In specific cases, the Euler method can be substituted with higher order explicit or implicit integration schemes to increase the stability and efficiency of the simulation [100].

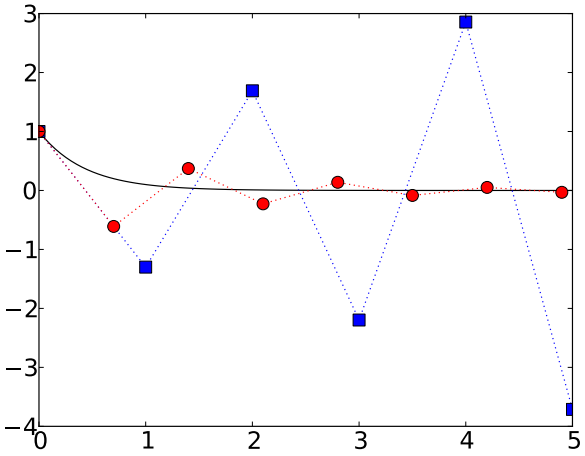

Figure 2.5: Solution of $y' = -2.3y$ computed with the Euler method with step size $h = 1$ (blue squares) and $h = 0.7$ (red circles). The black curve shows the exact solution Wikimedia file.

Impact duration

Having covered the fundamental definitions of DEM, it is important to understand the temporal resolution necessary to capture the impact event. For spherical and perfectly elastic elements, Raman [102] derived the duration of an impact based on Hertz's contact theory [48]. This analytical work provides the duration the sphere remains in contact with a surface during an impact at velocity v_{in}:

$$t_i = 2.865 \left(\frac{m^2}{RE^{*2} v_{in}} \right)^{\frac{1}{5}} \tag{2.4}$$

Let's consider a standard scenario involving an impact between steel elements with $E_1 = E_2 = 2e11$ Pa, yielding $E^* = 1.10e11$ Pa (see Eq. 3.3), and a radius $R = 5$ mm. For a sphere of this size, the mass is $m = 4.178$ g, assuming a density $\rho = 7980$ kg/m^3. Given an impact velocity of $v_{in} = 1$ m/s, the resulting contact time is $t_i = 35.4\mu$s. To put this value in perspective, in the same time the undisturbed sphere would move only 0.71% of its radius; also, t_i is only 0.035% of the time needed by the sphere to acquire the velocity v_{in} under gravity.

Within this exceedingly brief time interval, a wealth of critical information can be acquired with DEM. The impact's energy propagates through the particle, imparting motion and causing reflections at the interface. Some of this

energy is transmitted to the collision site, where it may transform into heat or even cause surface erosion by dislodging material. The particle and surface can form diverse bonds (van der Waals, liquid bridge, chemical interlocking, metallic bond, etc.), dissipating a portion of the energy as they separate. Localized plastic deformation may also occur, alongside an array of other events. All these intricate occurrences can be meticulously described and accounted for, using the appropriate constitutive models.

Rayleigh time-step

In DEM codes, the temporal resolution of particle interactions is often specified as a fraction of the time it takes for the impact's energy to propagate throughout the entire colliding body. When considering the energy transfer through acoustic superficial waves, Miller et al. [37] demonstrated that Rayleigh waves account for approximately 67% of the radiated energy, in contrast to dilational (7%) and distortional waves (26%). These three wave types are visually depicted in Figure 2.6. By selecting a sufficiently small time step in DEM, we restrict the propagation of disturbance waves from each particle beyond its immediate neighbors. A suitable time step, often referred to as the Rayleigh time step, is approximated based on the propagation speed of Rayleigh surface waves. Typically, a fraction of this time step is utilized to maintain realistic force transmission rates and mitigate numerical instability.

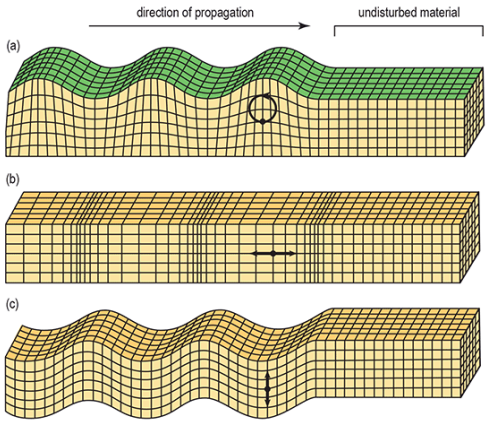

Figure 2.6: Three types of seismic waves: (a) Rayleigh wave, (b) dilational wave, and (c) distortional wave (Kansas Geological Survey website). Arrows indicate particle motion for each type.

An estimation of the critical time-step Δt_c can be determined using the method outlined in [21]. The fundamental equation is given by:

$$\Delta t_c = \frac{\pi R}{v_R} = \frac{\pi R}{\lambda}\sqrt{\frac{\rho}{G}} \tag{2.5}$$

$$\lambda = 0.8766 + 0.1631\nu \tag{2.6}$$

Here, v_R is the velocity of Rayleigh waves, ρ is density, ν is Poisson's ratio, and G is the particle's shear modulus, calculated from the Young modulus E as:

$$G = \frac{E}{2\ (1+\nu)}. \tag{2.7}$$

For a steel particle with a radius of 5 mm, the calculated critical time-step is $\Delta t_c = 5.47\ \mu$s.

The smaller the fraction of Δt_c, the better is the resolution of the impact phase. The obvious advantage of the increased resolution is contrasted by the steep increase in computational power needed to perform each operation.

Integrating the equation of motion for a particle, especially during impacts or while in motion through space, demands varying levels of time resolution. In response, many DEM codes utilize a *substepping* strategy. This involves employing a larger timestep for integrating particle motion through space and a significantly smaller timestep exclusively around the moment of contact between elements.

In the context of DEM simulations, especially for collision-dominated flows, reducing the Young's modulus to obtain a larger critical time-step is a common practice, since its impact on the results is limited [138]. However, when effects such as dense phase and cohesion are present, certain parameters may need to be scaled accordingly [133] [52]. Even lowering the elastic modulus by several orders of magnitude might be acceptable for most cases, resulting in adequate results and greatly reduced computation times.

2.1.2 Contact detection

Contact detection is the strategy implemented by each code to determine when different elements in the system become in contact, and the evaluation of the contact should be initiated. The positions of neighboring particles are compared after every time-step and if they are close enough, the process of the contact evaluation begins. Contact detection in discrete element modeling is a complex

mathematical problem, under active research given the huge impact on computational performance.

The contact detection evaluation is performed after each time-step advancement. The Courant-Friedrichs-Lewy condition is a mathematical tool for discrete calculations, and asserts that the time step must be sufficiently small to allow information to propagate adequately through the discretization of space [22]. To prevent issues like skipping across interactions or excessive overlap, the step advancements must be appropriately small. In DEM, this condition can be expressed as the ratio between the distance covered by a particle in the system and the size of each particle. The objective is to avoid the situations in which particles are allowed to transverse a distance that would put them on the other side of the impacting particle, skipping the contact altogether. Given the relative velocity of particles v_p, the time-step Δt, and the discretization distance L:

$$Co^{DEM} = \frac{v_p \, \Delta t}{L} < 1 \tag{2.8}$$

Respecting the Courant-Friedrichs-Lewy condition ensures that the contact can be effectively detected. Depending on the strategy employed by the DEM code, the discretization distance can correspond to the particle radius r_p, or to the size of a sub-grid on which the lagrangian elements move.

Spatial sorting

The most commonly used particle shape in DEM simulations is the sphere, which is both conceptually and computationally simple. Contact is detected if the distance between two spheres is less than the sum of their radii. In a brute-force approach, evaluating all the combinations to find the contacting spheres, the complexity of the problem scales as $O(N^2)$, where N is the number of particles in the computed domain: assuming a simulation of $N = 10\ 000$ particles. At each time-step, distances must be computed for all possible particle combinations, resulting in $N(N-1)/2 = 5\ 000\ 000$ force computations. For approximately equal-sized particles in a packed bed,each particle can realistically exchange forces only with 6 other particles, therefore only about $(6N)/2 = 30\ 000$ evaluations should be necessary. This process is computationally expensive and together with the force calculations takes about 70% of the DEM computational effort [135] [99]. Contact detection typically involves two main phases: spatial sorting and contact

resolution. The spatial sorting phase aims to reduce the computational load by minimizing the number of objects that need to be considered for potential contact with a given object, thus avoiding an exhaustive pairwise comparison. On the other hand, the contact resolution phase focuses on resolving the specifics of the contact between two identified objects.

Particle reordering can be performed according to a variety of methods, all with the objective to restrict contact search only with the most likely neighbors. Tree of the possible methods are [99]:

- **Verlet lists** help identify pairs of particles that remain close neighbors over a few subsequent time steps, allowing for efficient particle tracking. During the setup phase, particle pairs within a certain constant distance, also called *Verlet distance*, are recognized as close neighbors and their interactions are recorded. Each particle maintains its own Verlet list, documenting these neighboring particles for future reference.

- **Link cells algorithms** divide the simulation domain into a spatial grid consisting of uniformly sized boxes. Each box is allocated a list of particles present within it. The size of each box must be greater than the size of any particle it contains. This algorithm searches for collision partners among particles within the same box and neighboring boxes.

- **Lattice algorithms** follow a similar approach of subdividing the simulation domain into a spatial grid with equally sized boxes. However, each box is constrained to contain at most one particle at its center, and it must be smaller than any particle. Collision partners for a particle are identified within a subset of the domain containing a lesser number of particles.

A great effort is under way to improve these and similar algorithms, especially with the intention of adapting them to highly parallel computation and GPGPU architectures [144], and especially aiming to improve contact detection of non-spherical geometries [75].

2.1.3 Contact Distance and Contact Models

Figure 2.7 shows the four fundamental directions where the stresses can be applied at the point of contact. Understanding the normal contact model is fundamental

to comprehending the behavior of granular matter. In cases of tangential, twisting, and rotational motion, most models utilize the normal force to derive their magnitude.

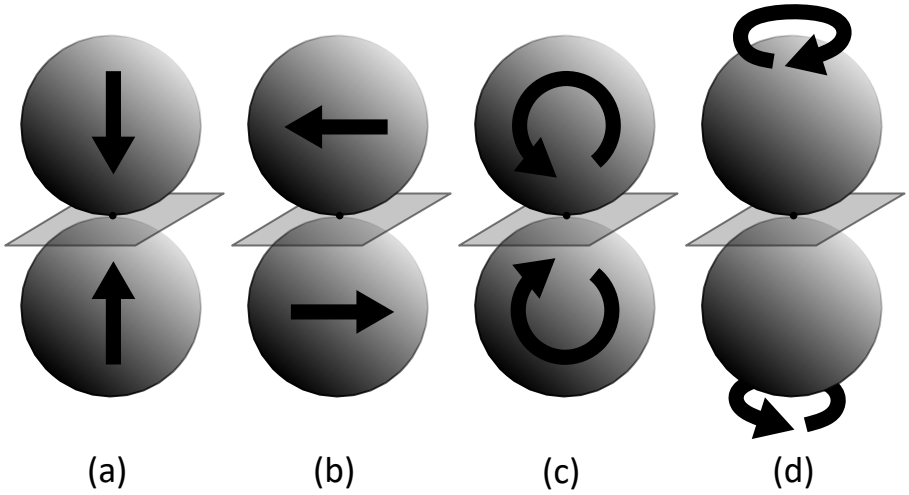

Figure 2.7: Applied stresses in the contact of two spheres: (a) normal force F_n, (b) tangential force F_t, (c) rotation torque M_r, (d) twisting torque M_t. The contact point and contact plane are represented.

In the contact's normal direction, most DEM software use the contact overlap δ to define the magnitude of the contact. Positive values denote that the bodies are in contact, and the normal contact model is evaluated. Negative values indicate that the bodies are at a distance, and the contact model is evaluated only in specific cases (forces acting at a distance, like electrostatic or magnetic, and adhesive models with contact point deformation). Figure 2.8 shows how the contact overlap is defined (δ, or δ_n for normal overlap).

Linear Elastic materials are the most basic representation of the behavior of solids. When they are deformed at a strain ϵ, the material responds with a stress σ (or the other way around). This process is considered reversible, and the slope of the line is the Young modulus E. In an object with an elastic-perfectly plastic behavior, after a determined stress Y, the material starts flowing under the action of the stress and deforms irreversibly. These two behaviors are represented in the diagrams of Figure 2.9. These two simple behaviors are already suitable for the majority of scenarios, depending on the detail needed to represent the phenomenon. When analyzing real materials, the models can be way more

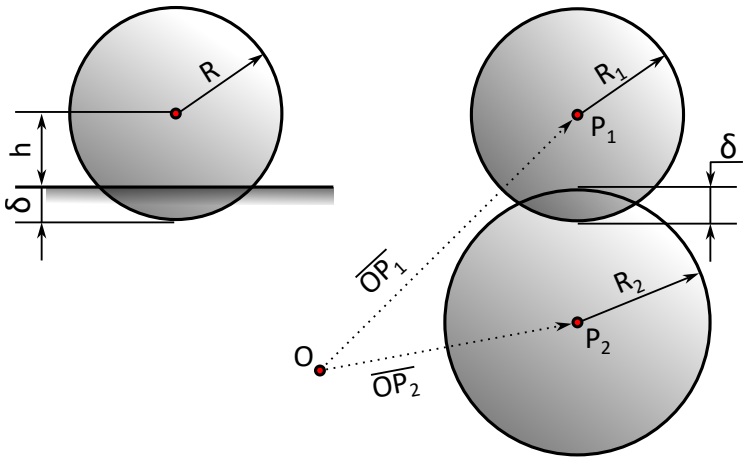

Figure 2.8: Visual definition of the contact overlap δ. When a sphere approaches a surface, the contact overlap is estimated using the center distance from the surface $\delta = R - h$. For two spherical particles, the contact overlap is $\delta = (R_1 + R_2) - |\overline{P_2P_1}| = (R_1 + R_2) - \left|\overline{OP_2} - \overline{OP_1}\right|$.

complex, encompassing non-linearity, hysteresys, strain rate dependency etc.

Figure 2.10 is a qualitative representation of the pressure profile between a perfect sphere and a plane. The first image (a) represents the behavior of a perfectly elastic material. It is the pressure profile calculated analytically by Hertz [48], assuming a linear elastic material. The integral of said pressure profile across all the surface is the net normal contact force. In the second image (b), the material is now allowed to yield under the action of the stress. Notice the flattened top of the pressure profile, corresponding to the yield pressure. This behavior is typical of perfectly plastic materials.

A third fundamental behavior that needs to be captured is the propensity of surfaces to adhere to each other. In Figure 2.10 the pressure profiles (c) and (d) result from the addition of an adhesive pressure, uniform across the surface. Notice the negative side of the pressure profile, which in this case can result in a net negative total normal force, resisting the separation of the element in contact.

2.2 Calibration Methods

Granular materials are formed by a large number of particles, or granules, that interact with each other. Generally, these materials do not interact by forming chemical or physical bond that change the integrity of the granules, and the

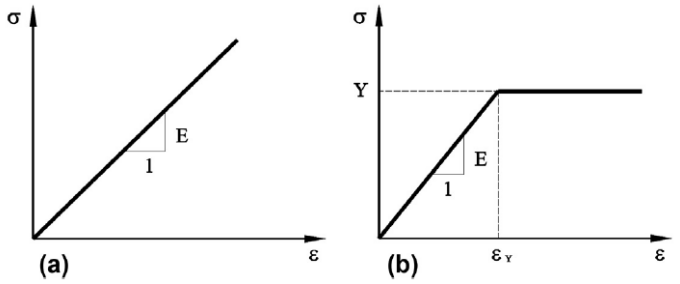

Figure 2.9: Stress-strain relationships for (a) elastic and (b) elastic-perfectly plastic materials, where E is the Young's modulus, Y the yield stress and ϵ_Y the yield strain [109].

granules size go from few hundredths of nanometers to several millimeters. The spectrum of application is very wide, and it is difficult to provide models that are adequate for all the scales. Generally, the granular material motion is complex and is the result of a multitude of interactions between each of its constituent granules. DEM codes aim to replicate these emergent complex behaviors by using models that are as simple as possible to represent the observed phenomena. The simulation of granular material requires a multi-scale perspective. This necessity is even amplified when considering the interaction with other domains, such as deformable structures and fluids.

Among the additive manufacturing processes described in Section 1.2, some employ granular materials. As a general indication, finer powders aid in obtaining parts with finer details. Figure 2.11 shows the typical PSD of a metal powder produced by gas atomization (black line). Of the whole prodution, DED typically utilizes powders with particle diameters in the range of 50 to 150 micrometers (μm), while powders for L-PBF tend to be finer, usually ranging from 10 to 70 micrometers (μm) [84]. The samples used in this work fall in this indicative size range.

Numerical models are an excellent tool to gain insight into a variety of processes, and are proving invaluable in contemporary scientific and industrial endeavour. The study of how complex behaviors emerge from simple rules, especially in computer simulations, also sheds light on the complexities found in nature. Varenne [128] highlights the significant role that modeling and simulation have played in the field of complexity science, which seeks to understand how large-scale

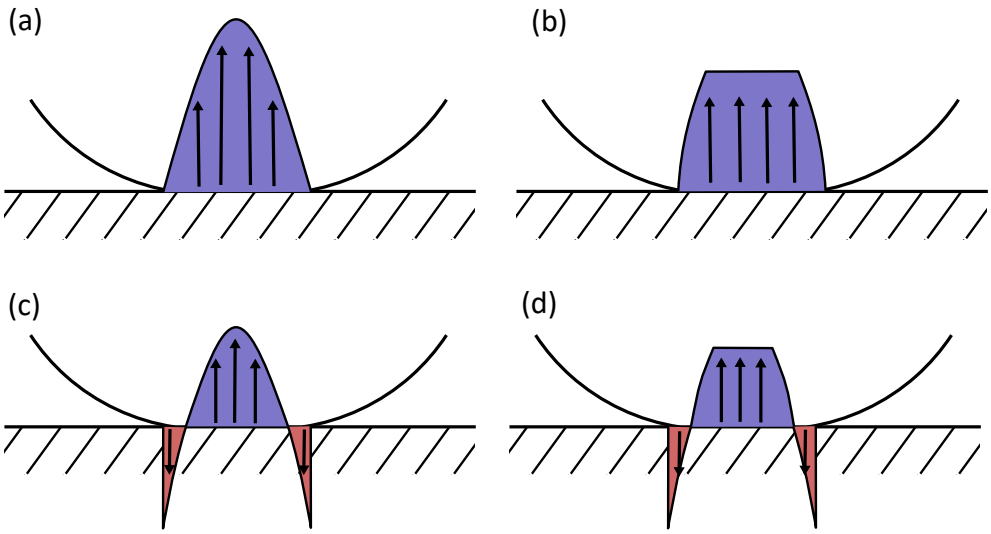

Figure 2.10: Simplified representations of the pressure profile on the contact area of a sphere on a surface: (a) elastic, (b) elastic-plastic, (c) elastic-adhesive, (d) elastic-plastic-adhesive. Arrows pointing towards the top represent a repulsive pressure; the integral of the pressure profile results in the net normal reaction force.

phenomena arise from the interactions of smaller elements. The advancements in computing since the Second World War have been particularly important for this field. Varenne's work outlines the evolution of modeling methodologies, showing how our ability to simulate both artificial and natural systems has grown. This progress in simulation technology not only improves our understanding of man-made systems but also offers insights into the complex behaviors found in the natural world, demonstrating how simple underlying rules can lead to rich complexity. However, the quality of the obtained information must be verified through the experimental validation of the results.

Using a relatively limited set of parameters, discrete element modeling (DEM) can replicate the often complete response of particulate materials [24]. Similarly, In CFD the relatively limited set of rules provided by the Navier-Stokes equations give rise to very complex behaviors [85]. Finding the appropriate parameters so that the simulation has predictive capability of the natural phenomena under observation is an area of active investigation [47]: some parameters can be directly measured with a high degree of precision, such as particle size or density. The KAT, described in Chapter 4, aims to aid in measuring the Adhesive Energy

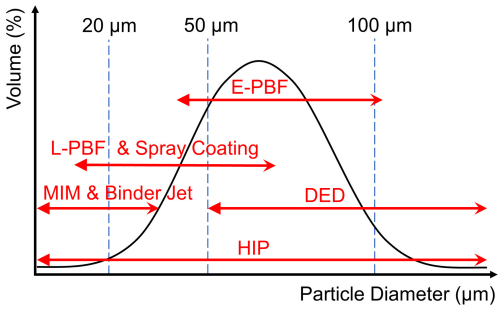

Figure 2.11: Schematic of the powder size distribution (PSD) for as-produced atomized powder (black curve) which shows volume distribution percentage against the particle diameter. Optimal PSD ranges for different applications such as L-PBF, E-PBF, MIM, HIP, binder jet, spray coating and direct energy deposition (DED) are shown as red arrows [84].

for the JKR contact model in a relevant and direct way. Other parameters are at best impractical to measure directly, and are usually inferred from the bulk behavior. Examples are the restitution coefficient (normal and tangential), sliding and rolling friction, and other parameters needed by the various possible contact models existing in literature (see Chapter 3).

A simulation can be calibrated by directly measuring the fundamental quantities needed by the model, followed by a verification step which should confirm the computed results. This is often the case for CFD, especially in the laminar regime and simple geometries. The Navier-Stokes equations can be written with the assumption of linear viscosity. This description can be solved analytically in very simple cases. In particular the Couette flow is a specific analytical solution to the N-S equations, which can give a definition for a test to measure viscosity directly. Ideally, the measured force $F = \mu \frac{u}{y}$ is directly and exclusively affected by the single material parameter, in this case viscosity (μ), while the rest are controlled variables (velocity u, and gap y). The Couette device, depicted in Figure , is a simple tool that directly relates the viscosity to a measurable quantity (the resisting torque), with few process variables: geometry and rotational velocity.

The physical variables are not always directly accessible experimentally. This is often the case in DEM simulations, where the physical variables such as the restitution coefficient, friction etc are at best impractical to measure, and at worst the values that best match the bulk behavior are quite different from those coming

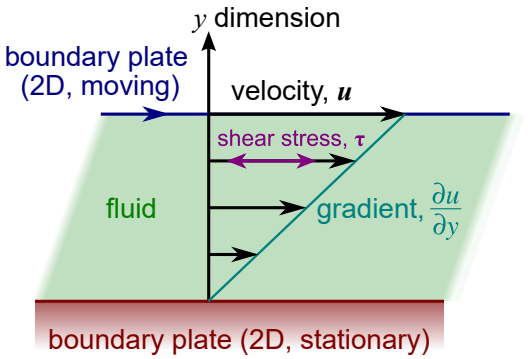

Figure 2.12: Figure showing a planar Couette flow. The shear stress (τ) is proportional to the dynamic viscosity (μ) by the formula $\tau = \mu \frac{\delta u}{\delta y}$. The resulting force on the plate indicates how viscous the fluid is [Wikimedia].

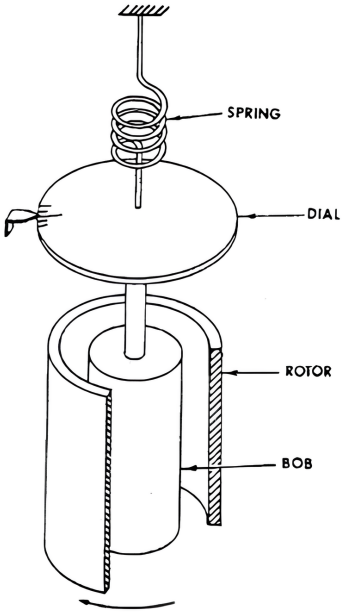

Figure 2.13: Couette device for viscosity measurement [Torsæter2003].

from a direct measurement.

In DEM simulations, accurately capturing the dynamics and bulk behavior of granular materials relies on the precise calibration of physical variables such as the restitution coefficient and friction. However, these variables are not always directly measurable through experimental methods, often due to the complex nature of the interactions within the material systems. As Coetzee [20] emphasizes, the process of calibrating DEM simulations involves a critical choice between direct measurement of parameters at the particle or contact level and reverse calibration, where parameters are iteratively adjusted to match the observed bulk behavior of an assembly of particles. This approach circumvents the inherent challenges in measuring physical variables directly, where the values obtained through calibration to match bulk behavior might significantly diverge from those that could be measured directly, underscoring the importance of a careful and informed calibration process to ensure the accuracy and reliability of DEM simulations.

The calibration process in DEM simulations is essentially a multi-objective optimization problem, requiring a combination of several variables and their sim-

ulated effects to closely match experimental data while minimizing an objective function directly linked to the error between simulation and experiment. This can generally be expanded to other simulation methods, including CFD. Sensitivity analyses emerge as powerful tools for understanding the influence of parameters. The use of Design of Experiments (DOE) tools, such as the Taguchi method, significantly aids in this endeavor by systematically analyzing the input parameters' influence on the simulated response of powder agglomerates. Hanley, O'Sullivan, et al. [47] applied the Taguchi method to optimize the DEM calibration process for bonded agglomerates. Their approach not only identified the most critical parameters for successful calibration of 2D and 3D models but also demonstrated the fundamental flaw in the conventional "one at a time" parameter analysis. This research underscores the efficacy of a carefully strategized application of Taguchi principles in providing a robust calibration procedure for DEM simulations, highlighting the importance of an integrated approach to parameter sensitivity analysis and optimization in the complex calibration process.

An alternative approach uses of Artificial Neural Networks (ANN) for the identification of DEM simulation parameters, as presented by Benvenuti et al. [13]. This innovative method establishes a link between macroscopic experimental results and microscopic numerical parameters using ANNs. Initially, a series of DEM simulations with varying parameters trains a feed-forward ANN through backward-propagation reinforcement. This trained network then predicts the macroscopic ensemble behavior based on new sets of particle-based simulation parameters, effectively creating a database that correlates specific macroscopic behaviors with microscopic simulation parameters. Once trained, the ANN provides a robust link between experimental outcomes and DEM parameters, streamlining the calibration process for any given granular material without the need for repetitive training.

Figure 2.14 provides a graphical representation of the calibration process in DEM simulations, focused on the optimization of parameters to minimize errors. The parameters P1 and P2 represent model parameters that are impractical to measure directly, or even that do not have a direct physical equivalent to measure directly. The results R1 and R2 represent physical quantities that can be effectively be measured in both the simulation and the experiment. The 3D surface

plot on the left depicts how variations in simulation parameters P1 and P2 influence the error in simulation result R1 when compared to experimental data. The diagram on the right shows the regions where the error for two different results, R1 and R2, is minimized. The overlapping area between these regions indicates the parameter settings that offer a balanced solution, minimizing error for both results. This visualization underlines the multi-objective nature of simulation calibration, where multiple outcomes must be simultaneously optimized.

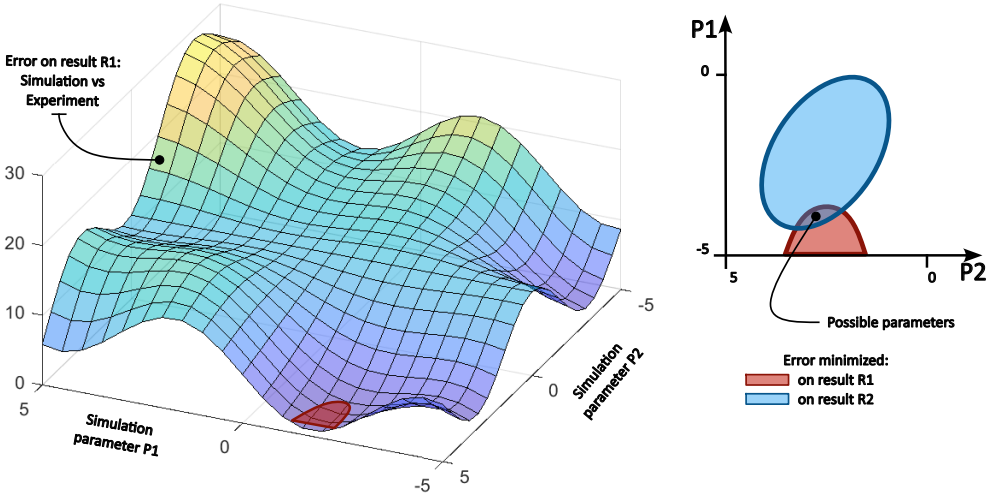

Figure 2.14: Graphical representation of the Multi-Objective Optimization principle applied to the choice of appropriate parameters (P1 and P2) that minimize the error of the simulation compared to experimental results (R1 and R2).

2.3 Coupled Modeling framework

In the book *Essentials of Fluidization Technology* [42], the sixth chapter *CFD and its application to fluidization* categorizes models for gas-solids flows, depicted in Figure 2.15. The level of detail is highest on the left-hand side, where the fluid-particle interaction is modeled directly, at the highest computational cost. This rough categorization distinguishes between the various models based on a balance between the level of detail of the granular motion and its interaction with the fluid, the number of particles (or, roughly, the scale of the system compared to the particle size), and the available computational resources. Especially large scale simulations, for instance of industrial chemical reactors, require a multi-

scale approach, an example of which is reported in Figure 2.16: on the left, simulating an industrial-scale fluidized bed using a two-fluid method with varying grid resolutions; in the middle, analyzing particle segregation and accumulation in homogeneous isotropic turbulence, considering inter-particle collisions; on the right, simulating the hydrodynamic interaction between colliding solid particles in studies on agglomeration using Lattice Boltzmann Method (LBM).

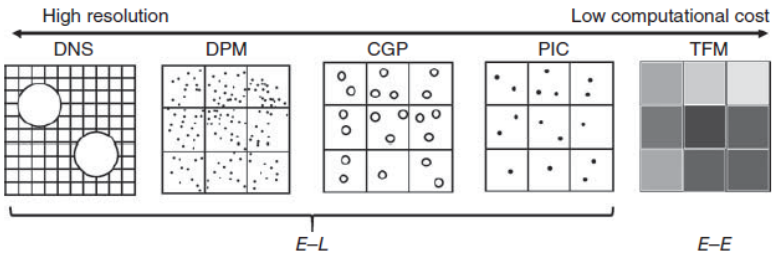

Figure 2.15: Different CFD models for gas-solid flows [42].

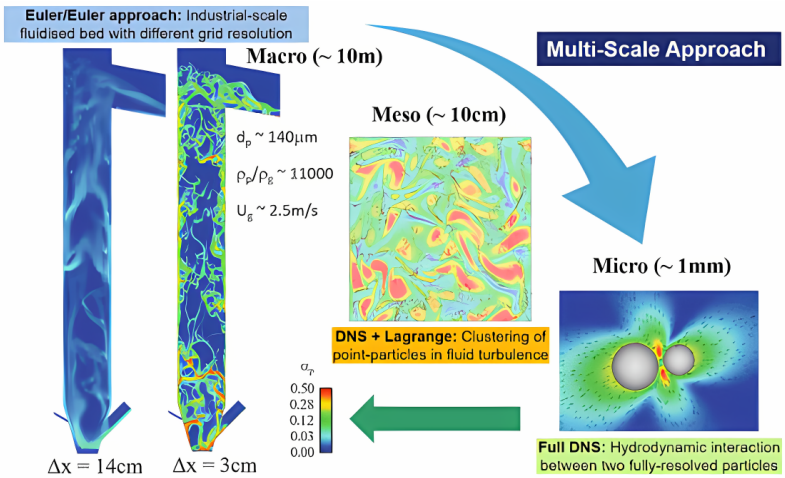

Figure 2.16: Representation of the multi-scale approach for numerically calculating dispersed two-phase flows, upscaled from Sommerfeld's chapter [117].

Resolved solvers calculate the fluid force on particles by integrating the pressure and velocity fields over their surfaces, requiring a dense grid for accurate fluid flow measurements in CFD applications. Isoz et al. report an interesting open-source implementation (openHFDIB-DEM) [53]. A very fine grid is used to capture the particles' boundaries with the advantage of correctly capturing

the particle-flow interaction. This very interesting code is able to model the flow around each particle and therefore eliminating the need of a dedicated drag model, which is especially useful for irregularly shaped particles. The desired domain sizes and particle numbers to be considered in this work, however, resulted in impossibly long computation times. These methods are extremely useful when dealing with a reduced number of particles in a relatively small domain, without limit in the particle packing.

Unresolved solvers use empirical drag models based on relative velocity and fluid volume fraction, which do not require a dense grid. These are suitable only if the particle size is smaller than the fluid mesh or if the domain is sufficiently large. The types of particle-fluid coupling are classified following Elghobashi [31]:

One-way coupling: The influence of particles on the fluid phase may be neglected if the volumetric concentration of particles is low.

Two-way coupling: The force exerted by the particles on the fluid is considered.

Four-way coupling: Interactions between particles are also included.

Discrete Phase Modeling (DPM) shares a lot of similarities with CFD-DEM: particles are represented by spheres, they can interact with the fluid phase (more commonly through one-way coupling). The main difference lies in the contact models. Whereas DEM employs non-trivial equations to determine the contact event, in DPM only binary impacts are considered, with reduced precision but also a much lower computational cost. The book by Pöschel is a great starting point on the underlying subject of Granular Dynamics (GD) [99].

Coarse Grain Particle (CGP) simulates many particles together using numerical parcels and statistical collision detection. The granular assembly behavior is determined to a lower level of precision than realistic-particle DEM, but it allows to scale the simulation computational load without losing the granular assembly nature. In their review, Di Renzo and Di Maio [27] correctly point out the unfeasibility of realistic (single-particle representation) of industrial systems. Fluidized beds may contain in the order of $10^8 - 10^{12}$ particles, with characteristic flow or transport time ranges of $10^1 - 10^4$ s. Correctly calibrated corse-grained simulations are able to represent these cases at a reasonable (and tunable) computation cost.

Two Fluid Models (TFM) treat both solid and gas phases as continuously

and fully interpenetrating within the same Eulerian frame of reference, leading to highly efficient computational codes. However, the popularity of TFMs is declining due to advancements in computational performance and the inherent loss of granular specificity, which necessitates modeling with complex and heavily empirical equations [117]. Despite these challenges, TFMs remain highly effective for large-scale industrial applications, such as pneumatic conveying, chemical reactors, and spouted beds, where the granular flow resembles a continuum [32]. These models abstract the flow from molecular to continuum levels, enabling the definition of continuum variables like granular temperature, pressure, and solids fraction for use in CFD meshed domains. While TFM is suited for studying powders or fine particles, particle mixtures requiring finer details and closer adherence to experimental data are better modeled using Lagrangian approaches [66].

MP-PIC stands at a higher level of abstraction compared to even unresolved or coarse-grained CFD-DEM simulations. While the interaction with the fluid (drag mode, bouyancy, etc) is treated using the same drag model as those used for spherical particles, the interaction among parcels is mediated by a pressure parameter which tends to keep them separate, but in principle the parcels can overlap. MP-PIC addresses flows of particles, considering factors like drag from a gas phase, inter-particle stresses, particle viscous stresses, and gas pressure gradients. Murer et.al. [86] used this framework to model the flow of particles exiting a Laser Metal Deposition (LMD) discrete nozzle, reaching the conclusion that it is superior to TFM in this context.

Given an average particle diameter for the metallic powders used in the equipment and available as samples, a first estimation of particle diameter is $d_p \approx 100\ \mu$m. Given the considered geometries it was estimated that the number of particles would be no lower than 10^3 and no higher than 10^6, which by experience resulted feasible with the available computational resources in a four-way coupled, unresolved CFD-DEM simulation, with spherical representation.

2.3.1 **Eulerian-Lagrangian Forces**

Unresolved CFD-DEM solvers rely on coupling models to determine the forces exchanged between the fluid and the particles, effectively bridging the Eulerian and Lagrangian frames. The particles' equations of motion are detailed in Section

2.1, where they are treated as rigid bodies with six degrees of freedom. Depending on the flow regime, laminar or turbulent, the governing equations for the fluid phase differ.

For laminar, isothermal, incompressible flow of a Newtonian fluid, the Navier-Stokes equations govern the mass and momentum transport in the fluid phase:

$$\nabla \cdot \mathbf{u} = 0, \tag{2.9}$$

$$\frac{\partial \mathbf{u}}{\partial t} + (\mathbf{u} \cdot \nabla)\mathbf{u} = -\frac{1}{\rho}\nabla p + \nu \Delta \mathbf{u} + \mathbf{f}_D, \tag{2.10}$$

where $\mathbf{u}$ is the fluid velocity, p is the pressure, ρ is the fluid density, $\nu = \eta/\rho$ is the kinematic viscosity, and $\mathbf{f}_D$ accounts for additional body forces.

For turbulent flow conditions, the Reynolds-Averaged Navier-Stokes (RANS) equations are used to account for the effects of turbulence:

$$\nabla \cdot \tilde{\mathbf{u}} = 0, \tag{2.11}$$

$$\frac{\partial \tilde{\mathbf{u}}}{\partial t} + (\tilde{\mathbf{u}} \cdot \nabla)\tilde{\mathbf{u}} = -\frac{1}{\rho}\nabla \tilde{p} + \nu \Delta \tilde{\mathbf{u}} - \nabla \cdot \tau^{RS} + \tilde{\mathbf{f}}_D, \tag{2.12}$$

where $\tilde{\mathbf{u}}$ and $\tilde{p}$ represent the Reynolds-averaged velocity and pressure, respectively. The term $\tau^{RS} = \rho\overline{u'u'}$ denotes the Reynolds stresses resulting from velocity fluctuations, which are modeled to close the equations.

To model the Reynolds stresses, this study utilizes two turbulence models in conjunction with wall functions: the standard k-ϵ model [68] and the k-ω SST model [78]. Both models are based on the eddy-viscosity concept and involve solving additional transport equations for the turbulent kinetic energy k and either the turbulent dissipation rate ϵ or the specific dissipation rate ω.

In principle, CFD-DEM simulations are capable of dealing with supersonic flows, which would require considering compressibility effects. However, in the scope of this work, the gas velocities are low enough to justify the assumption of incompressible flow, with a Mach number well below one.

2.3.1.1 **Drag forces**

The particle motion is computed using differential equations that assume spherical particles without heat and mass transfer. Particles are treated as point masses, neglecting torque equations:

$$\frac{d\mathbf{x}_p}{dt} = \mathbf{v}_p, \tag{2.13}$$

$$m_p \frac{d\mathbf{v}_p}{dt} = \sum \mathbf{F}_i, \tag{2.14}$$

where $\mathbf{x}_p$ is the position vector of the particle, $\mathbf{v}_p$ is the particle velocity, and m_p is the particle mass. The term $\sum \mathbf{F}_i$ represents the sum of all relevant forces,

$$\sum \mathbf{F}_i = \mathbf{F}_D + \mathbf{F}_B + \mathbf{F}_G, \tag{2.15}$$

where $\mathbf{F}_D$ is the drag force, $\mathbf{F}_B$ is the buoyancy force, and $\mathbf{F}_G$ is the gravitational force. These terms encompass the major influences on the particle trajectory, while other smaller forces are neglected. The buoyancy and gravitational forces are computed as:

$$\mathbf{F}_B + \mathbf{F}_G = \frac{(\rho_p - \rho)\pi d_p^3}{6}\mathbf{g}, \tag{2.16}$$

The drag force is calculated as follows:

$$\mathbf{F}_D = \frac{3}{4}\frac{\rho}{\rho_p}\frac{m_p}{d_p} \cdot C_D(\mathbf{u} - \mathbf{v}_p)|\mathbf{u} - \mathbf{v}_p|, \tag{2.17}$$

where d_p is the particle diameter and the drag coefficient C_D depends on the flow regime.

The drag force implementation can vary based on the conditions. The fundamental diagram for the ideal case is reported in Figure 2.17. In his book, Crowe points out that the empirical drag values have a lot of dispersion compared to the reported diagram, arising from the many unknowns of real particle-fluid interactions. However, the previous equations can still be used with reasonable accuracy.

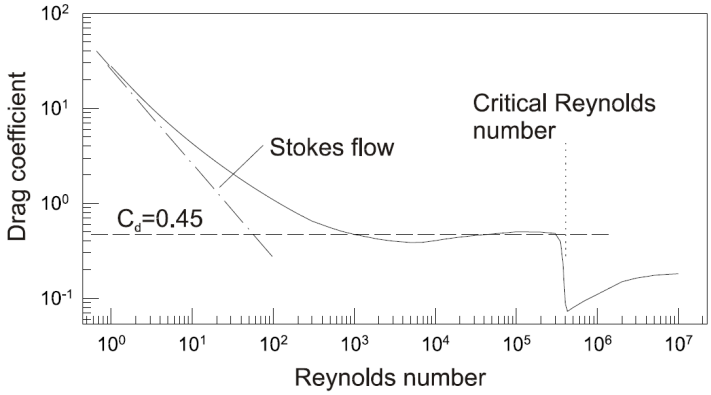

Figure 2.17: Drag coefficient of a non-rotating sphere as a function of the Reynolds number [23].

The disperse phase Reynolds number considers the particle diameter d_p as the length scale, and the relative velocity: $Re_p = \frac{d_p|\mathbf{u}-\mathbf{v}_p|\rho}{\mu}$. $\mathbf{u}$ and $\mathbf{v}_p$ are respectively the fluid's and particle's velocities relative to the same inertial frame, and μ is the dynamic viscosity of the fluid. Equations 2.19 and 2.18 are similar in nature, and approximate the empirical measurements of a sphere's drag. The drag coefficient C_D is related to the Reynolds number by the piece-wise relation [23]:

$$C_D = \begin{cases} 0.44 Re_p & \text{if } Re_p \geq 1000, \\ 24\left(1 + 0.15 Re_p^{0.687}\right) & \text{if } Re_p < 1000. \end{cases} \tag{2.18}$$

OpenFOAM employs the following slightly modified form [122]:

$$C_D = \begin{cases} \frac{24}{Re_p}\left(1 + \frac{1}{6} Re_p^{2/3}\right) & Re_p \leq 1000, \\ 0.424 & Re_p \geq 1000. \end{cases} \tag{2.19}$$

This work also utilizes the model proposed by Gidaspow [41], which integrates the Ergun dense phase model for volumetric fluid fractions $\alpha_c < 0.8$ with the Wen-Yu disperse phase model for larger fluid fractions. When working with dense concentrations of particles in the fluid, the flow disturbance of one particle can influence another, hence the need for models that account for the fluid volume fraction α_c. In OpenFOAM, this model is implemented as `ErgunWenYuDragForce`. The drag force relation is given by:

$$\frac{m_p}{\rho_p}\left(150\frac{(1-\alpha_c)}{\alpha_c}+1.75Re\right)\frac{\mu}{\alpha_c d_p^2} \quad \text{for } \alpha_c < 0.8, \tag{2.20a}$$

$$0.75\frac{m_p}{\rho_p}C_D Re_p \frac{\mu\alpha_c^{-2.65}}{\alpha_c d_p^2} \quad \text{for } \alpha_c \geq 0.8, \tag{2.20b}$$

Here, m_p and ρ_p are respectively the particle's mass and density.

2.3.1.2 **Other forces**

When immersed in a moving flow, particles can experience other forces. In the context of CFD-DEM codes these are most commonly additive, increasing the number of terms of Equation 2.15. This study considered lift forces, as they are expected to have a notable influence on the overall behavior. Lift forces act in an orthogonal direction to the relative velocity between fluid and particle. these are caused by a differential velocity on two sides of a particle, and can be caused either by particle's spin (therefore, Spin Lift), or the fluid's velocity gradient (Shear Lift).

OpenFOAM includes the Saffman-Mei equation to calculate the shear lift [122] [104]:

$$Re_w = \frac{\rho_c \left|\nabla \times \mathbf{u}_c\right| d_p^2}{\mu_c + \sqrt{\epsilon}}, \tag{2.21}$$

$$\beta = 0.5\left(\frac{Re_w}{Re+\sqrt{\epsilon}}\right), \tag{2.22}$$

$$\alpha = 0.3314\sqrt{\beta}, \tag{2.23}$$

$$f = (1.0-\alpha)\exp(-0.1Re)+\alpha, \tag{2.24}$$

$$C_{L,d} = \begin{cases} 6.46f & \text{if } Re < 40, \\ 6.46\times 0.0524\sqrt{\beta Re} & \text{if } Re \geq 40, \end{cases} \tag{2.25}$$

$$C_L = \frac{3.0}{2\pi\sqrt{Re_w+\sqrt{\epsilon}}}C_{L,d}, \tag{2.26}$$

The resulting lift force is given by:

$$\mathbf{F}_L = C_L\,\frac{1}{2}\,\rho\left|\mathbf{u}-\mathbf{v}_p\right|^2 d_p^2\,\mathbf{e}_L, \tag{2.27}$$

where $\mathbf{F}_L$ is the lift force and $\mathbf{e}_L$ is the unit vector in the direction of the lift force.

In addition to the Saffman shear lift model, the commercial software Siemens Simcenter Star-CCM+ includes the Sommerfeld Particle Spin Lift Force model. This force applies to a spinning particle moving relative to a fluid, and also extends the validity of the shear lift for a wider range of Reynolds number [112].

In addition to the spherical drag models, other models exist with the ability to account for different particle shapes. Maramizonouz's and Nadimi's research analyzes the drag coefficients of ellipsoidal particles with various flatness and elongation characteristics using numerical simulations and twelve different drag models [76].

CFD-DEM simulations are capable of handling a wide range of flow conditions, including supersonic flows where compressibility effects become significant. However, in the case of the present study, the flow velocities are relatively low, and thus, compressibility does not need to be considered, which greatly simplifies the problem.

2.4 Chapter Summary

This chapter delineates the comprehensive methodology employed to model and simulate particulate systems using the Discrete Element Method (DEM) in conjunction with Computational Fluid Dynamics (CFD). DEM serves as a robust tool for capturing the emergent complex behaviors of granular materials by tracking individual particles within a Lagrangian framework. The interplay between particles, governed by Newton's equations of motion and sophisticated contact models, underpins the accurate representation of phenomena such as collision dynamics, particle agglomeration, and deformation.

Furthermore, the integration of DEM with CFD through coupling methods like CFD-DEM enables a nuanced analysis of multi-phase flows, where the Eulerian perspective of the fluid phase complements the Lagrangian tracking of particles. This coupled approach is particularly advantageous for applications in Laser Metal Deposition (LMD), where the intricate interactions between fine metallic powders and fluid flows are critical. The chapter also underscores the significance of meticulous calibration processes, leveraging optimization techniques and artificial neural networks to align simulation parameters with experimental observations, thereby enhancing the predictive capabilities of the models.

CHAPTER

3

Particle contact models

The accurate simulation of particulate systems relies heavily on the detailed representation of interactions between particles. In the realm of Discrete Element Modeling (DEM), these interactions are governed by contact models, which provide the mathematical formulations necessary to describe the forces and deformations that occur when particles come into contact. This chapter delves into the various contact models used in this work, elucidating their theoretical underpinnings and practical implementations.

Contact models define the forces that arise during particle interactions, including normal and tangential forces, friction, and adhesion. These models account for the deformations of particles, as well as energy dissipation mechanisms such as hysteretic damping and viscoelastic effects. By accurately modeling these interactions, contact models are useful especially for dense particle assemblies, but the physical representation of the contact event makes them attractive also for sparser systems.

In contrast to contact models, the coefficient of restitution is a simpler concept used to describe the outcome of binary impacts. The restitution coefficient is a measure of the dissipation of a collision, defined as the ratio of the relative velocity after impact to the relative velocity before impact along the line of contact. The value encapsulates the energy loss during an impact, without detailing the underlying force-deformation relationship.

3.1 Hertz's theory of contact of elastic bodies

The Hertz contact model [48], named after Heinrich Hertz, is a fundamental framework used in the analysis of contact and deformation between elastic bodies. It assumes that the bodies in contact are linearly elastic and non-adhesive. It is based on several key assumptions:

- The materials in contact are linearly elastic, obeying Hooke's law.
- The bodies have a spherical or nearly spherical shape.
- Deformations occur only within the elastic limit of the materials.
- The contact area is small compared to the radii of curvature of the bodies.

For two spheres with radii R_1 and R_2 in contact under a normal load F_n, the contact overlap $\delta > 0$ and the contact force F_n can be calculated using Hertz's equations:

$$F_n = \frac{4}{3} E^* \left(R^* \delta^3\right)^{1/2} \tag{3.1}$$

$$\delta^3 = \frac{9 F_n^2}{16 R^* E^{*2}} \tag{3.2}$$

where E^* is the reduced modulus of elasticity and R^* the reduced radius, defined as:

$$\frac{1}{E^*} = \frac{1-\nu_1^2}{E_1} + \frac{1-\nu_2^2}{E_2} \tag{3.3}$$

$$\frac{1}{R^*} = \frac{1}{R_1} + \frac{1}{R_2} \tag{3.4}$$

where E_1, E_2 are the Young's modulus, and ν_1, ν_2 are the Poisson's ratios of the contacting materials.

The contact radius a is obtained by considering the pressure distribution on the surface, and results in:

$$a^3 = \frac{3 F_n R^*}{4 E^*} \tag{3.5}$$

Solving the Equations 3.1 and 3.2, the contact normal force and overlap can be expressed in function of the contact radius a:

$$F_n = \frac{4 E^* a^3}{3 R^*} \tag{3.6}$$

$$\delta = \frac{a^2}{R^*} \tag{3.7}$$

The Hertz contact model provides valuable insights into the contact mechanics of spherical bodies, serving as a foundational tool for analyzing more complex contact scenarios. While providing an analytical solution of the contact, it has limitations. It assumes linear elasticity and neglects adhesive forces and material plasticity. Real-world contact situations often involve non-linear behavior and adhesive effects, requiring more advanced contact models to accurately represent the interactions between materials.

The limitations become evident in Figure 3.1, which displays the measured force-displacement curve of a very smooth, very hard sample of alumina ($\gamma - Al_2O_3$) granules. Very small forces cause the flattening of micro-asperities, not visible in this case since the material was prepared with very low roughness. In this optimal case, the Hertz contact model is in good agreement for the lower part of the curve, until the material yields at the point of contact. From there on, the Hertz contact model overestimates the reaction force, and the return curve should not be conservative anymore. This is to demonstrate that while the Hertz contact model is generally accurate, its core assumptions must be very clear to the user.

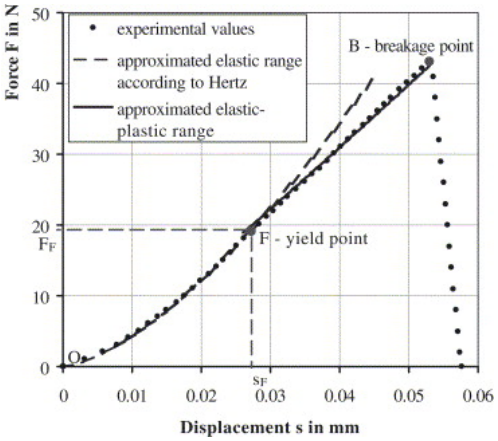

Figure 3.1: Quasi-static force-displacement ($F - \delta$) curve of alumina granulate ($\gamma - Al_2O_3$; diameter of the granules 1.17 mm; smooth surface): O–F-elastic deformation, F–B-elastic–plastic deformation [9]. In this case, the Hertz approximation is valid only between O-F.

3.2 Spring-Slider-Dashpot models

Thanks to its modular nature and ease of implementation, most DEM codes have a Spring-Slider-Dashpot (SSD) contact model implementation. The normal reaction force F_n is modelled by a spring whose elastic constant k_n is related to the material properties and the particle size (see Figure 3.2). For instance, if the spring represents a non-linear behavior according to Hertz's theory [48], according to Equation 3.1 the normal force becomes:

$$F_n = k_n \cdot \delta_n^{3/2} \quad \text{for} \quad \delta_n > 0 \tag{3.8}$$

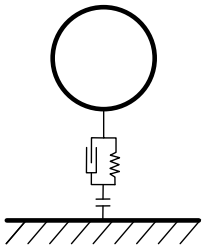

Figure 3.2: Simplified representation of the Spring-Slider-Dashpot (SSD) system representing the contact normal to a surface of a spherical particle.

The tangential force F_t model is based on the Mindlin-Deresiewicz work [82] [83]; in most cases the *no-slip* formulation is preferred over the *hysteretic* one. This model accounts for the Coulomb friction between particles. The tangential SSD model, visible in Figure3.3, is usually expressed in the incremental form, to more easily account for the sliding allowed by the Coulomb coefficient of friction μ:

$$F_t^{new} = F_t^{old} + k_t \Delta\delta_t \tag{3.9}$$

to be compared with the limiting value $F_t \leq \mu F_n$. The contact plane changes continuously during particle-particle interaction. The functional form of Equation 3.8 is recalculated each time according to the new direction of δ_n.

Viscous damping is usually applied as forces added in the normal (F_{nd}) and tangential (F_{td}) directions. Cundall and Strack [24] express the damping constants as the critical damping of one-directional linear oscillators:

$$\begin{aligned} \eta_n &= 2\sqrt{m^* k_n} \\ \eta_t &= 2\sqrt{m^* k_t} \end{aligned} \tag{3.10}$$

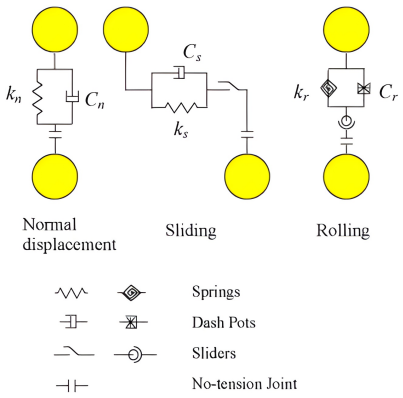

Figure 3.3: Simplified representation of the Spring-Slider-Dashpot (SSD) in the normal, tangential, rolling directions.

The requirement in their work was to dampen the oscillations as quickly as possible, as viscous dissipation has the collateral effect of contributing to numerical stability, avoiding infinitely oscillating solutions. The dashpot forces are added to the normal and tangential forces, and are given by:

$$\begin{aligned} F_{nd} &= 2\beta\sqrt{m^* k_n}\frac{\Delta\delta_n}{\Delta t} \\ F_{nt} &= 2\beta\sqrt{m^* k_t}\frac{\Delta\delta_t}{\Delta t} \end{aligned} \tag{3.11}$$

where $\Delta\delta_n/\Delta t$ and $\Delta\delta_t/\Delta t$ are essentially the relative velocities and $m^* = (m_1^{-1} + m_2^{-1})^{-1}$ is the reduced mass. The value of β is in the range $0.01 - 0.03$ [21].

Tsuji et.al. [126] propose a formulation to scale the damping coefficient to the coefficient of restitution $e = \frac{v_{out}}{v_{in}}$, which is more effectively measured for particles. In this case, the formulation of the non-linear oscillator (accounting for Equation 3.8) is:

$$m^* \frac{d^2\delta}{dt^2} + k_n \delta^{3/2} + \eta \frac{d\delta}{dt} = 0 \tag{3.12}$$

The damping coefficient η is scaled so that the rebounding velocity does not depend on particle size and impact velocity, therefore the coefficient of restitution $e = \frac{v_{out}}{v_{in}}$ is constant. The normal damping coefficient becomes:

$$\eta_n = \alpha(m^* k_n)^{1/2}\delta^{1/4} \tag{3.13}$$

The solution of Equation 3.12 shows that the restitution coefficient e depends only on the value of α, whose relation is reported in Figure 3.4. This implementation is used, for instance, in OpenFOAM [122].

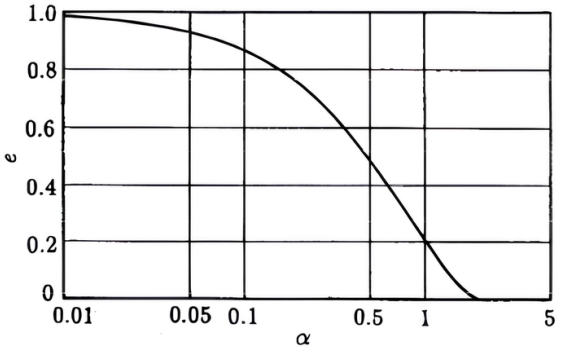

Figure 3.4: Relation between the coefficient of restitution e and the parameter α [126].

In addition to the normal and tangential forces, most computational models incorporate a Rolling Friction model, representing the resistance to rolling experienced within granular systems. The concept of "free rolling" refers to the scenario where there is an absence of resistance to rolling. However, this assumption is valid only when dealing with smooth, perfectly spherical granules, resulting in a negligible torque. The assumption of negligible torque can cause nonphysical behaviors in most practical industrial cases, where granules are often non-spherical and real-world conditions induce resistance during rolling.

During dynamic flow phases like avalanching or pneumatic transportation, the term "rolling friction" is used. Conversely, the term "rolling resistance" is used for pseudo-static systems. Despite the distinction, both scenarios converge on a shared framework, represented by a torque (M_r) opposite to the rolling direction, derived from an asymmetric contact pressure distribution.

Rolling resistance can stem from various sources at particle or surface contacts, including [2]:

(a) Micro-slip and Friction on the Contact Surface
(b) Plastic Deformation around the Contact
(c) Viscous Hysteresis during Rolling Contact between Viscoelastic Particles
(d) Surface Adhesion, Especially Relevant at (Sub)micron Particle Contacts
(e) Shape Effects due to Non-Spherical or Non-Circular Particle Shapes

Researchers have proposed various rolling resistance models to address diverse granular behaviors. These models can broadly be classified into four categories, as outlined by Ai et al. [2]:

Type A: *Directional constant torque models* apply a constant torque against the relative rolling direction ($\hat{\omega}_{\text{rel}}$)on each pair of particles or between particle and surface [145]. In this model rolling friction is not dependent on the rolling velocity (ω_{rel}). This model is represented by the equation:

$$M_r = -\hat{\omega}_{\text{rel}} \mu_r R^* F_n \tag{3.14}$$

Type B: *Viscous models*, where the torque is related to the relative angular velocity of the contacting bodies [145] [15]. The torque in this model is expressed as:

$$M_r = -\hat{\omega}_{\text{rel}} \mu_r^{'} R^* F_n V_{\text{rel}} \tag{3.15}$$

where V_{rel} is the peripheral velocity of the contacting pair (1 and 2).

Type C: *Elastic-plastic spring-dashpot models*, which operate similarly to translational Spring-Dashpot-Slider (SSD) models. The total resistance torque M_r in this model consists of an elastic component M_r^k and a viscous damping component M_r^d. A schematic representation of this model can be seen in Figure 3.3. In the elasto-plastic model proposed by Jiang et.al. [56], smaller rotations are considered elastic, but beyond a defined limit the rotation results in a constant energy dissipation akin to a plastic deformation. In addition to this, the damping exerts a resisting torque proportional with the relative rolling velocity. In incremental form:

$$\begin{cases} M_r^k(t+\Delta t) \ = M_r^k(t) - k_r(\omega_{\text{rel}}(t)\Delta t) \\ |M_r^k(t+\Delta t)| \leq M_r^m \end{cases} \tag{3.16}$$

where $M_r^m = \mu_r R^* F_n$ is the limiting torque. Given the critical damping coefficient $C_r^{\text{crit}} = 2\sqrt{I_r^* k_r}$, where I_r^* is the rotation inertia, the viscous rolling torque is:

$$M_r^d(t+\Delta t) = -C_r \omega_{\text{rel}}(t) = -(\eta_r C_r^{\text{crit}})\omega_{\text{rel}}(t) \tag{3.17}$$

Type D: *Contact-independent models*, expressing torque using the total rotation or rotational velocity of a particle instead of using relative terms. However, they often result in different torques applied to each particle, violating equilibrium, making them less practical for use [2].

Adding complexity to the rolling friction models is the distinction between pure rolling and the combined condition of sliding-rolling. The sliding-rolling is obtained by a superposition of the effects given by pure rolling and pure sliding motions. The torque deriving from the pure sliding motion can be expressed as $M_t = F_t R$, and the total torque on the particle is $M = M_t + M_r$.

Imagine a particle rotating at a velocity $\omega_1 = 10$ rad/s touching a second particle which is not rotating $\omega_2 = 0$ rad/s. The torque deriving from the sliding motion, or in general form the tangential force, can increase the relative rolling velocity of one particle on the other, exchanging momentum between the particles. If they have the same inertia, obtaining a final rotational velocity $\omega_1 = 5$ rad/s and $\omega_2 = -5$ rad/s tending to a pure rolling condition. At this point no more tangential force is applied, as the particles reached equilibrium.

The torque deriving from rolling resistance (or friction) is in principle always resistive, and reduces the relative rolling velocity. In the case expressed before, the particles begin in a pure sliding condition, making the rolling resistance irrelevant. As they reach equilibrium, condition the contact between the particles is in a pure rolling condition. Rolling resistance acts in the relative rolling direction, gradually dissipating the rotational energy of the system over time.

In DEM simulations, spherical particles are often chosen for their simplicity, allowing for the use of efficient algorithms. Real granular materials rarely have spherical particles, and large deformations can further contribute to particle non-ideality. Research has shown that the shape of these grains greatly affects the mechanical behavior of granular systems. The shape effect cannot strictly be classified as rolling friction, but a high rolling friction is often used to represent the non-sphericity of the granules of the system [33]. The rolling friction coefficient can be used to match the internal friction angle of large assemblies, which greatly increase with non-spherical elements [56] [90]. The average energy expense needed to move non-spherical grains and their resistance to rolling can be predicted with good agreement in dense granular systems. If an appropriate value of rolling friction coefficient is applied to the spherical particles, the method works well when the non-spherical particles flow with a relatively high speed [136]. The trade-off in this technique is some loss of information on the exact motion individual granules and no information on their orientation.

3.3 Adhesive Elastic Models

In this context, adhesion can be defined as the ability of objects to remain in contact, even under the action of limited external forces. The history of the understanding of adhesion phenomena closely follows the development of the models describing the interaction between atoms and molecules. In 1662, Robert Boyle (1627-1691) introduced the ideal gas law, $pV = constant$. Later works by Charles,Guy-Lussac, and Dalton showed the proportional relation with temperature: $pV = RT$ (where p is the pressure, V is the molar volume, R the gas constant, and T the temperature). This model can be described with a granular description of gases, where the product RT implies the propensity of atoms in a gas to repel each other: a decrease in their average distance (represented by a decrease in V) increases the force pushing them apart (represented by an increase of p).

This Ideal Gases model works in several cases of low-pressure, simple gases, however it falls short of predicting the behavior of Real Gases, for instance when the pressure is increased or the gas is composed by more or less complex molecules. The dutch physicist J.D. van der Waals (1837-1923) introduced the notion of attractive molecular forces, by trying to match the behavior of real gases. His formulation of the equation of state for gases is:

$$(P + a/V^2)(V - b) = RT \ , \tag{3.18}$$

where b is subtracted from V to account for the finite volume of molecules. The term a/V^2 is added to the measured pressure P to account for the attractive forces between molecules, and is at the base of the attractive intermolecular forces now known as *van der Waals forces* [54].

In this spirit, molecules are considered as puntiform entities, and Mie in 1903 proposed an interaction pair potential to include the repulsive force as well as the attractive term just discussed:

$$w(r) = -A/r^n + B/r^m \ . \tag{3.19}$$

The Lennard-Jones potential is a special case of Mie's equation: $w(r) = -A/r^6 + B/r^{12}$. By plotting this equation, we find the diagram of Figure 3.5. Fundamentally the area above the curve $F(r)$, or the integral of the force necessary to

separate the molecules from the equilibrium point r_e to infinity, is the binding energy of the system, equal to w_{min}. The force expressed by the Lennard-Jones potential is:

$$p_a(z) = \frac{8w}{3z_0}\left[\left(\frac{z}{z_0}\right)^{-9} - \left(\frac{z}{z_0}\right)^{-3}\right] \tag{3.20}$$

where z_0 is the equilibrium separation and w is the thermodynamic work of adhesion, commonly denoted in terms of Dupré surface energies by $\Delta\gamma = \gamma_1 + \gamma_2 - \gamma_{12}$ [54].

J. Tomas in 2007 [125] presents a variety of possible interaction modes that are relevant for fine ($d < 100$ μm), ultrafine ($d < 10$ μm), and nanosized particles ($d < 0.1$ μm). In metal 3D printing, specifically LMD, the metallic powders used are most commonly in the fine size range. The possible mechanisms of powder adhesion in that size range are:

- Surface and field forces at direct contact
  - Electrostatic force
  - Magnetic force
  - Van der Waals force
- Material bridges between particle surfaces
  - Hydrogen bonds of adsorbed surface layers of condensed water
  - Solid bridges by chemical bonds by solid-solid reactions
  - Solid bridges by contact fusion, sintering, or diffusion
- Interlocking of contacts by overlaps of surface asperities

3.3.1 The Tabor parameter, DMT model, and the M-D transition

Bradley demonstrated that, disregarding the elastic deformation of bodies, the adhesive interaction could be determined by integrating the Lennard-Jones potential (see Fig. 3.5). The surface forces p_a depend on the separation between atomic planes. Utilizing Equation 3.20, the total adhesive force between two spheres is given by [57]:

$$P_a = \frac{8\pi w R^*}{3}\left[\frac{1}{4}\left(\frac{z}{z_0}\right)^{-8} - \left(\frac{z}{z_0}\right)^{-2}\right] \tag{3.21}$$

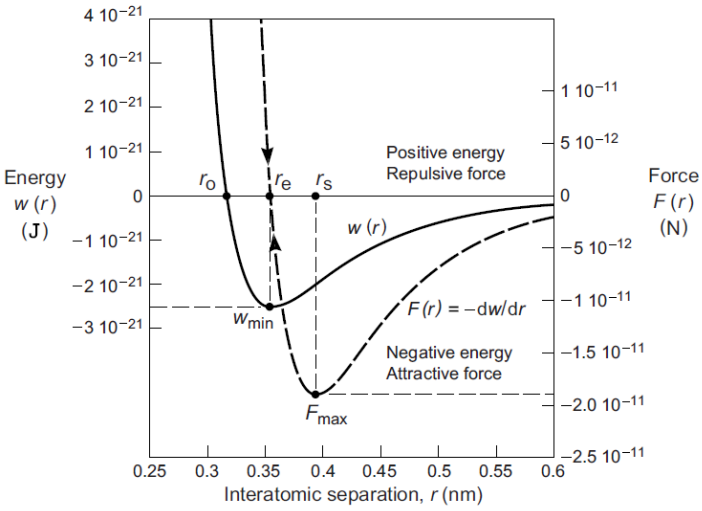

Figure 3.5: Typical van der Waals interaction energy (or potential) function $w(r)$ and force function $F(r)$ between two puntiform molecules at a distance r, also called Lennard-Jones Potential. When the applied force is zero the molecules stay in the minimum of the energy well w_{min} at a distance r_e, the equilibrium separation. When the particles tend to move closer together, the repulsive force grows quickly. When they tend to separate, the maximum attractive force F_{max} can be reached. These curves are plotted for for $A = 10^{-77}$ J m^6 and $B = 10^{-134}$ J m^{12} [54].

Here, $R^* = [1/R_1 + 1/R_2]^{-1}$. The maximum adhesive force, or pull-off force, is $P_{po}(z = z_0) = -2\pi w R^*$.

The contact models developed by Johnson et.al. [58] (JKR) and Derjaguin et.al. [26] (DMT) first introduced elastic deformation of the spheres, building on the foundation of Hertz's work [48]. At first the two models appeared in contradiction to each other. JKR considers the adhesion only on the surfaces in contact, while DMT allows the forces to act at a distance, more closely resembling Bradley's work. They are on opposite sides of a parameter μ, as Tabor showed [121] [57]:

$$\mu = \left(\frac{R^* w^2}{E^{*2} z_0^3} \right)^{1/3} \tag{3.22}$$

The parameter represents the ratio between the elastic deformation and the effective range of the surface forces (z_0). The work of adhesion w can be identified as Dupré's thermodynamic work of adhesion or, more appropriately, as the

Adhesive Energy Γ [61]. The JKR model applies to large, compliant spheres, for which the surfaces deform, i.e. large values of μ. The greatest contribution from the adhesive forces is at short distance, or essentially in the contact. Outside of it, the adhesive forces are negligible. In contrast, DMT better represents small, stiff spheres, or low values of μ. This means that the adhesive forces act significantly also around the contact area, since the gap at the edge of the contact is very narrow ($\sim z_0$) for a significant extension.

This can be easily seen in Figure 3.6, where the active location is highlighted, and Figure 3.7. In both DMT and Bradley the Lennard-Jones curve is identifiable, this means that the distance at which the forces act is significant. Note that the DMT model still approximates linearly the repulsive portion of the curve. The force does decrease with distance, but it does so at a significant distance from the contact's edge, or a significant fraction of a_0.

In the JKR model, adhesion operates over a relatively short distance, leading to forces becoming negligible in close proximity to the edge. Within the model, there are no forces acting at a distance around the edge, essentially resembling a delta function in the graph depicted in Figure 3.7. This approximation is justified by the fact that the separation between surfaces around the edge becomes sufficiently large, causing forces acting at a distance to become insignificant at distances much smaller than a_0.

The Maugis-Dugdale model is designed as a bridge model between JKR and DMT. The Lennard-Jones is approximated with a rectangular region (Dugdale approximation), simplifying the analytical integration [77]. If the region is narrow, the model is essentially JKR; if wide, it is almost equivalent to DMT. The model is often expressed as a function of the Tabor Parameter.

Johnson et.al. [57] propose a decision map to select the most appropriate model for the application, reported in Figure 3.8. As a simplified criteria, useful in DEM simulations, the JKR model is appropriate for $\mu > 5$, DMT for $\mu < 0.1$. If between the two case, the M-D model should be used. As an example, for 100 μm steel particles ($E = 206GPa$; $\Gamma \approx 1$ J/m^2; $z_0 \approx 0.3$ nm), the Tabor parameter is $\mu = 5.2$, therefore the JKR model is appropriate.

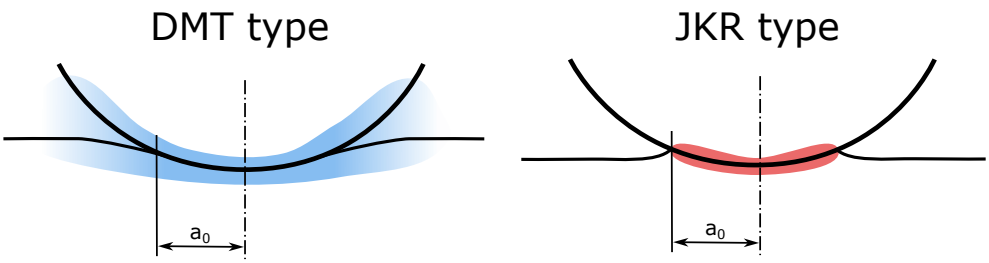

Figure 3.6: Zones of action of the adhesive forces. In DMT-type, the forces act with a relevant intensity outside the contact radius a_0. In JKR type, adhesive forces act only inside the contact radius.

3.3.2 **The JKR elastic-adhesive contact model**

A theoretical model for the adhesion of spheres is the JKR contact model [58]. It shares many of the same assumption as the Hertz contact model (smooth and regular surfaces, perfectly elastic behavior), therefore some of the limitations. Its formulation is based on the notion that an adhesive bond between two bodies is essentially equivalent to a crack in a solid, and the original work [58] reads "the approach followed in this analysis, is similar to that used by Griffith in his criterion for the propagation of a brittle crack". The energy needed to separate the bodies in contact is therefore fundamentally related to the energy to propagate a crack in a solid, as described in Linear Elastic Fracture Mechanics (LEFM).

Accepting this definition, we draw a connection between fracture mechanics and the adhesion of fine particles. Concepts from fracture mechanics, such as stiffening, bridging, and residual stress, are applicable in this context. The application of fracture mechanics to adhesive interfaces is elaborated upon by Kendall [61]. The method proposed in this work extends the idea of determining adhesive energy through an impact [139], treating the interface as a bond to be broken in an energy-driven event. This results in a high strain rate, to which adhesive energy is sensitive [61]. The centrifuge method employed by various researchers [110, 62, 97] can be viewed as a quasi-static counterpart to the one presented here.

The energetic description of the impact between elastic-adhesive particles has been successful in explaining dust coagulation in space [17], a critical stage in planetary formation. The JKR contact model is one of the most commonly used contact models in DEM simulations [21], with adhesive energy being a critical parameter.

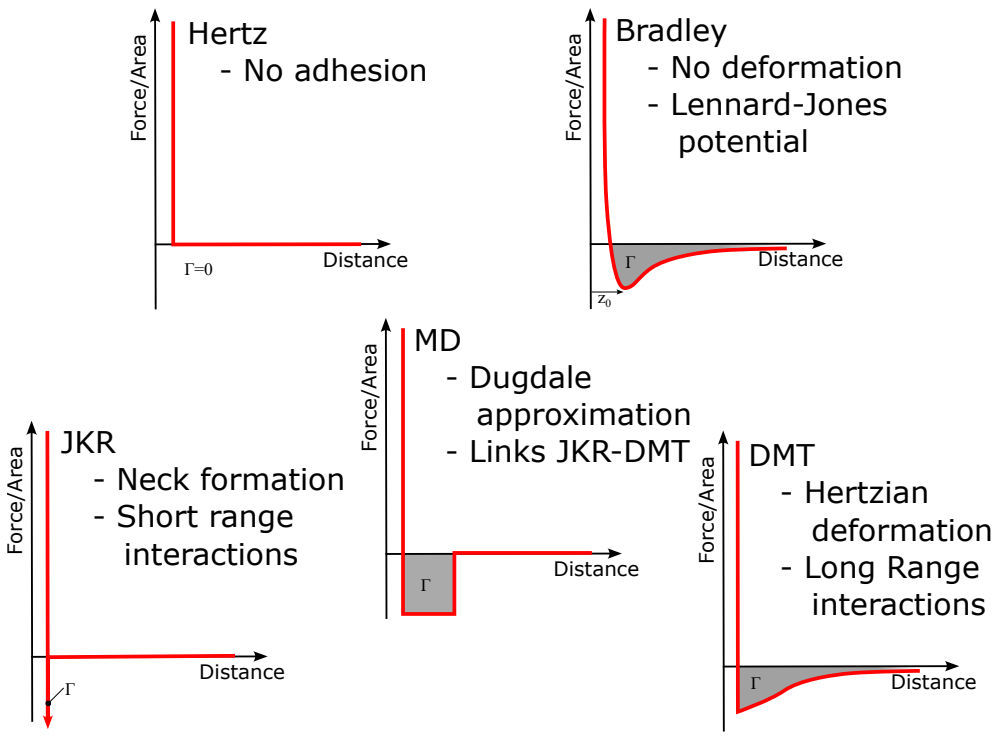

Figure 3.7: Force-distance diagrams contact models for elastic-adhesive spheres [19][43]. A negative value corresponds to attractive forces, corresponding to the Adhesive Energy Γ.

The Adhesive Energy of the contact Γ is often equated to the Dupre work of adhesion. For dissimilar surfaces $\Gamma = \gamma_1 + \gamma_2 - \gamma_{12}$, where γ_1 and γ_2 are the surface energies of the solids, and γ_{12} is the energy of the formed interface. For similar surfaces $\Gamma = 2\gamma$. Where Hertz contact model provides purely repulsive elastic forces, the JKR model expresses the interaction in energetic terms to include the attractive forces proportional to the contact radius a. The analytical solutions result in the contact shape compared in Figure 3.9 and in the represented pressure distributions. Notice the tensile component present in the JKR model p_{JKR}, which tends to an infinite value on the very edge. Compare this to the stress profile of a crack under tension, which also tends to infinity on the very edge [44]. While the infinite stress cannot happen in real materials, these mathematical descriptions have proven extremely useful in mechanical engineering and lay at the foundation of more complex theories.

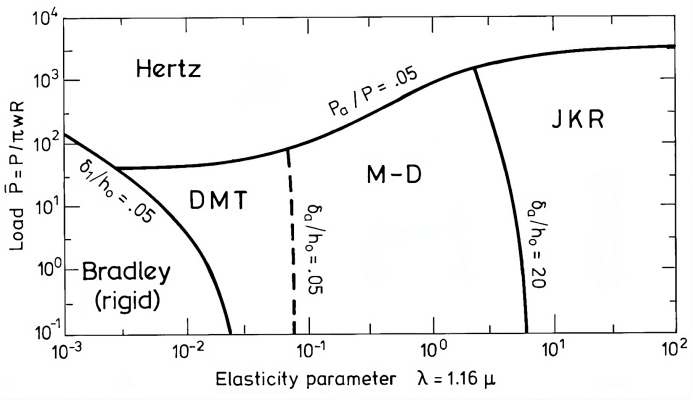

Figure 3.8: Adhesion map for a spherical particle. The Tabor parameter (μ) and the dimensionless load ($\overline{P}$) determine the most appropriate model [57].

The binding energy at the contact circle is defined as the surface energy per unit area of the surfaces multiplied by the area of the contact circle, of radius a:

$$U_S = -\pi a^2 \Gamma \tag{3.23}$$

The total energy U_T it the sum of surface, elastic and potential energy from the applied load: $U_T = U_S + U_E + U_P$. The equilibrium condition of the total energy determines the static contact radius a, which can be found by deriving $dU_T/da = 0$. Solving this derivative results in the JKR contact model [58], described by the following equations:

$$F_n = \frac{4E^* a^3}{3R^*} - \left(8\pi E^* \Gamma a^3\right)^{1/2} \tag{3.24}$$

$$\delta = \left(\frac{a^2}{R^*}\right) - \left(\frac{2\pi\Gamma a}{E^*}\right)^{1/2} \tag{3.25}$$

Notice that for $\Gamma = 0$ J/m^2, the solution is exactly the same as Hertz, reported in Equations 3.6 and 3.7.

Solving Equation 3.24 for the contact radius yields [17]:

$$a = \left\{\left(\frac{3R^*}{4E^*}\right)\left[F + 6\pi\Gamma R^* \pm sqrt(6\pi\Gamma R^*)^2 + 12\pi\Gamma R^* F\right]\right\}^{1/3} \tag{3.26}$$

where F in this case is the external applied load. A positive load forces the particles together (or the particle on the surface). Figure 3.10 represents the normalized forms of the external force, as $\overline{P}$, and the contact radius, as $\overline{a}$, as a function of the normalized contact overlap $\overline{\delta}$.

When no external loads are applied, the system is in equilibrium. Solving Equation 3.24 we obtain the contact radius at equilibrium:

$$a_0 = \left(\frac{9\pi\Gamma R^{*2}}{E^*}\right)^{(}1/3) \tag{3.27}$$

A negative load tends to separate the interface at a value labeled pull-off force: $F \leq -F_{po} = -3\pi\Gamma$. This value is minimum of Equation 3.24, in Figure 3.10 it is the minimum value of the normalized $\overline{P}$ curve, at point E, and is the separation condition at constant force. It corresponds to a contact radius $a = (2/3)^{2/3}a_0$.

Under a tensile force, the contact stretches forming a neck, before finally separating at a tear-off displacement $\delta_{to} = \frac{1}{2}\frac{a_0^2}{6^{1/3}R^*}$ [17]. Point D corresponds to this tear-off distance, or the separation distance at constant displacement, and is the minimum of Equation 3.25.

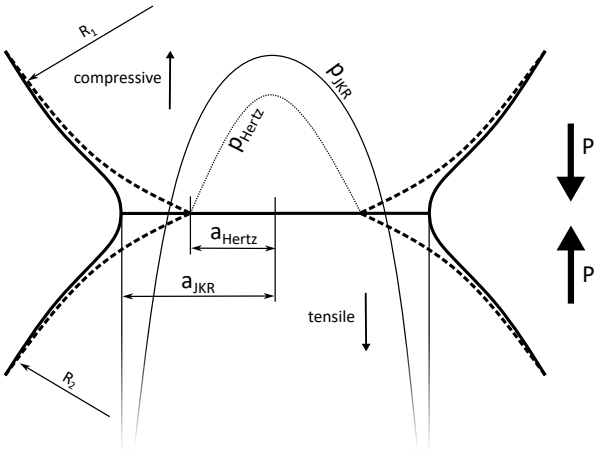

Figure 3.9: Contact shape comparison between the purely-elastic Hertz and adhesive-elastic JKR models [58]. The contact radius a is determined by the external load in the normal direction P. The contact overlap δ is not represented. For JKR, the pressure distribution p shows a tensile component near the edge of the contact surface. The value at the very edge tends to infinity, as in LEFM.

3.3.3 **JKR energetic balance**

Johnson and Pollock [59] explore the original model [58] to find the response of colliding adhesive elastic particles. The surfaces' deformation is caused by the sphere inertia, $m\frac{d^2\delta}{dt^2}$), balanced by the total force at the interface P. In the case of a static contact, an external load P would cause a deformation δ. In the article,

displacement and forces are normalized as:

$$\overline{\delta} = \delta \left(\frac{\pi^2 \Gamma^2 R}{3K^2} \right)^{-1/3} \quad \text{and} \quad \overline{P} = \frac{P}{3\pi\Gamma R} \tag{3.28}$$

Consequently, energies are normalized as:

$$\overline{U} = \left(\frac{9\pi^5 \Gamma^5 R^4}{K^2} \right)^{1/3} \tag{3.29}$$

where:

$$\frac{1}{K} = \frac{3}{4} \left(\frac{1-\nu_1^2}{E_1} + \frac{1-\nu_2^2}{E_2} \right) = \frac{3}{4} \frac{1}{E^*} \tag{3.30}$$

At any given time, the total energy of the system U_T is the sum of the surface energy U_S, the stored elastic energy deriving from the surface deformation U_E and the mechanical energy introduced by the external load U_M. Johnson and Pollock [59] defined the internal energy in the system as the sum of elastic and surface energy:

$$U_I = U_E + U_S \tag{3.31}$$

and expressed the values in normalized form, as follows:

$$\overline{U_I} = \overline{U_E} + \overline{U_S} = \frac{\frac{6}{5}\overline{P_1}^2 + \overline{P_1} - \left(2\overline{P_1}\right)^{\frac{3}{2}}}{\overline{P_1}^{\frac{1}{3}}} \tag{3.32}$$

$$\overline{\delta} = \frac{3\overline{P_1} - \sqrt{8\overline{P_1}}}{\overline{P_1}^{\frac{1}{3}}} \tag{3.33}$$

By using this convention, Figure 3.10 displays the contact model in terms of internal energy over displacement, with internal energy plotted on the Y-axis and displacement on the X-axis.

As the spherical particle approaches the surface, the energy remains zero until the contact point O for $\overline{\delta} = 0$, where the energy snaps to the value in point A. The energy $U_I(A) - U_I(O)$ is instantly dissipated in elastic waves. The static equilibrium of the contact is in point C, the minimum of U_I.

During an impact, the incoming particle with inbound kinetic energy T_i follows the curve through points $OACB$. If the energy is not enough, the particle oscillates around the equilibrium point C until the energy is dissipated.

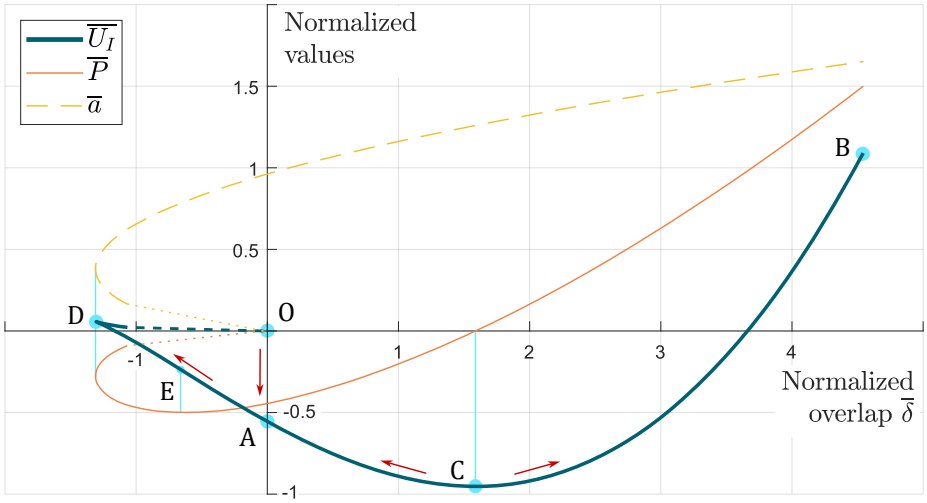

Figure 3.10: Variation in normalized internal energy $\overline{U_I}$ as a function of normalized separation, as predicted by the J-K-R-S model of elastic sphere/flat contact with adhesion, by Johnson and Pollock [59]. The same graph also reports the normalized contact force ($\overline{P}$) and contact radius ($\overline{a}$) predicted by the contact model. The particle touches at O and snaps to A, initial non-equilibrium contact. Between D and O, no stable equilibrium is possible. C is the point of static equilibrium at zero load. E is the equilibrium at maximum negative imposed load; D static equilibrium at maximum imposed displacement. Energy is dissipated during snap-on O-A and snap-off D-O. Detaching from the equilibrium requires enough energy to cross C-D.

3.4 Chapter Summary

This chapter has comprehensively explored the critical role of particle contact models in accurately simulating particulate systems within the framework of Discrete Element Modeling (DEM). By delving into the foundational Hertz contact theory, we established the basis for understanding normal and tangential forces, as well as the limitations inherent in purely elastic models when applied to real-world materials. The introduction of adhesive elastic models, including the Johnson-Kendall-Roberts (JKR) and Derjaguin-Muller-Toporov (DMT) frameworks, highlighted the significance of adhesive forces in both dense and sparse particle assemblies, particularly emphasizing the impact of the Tabor parameter in selecting appropriate models.

Furthermore, the discussion on Spring-Slider-Dashpot (SSD) models underscored their versatility and widespread adoption in DEM simulations, facilitating

the incorporation of frictional and damping effects essential for realistic particle interactions. The examination of rolling friction models provided insight into additional complexities such as torque generation and energy dissipation, which are pivotal for capturing the nuanced behavior of non-spherical and deformable particles.

CHAPTER

4

The Kinetic Adhesion Test

This section reports work presented in the original paper *Estimation of Mesoscale Surface Energy in the Kinetic Adhesion Test*, published the Journal *Powder Technology* [95], which reports the teoretical foundation of the test.

Also, the paper *Kinetic Adhesion Test to Determine Particle Surface Energy* [96], published the Journal *HardwareX*, outlines the construction of the hardware device designed specifically to conduct the test [96].

This work was developed during the mobility at Newcastle University, in Newcastle upon Tyne (UK), under the supervision of Dr. Sadegh Nadimi.

A portion of this work was presented at the *19th UK Travelling Workshop: GM3* (see Section 7.3.2), held in the Imperial College London.

4.1 Motivation

Effective handling of fine powders is essential for numerous industrial processes, including food processing, mining, pharmaceuticals, and additive manufacturing. However, cohesive flows often present a significant obstacle, particularly when it comes to powder transport, leading to slow or even stalled operations. This is a common issue that must be addressed for many industries to function efficiently. Fine particulate materials can be characterised by various levels of adhesion or stickiness. This characteristic affects their physical, mechanical, chemical and hydraulic behaviour and is significant in a range of applications from pharmaceutical processing to powder-based additive manufacturing [87].

For certain processes, such as Laser Metal Deposition, it can be challenging to devise an alternative means of delivery, highlighting the importance of understanding the effects of particle adhesion. According to Singh et al. [113], comprehending and mitigating the impact of particle adhesion is critical for the advancement of this process. Therefore, exploring new ways to handle fine powders and improve transport is an ongoing priority for many industries.

On the micro-scale, the adhesion between fine particles and particle-surface is determined by various interactions, including Van der Waals forces (dispersion, dipole-induced-dipole, charge-fluctuation...), Electrostatic forces (Coulomb, ionic, dipolar, hydrogen bonding...). Experimental studies involving particle detachment and peeling offer insights into particle adhesion forces and the adhesion energies of solid surfaces in contact, which are indicative of attractive short-range forces [54]. Such experiments hold significance in applications such as powder technology, xerography, ceramic processing, the production of adhesive films, and the comprehension of granular flow and crack propagation in solid materials. Several techniques, including the pendulum, spring-balance (Atomic Force Microscopy - AFM), centrifugation, vibration, impact, and airflow, have been suggested for quantifying adhesion forces [49].

Numerous commercial tools are available for the quasi-static bulk characterization of powder behavior [39], providing information regarding internal and wall friction angles, flow initiation stress, bulk cohesion, and other properties. These characteristics are determined by applying compressive, shearing, or tensile loads to a powder bed. When translating the results of bulk characterization into Discrete Element Method (DEM) simulations, it is necessary to calibrate the contact model parameters, which is an empirical process. During calibration, the real-world experiment is digitally replicated, and the disparities between reality and simulation are minimized through parameter exploration [4].

Atomic Force Microscopy (AFM) allows for a direct measurement of the force-displacement curve, for micron sized particles on atomically flat surfaces [106]. The obtained measurements are heavily influenced by the local curvature and asperities, resulting in values that are lower than what can be expected by the JKR theory. A single contact can be evaluated at any time, therefore several measurements are needed to characterize even a single particle, resulting in unpractical

long measurement times for engineering applications. To similarly determine the adhesive properties of a single particle, Shukla and Henthorn [111] use a microfluidic channel to determine the fluid velocity needed to detach a particle from the channel wall. Hoshino et.al. [51] use an electrostatic detachment method to determine the adhesion force of charged toner particles. This method is suitable only for charged particles.

The level of detail in Computational Fluid Dynamics-Discrete Element Method (CFD-DEM) simulations can be adjusted to meet specific process requirements. As discussed in Chapter 3, contact models must balance complexity with computational efficiency. The method proposed herein falls into the category of impact methods, offering the advantage of a mesoscale approach. It can capture the average behavior of small material samples, without the need for AFM to measure single, very localized interactions. At the microscopic level, the surface topography of particles and local surface conditions can lead to different responses in various orientations. However, in systems with numerous interactions, the effect on overall behavior averages out, making simplified meso-scale models more advantageous.

The Kinetic Adhesion Test (KAT) method is grounded in the well-accepted Johnson-Kendall-Roberts (JKR) contact model [58], presented in Section 3.3.2. The proposed KAT method is able to capture the average behaviour of a small material sample, without recurring to AFM, and able to measure the interaction of a single particle, or bulk models.

Van der Waals forces are dominant in fine particles, followed by electrostatic forces in the presence of high charges, and capillary forces at high humidity levels. Magnetic interactions can be relevant ferrous materials. Johnson, Kendall and Roberts (JKR) proposed one of the widely adopted elastic-adhesive contact models [58][59]. In this model, a spherical particle in contact with a surface, under no external loads, produces a finite contact radius a as described by Hertz theory [48] for the contact of perfectly elastic spheres due to the attractive forces. In its formulation, a contact is essentially equivalent to a crack, and reads "the approach followed in this analysis, is similar to that used by Griffith in his criterion for the propagation of a brittle crack". For dissimilar surfaces, the Dupré work of adhesion is $\Gamma = \gamma_1 + \gamma_2 - \gamma_{12}$ [30], where γ_1 and γ_2 are the intrinsic surface ener-

gies of the solids, and γ_{12} the interface energy. The binding energy at the contact circle is defined as the surface energy per unit area of the surfaces multiplied by the contact circle area of radius a:

$$U_S = -\pi a^2 \Gamma \tag{4.1}$$

The contact radius a determined by the balance between surface (U_S), elastic (U_E) and potential energy from the applied load (U_P) is the base to derive the JKR contact model [58].

By accepting this definition, the relevant implication is the connection of fracture mechanics to the adhesion of fine particles. The considerations that apply to fracture mechanics such as stiffening, bridging, and residual stress also apply to this field. The application of fracture mechanics to adhesive interfaces is explained by Kendall [61]. The method proposed in this work elaborates on the notion of the adhesive energy determination through an impact [139], treating the interface as a bond to be broken in an energy-driven event. This translates into a high strain rate, to which the adhesive energy is sensitive [61]. The centrifuge method used by many authors [110, 62, 97] can be seen as the quasi-static complement to the one proposed.

The energetic description of the impact between elastic-adhesive particles is successful in the description of dust coagulation in space [17], a critical stage in planetary formation. The JKR contact model is one of the most adopted contact models in DEM simulations [21], for which adhesive energy is a critical parameter.

4.2 Test procedure

The Kinetic Adhesion Test (KAT) is divided into five phases, represented in the flow diagram of Figure 4.1.

Particle distribution

Proper particle sampling and dispersion onto a substrate are critical steps for accurately representing the Particle Size Distribution (PSD) of powders. Manual or dedicated distribution tools can be used to ensure optimal dispersion and avoid overcrowding, which facilitates subsequent processing stages. The dispersion of powders is complex and requires guidance from relevant literature, such as [16].

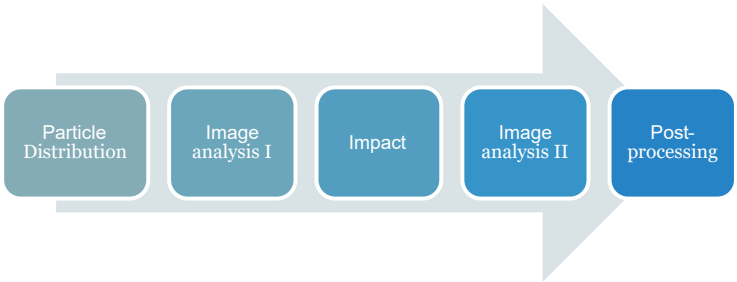

Figure 4.1: Flow diagram of the Kinetic Adhesion Test.

Determining the correct width of the PSD is crucial, as it affects the amount of data that needs processing. Once particles are dispersed without clustering, the following steps use relative assessments to determine cohesion, and sample segregation should have a limited influence on the results.

The substrate must be prepared according to the measurement requirements. In the present work, the smooth surfaces were cleaned using a $50\% - 50\%$ solution of acetone in water, and dried in ambient air. Surface roughness, contamination and humidity can be introduced to represent the desired real-case scenario, determining the mesoscale adhesive energy.

Image analysis I

In this work, the powder sample was analyzed by means of an optical microscope. The images were digitized for a resulting resolution of 0.95 px/μm. The objective is to obtain at least $10px$ per particle diameter, which is the minimum required for viable diameter information [6]. Using the open-source Fiji image processing tool [107], the microscopic images were filtered, labelled and the resulting binary image was used to determine the PSD: one of the acquired images is presented in Figure 4.4a. Figure 4.5 reports an expected distribution. This semi-automatic process allowed for the consideration of samples composed of up to several thousand particles.

Impact

The suggested testing approach employs the hardware described technically in [96] and shown in Figure 4.2. The open-source design files are stored in an open-access repository [93]. It allows recording the velocity of the falling sample at the moment

of impact with the surface. The hard impact grants an almost instantaneous stop of the substrate, while the particles' momentum must be balanced by the adhesive energy, as described in Section 4.3. In this phase, the larger particles tend to detach while smaller ones do not, as is represented in Figure 4.3.

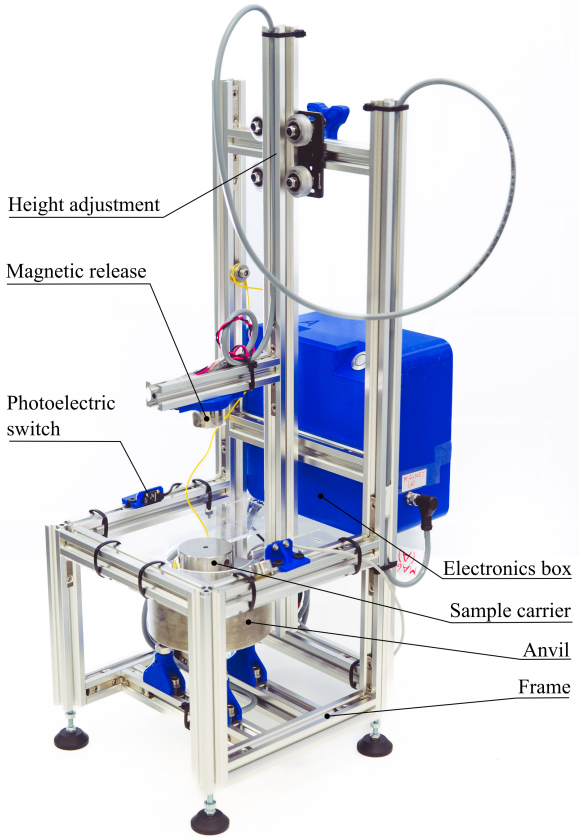

Figure 4.2: Annotated view of the test device [96].

Image analysis II

The PSD is determined again for the sample after the impact, with a procedure similar to 4.2. An example image is Figure 4.4b. In an ideal case, the resulting distribution is truncated at a specific diameter d_C, and the cumulative curve consequently changes (see Figure 4.5).

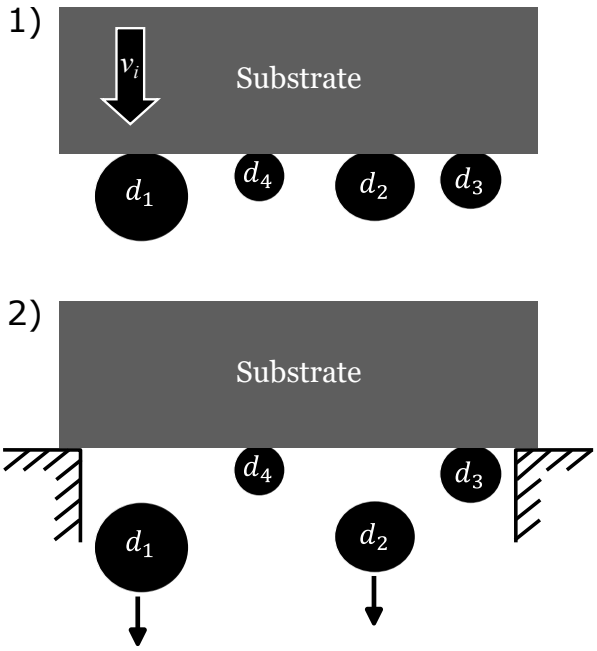

Figure 4.3: Sketch depicting the detachment of the particles during the impact, from 1) to 2).

Post-processing

The two PSDs before and after the test are then compared. If no unexpected deviation occurs, the distribution is truncated at the critical diameter d_C. In an ideal case of perfectly spherical particles and uniform adhesion, Figure 4.5 displays how the PSD changes before and after the test, indicating the critical diameter. Smaller particles constitute a bigger fraction of the total after the impact, therefore the PSD curve after the impact should be steeper and end sharply at the top. After acquiring the exact drop velocity and the exact critical diameter, Equation 4.5 is used to determine the adhesive energy Γ.

The deviation from the ideal case results in a distorted PSD after the test. Therefore, the proposed test is able to quantify the mesoscale adhesive energy between particles and a substrate. It is expected that each individual particle presents a slightly different adhesive bond. Reasons include and are not limited to particle shape, particle and/or substrate roughness, uneven interface oxidation or contamination. Also, if only a small number of larger particles compose the sample, the distribution (closer to unity) might get distorted.

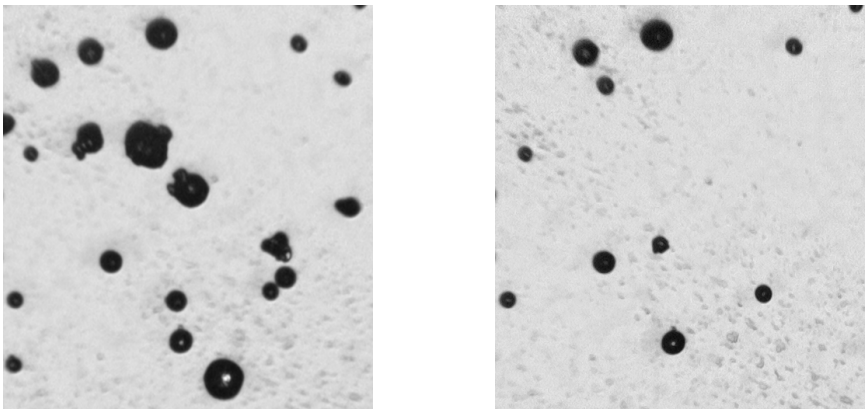

(a) Sample before the test.

(b) Sample after the test.

Figure 4.4: Example of the microscopy images captured before and after the impact ($v_i = 2.21$ m/s), carefully picked to show the same location. 316L steel powder sample on a glass substrate. The maximum diameter after the impact (particle at the top) is 39 μm, which is compatible with the values determined in Section 4.4.

In Shimada et.al. [110], a centrifuge method measured particle adhesive strength on a substrate, defining critical diameter as the average size range for 50% particle removal. A similar metric applies to the proposed method. Results showed medium-sized particles had the highest adhesion strength, while smaller and larger particles had lower strength. This effect can also deviate the PSD after the proposed test from the ideal case.

4.3 Theory and calculation

Johnson and Pollock [59] explore the original model [58] to find the response of colliding adhesive elastic particles. The surfaces' deformation is caused by the sphere inertia, $m\frac{d^2\delta}{dt^2}$), balanced by the total force at the interface P. In the case of a static contact, an external load P would cause a deformation δ. We recall the definitions of the JKR contact model of Section 3.3.2, as well as Figure 3.10, which displays the contact model in terms of internal energy over displacement, with internal energy plotted on the Y-axis and displacement on the X-axis.

During an impact, the incoming particle with inbound kinetic energy T_i follows the curve through points $OACB$. If the energy is not enough, the particle oscillates around the equilibrium point C until the energy is dissipated through, therefore the energy state corresponds to the equilibrium.

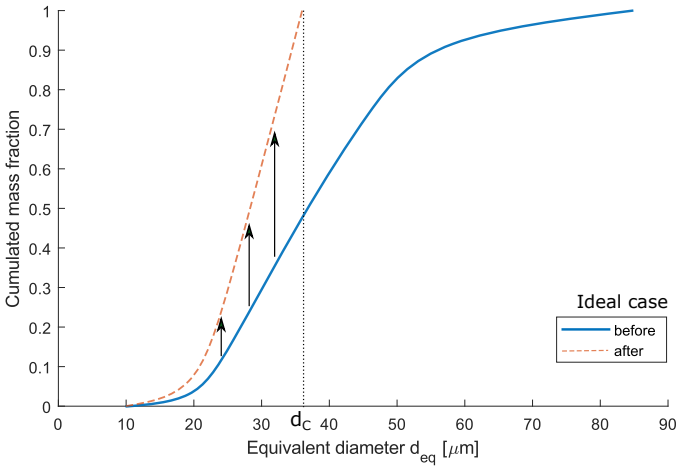

Figure 4.5: Ideal case of a cumulative PSD before and after the test.

During free fall, the interface is not subject to any additional external forces since the system is accelerating as a whole and is, therefore, essentially free from the influence of gravity. Before the impact with the stopping surface, the particles are in the energy well $U_I(C)$, represented in the diagram of Figure 3.10, and at the same time potential energy is being converted into kinetic energy T_{in}.

The critical condition can be determined by balancing the kinetic energy available to the particle with the total energy required for it to escape the energy well, from point C to point D of Figure 3.10:

$$T_{crit} = U_I(D) - U_I(C) \tag{4.2}$$

The minimum value of Equation 3.32 is $\overline{U_I}(C) = -0.95244$, obtained for $P_1 = 2$. At the detachment point $\overline{U_I}(D) = 0.05824$ at $P_1 = \frac{1}{18}$. Therefore, considering the normalization reported in Equation 3.32:

$$T_{crit} = 1.0107 \left(\frac{9\pi^5 \Gamma^5 R^4}{K^2} \right)^{\frac{1}{3}} \tag{4.3}$$

The kinetic energy can be expressed as

$$T = \frac{1}{2} m v^2 = \frac{2}{3} \rho R^3 v^2 \tag{4.4}$$

Solving Equations 4.3 and 4.4 for Γ gives:

$$\Gamma = v_i^{\frac{6}{5}} \cdot R_c \cdot \left(\frac{2^3 K^2 \rho^3}{3^5 \pi^2 (1.0107)^3} \right)^{\frac{1}{5}} \tag{4.5}$$

where R_c is the critical radius, or the size of the biggest particle able to stay attached to the surface, and v_i is the velocity at the moment of impact. The same formula can be used if considering the potential gravitational energy since, for the simple case of a falling object from a standstill, the impact velocity would be directly related to the dropping height h by $v = \sqrt{2gh}$.

As mentioned in the Introduction, the JKR solution for the adhesion of elastic spheres [58] is conceptually identical to Griffith's theory of elastic fracture [44]. By balancing the load's potential energy, strain energy, and the surface energy of the crack faces, Griffith derived the criterion for stability of a crack of length $2c$ in an infinite elastic sheet, with tensile stress σ applied in the orthogonal direction of the slit. As a sanity check, the reader can recall the theory to express the fracture criterion in terms of adhesive energy, to compare the magnitude of the values obtained. The proposed mesoscale approach is well suited to be compared with Linear Elastic Fracture Mechanics, as it shares many of the underlying assumptions. Conversely, the adhesive energy values obtained with this method might not be compared on the micro-scale, where different assumptions are necessary.

4.4 Results

Initial validation has been carried out using a stainless steel metal powder on a polymer film and on a microscope glass slide, for which the material characteristics are presented in Table 4.1.

Easterling et.al. [29] used the same JKR contact model, measuring the geometry of the contact (a_0) to determine the adhesion between metallic particles observed through electron microscopy: the interface energy for Fe-Ni contact was estimated to be in the order of 6 J/m^2. In this section, the contact radius a_0 is measured using optical microscopy.

Table 4.1: Material properties used in this study.

	ρ $[kg \cdot m^{-3}]$	E $[Pa]$	ν $[-]$
316L Stainless steel [87]	7980	$2.11e11$	0.3
Borosilicate glass (Ted Pella inc.)	2510	$7.3e10$	0.2
UPVC film (azom.com)	1440	$3.0e9$	0.3

Polymeric film

The polymeric film has been securely adhered to a stiff substrate in the carrier. A small sample of metallic powder was carefully distributed on the substrate, from a low drop height. The dispersion was carried out manually, given the forgiving nature of the powder under analysis, but an automatic tool would have greatly helped in guaranteeing a better, uniform dispersion [16].

The test was conducted at room temperature and humidity (approx. 20 °C, RH 50%); no particular tool was used to eliminate static charges. PSD was determined through optical microscopy and image analysis, as reported in Figure 4.6. The sample was loaded in the apparatus, and it impacted the anvil at a velocity of $v_i = 1.40$ m/s. The same optical method has been used to determine the PSD after the impact, also reported on the same graph. The imaged sample is composed of about 500 particles before the impact and 340 after. The image resolution for this case is 0.93 μm/px.

The PSD is reported in Figure 4.6, from which it is possible to determine the critical size or the diameter of the largest particle still attached to the substrate after the impact. The PSD changed as expected, with a little deviation from the ideal case of Figure 4.5. This can be attributed to the non-perfect sphericity and smoothness of the particles and the fact that only a few elements represent the higher side of the distribution. The critical diameter determined from the PSD in Figure 4.6 is $d_C = 46$ μm.

Using the values of this case from Table 4.1 and Equation 3.30 we obtain $K = 4.33e9$ Pa. Equation 4.5 is then used to determine the interface's Adhesive Energy, resulting in $\Gamma_{KAT} = 17.53$ J/m^2.

The same polymeric film has been carefully extended in support spanning a distance of 15 mm, applying a negligible stretch to avoid sagging. A small sample of particles was distributed on the surface, and the sample was flipped upside-down. By employing a reflective optical microscope it was possible to image the contact point of the particles and, by switching the focus, the diameter of the same particle. An example is reported in Figure 4.7. Since the contact could be irregular, the equivalent contact diameter is assumed to be $a_0 = \sqrt{A/\pi}$.

At equilibrium, the contact radius of the spherical particle on a surface is a_0

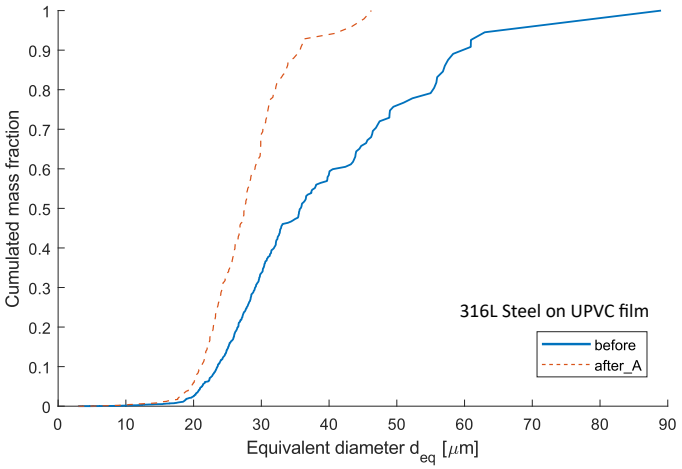

Figure 4.6: Cumulative mass distribution of 316L stainless steel powder particles on a UPVC film, measured before and after the impact. The calculated adhesive energy in this case is $\Gamma_{KAT} = 17.53$ J/m^2.

[58]:

$$a_0^3 = \frac{6\Gamma\pi R^2}{K} \tag{4.6}$$

which can be rewritten to express the surface energy Γ:

$$\Gamma = a_0^3 \frac{K}{6\pi R^2} \tag{4.7}$$

Using this formulation, the example reported in Figure 4.7 has a value $\Gamma_{a0,1} = 18.1$ J/m^2. A sample of 8 particles gave as a result an average of $\Gamma_{a0} = 19.8$ J/m^2, with standard deviation $\sigma_{a0} = 4.4$ J/m^2.

The contact area has been observed optically to be delimited by the first Newton ring; this is acceptable given the expected contact geometry. Johnson [58] analytically derived the deformed shape of the contact. The stress at the contact's edge tends to form a neck, Figure 3.9 represents it visually. For this reason, it is assumed that the first visible edge is indeed the contact's edge. This technique, analyzed by Raedler et.al. [101] and by Waschke et.al. [132], in its more complete form is called Reflection Interference Contrast Microscopy (RICM), and is an appropriate method to determine the contact radius of particles on a flat, transparent substrate.

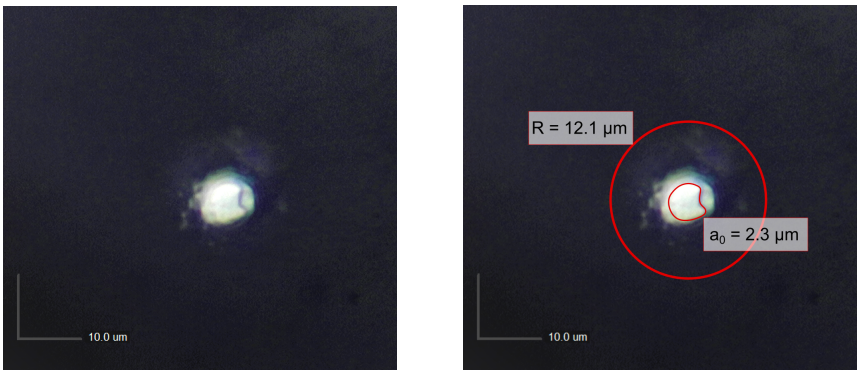

Figure 4.7: Optical microscope image of the contact of one 316L stainless steel powder particle on UPVC film.

Borosilicate glass

The same procedures were followed changing the substrate material to borosilicate glass, whose characteristics are reported in Table 4.1. In this case, the test has been conducted two consecutive times with increasing impact speeds. Figure 4.8 reports the PSD of the test. It is interesting to note that the shape of the distribution is somewhat preserved between the three curves, as expected from the considerations in 4.2.

Case A: impact speed $v_i(A) = 2.21$ m/s. The critical diameter $d_C(A) = 52.9$ μm determines an adhesive energy of $\Gamma_{KAT}(A) = 103.34$ J/m^2.

Case B: $v_i(B) = 2.96$ m/s; $d_C(B) = 35.6$ μm; $\Gamma_{KAT}(B) = 98.78$ J/m^2.

The images in Figure 4.4 are relative to Case A, for which the expected values are in line with the ones determined in this section.

The use of a thin slide allowed us to see through the glass, and capture an image of the contact surface as with the previous case. The measured value across 8 samples is $\Gamma_{a0} = 95.4$ J/m^2. A wide standard deviation of 34 J/m^2 was observed. Adhesion phenomena exhibit inherent stochastic characteristics, particularly within the mesoscale considered in this study. The substantial dispersion observed suggests that particles, adhering to the surface in random orientations, possibly interact with the surface with a degree of variability. One hypothesis is that, for these higher Adhesive Energy values, some particles can stick in unfavorable orientations, while others either fall or reorient to touch the surface in more favorable spots.

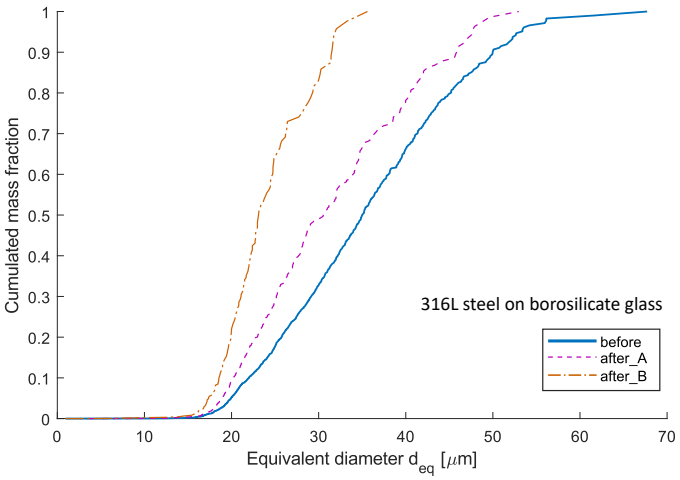

Figure 4.8: Cumulative mass distribution of 316L stainless steel powder particles on a borosilicate glass slide, measured before and after the impacts.

4.4.1 **Validation using a DEM model**

The particle response normal to the surface is the most relevant to the presented Kinetic Adhesion Test, and a simplified representation is provided in Figure 3.2. Most DEM codes have an implementation of the purely elastic Hertz-Mindlin contact model: once the particle enters contact with the surface, the reaction force can be modelled by a non-linear spring whose elastic constant is related to the material properties and the particle size [48]. The tangential force model is based on the Mindlin-Deresiewicz work [82][83], but is not relevant for the simulation of this test. Additionally, a damping force F_d is applied where the damping coefficient is related to the coefficient of restitution according to the work by Tsuji et.al. [126]. This translates to a certain measure of viscous dissipation, which has the collateral effect of contributing to numerical stability.

The JKR contact model, previously discussed and represented in Figure 3.10, is implemented in EDEM as "*Hertz-Mindlin with JKR Version 2*" where the normal force is adhesive-elastic according to JKR, and the damping force is the same as the pure Hertz-Mindlin model.

To have a simulation representing the test, a surface is placed in the origin, and a large number of particles are dispersed onto it. The spherical particles interact exclusively with the surface, not with each other. The first phase of the

simulation is run until the particles settle to a null velocity. The particles' size is determined by a random distribution to cover a useful size range around the expected critical diameter, roughly matching the size range of the experiment.

The following result is used to validate the case of 316L stainless steel particles on UPVC film. A similar analysis was conducted for the data on glass substrate, with similar results. In the simulation, particle size is a uniform distribution from 30 μm to 72 μm. Material properties correspond to the 316L stainless steel and UPVC film already reported in Table 4.1, and the spherical particles are allowed to interact exclusively with the substrate plane. The normal model is set to JKR, with a surface energy of 17.53 J/m^2, the same value as the measurement reported in Section 4.4.

The substrate is accelerated to the desired falling velocity, the particles are pressed into the surface and accelerate with it. Once the velocity is reached, it is maintained constant until the particles have stabilized. The coefficient of restitution is set to a very high value $e = 0.99 - 0.999$, to interfere as little as possible with the detachment. It is used to provide some numerical damping during the rest of the simulation, by setting it to a lower value. If the restitution coefficient is set to unity, the particles would oscillate indefinitely around the equilibrium position and velocity. Gravity is considered in the simulation both on the particles and the substrate.

Once the simulation is stable, with the substrate and particles falling at the same velocity, the substrate velocity is immediately set to zero, effectively realizing a step input. From the simulation, we expect the particles to detach if their diameter is larger than a critical diameter, with a velocity that corresponds to the residual kinetic energy after breaking the contact. Figure 4.9 represents the result of the simulation after the substrate stops at $t = 0.0002$. Some additional time is allowed to pass to allow the kinetic energy of the smaller particles to be dissipated in oscillations around the equilibrium.

We recall as expected value the obtained critical diameter from Figure 4.6. Indeed, running the simulation leads to particles detaching for a critical diameter of $d_c = 46.0$ μm, as highlighted from the graph in Figure 4.10. Smaller particles dissipate all their kinetic energy by oscillating around the equilibrium through viscous dissipation. Larger particles detach from the surface, retaining an increasing

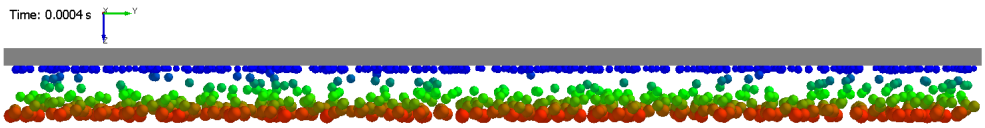

Figure 4.9: Result of the simulation - 316L steel powder on UPVC film. The particles are coloured according to the velocity, and the substrate is represented in grey. Bigger particles were able to detach and proportionally retained more kinetic energy. Smaller particles did not detach and their kinetic energy was dissipated in the oscillations around equilibrium.

fraction of their kinetic energy acquired during the drop, determining a velocity that tends asymptotically to the value just before the impact for larger and larger particles. A similar result can be obtained for the stainless steel powder dispersed on borosilicate glass.

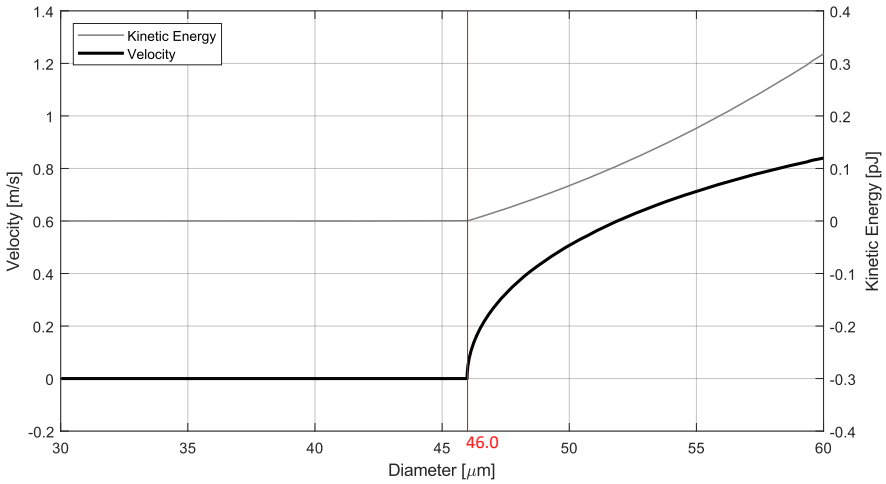

Figure 4.10: Result of the simulation - 316L steel powder on UPVC film. The critical diameter obtained from the simulation is highlighted by the vertical line. Bigger particles were able to detach and proportionally retained more kinetic energy, for a residual velocity asymptotically approaching the velocity before the impact. Smaller particles did not detach and their kinetic energy was dissipated in the oscillations around equilibrium.

As mentioned, the presented test is able to give a representative value for the adhesive energy Γ of the interface between particle and substrate. This mesoscale values does not differentiate between the contribution of some real-world features such as surface roughness, contact plasticization, liquid bridges, and electrostatic

charge. This work follows the considerations of the JKR contact theory [58], ensuring an agreement between the underlying assumptions. For this reason the calculated Adhesive Energy values are useful in simulation, resulting in a good agreement of the considered quantities whenever the same JKR contact model is used.

4.4.2 **Strain-rate dependency**

The influence of strain rate on adhesive energy is explored through analytical and molecular dynamics approaches in two distinct papers. The analytical study by Kendall [61] delves into strain-rate dependency during detachment, revealing a tendency for the apparent adhesive energy to increase. The work provides valuable insights into the formation and fracture of adhesive interfaces between rubber and glass, with a particular focus on the influence of strain rate. The experiments involved applying forces to propagate interfacial cracks, revealing complex kinetics and hysteresis phenomena akin to liquid droplets wetting solid surfaces. Notably, Kendall observed an increase in adhesion with contact time and crack speed, introducing the concept of Adhesive Energy (Γ), encompassing both reversible and irreversible work. The molecular dynamics investigation conducted by Chowdhury et.al. [18] utilizes simulations to elucidate the strain-rate-dependent behavior of adhesive contacts mediated by silane groups on glass surfaces.

The work from Zafar et.al. [139] reports values obtained from a setup compatible with the one used for this work. In their drop test, they measured the falling velocity of the stub, onto which a silanized glass was dispersed on a silanized glass substrate. The paper reports the values for *Impact Velocity* and *Critical Diameter* resumed in Table 4.2. The material properties used for the borosilicate glass are in Table 4.1.

With only these two values and the material properties it is possible to apply Equation 4.5, obtaining the *Adhesive Energy* Γ.

A further verification step can be performed. Adhesive energy can be determined by considering the deceleration the particles are subjected to. In his book, Thornton [21] reports a formula to determine the critical impact time or the duration of a Hertzian elastic impact of a spherical particle on a flat surface

[102]:

$$t_c = 2.865 \left(\frac{m^2}{RE^{*2} v_i} \right)^{1/5} \tag{4.8}$$

As a crude approximation, we can consider the detachment time t_d to be half of that. Both values are reported in Table 4.2, but it must be clear that this formula is exact for the mentioned conditions, and the adhesive term can generate significant discrepancies. The adhesive energy can be estimated by equating the detachment force to the adhesive force, as proposed by Zafar et.al. [139]. However, in this case, the detachment force values would be determined by $F_{det} = mv_i/t_d$.

$$\frac{F_{det}}{F_{ad}} = \left(\frac{mv_i}{t_d} \right) / \frac{3}{2} \pi R_c \Gamma_{td} = 1 \tag{4.9}$$

therefore

$$\Gamma_{td} = \frac{8}{9} \rho R_c^2 \frac{v_i}{t_d} \tag{4.10}$$

resulting in the values reported in Table 4.2, which are consistently 1.8% lower than the ones determined by Equation 4.5. This difference is compatible with the approximation of the detachment time, which is considered a perfectly elastic impact.

Table 4.2: Impact velocity and critical diameter determined by Zafar et.al. [139]. Adhesive energy Γ is determined using the method proposed in this work. Calculations were repeated by using the theoretical time needed for a normal rebound [21] and the corresponding deceleration.

Impact Velocity							
v_i $[m/s]$	1.8	2.3	3.0	4.1	4.8	5.4	6.0
Critical Diameter							
d_c $[\mu m]$	66.4	63.8	59.8	53.0	47.5	42.3	37.3
Adhesive Energy							
Γ $[J/m^2]$	44.8	57.7	74.5	96.0	103.9	106.6	106.7
Rebound Time [21]							
t_r $[ps]$	201.3	184.2	163.7	136.3	118.4	103.0	88.9
Detachment Time							
$t_d \approx t_r/2$ $[ps]$	100.7	92.1	81.9	68.2	59.2	51.5	44.4
Gamma considering detachment Time							
Γ_{td} $[J/m^2]$	44.0	56.7	73.1	94.3	102.1	104.7	104.8

Given these considerations, we can trace the graph of Figure 4.11, which shows a dependency of the adhesive energy to the impact velocity, which is related to the strain rate of the contact given its influence on t_c. Faster impacts determine

a faster strain rate of the contact. Silane groups on the glass surface greatly increase their cohesion. Chowdhury et.al. [18] performed molecular simulation precisely to determine whether the strain rate has an influence on glass adhesive contacts mediated by silane groups. Different domains are highlighted in the research, based on both the bond strength (in $[GPa]$) and the adhesive energy (in $[J/m^2]$). Domain 1 corresponds to low strain rates and the lowest values for both the bond strength and adhesive energy, where a weak dependency is highlighted. Domain 2 is a transition towards the much higher values of Domain 3. Their argument is that the specific chemical interlacing mediated by the silane groups on the surfaces change their response to a high strain rate detachment. When the bond breaks gradually, molecular thermal movements assist in separating it. However, as the strain rate increases, there's less time for these molecular movements to untangle the bond, leading to a gradual increase in adhesive energies. This trend continues until it reaches a maximum, where the molecular groups separate abruptly, primarily without relying on thermal movements. The maximum values reported by the paper are between 80 J/m^2 and 120 J/m^2, depending on the surface concentration of silane groups. The adhesive energy values obtained by this work, reported in Fig. 4.11, appear to correspond to Domains 2 and 3, where the transition tapers off on the higher end of strain rates.

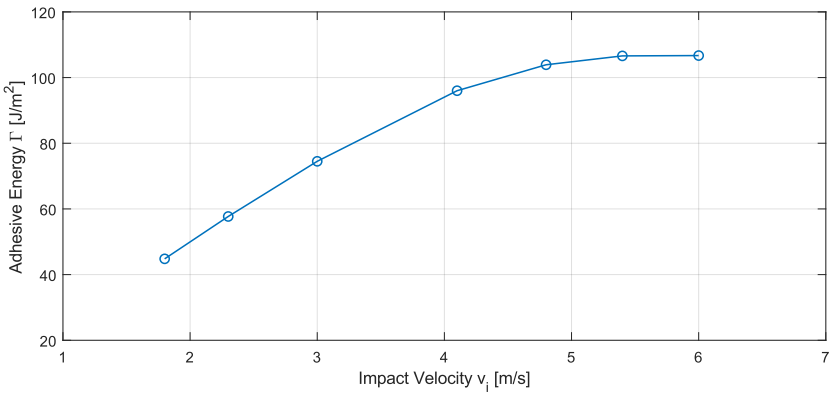

Figure 4.11: Adhesive Energy values of silanized glass beads on silanizad glass substrate [139]. The values are those of Table 4.2.

4.5 The KAT device

The presented device aims to provide a reliable platform to conduct particle's adhesion test through kinetic impacts. It consists of a sample carrier which falls on an anvil. The carrier is magnetically held in place until the moment of release. Figure 4.2 reports the annotated view, highlighting the main elements of the apparatus. All the necessary build instructions and design files are available in the repository [93] in the spirit of Open Hardware and Open Source movements. Making the design publicly available encourages the replication and improvement of the apparatus. This information is published as a peer-reviewed article [96].

In principle, this device can be used to:

- Characterise particles' surface energy
- Sharp impact testing of a sample
- Adapt to strain-rate dependent tests

The micro-controller unit monitors the fall through a precise timing of the release, the passage through a photoelectric switch beam, and the moment of impact. It also handles the communication with the operator and the sequence of events of the test. The sensors are active only during the test, and deactivated otherwise. The IONO MKR platform has been chosen to support the 24 V sensors and provide a layer of protection to the Arduino MKR WiFi 1010 board, which has been chosen to provide Bluetooth Low Energy (BLE) connectivity.

The aluminium frame is built using OpenBuilds extrusions and carriage. The anvil height adjustment and the photoelectric switch are held by 3D-printed parts. The wiring is held in a 3D printed enclosure with a laser-cut lid.

4.5.1 Design files summary

Design filename	File type	Open source license	Location of the file
Mechanical assembly	CAD files	CC BY 4.0	Onshape repository
Blueprints	PDF	CC BY 4.0	Zenodo
Firmware sketch	INO	CC BY 4.0	Zenodo Github
Pictures	JPG	CC BY 4.0	Zenodo
Assembly	STEP and PARA-SOLID	CC BY 4.0	Zenodo
toPrint	STEP and STL	CC BY 4.0	Zenodo

The information on this project is publicly available in the Zenodo repository. It includes the relevant design information: the firmware, the complete Bill of Materials, the complete CAD assembly in the standard STEP format, and additional pictures of the completed device.

Mechanical assembly is the complete CAD design, realized in Onshape®. The complete design can be cloned or exported. The file structure is self-explicative: the design files are organized in subfolders according to their hierarchy as subassemblies.

Blueprints are the complete design files for the device's structure, derived from the CAD design, for parts and assemblies.

Firmware sketch is the Arduino sketch to load on the microcontroller. It is provided as a GitHub project.

Pictures of the completed device.

Assembly additional design files in Step format.

toPrint is a STEP and STL files collection of the parts that can be manufactured using a low-cost FDM 3D-printer.

4.5.2 **Hardware description**

Anvil

The anvil's mass and surface hardness are responsible for the dynamic of the impact. The impact is suspended on three springs to isolate its response from the surrounding elements: the structure and the bench. The top surface is ground flat and ideally is hardened. The bottom presents three flat-bottom holes for the spring sleeves and six mounting holes for the sensors.

The objective is to approximate a two-bodies elastic collision, where one body is reasonably larger than the other. In this hardware, the anvil size has been chosen to be approximately 10 times the mass of the impacting carrier and sample. Given a mass of 2.7 kg, or a weight of 26.6 N, the anvil is suspended on three springs with an elastic constant of $0.7N/mm$ each. The total compression at rest is then 12.7 mm, and the characteristic frequency f_c is much lower than the expected impact dynamic, providing isolation between the impact and the ground:

$$f_c = \frac{\omega}{2\pi} = \frac{1}{2\pi}\sqrt{\frac{k}{m}} = 27.8 \text{ Hz} \tag{4.11}$$

The spring sleeves and adjustment screws can be easily modified to accommodate springs of different stiffness. The adjustment screws (#220-002) are held by three respective 3D-printed brackets, fixed on the base of the frame by screws and T-nuts.

One normally closed vibration switch is present under the anvil. As the anvil is disturbed, it activates and sends an interrupt signal to the microcontroller, which records the impact instantly. This value will be used in addition to the photoelectric switches activation times to determine the impact velocity. Compared to the direct measurement of the touch between the carrier and anvil there is a 66 μs delay (measured through a 100 MHz oscilloscope), attributable to the elastic wave propagation, retarded motion of the anvil, and the response time of the switch.

By placing the three switches in a triangular pattern it should be possible to detect impacts happening in a non-flat orientation. In such a configuration, a comparator would trigger the interrupt, then an analog reading could be used to determine which and how many switches activated. The schematic provided in Figure 4.12 suggests a simple resistor network to perform that. If all the resistors

have the same value (10 kΩ), it is possible to know how many are activated. If the supply is 24 V, the voltage readings are resumed in Table 4.3. In the final version, this technique has not been implemented due to the higher complication of the switch circuitry, and the need of a reliable interrupt signal conflicting with an analog value read.

Table 4.3: Analog values to determine number of closed switches.

Number of closed switches	**measured voltage**
3	18
2	16
1	12
0	0

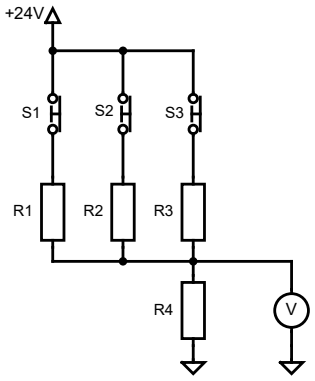

Figure 4.12: Circuit to detect multiple switches activation using one analog pin.

A piezoelectric accelerometer can be used to record the anvil acceleration upon impact, a_{anvil}. It is advisable to consider it as an option. Using Newton's second and third laws of motion, the mass ratio between anvil and carrier can be used to determine the acceleration of the carrier, and therefore of the particles that are able to remain in contact with the test surface:

$$a_{carrier} = a_{anvil} \frac{m_{anvil}}{m_{carrier}} \tag{4.12}$$

The carrier deceleration value can be used to determine the surface energy per unit area:

$$a_{carrier} = \frac{3}{2} \pi R_c \Gamma \frac{1}{m_c} \tag{4.13}$$

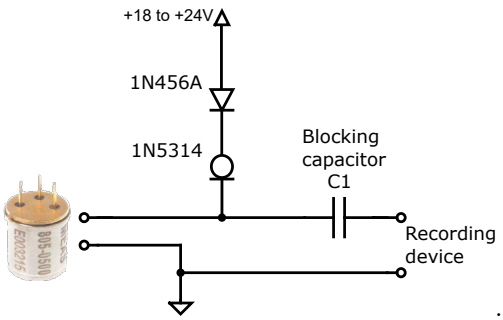

Figure 4.13: Accelerometer 2-wire circuit suggested by TE Connectivity.

where R_c and m_c are respectively the critical radius and mass from the sample powder. The highest value reported in [139] is 44.6×10^3 m/s^2, or 4542 g. Considering Equation 4.12, the accelerometer should be able to read at least 500 g. A starting point is the low-cost embeddable accelerometer model 66102APZ1 by Amphenol PCB Piezotronics, or the equivalent 805-0500 by TE Connectivity. Both of these products use a two-wire read configuration, which requires a current setting diode, to provide a constant current of $2 - 20$ mA. From the TE Connectivity datasheet, the suggested circuit is reported in Figure 4.13. The blocking capacitor C1 realizes an AC coupling to the recording circuit, but it is needed to pre-condition the signal against slow drift. A simple resistor network can be used to shift the signal back to the center of the ADC sensing range. It must be noted that the accelerometer signal can go as high as the supply voltage (24 V), therefore it must be carefully conditioned before being passed to the microcontroller. The board selected for this application (IONO MKR) allows for voltage readings with the range $0 - 30$ V.

Carrier

The carrier, made of ferromagnetic steel, can be attached to the top magnet, from which it is dropped to the anvil. Ideally, the impacting surface is hardened. In this design, the carrier presents a cavity for sample stubs of $\varnothing 30 \times 10$ mm, with one of the circular surfaces holding the powder particles. A hole on the back of the carrier can be used to insert either a screw or a stick to aid in lowering and raising the sample. Once it is placed, three setscrews hold the sample in place. Once the sample has been loaded, the mass should be recorded for Equation

4.12. The presented design suggests the use of monolithic sample stubs, where the substrate is the top surface in Figure 4.14. This is possible for commonly available materials, but a thin substrate can be securely adhered to the surface, for instance using cyanoacrilate adhesive or any appropriate bonding method. The stub can also be molded in resin, containing samples which might be used for metallographic analysis at any point before or after this test: the 30 mm diameter was motivated by this use case.

The carrier has a wire that connects it to the micro-controller. This has been added to precisely record the contact duration between the carrier and the anvil. Inside the IONO MKR unit, the digital inputs have a pulldown resistor, therefore the carrier is at ground potential. The anvil is connected to the supply voltage (24 V) through a 10 kΩ resistor. The voltage is applied only during the testing phase, when the operator should not touch the device. At the moment of impact the circuit is closed, and the signal goes high. As the carrier rebounds and leaves the anvil, the circuit opens again and the signal is pulled down to ground. The typical contact time during the impact has been measured using a 100 MHz oscilloscope to be in the order of 50 to 200 μs. The micro-controller is able to record the contact time with a precision in the order of 1 μs.

The total height of the carrier must be recorded, as it provides the input parameter for the velocity calculation through the photoelectric switches. The switches used in the prototype are the Panasonic EX-11A-PN, which have been chosen due to the high repeatability (0.05 mm), fast response time (< 500 μs), narrow beam (1 mm), as well as the robust construction against contamination and vibration. The same sensor is reading the arrival and leaving of the carrier on the beam, therefore both measurements have the same relative delay between each other, mitigating the error deriving by its response time.

Figure 4.14: Examples of sample stubs as-manufactured, prior to surface polishing. From the left, the materials are AISI 316L steel, PTFE, unalloyed copper (99.9%).

Frame

The frame is composed of 20 × 20 mm beams from the OpenBuilds®framework. Connections are made with 90° links. M5 T-nuts provide anchor points for the other elements.

A V-Groove gantry has been used to allow vertical movement of the slider, which is then locked in place by a screw and T-nut. Two T-nuts fixed in position at the top and bottom are the end-stops.

Four feet on the base allow the leveling of the device. The reference level for the whole system is placed by the electromagnet on the slider. A second level is used for the alignment of the anvil.

Microcontroller

Since both the accelerometer and photoelectric switch operate at 24 V, and to improve the resilience of the apparatus, the choice fell to an industrial shield based on Arduino: the Sferalabs IONO MKR. The microcontroller integrates wireless connectivity capability through the WiFiNINA library. BLE connection was chosen because of it ease of direct connection with smartphone devices, and the data transfer rate is more than adequate. Communication is handled through a BLE UART communication protocol, which is implemented through the HardwareBLESerial library. Small modifications to the device code can make it compatible with the more traditional Arduino serial protocol through USB. The version with Arduino MKR WiFi 1010 has been chosen to have at least two interrupt capable connections. The microcontroller is located in the electronics box on the back of the machine, visible in Figure 4.15.

4.6 Chapter Summary

This chapter introduced the Kinetic Adhesion Test (KAT) as a novel method for quantifying the mesoscale adhesive energy between fine particles and substrates. Building on the theoretical framework of the Johnson-Kendall-Roberts (JKR) contact model, KAT effectively bridges the gap between microscopic adhesion measurements and bulk powder behavior, providing valuable insights for industries reliant on fine particulate handling.

The development of a dedicated hardware device, detailed in this chapter, en-

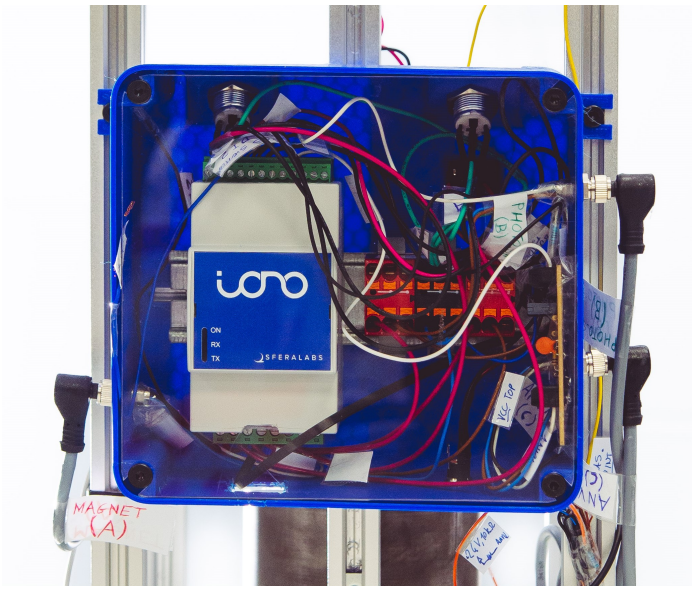

Figure 4.15: Electronics box of the device, view from the back.

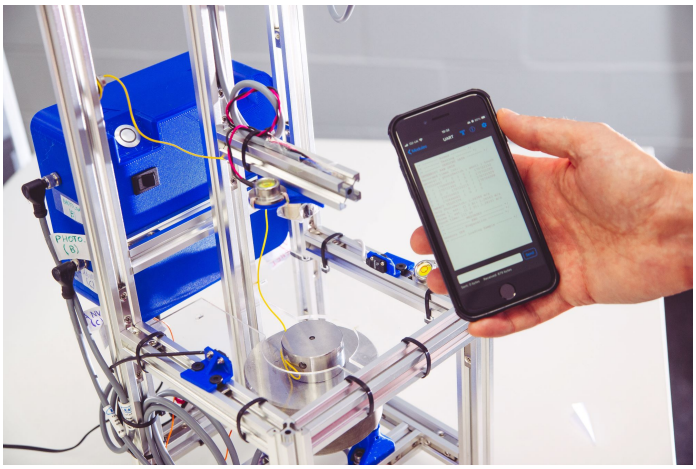

Figure 4.16: The device communicates through BLE UART terminal emulation. Any smartphone can connect to the device by installing an open-source app.

ables precise execution of the KAT procedure. Through a systematic five-phase test sequence—including particle distribution, impact, and post-processing—KAT accurately determines the critical diameter at which particles detach from a substrate upon impact. Experimental results demonstrated the method's reliability, with adhesive energy values aligning closely with theoretical predictions and validating against discrete element method (DEM) simulations.

Notably, the KAT method revealed a strain-rate dependency of adhesive energy, consistent with existing literature and molecular dynamics studies. This dependency underscores the method's capability to capture dynamic adhesion phenomena relevant to high-speed industrial processes. Additionally, the open-source nature of the KAT device fosters reproducibility and facilitates further refinements, promoting its adoption across various applications.

The Kinetic Adhesion Test offers a practical approach to measuring particle adhesion at the mesoscale, enhancing the understanding and simulation of cohesive powder flows. Its integration of theoretical principles, experimental rigor, and accessible hardware design positions KAT as a valuable tool for advancing powder technology and related fields.

CHAPTER

5

Studies on the Pneumatic Conveying

This chapter presents original work *Comparison of CFD-DEM and MP-PIC in the Simulation of Metal Powder Conveying for Laser Metal Deposition*, that has been published in the OpenFOAM Journal [94]. Part of the work was presented at the *17th OpenFOAM Workshop*, held at Cambridge University.

The experimental data presented in this chapter was recorded during the mobility in the University of Trento, under the supervision ofProf. Luigi Fraccarollo.

5.1 Motivation

Pneumatic conveying is a technique for transporting solid materials through pipes using a gas as the carrier medium. The article by Klinzing [64] provides a historical review of this technology, highlighting the main researchers and their contributions in different countries and regions. The work suggests that grain was being unloaded from ships using pneumatic conveying methods in ports such as London, Rotterdam, Hamburg, and Leningrad between 1856 and 1876. While there may have been earlier applications, this is the earliest documented use found so far. Vacuum pumps and air compressors predate industrial times, as early as Roman times, and these devices are a necessary condition for the construction of pneumatic conveying systems. The presence of vacuum pumps and air compressors during these times indicates the potential existence and feasibility of pneumatic

conveying processes, but the exact details and applications prior to the grain unloading system mentioned above remain elusive [64]

The beginning of the scientific work on pneumatic conveying of powders coincides with the early work of Gasterstädt (*Die experimentelle Untersuchung des pneumatischen Fördervorganges*, Germany 1924), which identified the linear relationship between pressure drop and particle mass flowrate [64].

Industrial pneumatic conveying consisted almost exclusively of dilute phase conveying until around the 70's, when work began on the dense phase conveying of solids. The latter allowed the reduction of energy requirements, limit pipe erosion, reduce the damage sustained by the conveyed goods.

The use of numerical models in pneumatic conveying has increased with computational technology. Continuum-based models, such as the Two-Fluid Model (TFM), are widely used, but their effectiveness depends on constitutive relations, and developing a TFM model that can reproduce all flow regimes and transitions remains a challenge. TFM studies focus on powders or fine particles, but mixtures of particles require increased detail and adherence to experiments, which can be achieved using Lagrangian models [66].

As discussed in Section 2.3, the coupling between the fluid and the particles can be resolved on a spectrum. The highest resolution method DNS directly simulates the flow around each particle, or the particles are larger than the fluid mesh size, also called fully resolved methods. The TFM relies on having a large enough system compared to particle size, so that using clumped quantities is justifiable, much in the same way as CFD relies on the averaging of the fluid behavior when enough molecules are involved. Between these extremes, unresolved methods represent particles as entities whose motion is determined through constitutive models (drag models, contact models, and other), and are very effective in simulating many industrial processes, sacrificing some resolution of the finest flow structures for computational efficiency.

CFD-DEM vs MP-PIC The coupled Computational Fluid Dynamics - Discrete Element Modeling (CFD-DEM) and MultiPhase - Particle In Cell (MP-PIC) are two popular unresolved Eularian-Lagrangian models, which can be used to simulate particle laden flows. Both currently have an implementation in the open-source software OpenFOAM. Section 5.2 reports the study performed to assess

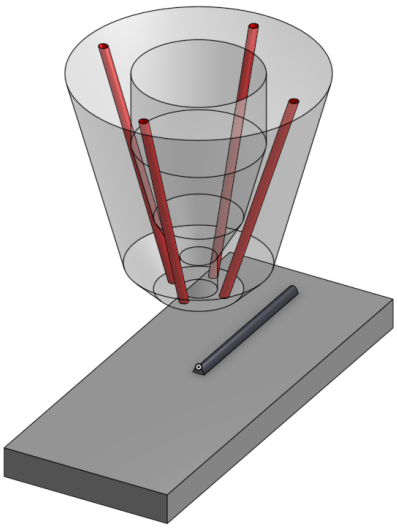

Figure 5.1: Example draft of a typical discrete LMD nozzle with four converging powder conveying channels (highlighted in red), and a central hole for the laser to shine through and for the shielding gas.

which model would be more appropriate in the simulation of the flow structures in the scale of interest for the nozzles of LMD equipment. Results from the two methods differ significantly, with CFD-DEM offering a more accurate representation of the physical reality, while MP-PIC is more computationally efficient, however the first is clearly more appropriate.

The additive manufacturing process LMD relies in all of its parts on the correct knowledge of the pneumatic conveying characteristics of the powder material feedstock. The powder is gradually fed to the pneumatic conveying system using metering equipment, which provide a uniform gas/powder mixture flow. Reaching the nozzle, several different configurations are possible: off-axis, discrete coaxial, continuous coaxial, annular continuous and discrete laser beam [113]. Figure 5.1 represent an example configuration of a discrete coaxial nozzle, with four distinct channel conveying the metallic powder towards the melt pool. The channels highlighted in red are only the last part of the conveying path, where the flow overlaps just before exiting the nozzle and travelling in the free stream leading to the melt pool.

The investigation is motivated by the existence of irregularities in the track width in the deposition head direction of travel, also visible in the roughness

profiles reported by Dadbakhsh et.al. [25].

The periodic variation over time of the powder fed to the process is certainly not the only factor influencing part's quality, however it might have a measurable effect. Previous studies on LMD equipment consider time-averaged powder flows [86][140], whereas the variability of the mass flow rate in pneumatic conveying systems is a known and documented phenomenon [80] [12] [49] [69]. The pneumatic conveying flow is influenced by a number of factors, which are abundantly discussed in literature [21] [63] [81], and are still under active investigation due to the great variability in the characteristics of powders and the levels of detail needed by each application.

Variations in the pneumatic conveying flow can be self-induced and regular. This variation in particle velocity and instantaneous powder mass flow rate directly affects the material deposition rate of the LMD process. Zhou et al. [143] present a study for a larger-scale pneumatic conveying system, where pulsating flow phenomena and periodic flow regimes can be observed in a pipe with a flat rectangular section, both in experiments and simulations. The flow oscillations seem to be self-excited and can be correctly simulated when employing a four-way coupled simulation, but do not appear when the effect of particles on the carrier flow is not accounted for. In the CFD-DEM dilute phase simulation of a horizontal channel by Zhao [141], where the Lagrangian phase does not influence the continuous phase (1-way coupling), a uniform particle motion and velocity driven by viscous effects is displayed. However, when the particle influence is taken into account, the fluid flow exhibits periodic bands of particle concentration in the flow direction.

Pulsations in the mass flow rate of pneumatic conveying systems have been measured experimentally. Alkassar et al. [5] analyzed a pneumatic conveying pipeline with dilute and dune flow regimes. The study showed regular pulsations in the pressure along different positions on the pipe, with wavelet analysis revealing a dependence of the pulsations on the solid loading and characteristics. These studies indicate that flow irregularities are inherent in pneumatic conveying systems due to complex interactions between particles and the carrier gas, especially when particle-particle interactions are significant.

In the context of LMD processes, such flow irregularities can lead to fluctu-

ations in the powder feed rate, which may affect the quality and consistency of the deposited material. The formation of particle clusters and the resulting mass flow rate fluctuations are phenomena that are expected and need to be accounted for in simulations. Previous studies report how particle-particle interactions in CFD-DEM simulations lead to the formation of clusters [80, 116], which directly contribute to flow irregularities.

Existing literature on LMD nozzle systems that employ a Lagrangian model for the powder phase mostly analyze the process using MP-PIC [72, 86] or Discrete Particle Models with 1-way or 2-way coupling [72], motivated by the low particle loading in the system. However, these models may not fully capture the clustering phenomena and flow irregularities due to their simplified treatment of particle interactions. Even though the MP-PIC model finds most of its applications in large reactor models, it is used in the modeling of pneumatic conveying of solids [118], but may not adequately represent the expected flow irregularities in fine-scale applications like LMD.

5.2 Pipe Model - Comparison of Eulerian-Lagrangian methods

LMD deposition nozzles can present in different designs, with different applications. This work is conducive to the analysis of more complex cases. Of particular interest are discrete nozzles and continuous nozzles with internal channels. An example draft of such a nozzle is represented in Figure 5.1, where the four converging channels are highlighted.

This section compares ways of simulating the presence and emergence of powder mass flow rate fluctuations in the pipelines within the Laser Metal Deposition (LMD) equipment, especially in the final length of thin tubing inside the nozzle. Using OpenFOAM's `denseParticleFoam` library [122], the objective is to compare a fully coupled, unresolved CFD-DEM simulation with a less computationally expensive MP-PIC one [115] [70], even though the latter requires more empirical parameters [127]. If the two methods are both compatible with the phenomenon, their results should agree to a certain measure, otherwise one has to be preferred over the other. Unresolved CFD-DEM solves the physical interactions between particles and between each particle and fluid, in this case completing the picture to 4-way coupling, and for this reason it is expected to be the one which gives the most physically accurate results, whereas MP-PIC should capture more averaged behaviors.

The considered geometry is a straight pipe with circular cross-section, placed horizontally. The inlet is on the origin, and the pipe is oriented along the positive Z axis in the reference frame XYZ, the flow is introduced in the positive Z direction. Gravity has the value of $\vec{g} = [0, -9.81, 0]$ m/s^2, therefore acting in the radial direction negative Y. Typical LMD applications see the pipe close to vertical; this can be obtained simply by changing the vector component values in the appropriate case file, but a horizontal configuration simplifies the representation.

The pipe has a diameter of $D = 1.25$ mm and a length of $L = 300$ mm, resulting in an L/D ratio of 240, higher than Li et al.'s work on simulating powder stream characteristics in a laser metal deposition nozzle using a 3D model [72]. In this case, the length was chosen to ensure the full development of the flow conditions, as highlighted in Section 5.3. Since the OpenFOAM code is written for unresolved simulations (see Sec. 2.3), the pipe was discretized with a mesh

with cell volume larger than the maximum particle size. Convergence of the fluid flow was verified for a mesh with 33600 elements, as shown in Figure 5.3.

The pressure was measured at a point 3 cm from the inlet; the pressure and velocity trends observed at this point were consistent with the trends observed at other measurement points, which all exhibited similar behavior with the mesh refinement. For the convergence analysis, the case with higher inlet gas velocity is reported, $U_{g,A} = 10$ m/s, as it shows the most significant differences in flow behavior.

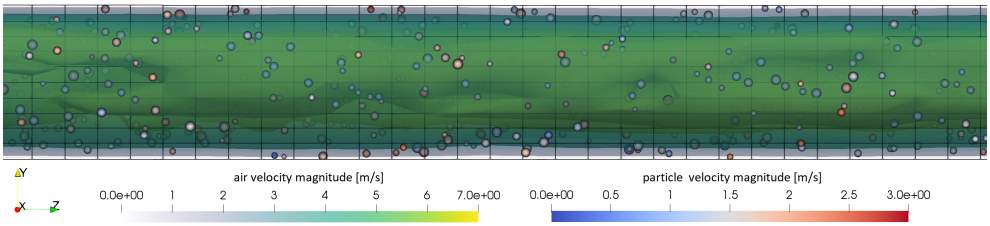

Figure 5.2: Lateral view of the simulation domain with velocity magnitude contours for Case A ($U_g = 10$ m/s). The complete domain is a simple, straight pipe. The image highlights the spatial distribution of particles in the diameter.

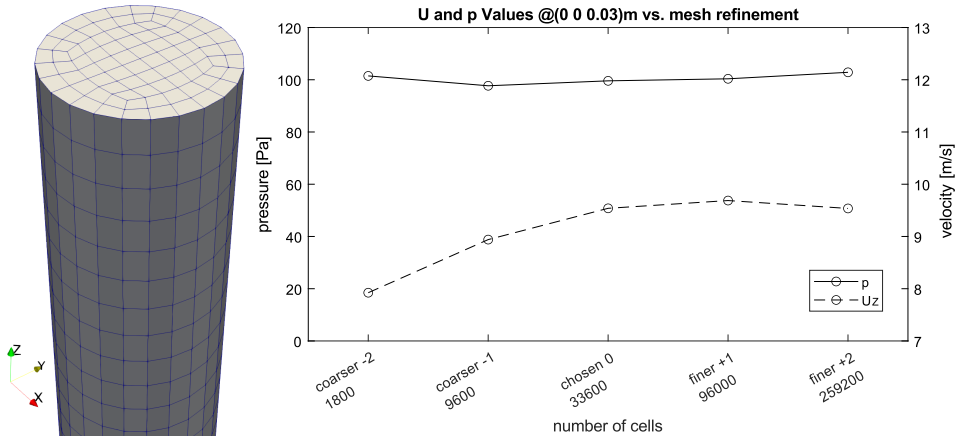

Figure 5.3: End view of the pipe, with detail on the chosen mesh. Convergence analysis of the fluid flow verified for a mesh with 33600 elements, for the pressure p and axial velocity U_Z, at a point 3 cm from the inlet. Results shown for Case A ($U_g = 10$ m/s).

The imposed inlet velocity set is in Table 5.1, the comparison is for the values $U_{g,A} = 10$ m/s and $U_{g,B} = 5$ m/s. The corresponding flow rates $\dot{V}_g$ are calculated

for the 1.25 mm diameter pipe. As found in [86], the particles will be introduced with the same velocity as the gas, from the inlet plane, with the injection rate $\dot{Q}_p$ specified in particles per second. Considering the median diameter of the distribution shown in Figure 5.4, and being $\bar{V}_p$ the median particle's volume, in both cases the estimated volumetric solid fraction being transported is:

$$\alpha_p \leq \left(\bar{V}_p \cdot \dot{Q}_p\right) / \left(\dot{V}_g\right) = 0.004 \ , \tag{5.1}$$

which is well within the dilute flow particle loading [23]. The pipe length was chosen to allow the transition from the virtual inlet conditions (both for particles and gas) to the established flow [65], and verified in Section 5.3.

In this discussion, the flow is modeled with four-way coupling to account for both particle-fluid and particle-particle interactions. This modeling approach is crucial because it considers the forces exerted by particles on the fluid, as well as the reaction of the particles to these forces. Neglecting these forces would result in an incomplete representation of the physical phenomena within the system.

Table 5.1: Inlet conditions for gas $[\cdot]_g$ and particles $[\cdot]_p$

Parameter Name	Symbol	Case A	Case B	Unit
Gas velocity	U_g	10	5	m/s
Gas flow	$\dot{V}_g$	0.74	0.37	l/min
Particle injection rate	$\dot{Q}_p$	300×10^3	150×10^3	particles/s

Kussin and Sommerfeld [67] observed that the presence of small particles in gas-particle flows tends to reduce turbulence rather than enhance it. Specifically, for particles with diameters up to 200 μm—including the 60 μm particles used in this study—there was a significant decrease in turbulent intensity due to the particles dissipating momentum. These particles have a slower response to turbulent fluctuations, which causes them to extract energy from the fluid's turbulent eddies, thereby acting as a source of additional turbulence dissipation.

In this study, argon is considered as the shielding gas, a common choice for Directed Energy Deposition (DED) processes. The properties of argon used in the simulation are summarized in Table 5.2, for standard conditions of $T = 25°C$ and $p = 1$ atm. Given the flow velocities shown in Table 5.1, the Reynolds number for the fluid phase is calculated to be $Re_f < 1000$ in both cases. This low Reynolds number indicates that the flow remains laminar throughout the pipe, without

transitioning to turbulence.

Furthermore, the presence of small particles contributes to additional stabilization of the flow by dissipating energy, which further suppresses the potential for turbulence development.

Thus, the combination of a low Reynolds number in the fluid phase and the damping effect of small particles on turbulence fully justifies the assumption of laminar flow for the CFD-DEM simulation. The interaction between the fluid and particles promotes a laminar flow regime and reduces the likelihood of turbulence formation.

Table 5.2: Carrier gas properties, Argon.

Parameter Name	Symbol	Value	Unit
Density	ρ_g	1.6355	$\mathrm{kg/m^3}$
Dynamic viscosity	μ_g	2.2624×10^{-5}	$\mathrm{Pa \cdot s}$
Kinematic viscosity	ν_g	1.385×10^{-5}	$\mathrm{m^2/s}$

In the present case, the gas velocities are low enough to justify the assumption of incompressible flow, greatly simplifying the problem. The Mach number, defined as the ratio of the fluid velocity to the speed of sound in the gas, is calculated as follows:

$$Ma = \frac{U_g}{c} = \frac{10}{323} \approx 0.03 \tag{5.2}$$

where U_g is the gas velocity for case A, and c is the speed of sound in argon at standard conditions. Since $Ma \ll 1$, the flow is well within the subsonic, incompressible regime.

The material under investigation is AISI 316L austenitic stainless steel gas-atomized powder (MetcoAdd$^{\mathrm{TM}}$ 316L), which is fully dense and spherical in shape. The sample was provided by a source which is currently using LMD equipment, and its manufacturer (Oerlikon metco) declares it to be suitable for DED processes. The Particle Size Distribution (PSD) is represented by a Rosin-Rammler model and depicted in Figure 5.4. The median diameter of the powder is $d_{50} = 66.9$ μm, with minimum and maximum cutoffs of 40 μm and 110 μm, respectively. The parameters of the Rosin-Rammler distribution used in the analysis are experimentally determined by fitting the PSD of a powder sample, using

the procedure detailed in Appendix A. The resulting distribution is numerically generated and shown in Figure 5.5.

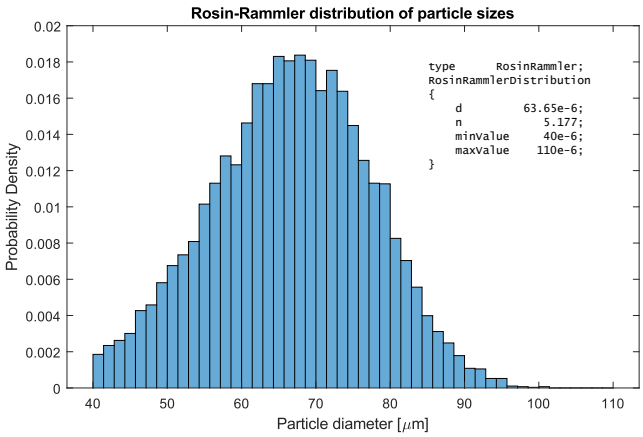

Figure 5.4: Probability density of the particle size. 10 000 particles are generated using the same Rosin-Rammler model implementation as OpenFOAM 9. The parameters d and n have been measured form the powder sample, according to the procedure in Appendix A.

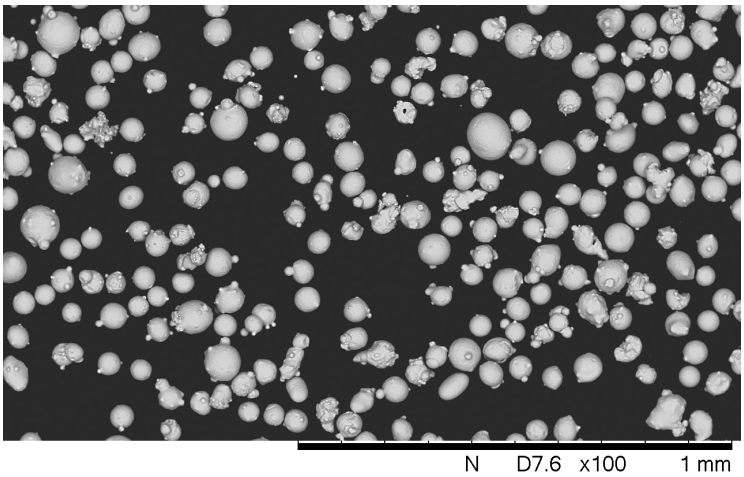

Figure 5.5: A single SEM image from a set, collectively analyzed to establish the Particle Size Distribution (PSD).

Recalling Chapter 2.1, CFD-DEM calculates the motion of particles by following Newton's second law and quantifies the interactions between particles or between particle and wall by soft-sphere models: this work uses the spring-slider-dashpot (SSD) contact model available in OpenFOAM v9. It implements the no-slip model of Mindlin, which combined with the Hertzian theory of contact between spheres results in a non-linear spring model, to which dashpots are added in parallel to dissipate energy and account for the eventual hysteresis of the materials [21]. The tangential forces are modeled using a dashpot in parallel to a linear spring [126]. The SSD contact model parameters are set according to the AISI 316L powder properties reported in Table 5.3, based on the values reported in [87]. By adopting a soft-sphere approach rather than relying on hard spheres, one can accurately capture the intricate dynamics of particle interactions and material behavior. This becomes particularly significant when considering the eventual formation of dense clusters.

Table 5.3: DEM particles properties for SS316L.

Parameter Name	Symbol	Value	Unit
Density	ρ_p	7980	kg/m^3
Poisson ratio	ν_p	0.3	–
Young modulus	$E_{p,0}$	2.11×10^{11}	Pa
Reduced Young modulus	E_p	2.11×10^{7}	Pa
Shear modulus (calculated)	G_p	8.11×10^{6}	Pa
Restitution coefficient	e	0.9	–
Damping parameter (calculated) [126]	α	0.12	–
Friction coefficient	μ	0.52	–

5.2.1 Simulation models and configuration

CFD-DEM calculates the motion of particles by following Newton's second law and quantifies the interactions between particles or between particle and wall by soft-sphere models: this work uses the spring-slider-dashpot (SSD) contact model available in OpenFOAM v9, described in 3.2. It implements the no-slip model of Mindlin, which combined with the Hertzian theory of contact between spheres results in a non-linear spring model, to which dashpots are added in parallel to dissipate energy and account for the eventual hysteresis of the materials [21]. The tangential forces are modeled using a dashpot in parallel to a linear spring [126]. The SSD contact model parameters are set according to the AISI 316L powder properties reported in Table 5.3. By adopting a soft-sphere approach rather than relying on hard spheres, one can accurately capture the intricate dynamics of particle interactions and material behavior. This becomes particularly significant when considering the eventual formation of dense clusters.

The critical time-step is calculated as a function of the Rayleigh waves propagation speed [21], considering Equation 2.5:

$$\Delta t_c = \frac{\pi R_{min}}{v_R} = \frac{\pi R_{min}}{\lambda}\sqrt{\frac{\rho_p}{G_p}} \tag{5.3}$$

$$\lambda = 0.8766 + 0.1631\nu_p \tag{5.4}$$

According to this formula, for a minimum diameter of 40 μm, with the real Young modulus $E_{p,0}$ for 316L stainless steel from Table 5.3, the critical timestep would be $\Delta t_c = 2.13 \times 10^{-8}$ s. Such a small value would dilate the computation time by orders of magnitude.

To maintain computational efficiency, the Young's modulus was reduced to $E_p = 2.11 \times 10^7$ Pa, resulting in a critical timestep of $\Delta t_c = 2.13 \times 10^{-6}$ s. This adjustment is a common practice in DEM simulations for collision-dominated flows, as the reduced modulus has a limited impact on the overall simulation results [138]. In cases involving denser phases or cohesive materials, other parameters, such as the damping coefficient α, must be scaled accordingly, as described in the SSD model [133, 126].

In OpenFOAM, the Rayleigh critical timestep Δt_c is calculated internally based on particle properties, using a re-elaboration of Equation 5.3. The software uses the following formula within the `PairSpringSliderDashpot` collision model:

$$\Delta t_{\min} = \frac{5.429675 \cdot R_{\min}}{\text{collisionResolutionSteps}} \left(\frac{\rho_{\max}}{E^* \sqrt{U_{\max}} + v_{\text{small}}} \right)^{0.4} \tag{5.5}$$

where:

- $R_{\min}$ is the smaller particle radius involved in the contact.
- $\rho_{\max}$ is the maximum particle density.
- E^* is the effective Young's modulus.
- $U_{\max}$ is the maximum particle velocity.
- v_{small} is a small value to prevent division by zero.
- `collisionResolutionSteps` is a user-defined parameter controlling the number of sub-steps.

To accurately resolve particle contacts, sub-stepping is applied during collision events. The global timestep Δt, shared between the Eulerian and Lagrangian domains, is divided into smaller increments known as sub-steps. The number of sub-steps n_{sub} is determined by the ratio of the global timestep to the minimum collision timestep:

$$n_{\text{sub}} = \left\lceil \frac{\Delta t}{\Delta t_{\min}} \right\rceil \tag{5.6}$$

This method ensures that particle interactions are captured without skipping or excessive overlap, even when the global timestep exceeds the critical timestep Δt_c. The sub-stepping algorithm dynamically adjusts the number of sub-steps based on particle properties and velocities, maintaining accurate resolution of particle collisions.

In addition to contact resolution, particle movement during the global timestep must be considered. For instance, a particle traveling at $u_p = 10\,\text{m/s}$ would move $s_p = u_p \cdot \Delta t = 100\,\mu\text{m}$ during a global timestep of $1 \times 10^{-5}\,\text{s}$. In OpenFOAM, interactions are approximated using a separation margin defined by the `maxInteractionDistance` parameter, typically set to the maximum particle diameter.

To further ensure the accuracy of the simulation, the Courant number Co^{DEM}, based on particle velocity and timestep, is used to determine the necessary interaction distance:

$$Co^{\text{DEM}} = \frac{U_p \Delta t}{\Delta \delta_{\max}} \tag{5.7}$$

where U_p represents the particle velocity, and Δt is the global timestep. To avoid skipping any contacts, the interaction distance $\Delta\delta_{\max}$ (typically the maximum particle diameter) is determined by ensuring that Co^{DEM} remains less than one. This guarantees that particles will enter the interaction zone with sufficient time resolution, preventing them from bypassing interactions due to large global timesteps.

In the simulations, global timesteps of $\Delta t = 5\times10^{-6}$ s and 1×10^{-5} s were used for cases A and B, respectively. OpenFOAM calculates the minimum collision timestep $\Delta t_{\min}$ internally using the aforementioned formula. By employing 24 `collisionResolutionSteps`, the sub-stepping ensures that the sub-step timestep is sufficiently small to resolve particle collisions accurately.

The external forces acting on both the MP-PIC parcels and DEM particles are compatible for this study. In both cases, each Lagrangian discrete phase element is described by the same PSD and has the same density, since in both cases each element describes a single particle. The drag model is the one described by Gidaspow [41], explained in Section 2.3. This is used and validated for spherical particles, for any particle concentration up to close packing.

The `coneInjection` model, employing a disk injector, might be utilized to generate particle flow. However, it lacks a mechanism to detect particle overlap within the disk, a phenomenon that occurs randomly, particularly at high parcel flow rates and low velocities. It is advisable to incorporate an overlap check functionality into the injection model. The occurrence of initial particle overlaps results in the creation of stray particles with high transversal velocities, which can introduce uncontrolled disturbances in the pipe. Another adverse consequence is the potential spike in the local Courant number, rendering the simulation more unstable. It is recommended to mitigate this issue.

To circumvent these issues, particles are introduced into the system using the `coneInjection` model in the point injector configuration. A hexagonal pattern composed of 99 points is uniformly distributed on a disk located 1 mm ahead of the inlet patch. The diameter of the disk is 1 mm, slightly smaller than the pipe diameter, to prevent initial overlaps between particles and the wall boundary. Particles are injected with a uniform velocity and a randomized start of injection, resulting in a continuous stream of particles. The diameter of the particles is

randomly chosen to align with the size distribution model.

5.2.2 Boundary conditions

5.2.2.1 Fluid phase

For the fluid phase (argon gas), boundary conditions are specified for the velocity field $\mathbf{U}$ and the pressure field p. At the inlet and the injection plane, a fixed velocity $\mathbf{U} = (0, 0, U_g)$ is prescribed, where U_g is the gas velocity specified in Table 5.1. This ensures a consistent gas velocity entering the domain in the positive Z-direction, matching the experimental conditions of the LMD process. At the outlet, a zero-gradient condition is applied to the velocity field, allowing the flow to develop naturally as it exits the domain without imposing any artificial constraints. The walls are modeled with a no-slip condition, enforcing $\mathbf{U} = \mathbf{0}$ due to viscous effects at the pipe walls, which is appropriate given the laminar flow regime and the importance of wall effects on the flow development in such small diameters.

For the pressure field p, the internal field is initialized with a uniform value of zero. At the outlet, the pressure is set to a fixed value of zero, providing a reference pressure level corresponding to atmospheric conditions, which is a common practice in incompressible flow simulations. At the inlet and walls, a zero-gradient condition is applied to the pressure field. This is appropriate when the velocity is prescribed at the inlet, as it allows the pressure to adjust based on the flow without introducing artificial pressure gradients that could affect the solution.

5.2.2.2 Particle phase

The boundary conditions and interaction models for the particle phase differ between the CFD-DEM and MP-PIC simulations due to their inherent modeling strategies.

CFD-DEM simulation

In the CFD-DEM simulation, particle-particle interactions are modeled explicitly using the soft-sphere approach with the spring-slider-dashpot (SSD) contact model, as described in Section 2.1. The collision model employed is the

`pairCollision` model, which accounts for collisions between particles and between particles and walls. Key parameters for this model include the maximum interaction distance, restitution coefficient, friction coefficient, and collision resolution steps, as specified in Table 5.3 and configured in the simulation setup.

At the walls, particles experience collisions governed by the wall-specific SSD model, ensuring realistic interactions that are important for predicting particle trajectories and potential clustering. At the inlet and outlet, an escape condition is applied to the particles, allowing them to enter and exit the domain freely without artificial reflections or constraints.

MP-PIC simulation

In the MP-PIC simulation, particle interactions are modeled using continuum-based stress models suitable for dense particulate flows. The `packingModel` is set to `explicit`, employing the `HarrisCrighton` particle stress model to represent inter-particle stresses as the local particle concentration approaches the packing limit. Key parameters such as the maximum packing fraction α_{packed}, solid pressure p_{Solid}, and stress coefficients β and ϵ are configured to match the physical properties of the particle material.

A damping model is also utilized to account for the relaxation of particle velocities towards a local equilibrium, which helps stabilize the numerical solution in regions of high particle concentration. The `relaxation` damping model is employed, with parameters adjusted according to the particle properties and flow conditions.

In the MP-PIC simulation, particle-wall interactions are less detailed compared to CFD-DEM. However, boundary conditions are specified to allow particles to interact appropriately with the walls. Similar to the CFD-DEM case, an escape condition is applied at the inlet and outlet to allow particles to enter and exit the domain freely.

Particle injection

Particles are introduced into the system using a point injection method. A hexagonal pattern of injection points is distributed over a disk of diameter 0.9 mm, slightly smaller than the pipe diameter, to prevent initial overlaps with the wall boundary. The particles are injected at a position 1 mm downstream of the inlet

patch, with a velocity equal to the gas inlet velocity U_g. The particle diameters are randomly sampled from the Rosin-Rammler size distribution determined for the powder sample (Figure 5.4). Randomizing the start time of injection for each point helps simulate a continuous particle flow and avoids synchronization effects that could lead to artificial clustering or numerical instabilities.

5.2.2.3 **External forces**

Gravity is included as an external force acting on the particles, with a gravitational acceleration vector $\vec{g} = (0, -9.81, 0)$ m/s^2, acting downward in the negative Y-direction. Including gravity is essential even in horizontal flows, as it can influence particle settling and distribution across the pipe cross-section, affecting the overall flow behavior. The drag force between particles and the fluid is modeled using the Gidaspow drag model [41], which accounts for particle concentration effects on the drag coefficient. This model is suitable for spherical particles and is validated for a wide range of particle concentrations up to close packing, making it appropriate for the present dilute flow conditions.

5.2.3 **Solution schemes**

To aid with the comparison, solver settings were kept consistent between the two simulations. Separate steady-state simulations were used to initialize the Eulerian phase flow, which was then transferred to the transient case with `mapFields`.

The `cloudProperties` dictionary was used to define a `cellPoint` interpolation for both the velocity `U.air` and phase concentration `alpha.air` for Eulerian field values interpolation to the Lagrangian phase, as it demonstrated improved stability over `cell` interpolation. A semi-implicit Eulerian integration scheme was employed for the Lagrangian phase.

To solve the pressure field, `smoothSolver` with a `GaussSeidel` smoother was used, as it was observed to be more stable than `GAMG`. The latter sometimes caused pressure instability, leading to simulation crashes. However, the filtered pressure values were found to be similar in both cases. `GAMG` with a `GaussSeidel` smoother was used to solve the `alpha` field, while for the velocity field `U.air`, better residual stability was obtained using `PBiCGStab` with a `DILU` preconditioner.

To ensure stability during the simulation, a time-step was chosen that guaranteed both a Courant number $Co < 1$ for the Eulerian phase and $Co^{DEM} < 1$ for

the Lagrangian phase. The transient simulation was performed using the PISO scheme with `nCorrectors` 3, which specifies the number of pressure correction loops. The residuals were found to reach convergence at each time-step without any issues.

5.3 Pipe model results

5.3.1 Pressure profiles

To determine whether the simulation had reached the condition of established flow, we evaluated the calculated inlet pressure. As depicted in Figure 5.6, the pressure value at the inlet exhibited a distinct oscillation until 0.005 s and 0.010 s respectively for the two velocities considered. The two methods demonstrated almost no difference, and the reason for this can be attributed to the fact that the Eulerian flow was initialized using a different steady-state simulation, and the resulting values were mapped to the E-L case domain. Thereafter, the transient was governed by the rate at which particles filled the pipe. The elbow on the diagram at 0.08 s and 0.15 s, respectively for the two velocities considered and the CFD-DEM case, was clearly linked to the instant at which the particle flow reached the end of the pipe. As a result, these times were utilized to differentiate between transient and established flow conditions.

In addition, it is important to identify the settling length where the flow develops and the remainder of the pipeline where the flow is fully developed in the longitudinal direction. Figure 5.7 shows the longitudinal pressure of the CFD-DEM case A ($U_g = 10$ m/s), averaged for $t \in [0.1, 0.2]$ s. The pressure demonstrated a nonlinear behavior from the inlet to 0.2 m, representing the development of gas-particle flow. From there to the outlet, the pressure profile becomes linear, indicating a fully developed flow. This was assumed to be the settling length for all other cases.

The inlet pressure profiles over time for the two methods are reported in Figure 5.6 and demonstrate substantial differences. The CFD-DEM simulated pressure presents an initial linear increase phase, which is consistent with the pipe filling up with particles after injection. When this phase ends, there is a plateau, indicating stable conditions. The pressure required to transport the material through the pipe, as opposed to gas only, is approximately five times higher, as reported in

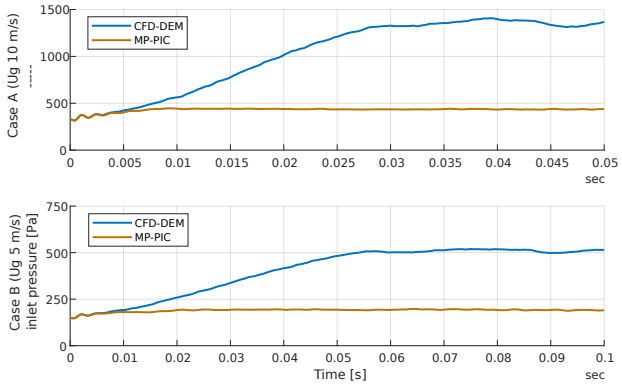

Figure 5.6: Comparison of the inlet pressure over time for the two methods. Data filtered with moving average over 10^{-3} s (A) and $2 \cdot 10^{-3}$ s (B).

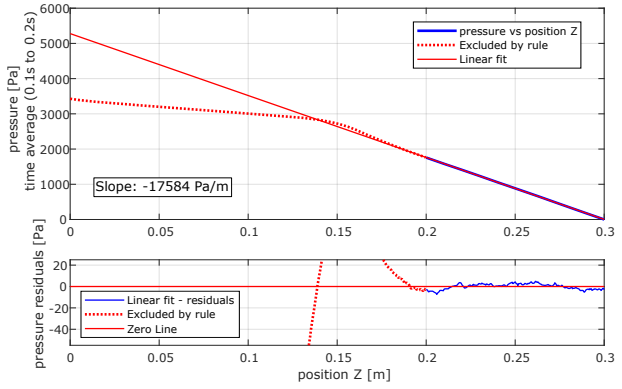

Figure 5.7: Linear fit of the pressure over the pipe length for CFD-DEM case A, at $U_g = 10$ m/s, and residuals.

Table 5.4, indicating that the majority of the energy is required to push the particles through.

MP-PIC shows a lower pressure drop, being only around double that of the empty pipe simulated condition. This difference between the two methods is notable and may have implications for estimating the energy requirement for particle transport through pneumatic conveying. Table 5.4 shows the pressure drop along the pipe at established flow conditions, evaluated through linear fit.

Table 5.4: Pressure drop along the pipe at the established flow conditions, evaluated through linear fit (example in Figure 5.7).

	Slope [Pa/m]	
	Case A	Case B
CFD-DEM	17584	6076
MP-PIC	8639	3293
empty pipe	3164	1465

5.3.2 **Particle velocity distribution**

. A comparison with the MP-PIC case A in Figure 5.9 reveals notable differences. As discussed in Section 5.3, there are differences in pressure profiles between the two cases. The velocity diagrams in Figures 5.8 and 5.9 also display distinct behaviors. In the CFD-DEM case, particles reach an average velocity of 3.040 m/s, and once the flow is established, the velocity dispersion is relatively low, as evidenced by the error band displaying the standard deviation as $\sigma = 0.61$ m/s. The normalized probability density of the particle location histogram at the top of both Figures 5.8 and 5.9 shows that there are volumes with different particle concentrations along the pipe, which move along with the flow. In contrast, the MP-PIC simulation under the same conditions exhibits a more uniform particle distribution along the tube, with particle velocities deviating less significantly from the inlet condition and not displaying the terminal velocity seen in the CFD-DEM case.

It is worth noting that drag is treated identically in both cases, and the difference in behavior is attributed to the contact and compaction laws. These observations suggest that the two methods capture different aspects of the parti-

cle flow, and further analysis is required to determine which method provides a more accurate representation under these conditions.

Figure 5.11 distinctly illustrates a crucial aspect regarding the necessary length to achieve a fully developed flow. The presented diagrams depict the average Y position of particles, binned into 100 segments along the Z direction, for all considered cases. Given the assumptions of laminar flow and uniform velocity injection, the particles tend to travel through the pipe relatively undisturbed in a metastable state. The influence of gravity alters their trajectory, causing them to follow a parabolic path towards the bottom of the pipe, where they subsequently rebound. During this rebound, they initiate disturbances in the incoming parcels, consequently unsettling the metastable equilibrium dictated by the simulation conditions. The flow described in this study attains a developed state, herein referred to as the stable flow condition. Initially, almost no interactions between particles happen, as they differentially accelerate or slow down under the action of drag across the pipe diameter. The action of gravity is important, as it provides the first disturbance to the system. As the gravitational settling takes place, more and more rebounds can take place, resulting in a cascade effect that leads to the stable, pseudo-steady-state behavior previously observed.

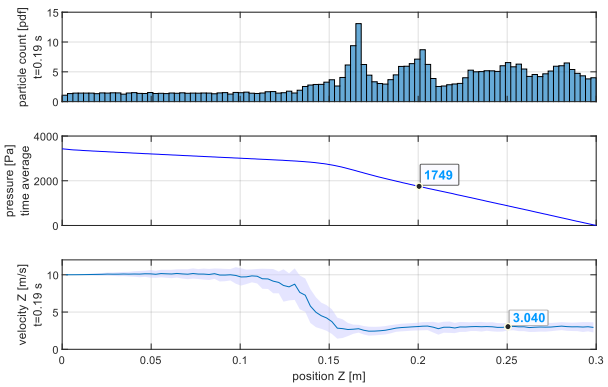

Figure 5.8: Salient metrics of particle flow in CFD-DEM case A.

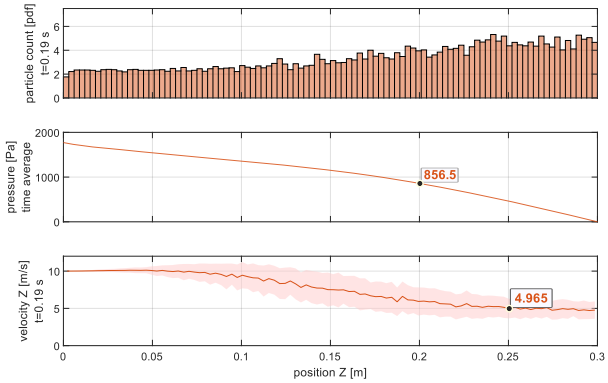

Figure 5.9: Salient metrics of particle flow in MP-PIC case A.

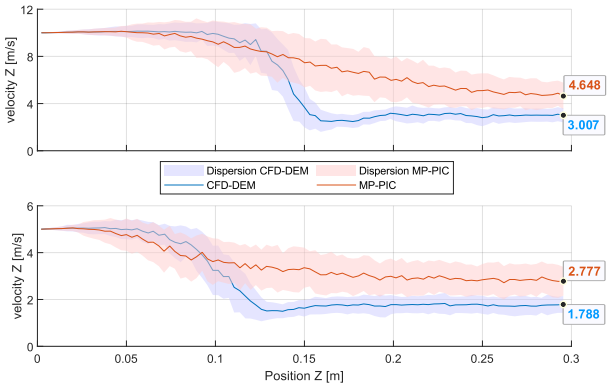

Figure 5.10: Comparison of the established particle velocity profiles in MP-PIC and CFD-DEM simulations, at $t = 0.2$ s for case A and $t = 0.4$ s for case B.

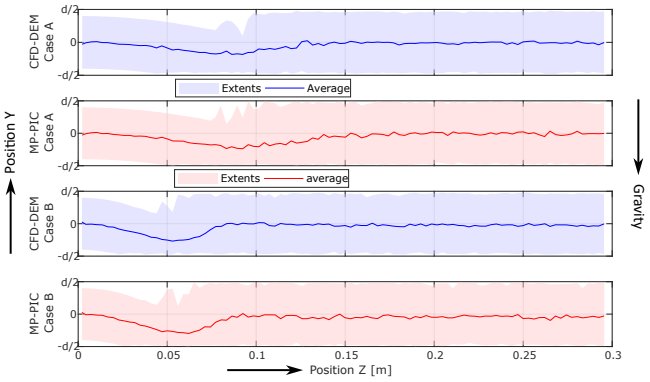

Figure 5.11: Comparison of parcel position characteristics along the Y-axis, considering the extents (minimum and maximum values) as well as the average positions. The gravitational force acts in the negative direction. The particle positions are depicted at $t = 0.2$ s for Case A and $t = 0.4$ s for Case B, with the positions binned into 100 segments along the Z-axis.

5.3.3 **Solids flow rate**

The determination of the solids flow rate is crucial for understanding the material available for deposition and capture over time in Laser Metal Deposition (LMD) processes. In this study, the mass flow rate through the pipe was obtained by counting the mass of each particle escaping the outlet boundary over time. The aim of this study was to investigate the uniformity of this value.

Figure 5.12 shows the resulting solids mass flow over time for both the CFD-DEM and MP-PIC methods. The data was filtered with a moving average over 10^{-3}s. The 10m/s case is of particular interest and is representative of the 5 m/s case. The graphs have been scaled in both axes to display an equivalent picture. The first parcels arrive at around 0.01 s, which is the time needed to traverse the 0.1 m pipe at the injection velocity of 10 m/s.

The CFD-DEM simulated case shows a noticeable delay between the first particles escaping the boundary and the establishment of the quasi-periodic flow. This is due to the fact that the first few injected particles can traverse the pipe in a diluted phase, without losing much energy. However, as the injection progresses uniformly, the particles progressively slow down due to the impacts. When the flow is established, Figure 5.13 displays how the particles in progress form clusters, which move with the flow. These clusters persist until the outlet boundary, giving

rise to the solids flow irregularities that this study is interested in.

The deviation from the average mass flow rate is expressed in terms of the Root Mean Square (RMS), a statistical measure that quantifies the spread or variability of a set of values, or a continuous function, around the average. Assuming a finite number n of virtual measurements, the i-th mass flow rate measurement $\dot{m}_i$ and the average at the outlet $\overline{\dot{m}}_{out}$, the RMS value is defined as:

$$\dot{m}_{RMS} = \sqrt{\frac{1}{n}\sum_{i=1}^{n}\left(\dot{m}_i - \overline{\dot{m}}_{out}\right)^2} \tag{5.8}$$

The MP-PIC method displays a smooth increase to the average value, with low fluctuation after that. On the other hand, the CFD-DEM method shows significant fluctuation in the solids flow rate due to the clusters formed by the particles. The results are presented in Table 5.5, where the average and RMS of the solids flow rates are evaluated at the pseudo steady-state conditions: from 0.1 s and 0.2 s for cases A and B respectively.

Table 5.5: Solids flow rates values in g/s.

Case	CFD-DEM			MP-PIC		
	avg	RMS		avg	RMS	
A : 10 m/s	0.3026	0.0829	(27.4%)	0.3075	0.0145	(4.71%)
B : 5 m/s	0.1542	0.0271	(17.6%)	0.1542	0.0106	(6.90%)

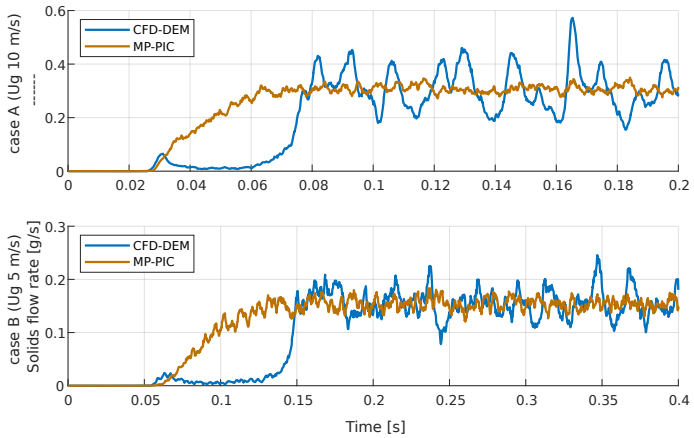

Figure 5.12: Comparison of the solids flow rate over time for the two methods. Data filtered with moving average over $2 \cdot 10^{-3}$ s.

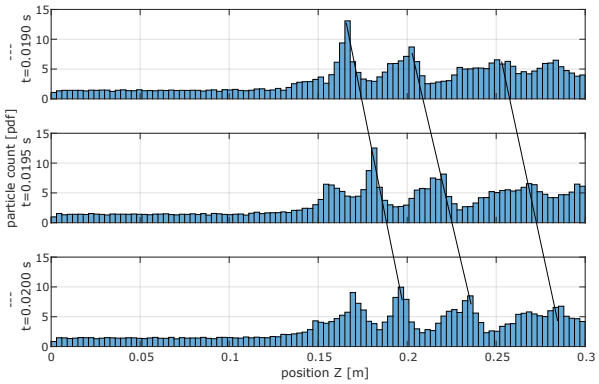

Figure 5.13: Particle distribution along the pipe, three snapshots at different times for the CFD-DEM case A (10 m/s).

5.3.4 **Computation time**

Table 5.6 reports the execution times of the presented simulations. It is easy to see that the execution time of the CFD-DEM simulation is three to five times higher than MP-PIC, is dominated by the solution of the Lagrangian domain, and shows a dependency to the number of move-collide subcycles per timestep.

With such a difference, MP-PIC remains an attractive alternative to simulate the pneumatic conveying of fine particles. The presented case, however, shows a limit in its applicability, as it fails to capture the very phenomenon under investigation: the variability of powder mass flow rate over time.

Table 5.6: Computation time of the presented cases, on a 4-core PC with an i5-4570 CPU.

	Case A	**Case B**
timestep	$5 \cdot 10^{-6}$ s	10^{-5} s
CFD-DEM		
Execution time	170777 s	258370 s
Avg. number of parcels	16656	16650
Avg. move-collide subcycles per timestep	83	144
MP-PIC		
Execution time	51704 s	45082 s
Avg. number of parcels	11171	11574
Empty pipe		
Execution time (`simpleFoam`)	13.16 s	13.72 s

5.4 Experimental investigation setup

The second mobility's aim, introduced in 7.3.4, is to gather comprehensive data on pneumatic conveying of metallic powders in a controlled experimental setup. By collecting measurements across a range of meaningful conditions, it is possible to determine a robust calibration procedure. The resulting test platform aims to serve as a tool for calibrating the simulations in addition to the collection of existing resources available to simulation specialists.

The calibration of a simulation is more effective the closer it is to the real process conditions, as presented in Section 2.14, and another reason to perform an experiment is to validate the results and the insights obtained by the simulations. Section 5.2 presents the simulation performed on the hypothesized conditions for the pneumatic conveying of metal powders. This Section shows the experimental procedure performed to gather the data on the particle flow, which is then compared with the simulation.

Experiments were conducted with the three pipes at different gas flowrates, and using different materials, summarized in Table 5.7. The particles were introduced into the system via the rotary valve feeder. However, the exact particle flowrate was determined after the experiment, as metering the particle flowrate precisely during the experiment can be challenging due to the complexity of the metering process. Therefore, the particle loading was not fixed but determined based on the combination of inlet gas flowrate, distributor settings, and post-

experiment measurements. By analyzing the collected data, the particle flowrate and loading were calculated as part of the post-processing of the experimental results.

Pipes	**Materials**	**Inlet flowrate** [L/min]
Circular ∅1.15 mm	Stainless steel 316L (normal/fine)	0.2
Square 1 × 1 mm	Inconel 718	0.4
Rectangular 6 × 0.6 mm	Titanium Ti6AlV	0.6
		0.8
		1.0

Table 5.7: Variables changed during the experiments. Combining all of them results in 60 different conditions.

5.4.1 **Circuit**

The setup is captured in the picture of Figure 5.16, where also the camera and lighting system are visible. Notice the vertical adjustment of the whole pipe, other adjustments were done by strategic placement of shims and adhesive tape. The pneumatic conveying circuit is presented in Figure 5.14.

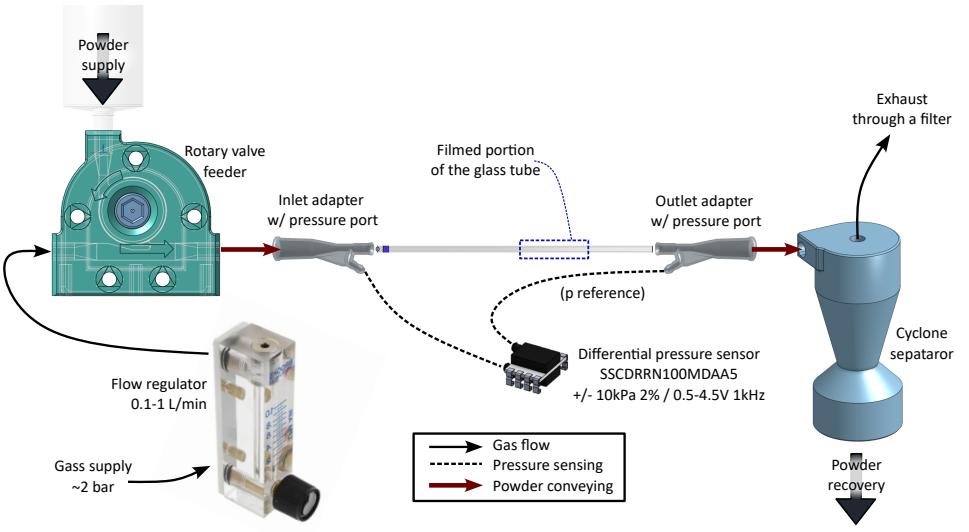

Figure 5.14: Schematic of the pneumatic conveying circuit used in the experiment.

The central part of the circuit is the glass pipe, sourced from CMscientific.

The material for all of the pipes is borosilicate glass, and the glass wall is 0.2 mm thick. This setup can employ three different shapes:

Circular, with an internal diameter of 1.15 mm;

Square, with a passage section of 1×1 mm, and relatively sharp corners;

Rectangular, with a passage section of 6×0.6 mm, with a complete rounding of the short sides.

For the present work, only the experimental data related to the circular section pipe is analyzed, as this geometry is directly relevant to the simulations discussed in Sections 5.2 and 5.3. The data for the other geometries and materials listed in Table 5.7 has been collected and will be made available in an open-access repository.

5.4.1.1 SLA 3D printed parts

The development of the system involved the design of the small-scale couplers for the pipe. This task was performed by using a Stereolithography (SLA) 3D printer, which allows to produce strong and dense parts with very fine details. The 3D model dimensions were adjusted to obtain the desired fit of the parts. Careful part orientation allowed to manufacture the static pressure measurement ports, which are only a fraction of a mm wide, and any resin trapped in it would cause the opening to clog shut and the part to fail. Figure 5.15 shows the finished result

The same technology allowed to manufacture and iterate on a rotary valve feeder. This element is the weak point of the setup and needed to be substituted every few minutes due to excessive erosion, and it is one interesting point of improvement, but it allowed to effectively feed the powder in the circuit for the short duration of the measurements. The main body presents a powder inlet and a wheel, which transports the powder towards the bottom of the component. There, a small venturi accelerates the gas flow, picking up the powder and sending it downstream through the glass pipe.

The gas supply is provided by a high-pressure tank of clean, dry, pure nitrogen gas. Two line regulators step down the pressure first from $\sim$ 200 bar to 8 bar, and a second regulator further steps it down to the pressure used in the setup

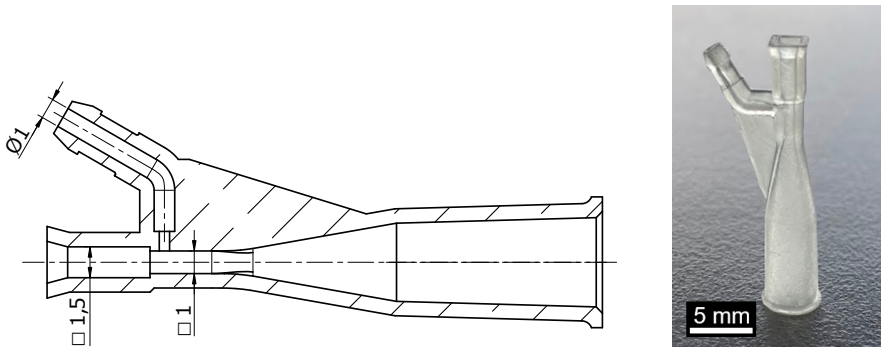

Figure 5.15: One of the couplers used for the square pipe. The opening of the static pressure port is barely visible to the naked eye. A section view presents the internal channels. The conic section is used to fit the coupler to the flexible pipe.

($\leq$ 2 bar). This high purity gas supply ensures that the contamination from moisture or oils is not present, and completely avoids a compressor which might send vibrations down the gas line. A needle regulator was used to set the gas flowrate between 0.1 and 1 L/min.

5.4.1.2 **Sensors integration**

The circuit schematic in Figure 5.14 shows that the pressure ports are connected to a Honeywell SSCDRRN100MDAA5 [50] piezo-resistive differential pressure sensor. The sensor provides a $0.5-4.5$ V analog output, with a full scale of ± 10 kPa, in accordance with the simulation results of Section 5.3. The 3D-printed couplers, see Figure 5.15, were designed to have a lateral port to measure the static pressure at the inlet and outlet of the pipe. A batch of coupler was printed, selecting those that provided best alignment of the central channel between the glass pipe and the coupler. Therefore, minimum disturbance is expected when measuring the static pressure.

The calibrated output values are updated at 1 kHz, and recorded using a 14-bit USB oscilloscope. The sensor provides an accuracy of $\pm 0.25\%$ FSS (Full Scale Span) in the same measurement period. When accounting for other effects (temperature variation, voltage offset, calibration, orientation respective to gravity), the manufacturer declares a total error band of $\pm 2\%$ FSS. Consequently, while the absolute value of the differential pressure can be determined within ± 0.2 kPa, the accuracy for tracking pressure changes over time remains at ± 0.025 kPa.

The second channel of the oscilloscope was connected to a photodiode, which has vastly superior response times (μs or lower) compared with the more common photoresistors (several ms). The photodiode is a Vishay BPW34, with a sensing area of 3×3 mm, and ability to sense visible light (but the sensitivity peak is in the infrared, at 900 nm). A simple voltage divider and amplifier was used as preconditioning circuit.

5.4.2 **Camera**

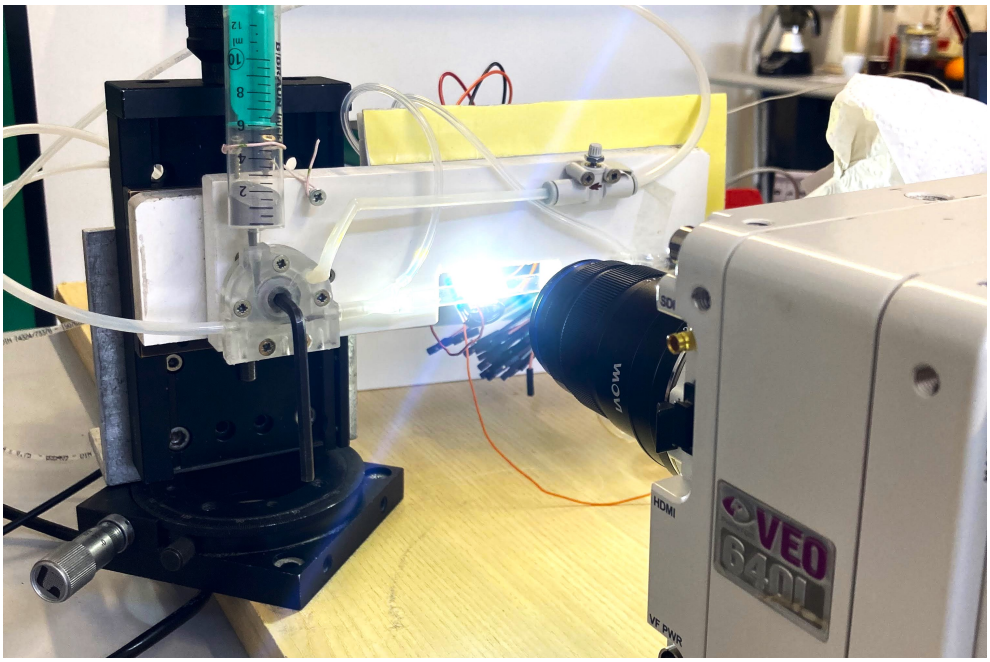

Figure 5.16: Photo of the setup for the pneumatic conveying experiment.

The host university provided a Pantom VEO 640L high speed camera, visible in the setup of Figure 5.16. It carries a CMOS (global shutter) sensor, with 2560×1600 px at 1400 fps, each pixel is a square of side 10 μm. The acquisition window can be reduced in multiples of 128×4 px to increase the framerate, for a total throughput of 6 Gpx/s. The camera has an electronic global shutter which duration can be selected independent of the fps. With good illumination the optimal balance was found at around 10 μs; longer times result in better illumination but the particles form a streak if they are moving too fast.

Small glass pipes are available on the market of chemical lab supplies, specifically in sizes that are comparable to the LMD equipment conducts. Pipes of different sections were bought from CMScientific: circular (d1.15 L75)mm, square (1x1 L100)mm, rectangular (6x0.6 L100)mm.

The camera is equipped with a Laowa 25mm f/2.8 2.5-5X Ultra Macro lens. The lens costs around 400€ at the time of writing, giving a magnification of 2.5-5x. Compared with similar models, it has a good aperture (F2.8), meaning it is expected to deliver more light to the sensor compared to other alternatives. The aperture can be reduced (down to F16) to improve the depth of field. Given the camera's sensor size of 25.6×16 mm (circa APS-C), pixel size of 10um. Higher framerates are achieved by reducing the acquisition portion of the sensor, therefore resolution and field of view reduce accordingly. The recording window for the circular and square pipes was selected at 1280×400 px, achieving a sample rate of 10 000 fps. At full acquisition window, the lens can provide an image:

Magnification	Field of View	Pixel Size
2.5x	10.24x6.4mm	4um
5x	5.12x3.2mm	2um

The magnification of the lens was used to obtain focus: the magnification is just an indication, during the post-processing it is possible to adjust the scale. The camera is also mounted on a slider with micrometric screw, which allows it to move closer or farther from the pipe in a precise manner, changing the focus. Especially with full aperture, the field of view is quite shallow, and it is crucial to put the focus plane on the center of the pipe. The pipe assembly is allowed to rotate around the vertical axis, to align the length of the pipe with the focal plane, and to move up and down to move it in the center of the frame. The image is captured around the middle of the pipe length. The resulting pictures are of good quality and an example with minimal post-processing is shown in Figure 5.17.

Figure 5.19 presents a detail view of a group of medium sized particles, where the pixel size is approximately 3 μm/px. The image resolution allows a direct estimation of the PSD, since the expected particle diameter is around 100 μm. The exposure, or the time when light is actually collected by the sensor, must be relatively short to avoid blur in the direction of motion. An exposure of around

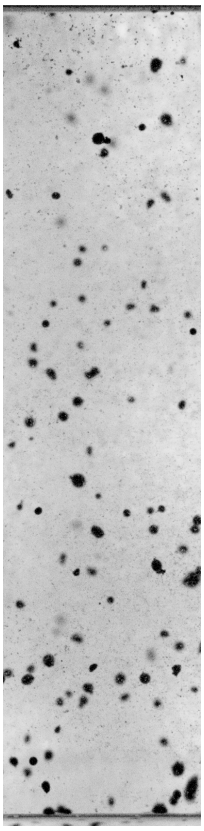

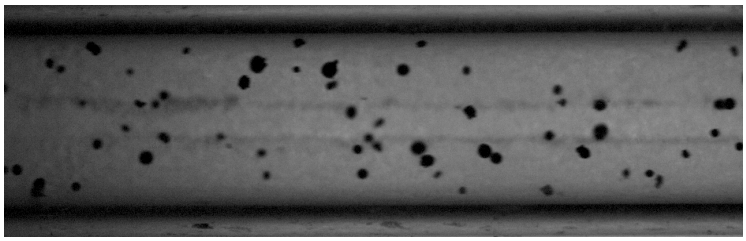

(A) Circular pipe (⌀1.15 mm), 1280x400 px, exposure 6.5 μs, aperture F8, sample rate 10 000 fps

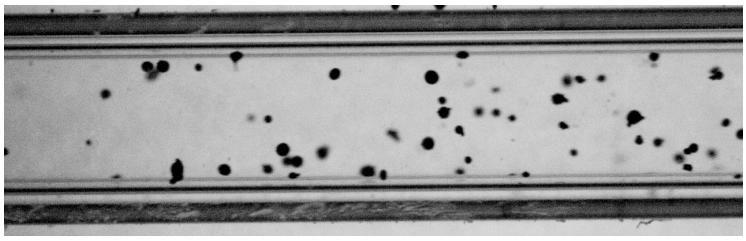

(B) Square pipe (1x1 mm), 1280x400 px, exposure 7.0 μs, aperture F5.6, sample rate 10 000 fps

←(C) Rectangular pipe (6x0.6 mm), 384x1600 px, exposure 5.0 μs, aperture F5.6, sample rate 5 000 fps

$\Longrightarrow$ **Flow direction** $\Longrightarrow$

Figure 5.17: Images captured with Phantom VEO 640L high-speed camera and Laowa ultra-macro lens for circular (A), square (B), and rectangular (C) pipe sections.

10 μs almost completely eliminated the streaks while maintaining a good image luminosity with an aperture between F5.6 and F8.

Illumination of the section of interest is directly from the side opposite from the lens. A high powered LED light shines light towards the pipe and to the lens. It is extremely bright, and it is advisable to use some level of PPE when on. A layer of frosted acrylic sheet in front of the LED diffuses the light, resulting in sharper images and a more uniform background.

The LED array is powered in constant current mode, at 800 mA and around 12 V, for a total power of 10 W. The simple circuit in Figure 5.18 uses a common LM317 linear regulator, and a resistor R1 = 1.5 Ω. In this way the LED does not present any flicker, which would be picked up by the high speed camera.

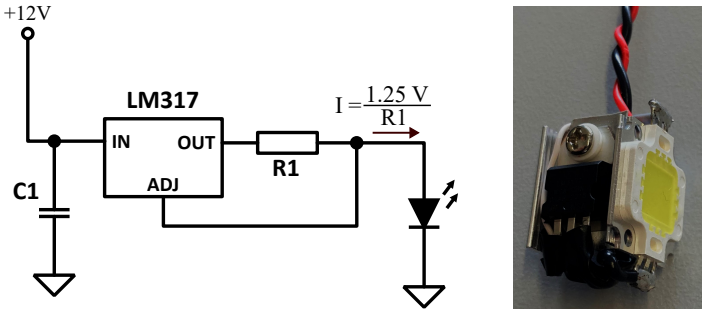

Figure 5.18: Constant current supply circuit for the LED array.

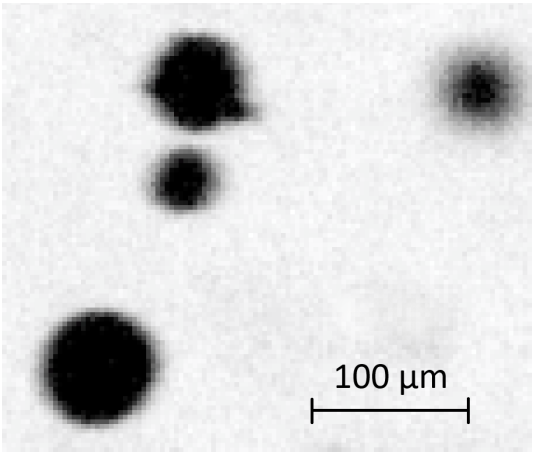

Figure 5.19: Detail view of four particles captured in Figure 5.17 (B).

5.4.2.1 **Telecentric lenses**

In Figure 5.19 it is evident that one of the particles is slightly out of focus. This is not easily avoidable with the current setup and depends on the type of employed lens. Lowering the aperture mitigates the issue, allowing to extend the focus distance. Ideally, the experiment would use a Telecentric Lens, however it was not possible to procure it due to budget limitations. They offer a consistent field of view (FOV) regardless of object distance, unlike conventional lenses which exhibit parallax error. This characteristic ensures accurate measurements even when objects are moved within the depth of field (DOF). With telecentric lenses, magnification remains constant, crucial for precision in automated inspection tasks where objects may vary in distance or position. By eliminating parallax error, telecentric lenses provide reliable and repeatable measurements, essential

for high-precision applications, such as in machine vision systems. In this case, the advantage would be the increased accuracy of the particle size measurement. Figure 5.20 clearly presents this advantage: two identical screws placed in different planes appear to be of different sizes with a conventional lens setup, but they appear of the exact same size by using a telecentric setup. Future developments of this experiment should certainly use a telecentric lens.

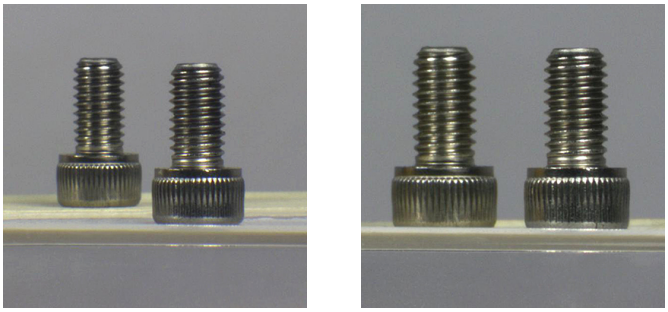

Figure 5.20: An image of two identical 8-32 cap screws taken by a conventional lens (left) and a telecentric lens (right). Although in the image on the right the screws appear of the exact same size, they are actually separated by 45 mm along the viewing direction [Thorlabs.com].

5.5 **Particle Tracking**

Figure 5.17 reports static snapshots of the flow conditions. To track the movement of particles over time, the positions should not change excessively from a frame to another. The image sequence is presented in Figure 5.21, where the particles' movement is immediately evident. Each recording is in the order of 10^4 frames, for a total duration of around 1 s. Counting all the particles present in all the frames, the number of spots to be considered for the tracking procedure is approximately $3 * 10^5$.

The videos captured using the setup described in this Section were analyzed as an "image stack", or a sequence of 8-bit gray scale images, in the image processing software Fiji/ImageJ [107]. In the pre-processing step, the original video is rotated, cropped, and transformed into a black and white binary mask according to a brightness threshold. More advanced image filtering and segmentation methods are available in the software and were tested, but resulted superfluous thanks to the camera and lighting setup, which already provide very easily identifiable

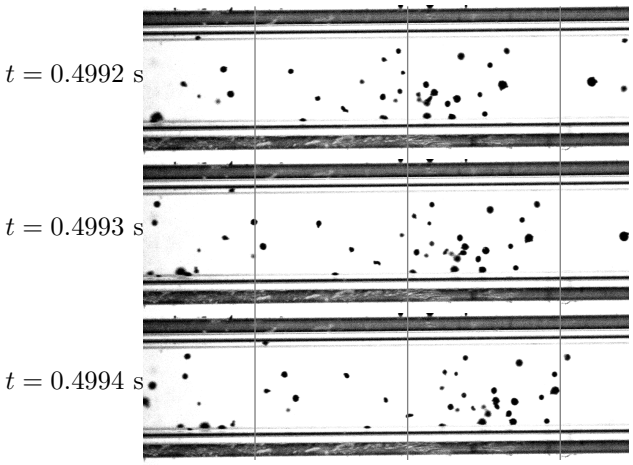

Figure 5.21: Image sequence from the same conditions as Figure 5.17 (B). The gas flow in this case is 0.4 L/min.Notice the particles' movement relative to the vertical grid lines.

spots. In this discussion, particles are the physical, 3-D objects that compose the powder; spots are their 2D shadows captured on each image of the high-speed video.

Particle tracking and analysis was performed using TrackMate [124], an additional plugin to Fiji. Essential to this work is its implementation of the linear motion tracker, which can deal with particles moving with a roughly constant velocity. It is based on the LAP framework [55], which approximates multiple-hypothesis tracking using a linear assignment problem: a cost matrix penalizes the least likely movements. It was developed mostly to track the Brownian motion of bacteria, but it is used in TrackMate to track fast moving objects using a Khalman filter strategy: the particle tracks are analyzed, in the hypothesis of mostly linear motion, and a prediction is made for the subsequent steps. If there is a particle within a tolerance of the expected landing spot, a new segment (called edge) is added to the track. With enough information, the implementation can track the particle even if it is not visible for a predefined number of steps. Penalties can be assigned to several conditions, namely the spot area and perimeter, increasing the robustness of the system to track objects that are not expected to change in shape and size; lower weights can be assigned to loosen the condition, accounting for rotating particles. Conveniently, the spot identification step of

TrackMate records the geometric descriptor of each spot: area and perimeter are used to calculate the equivalent diameter, along with other shape descriptors like circularity, Feret diameters, and ellipsoid axes. The post-processed high speed videos result in four different files:

`spots.csv`
: containing the position of each spot in time and space, a unique numeric identifier (ID), geometrical information (area, perimeter, circularity, ...), as well as the ID of the track it is included in.

`edges.csv`
: specifies the source and target spot IDs, the displacement and duration (which may be multiples of the frame Δt), the speed, and again the ID of the track it is included in.

`tracks.csv`
: specifies the overall track information, like total track duration, average speed, and more.

`allspots.csv`
: is the same as `spots.csv`, but it also includes the spots that do not participate in a track, therefore is preferred when determining the concentration.

5.5.1 Open-source code development

In the Jaquaman linking step of the tracker, the software needs to look for possible *targets* for each *origin* spots in order to initiate a track. The search radius, by default, is centered on the origin spot, and must be relatively large to account for the movement. After the track is initiated, the next search circles can be much smaller thanks to the predictive step of the Kalman filter.

In the fast flows, initiating a track is not optimal, as the spots might move a lot in a preferential direction, leading to an impractically large search radius. Most of the initiated tracks ended up being incorrect, and terminated only after one or two steps. The presence of these artifact tracks also impedes the initiation of the true tracks, therefore some visually very clear cases are ignored. In the end, only few tracks per frame were visible, most particles were unable to be traced.

To solve this issue, the TrackMate plugin [124] was modified, in order to include a manual first guess. In this strategy, the Jaquaman linking step of the

	Before	After
Spots	259364	247619
Edges	63346	129730
Tracks	9867	17678

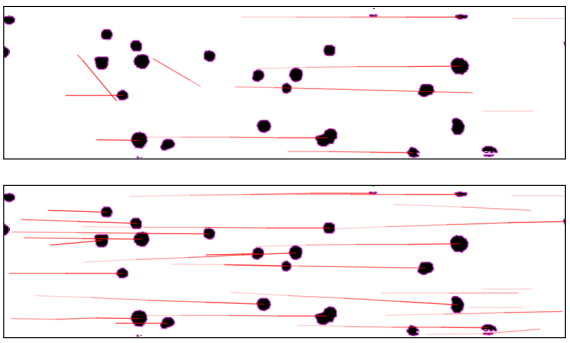

Figure 5.22: Enhancement in particle tracking capabilities in the same recording.

tracker sees the unmodified target spot, but the origin spot is translated by a displacement vector, specified a manual input. Moving the origin spots closer to the expected position of the target spots allows for a much smaller initial search radius, increasing the efficacy of the Jaquaman linking step. After determining the relation between an origin and a target spot, the tracking can then proceed using the unmodified Kalman filter. The modification has been submitted to the GitHub repository of the plugin.

The improvement in tracking the particles in this situation is evident, and reported in Table 5.22, without which the particle tracking was rather inefficient. The difference in the number of total recognized spots is negligible, and due to the fact that the filtering on the particle size is done through sliders instead of text input. The recorded particles in the correct size range is essentially exact. The greatest difference is in the numbers of edges and tracks, which mean that there is more information on the movement. But, more importantly, before the improvement there were several tracks moving in unpredictable directions, as seen in the image, which is incorrect.

5.5.2 **Occlusion**

At this stage, no specific assumptions were made regarding the depth of the pipe along the camera axis. However, occlusion significantly impacts the accuracy of volumetric density measurements. Spinewine et al. [119] offer a detailed analysis of occlusion effects observed when imaging particles at increasing depths within a channel, as depicted in Figure 5.23. This figure clearly demonstrates that the observable particle volumetric density ($\hat{\phi(y)}$) is merely a fraction of the actual

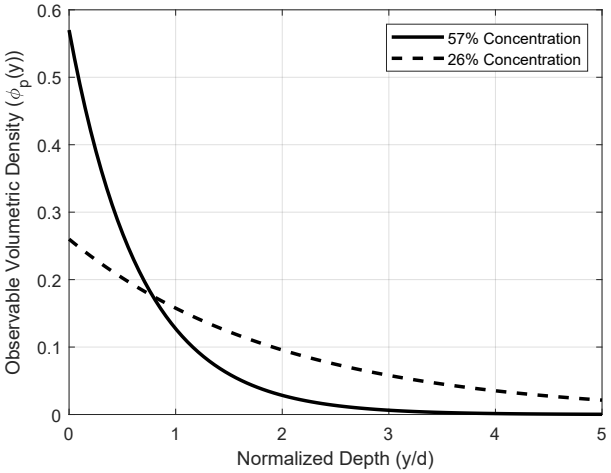

Figure 5.23: Distribution of visible particle centers relative to depth (perpendicular to the wall) for two distinct concentrations (thick line for 57%, thin line for 26%). The theoretical distribution is modeled using a 3D Poisson process. [119]

volumetric density ($\phi(y)$), with the discrepancy widening as the depth from the camera's viewpoint increases (y, normalized to the particles' diameter d).

5.5.3 **Particle volume estimation**

The computational model assumes spherical particles, which, when projected onto a plane, create circular shadows that may overlap. As observed in Figure 5.25, some overlapping particles are not involved in the tracking but need to be considered to evaluate the volume accurately. The following method reduces the error using a simple algebraic model, which could be further improved with additional data, potentially using an artificial neural network (ANN) or more rigorous mathematical definitions. However, the current method already provides satisfactory results under the presented conditions.

The equations describing relationships for the perimeter, area, and volume for a system composed of multiple circular objects (in 2D) or spherical objects (in

3D), each with radius R_i are:

$$\begin{cases} P = 2\pi \sum R_i = 2\pi n R_{\text{eq}} \\ A = \pi \sum R_i^2 = \pi n R_{\text{eq}}^2 \\ V = \dfrac{4}{3}\pi \sum R_i^3 = \dfrac{4}{3}\pi n R_{\text{eq}}^3 \end{cases} \tag{5.9}$$

They express the idea that the total perimeter, area, and volume can be represented by equivalent sums of the contributions of individual objects with a mean or effective radius R_{eq} and a total number of objects n. The objective is to attempt to estimate V from the first two, P and A, deriving R_{eq} and n.

From the perimeter and area, we derive R_{eq} as:

$$\begin{cases} R_{\text{eq}} = \dfrac{P}{2\pi n} \\ R_{\text{eq}}^2 = \dfrac{A}{\pi n} \\ R_{\text{eq}} = \sqrt{\dfrac{A}{\pi n}} \end{cases} \tag{5.10}$$

Equating the expressions for R_{eq}:

$$\begin{cases} \dfrac{P}{2\pi n} = \sqrt{\dfrac{A}{\pi n}} \\ n = \dfrac{P^2}{4\pi A} \end{cases} \tag{5.11}$$

Divide area and perimeter to find R_{eq}:

$$\begin{cases} \dfrac{A}{P} = \dfrac{\pi n R_{\text{eq}}^2}{2\pi n R_{\text{eq}}} \\ R_{\text{eq}} = \dfrac{2A}{P} \end{cases} \tag{5.12}$$

At this point, n and R_{eq} can be used to find the volume:

$$\begin{cases} V = \dfrac{4}{3}\pi n R_{\text{eq}}^3 \\ \quad = \dfrac{4}{3}\pi \left(\dfrac{P^2}{4\pi A}\right)\left(\dfrac{2A}{P}\right)^3 \\ \quad = \dfrac{8}{3}\pi \dfrac{A^2}{P} \end{cases} \tag{5.13}$$

This method has an error proportional to the overlap. Considering only two particles: from no overlap, where the error is theoretically zero, the real area

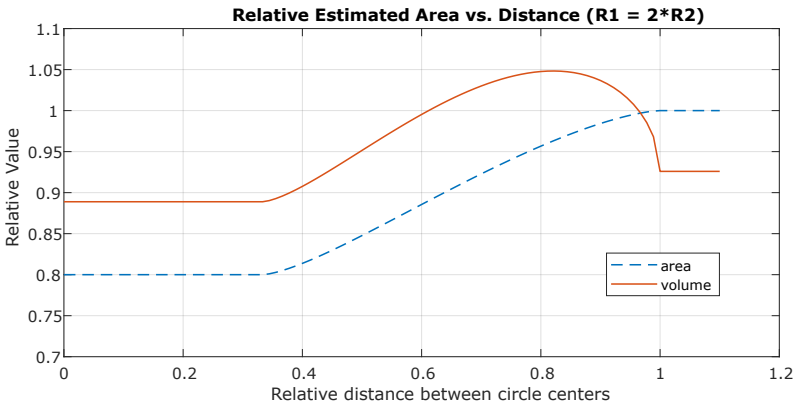

Figure 5.24: Relative values of volume and area estimated using the measured apparent area and perimeter of overlapping disks.

and volume are underestimated by half when both particles are exactly the same size and completely overlapped. If the particles are of different sizes, the error is less than that. This is verified using the script `circleOverlapSimulation.m`, resulting in Figure 5.24. The error at distance greater than 1 disappears for more dissimilar sizes, and the global error reduces for more dissimilar sizes. The worst case scenario is for equal radius, where both estimated values are half of the real area and volume, when both particles are totally overlapped. If only one circle is evaluated (or $R_2 \to 0$), the formula is exact.

5.5.4 **Tracking verification**

The particle tracking software was tested on a simulated dataset to estimate the performance of the technique, having control on all possible variables. The model discussed in Section 5.2 was adjusted to replicate the flow within a square-section pipe measuring 1×1 mm. This adaptation yielded a series of datasets containing particle positions and velocities recorded at intervals of 10^{-4} s, matching the framerate of the high-speed videos. These datasets serve as the baseline, or "ground truth," for assessing the error introduced during the particle tracking phase of the analysis.

Using Paraview [11], the simulation output was post-processed into a series of images, replicating those captured by the experimental setup. In these images, particles are depicted as dark circles against a white background, as shown in

Figure 5.25 (A), occasionally overlapping. Overlapping particles pose a challenge for tracking. To address this, the chosen approach involves selecting only fully visible particles, employing the Kalman filter strategy implemented in TrackMate [124]. Figure 5.25 (B) illustrates the same frame as (A), overlaying the spots utilized in tracking and their corresponding tracks. It is worth noting that while the tracks may be incomplete, they provide sufficient data for velocity analysis.

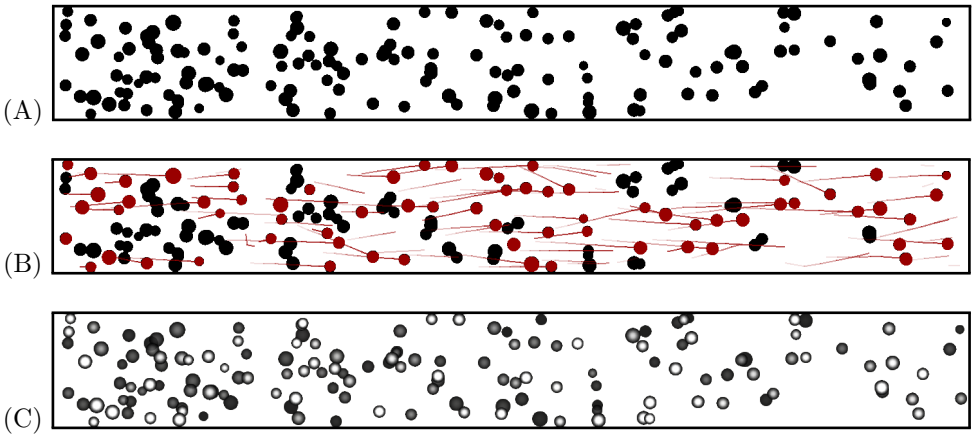

Figure 5.25: Example snapshot of the simulated particle tracking. (A) shows particles represented as uniformly colored dark circles. The tracking result in (B) highlights the tracked spots and their respective tracks (backwards in time). The shaded representation in (C) demonstrates particle overlapping, with darker particles being farther from the observer.

The tracking information was exported from TrackMate as CSV files containing all the *Spots*, *Edges*, and *Tracks*. Tracks consist of a series of edges, each defined by an origin and target spot. These elements are interconnected through identifier numbers (IDs), with edges containing the IDs of their respective origin and target spots.

Matlab scripting was the tool of choice to analyze the results, and get to the values of interest. Most relevant for the LMD process, as explained in 5.3, is the instantaneous mass flowrate of metallic powder. The resulting values are depicted in Figures 5.26 and 5.27. The values labelled as *OpenFoam data* refer to the direct extraction of particle diameters and velocities from the simulation. Both the result of the tracking and the raw data was processed the same way, for consistency. The area concentration from the particle tracking is the direct measurement of the dark spots against the light background, essentially equivalent to counting

the black vs white pixels of the binary map represented in Figure 5.25 (A).

Figure 5.26 displays the difference between the ground truth (*OpenFOAM data*) and the simulated *Particle Tracking*. In both cases, area and volume fraction concentrations, there is a discrepancy. The volume fraction discrepancy was plotted as a function of the volume fraction ϕ determined using the Particle tracking and the expected one determined by the simulation. This results in a clear linear relationship. This is easily explained by the occlusion phenomena, represented by Figure 5.23, therefore the line passes through the origin since the occlusion error should tend to zero for very low concentrations. Compared to that graph, in this case the concentration is much lower, therefore the linear fit will be used directly to correct the volumetric concentration in order to calculate the mass flowrate.

Knowing the bulk density of the material ρ_s, the mass flowrate of the solid particles is calculated as $\dot{m} = \rho_s(V_tot \cdot \phi)\hat{v_Z}$, where $\hat{v_Z}$ is the average velocity of the particles along the pipe, determined using the particle tracking of Figure 5.25. Without applying the correction on the volume this results in the mass flowrate reported in Figure 5.27. This diagram also reports the average particle velocity and the standard deviation intervals in of the velocities in the frame, which coincide almost perfectly (the average error is less than 1%). The flowrate corrected using the linear fit is not represented in the figure as the two lines effectively overlap, and the error is also less than 1%.

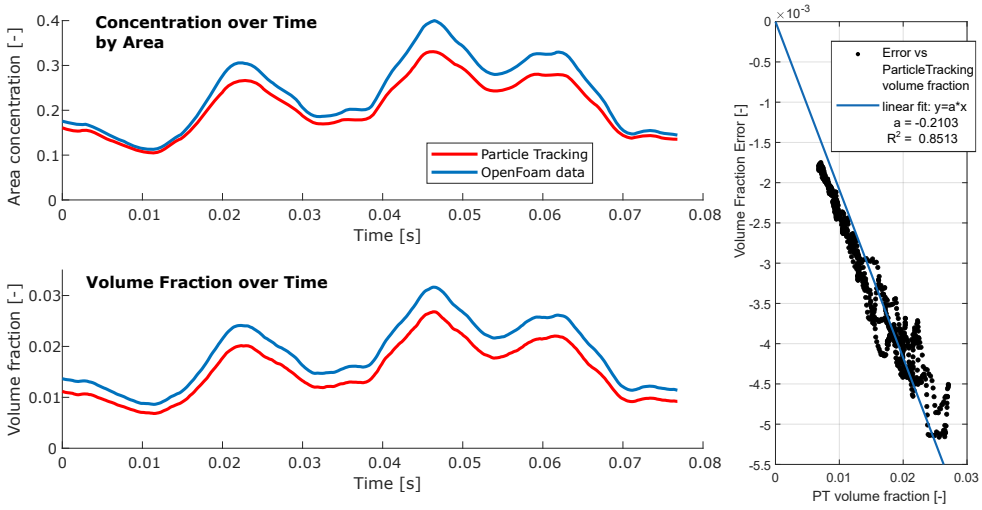

Figure 5.26: Solids concentration in the simulated flow, both as projected area and volumetric. The data coming from the Particle Tracking method is compared with the direct three dimensional values. All data was filtered with a 2 ms moving average. On the right, the error in the estimated volume fraction is fitted by a line passing through the origin.

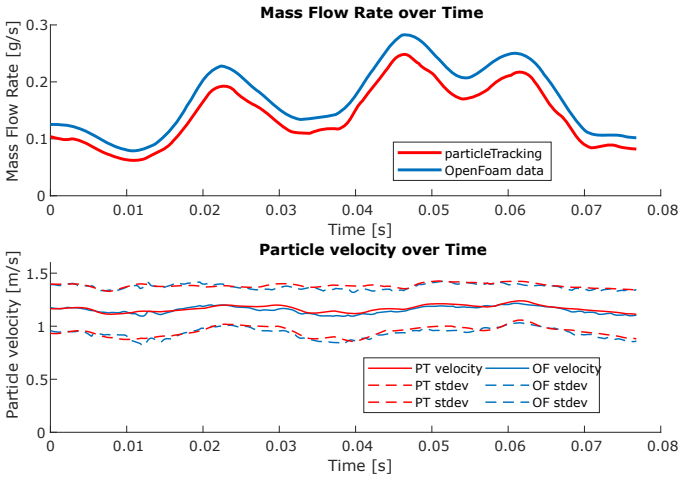

Figure 5.27: Particle average velocity and standard distribution in the observed section of the simulated flow over time, and resulting mass flowrate. The data was filtered with a 2 ms moving average. This data was not corrected with the information of Figure 5.26.

5.6 Experimental results

This discussion presents the measurements performed on the circular glass pipe, introduced by Table 5.7, with an internal diameter of $d = 1.15$ mm. The material is AISI 316L stainless steel, in the commercial form *Oerlikon MetcoAdd 316L-D* with a nominal PSD $D_{90} = 106$ μm and $D_{10} = 45$ μm. The same PSD was used in the pneumatic conveying simulations of Section 5.2, and is reported in 5.4. For the main presented case, the flowrate of clean and pure Nitrogen gas was set to 0.8 L/min, which corresponds to a calculated 12.8 m/s average gas velocity.

5.6.1 Particle Size Distribution

The PT algorithm uses the spot area and other metrics to find the most likely trajectories. As indicated, all this information is available in the output files. When determining the Particle Size Distribution, it is appropriate to use the method described in Section 5.5.3 to correct for the occlusion. Finding a PSD skewed towards larger particle size is to be expected, but the large assemblies of particles that would cause noticeable outliers are avoided.

Figure 5.28 reports the PSD measured in the 0.8 L/min test, and is repeatable across different runs. The Distribution is very similar to the expected, an encouraging result that shows that the setup is indeed appropriate.

The accuracy of this measurement is very dependent on the sharpness of the original images, and on the parallax error. The camera stup can be improved by a telecentric lens (see Section 5.4.2), and secondarily by a parallel rays light source.

5.6.2 Mass flowrate estimation

Figure 5.29 reports the final results of the particle tracking. Considering the established flow for $t \geq 0.3$ s, the particles' average velocity remains relatively constant, with a narrow distribution. Indeed there is a small dependency on the particle loading, as a denser flow determines a slightly lower average velocity, but the flowrate variation is to be attributed for the most part to the variation of particle concentration.

This is similar to the simulation where, for established flow conditions reported in Figure 5.8, the velocity is also relatively constant and with a narrow

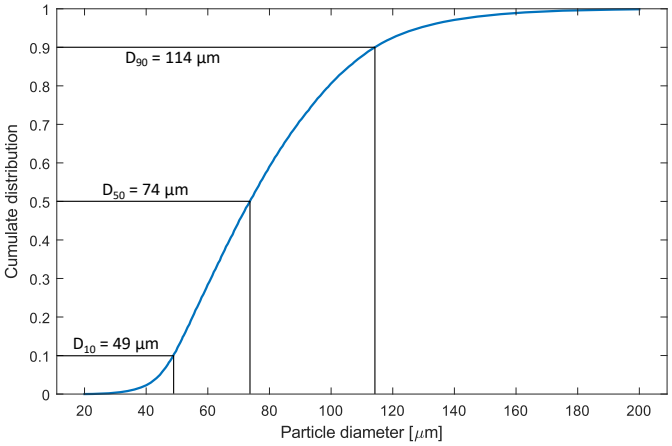

Figure 5.28: Particle Size Distribution (PSD) measured by the Particle Tracking (PT) algorithm.

distribution, while the particles' movement generates concentration waves that move through the pipe, which is indeed what is observed experimentally. This determines one first validation of the adequacy of the CFD-DEM simulation to represent such a situation.

The initial transient of the mass flowrate, starting at $t = 0$ s, poses a striking similarity to the one in Figure 5.12 determined by CFD-DEM simulation. In the real case the slope is somewhat slower, but it was tricky to exactly match the experimental setup to the simulation, as they happened at different times. Further simulations are on the way.

5.6.3 **Flow irregularities**

As seen in Figure 5.30, the average mass flow rate and RMS values, which represent the intensity of the conveyed flow irregularities, have been calculated in line with Equation 5.8, used for the simulated results. These values allow us to directly compare experimental and simulated flow irregularities.

While the overall intensity of the flow irregularities in the experimental data is quite close to the simulation results from the CFD-DEM, there are some noticeable differences. One key factor is the disparity in total observation time between the two datasets. The simulations cover a much shorter time span, roughly a tenth of the experimental window, leading to a clearer periodicity in the simulation that

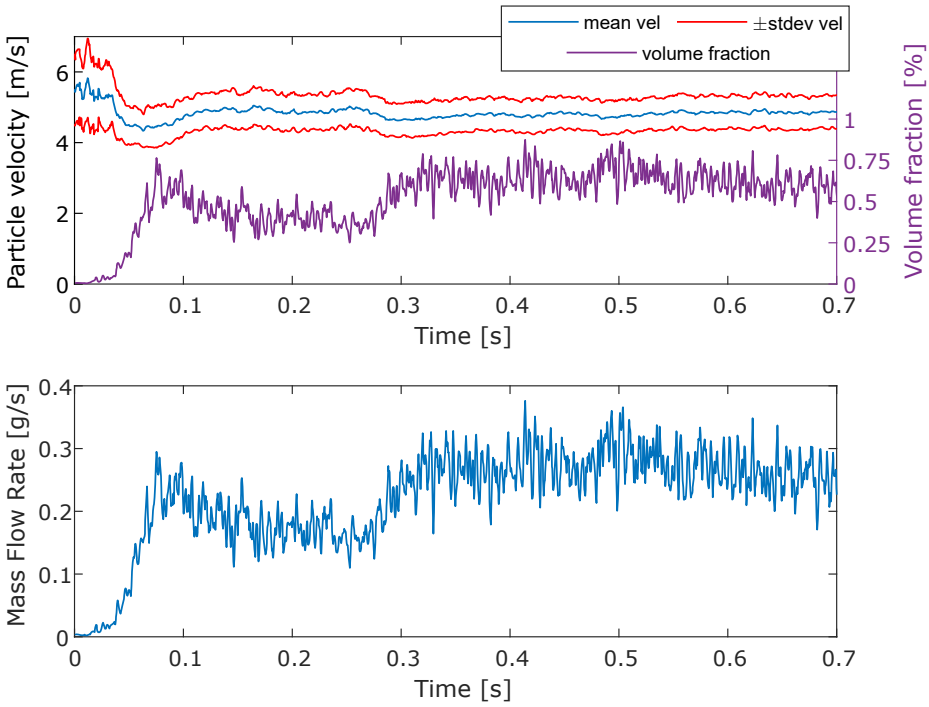

Figure 5.29: Particle tracking result for a conveying flow of nitrogen of 0.8 L/min, corresponding to an average gas velocity of 12.8 m/s. The diagram reports the particles' velocity distribution and volumetric concentration, averaged over the recorded frame ($L = 3$ mm) and over a moving time window (2 ms). These are used to calculate the mass flowrate.

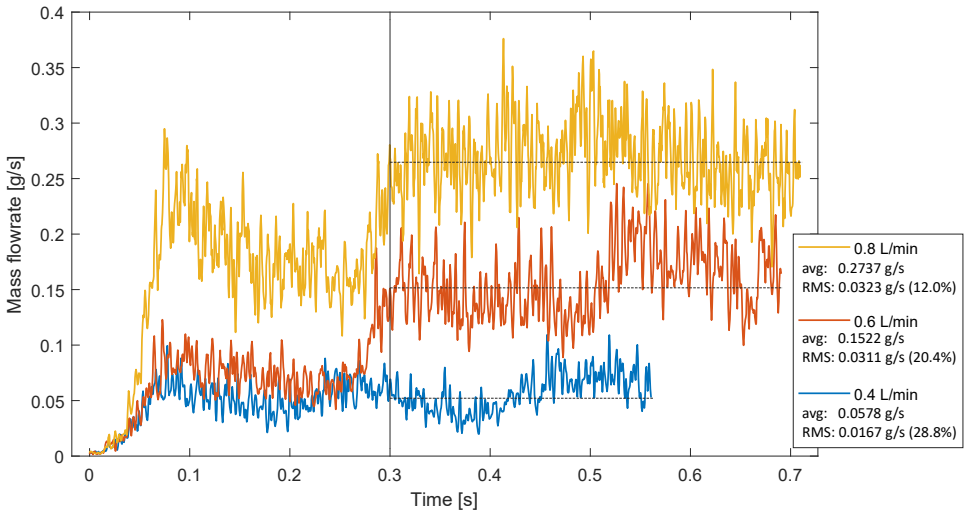

Figure 5.30: Powder mass flowrate determined usung PT for three conditions. The resulting average and RMS values are determined for what are considered as established flow conditions, or $t \geq 0.3$ s. The signals are filtered using a moving average window of 2 ms.

becomes harder to discern in the longer experimental data. Additionally, the results in both the experiment and simulation have been filtered with the same moving average window of 2 ms, ensuring consistency across the comparison.

These results suggest that, despite some limitations in matching all the experimental conditions perfectly to the simulation, the CFD-DEM model provides a robust representation of the flow irregularities observed in the experiments. Future work could involve more advanced filtering techniques, such as wavelet analysis, to better capture the noise and periodic patterns present in the flow.

5.6.4 **Photodiode calibration**

The values measured by the photodiode and the differential pressure sensor are reported in Figure 5.31. The figure shows an evident correlation of all the signals, which suggests the possibility to calibrate inexpensive and small sensors to determine the powder flowrate in positions close to the nozzle.

The signal from the photodiode was directly scaled to the mass flowrate by matching on the average values of the two signals between 0.3 s and 0.7 s. This resulted in an extremely good agreement, with the signals almost superimposed,

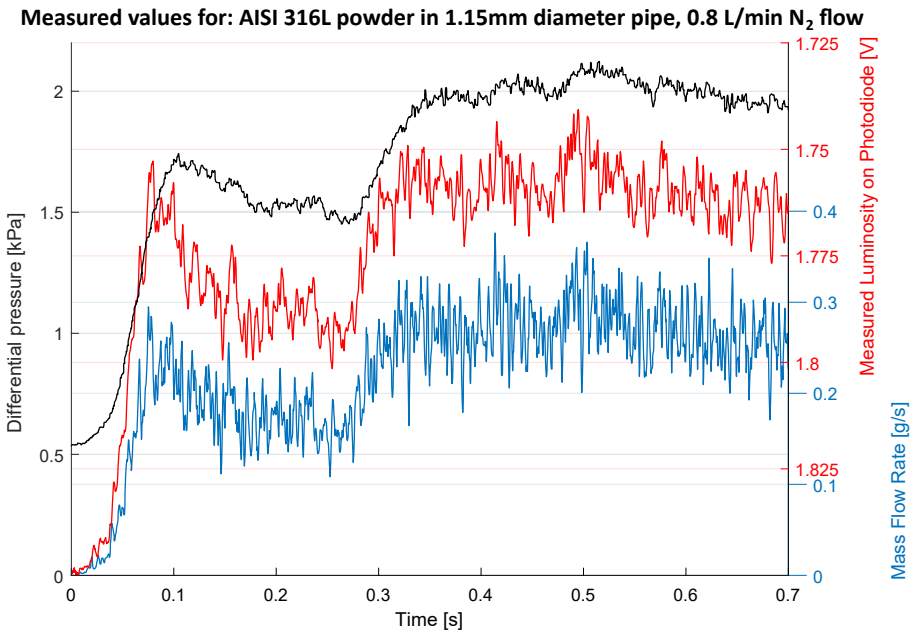

Figure 5.31: Particles' mass flowrate, for a conveying flow of nitrogen of 0.8 L/min, corresponding to an average gas velocity of 12.8 m/s. The pressure measurement and transmitted luminosity are included, each on the respective axis.

as shown in Figure 5.32. Evaluating the calibrated flowrate in the stable conditions, or for $0.3\ \text{s} \leq t \leq 0.7\ \text{s}$, returns RMS = 11.7%, only slightly lower compared to the value determined using PT.

Even if the acquisition rate was higher, at 50 kHz, the measurement performed via the photodiode shows less steep changes than PT, deriving the physical construction of the device itself. A diode with lower parasitic capacitance, and a better preconditioning circuit, can certainly improve the response time of the sensor, capturing faster varying phenomena. It is unlikely that the photodiode sensing element size, which is 3×3 mm, caused this smoothing: when analyzing the high-speed video, the observed pipe length was a similar value.

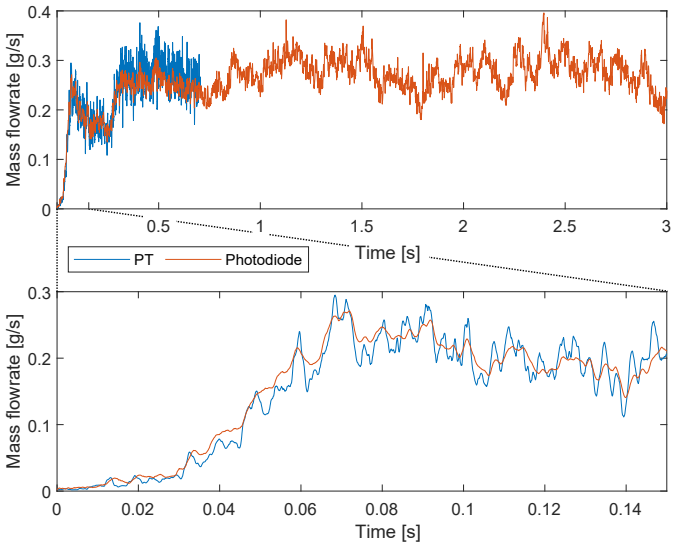

Figure 5.32: Particles' mass flowrate measured using Particle Tracking (PT) and the photodiode signal, linearly calibrated. This case is for a conveying flow of 0.8 L/min, corresponding to an average gas velocity of 12.8 m/s.

5.6.5 **Pressure measurement**

The pressure sensor is an internally compensated and calibrated Integrated Circuit (IC), therefore it was easy to compare the readings between runs. The average values for $t \geq 0.3$ s are reported in Figure 5.33, as well as the initial values for the empty pipe. The values' magnitudes are in agreement with what was obtained

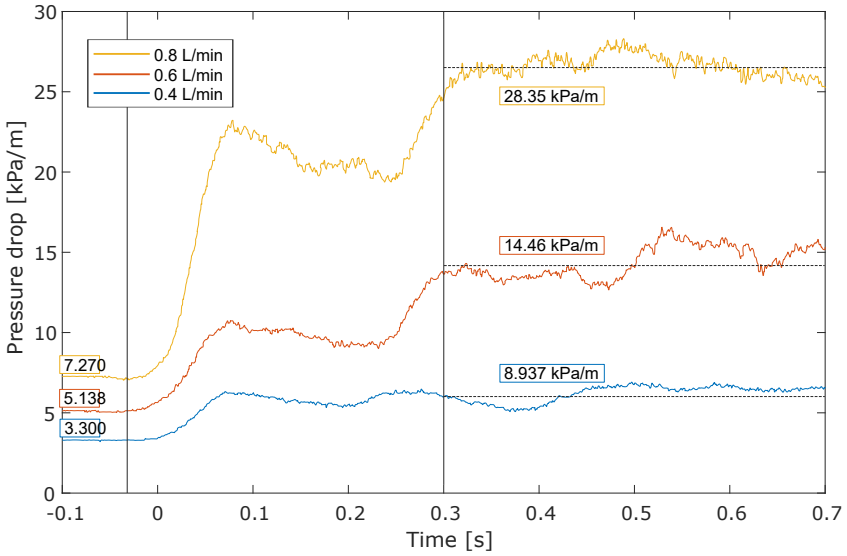

Figure 5.33: Measured pressure drop along the pipe. The slope is calculated for the nominal pipe length.

by the CFD-DEM simulation, reported in Table 5.4.

The signal is directly affected by the volumetric fraction present in the pipe, but the faster variations are not captured. The differential sensor, connected at the entrance and exit of the pipe, is affected by the average drop necessary to convey the powder present in the whole pipe. Therefore, even if the sensor declares a response time of 1 ms, the faster variations are averaged over the whole pipe length.

One issue to be aware of when deploying such sensors is that the static port, visible in the coupler of Figure 5.15, is a few tenths of a mm wide and could become clogged. On the other hand, a visible amount of fine particles were able to pass through the small orifice, and make their way through the connecting transparent silicone tube. This could cause issues on the delicate MEMS, which can work in humid conditions, but is not qualified in terms of dust protection.

5.7 Chapter Summary

This chapter explored the pneumatic conveying of metal powders, focusing on its application in Laser Metal Deposition (LMD) processes. By comparing two

numerical modeling approaches—Computational Fluid Dynamics coupled with Discrete Element Modeling (CFD-DEM) and MultiPhase Particle In Cell (MP-PIC)—we gained insights into their effectiveness in simulating particle-laden flows.

One of the key findings is that the CFD-DEM approach provides a more accurate representation of the flow dynamics and mass flow rate fluctuations observed in pneumatic conveying systems. The simulations aligned closely with experimental data, particularly in capturing the formation of particle clusters and the associated pressure drops. This demonstrates CFD-DEM's strength in detailed flow characterization, despite its higher computational demands.

On the other hand, the MP-PIC method proved to be more computationally efficient, making it suitable for scenarios where resources are limited. However, it tended to underestimate pressure drops and did not capture flow irregularities as effectively as CFD-DEM. This suggests that while MP-PIC is useful for quicker simulations, it may not always provide the level of detail required for certain applications.

The experimental work conducted at the University of Trento supported the simulation results, especially those from CFD-DEM. The agreement between experimental measurements and CFD-DEM simulations reinforces its reliability in modeling real-world pneumatic conveying behavior. Additionally, the use of high-speed imaging and differential pressure sensors enhanced our understanding of flow uniformity and helped in calibrating the simulations accurately.

CHAPTER

6

Study on the LMD Nozzle

The nozzle's setup, as a part of an LMD system, is crucial in ensuring the proper powder delivery to the melt pool. The metered stream of powder flows through a length of conveying system and reaches the deposition head, exiting through the nozzle. The deposition head is the defining system of the LMD technology, providing the laser power, shielding gas, and a constant stream of filler material in powder form.

Several configurations exist for laser cladding and LMD, but for the latter, two configurations are most commonly employed: **continuous coaxial** and **discrete coaxial**. In both cases, the laser beam is central, forming a central melt pool, and the powder is delivered from the sides at a converging angle.

6.1 Nozzle Configurations

In the continuous coaxial nozzle shown in Figure 6.1a, the powder exits an annular slit surrounding the central orifice. This type of construction generates good and uniform results, not being affected by the (planar) direction of deposition. However, it is susceptible to inclination changes. The nozzle construction in this specific case is more complex, containing a distributor structure to guide the powder.

In contrast, the discrete coaxial nozzle depicted in Figure 6.1b releases powder through three or more small nozzles placed around the central orifice. This design can also produce good results but is more susceptible to the (planar) direction of

deposition. It tends to be less affected by inclination changes, making it preferable for mounting on anthropomorphic robots.

For the further studies presented in this chapter, the continuous coaxial nozzle is used due to the more complete information available.

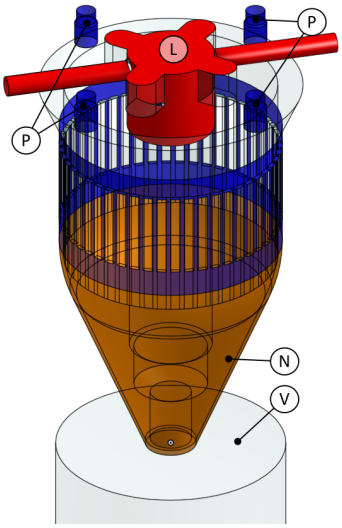

(a) Continuous coaxial nozzle, courtesy of *Universidad del Pais Vasco* (UPV).

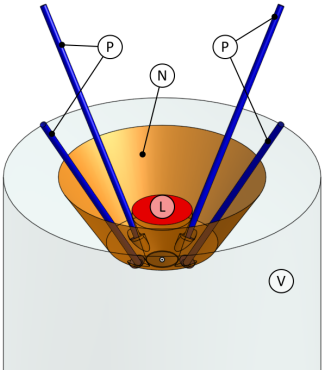

(b) Discrete coaxial nozzle, courtesy of IMH Campus.

Figure 6.1: 3D CAD models of the nozzles analyzed in this work. Annotations indicate: the powder ports Ⓟ, the laser and shielding gas port Ⓛ, the nozzle body Ⓝ, the discharge volume (used in the simulations) Ⓥ.

6.2 Previous Studies

Previous research has investigated the behavior of powder delivery systems in Laser Metal Deposition (LMD) processes. Tabernero et al. [120] conducted a detailed study on the continuous coaxial nozzle, focusing on the numerical simulation and experimental validation of powder flux distribution. They used one-way coupled particle tracking to simulate particle paths, verifying their findings by comparing the particle concentrations deposited in cylinders of various diameters at a known distance from the nozzle.

In another study, Ostolaza et al. [92] performed a Computational Fluid Dynamics (CFD) analysis on the continuous coaxial nozzle, as depicted in Figure 6.1a. Their research concluded that the $k-\omega$ turbulence model is most suitable

for simulating the flow characteristics in this scenario. They emphasized the importance of accurately determining process parameters, especially when switching materials. The study compared simulation results with experimental data using long exposure images to map particle concentration, as shown in Figure 6.2a.

Additionally, Gao et al. [38] explored the dynamics of powder flow in LMD nozzles through both experimental and numerical methods. They highlighted how variations in nozzle design and process parameters significantly affect powder distribution and deposition efficiency. Their findings underscore the necessity of optimizing nozzle configurations to achieve uniform and efficient material deposition.

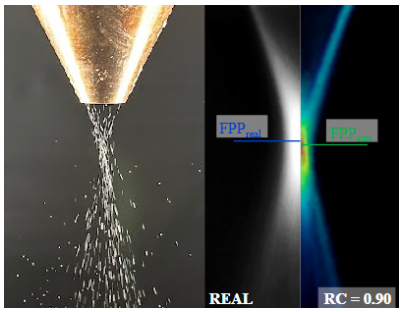

(a)

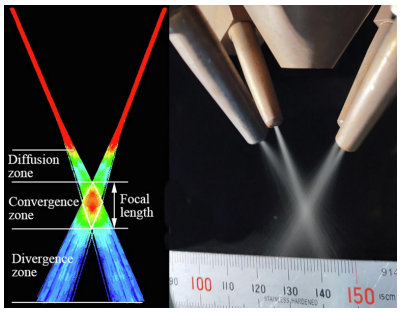

(b)

Figure 6.2: (a) Comparison of simulated and experimental powder distribution morphology. Adapted from Ostolaza et al. [92], who uses the same continuous coaxial nozzle as Figure 6.1a. (b) Powder flow zones and focal length in a discrete coaxial nozzle, highlighting the diffusion, convergence, and divergence zones. Adapted from Gao et al. [38].

The review by Guner at.al. [45], jointly with the one from Piscopo et.al. [98] complete the picture, denoting a gap in the research related to the flow uniformity during the deposition. Existing experimental studies determine the particle concentration on the focus spot using time-averaged data and long exposures. Existing numerical studies employ DPM, one-way coupled simulations due to the relatively low particle loading, whereas no studies use Discrete Element Modeling to more closely capture the material behavior in the process conditions.

6.3 Experimental study of the Continuous Coaxial Nozzle

An investigation on the influence of process parameters and flow through the nozzle was carried out with the collaboration of the University of the Basque Country (UPV). The nozzle structure is described in Figure 6.1a, and three main flowrates can be controlled in the experimental setup: the powder, the conveying gas, the lens protection gas.The conveying and shielding gas are both Argon, coming each from a separate flowmeter. The experiment is run "cold," in the sense that a nozzle was mounted on a stand outside the machine and run without the laser, as represented in Figure 6.3.

The experiments involved high-speed video recordings to capture the powder flow dynamics. The primary parameters varied in the experiments were the rotational speed percentage (RPM) of the distributor, powder flow rate in grams per minute, carrier gas flow rate, and shielding gas flow rate. These parameters were selected based on their significant impact on the powder flow characteristics and the overall quality of the deposition process.

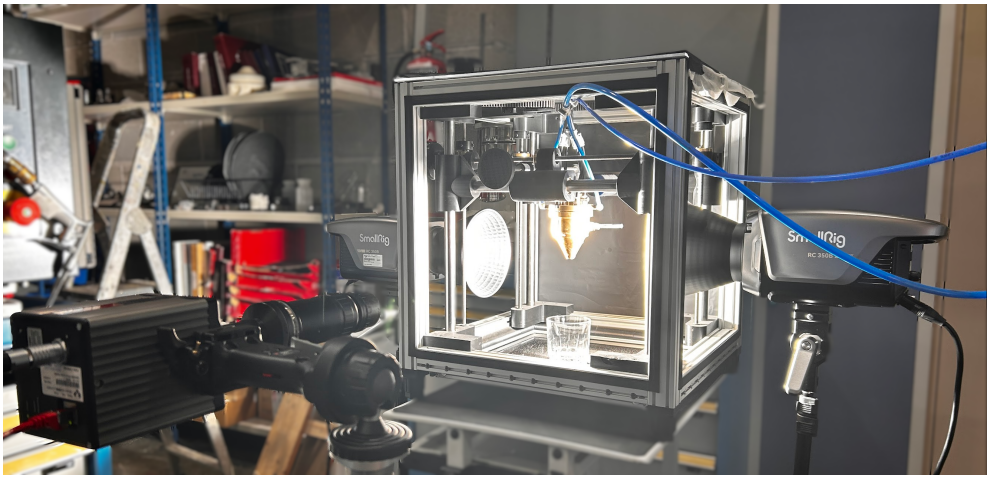

Figure 6.3: Experimental setup for powder flow analysis in the LMD process, see Figure 6.5a.

6.3.1 Experimental Parameters and Levels

The experimental matrix was designed using a Taguchi Orthogonal Array (L9) to systematically investigate the effects of these parameters with a minimal number of runs. The parameters and their corresponding levels used in the Taguchi array are listed below:

Powder Flow (g/min): 1.5, 4.5, 3

Carrier Gas Flow Rate (L/min): 2, 3, 5

Shielding Gas Flow Rate (L/min): 5, 10, 15

The specific combinations of these levels for each experimental run are shown in Table 6.1.

Run	Powder Flow (g/min)	Carrier Gas (L/min)	Shielding Gas (L/min)
1	1.5	2	5
2	1.5	3	10
3	1.5	5	15
4	4.5	2	10
5	4.5	3	15
6	4.5	5	5
7	3	2	15
8	3	3	5
9	3	5	10

Table 6.1: Parameters and levels for the Taguchi Orthogonal Array (L9) used in the experiment.

6.3.1.1 Taguchi Orthogonal Arrays

The choice of the experimental array depends on the balance between cost, time, and required accuracy:

Full Factorial Array: best for high accuracy when cost and time are not constraints.

Taguchi Orthogonal Array: ideal when cost and time are significant factors, but moderate accuracy is sufficient.

Taguchi Non-Orthogonal Array: suitable when experiments are extremely costly or time-consuming, and limited accuracy is acceptable.

The Taguchi method, developed by Dr. Genichi Taguchi, is a statistical approach used for improving product quality and process performance through robust design of experiments. This method leverages orthogonal arrays (OAs) to efficiently investigate the effects of multiple factors on performance characteristics, reducing the number of experimental runs required compared to full factorial designs [35, 89].

Taguchi Orthogonal Arrays are characterized by the following features:

Balanced Design: each level of every parameter is tested an equal number of times, ensuring a balanced design. This balance helps in isolating the effects of each factor on the outcome.

Efficiency: orthogonal arrays require fewer experimental runs than full factorial designs. For example, a full factorial design with three parameters at three levels each would require 27 runs (3^3). In contrast, an L9 orthogonal array requires only 9 runs.

Data obtained from Taguchi experiments can be analyzed using various statistical methods, such as Analysis of Variance (ANOVA) and Signal-to-Noise (S/N) ratios, to determine the most significant factors affecting the process and to optimize the parameter settings [36, 46, 47].

6.3.2 **Powder metering**

The powder is delivered through a disk metering device. The working principle is similar to that of the Metco Twin 150 powder feeder [79], whose operating principle and general construction is reported in Figure 6.4. This type of system employs a rotating powder disk with an annular groove, its cross section determines the maximum flowrate. A spreader unit ensures that the powder does not overfill the groove. An suction unit (outlet) runs on the groove, and the internal pressure of the system pushes the powder through the line. The powder feed rate is proportional to the rotational speed of the powder disk and can be varied to the desired value within the feed range. To discharge any potential static that may build up in the feeder, the hopper is grounded, and a stirrer in the powder prevents arching.

6.3.3 Camera setup

High speed videos were recorded in two different setups. In all the recordings the camera used is an AOS L-PRI, which is rated for 1080p monochrome recordings at 3500 fps; the framerate can be increased by reducing the resolution. The lens uses a c-mount and is a standard 100mm lens, which allowed to cover almost the whole sensor with the field of interest.

6.3.3.1 Illumination from the side

The illumination for the recordings was provided using flicker-free LED lights. The most common configuration in such cases is with two lights at the sides of the nozzle, camera in the front and a black background, as represented in Figure 6.5a. The particle's reflection is captured by the camera, generating white dots. This type of setup is the most common in literature [120, 91, 38].

Using this same setup it is also common to take long exposure pictures, and correlating the luminosity with particle concentration, exemplified by Ostolaza et.al. [92], reported in Figure 6.2a.

With this setup the light reflecting on the particles is captured by the camera, generating white dots. The particle position can be determined with good accuracy, as shown in Figure 6.5c. There are however two issues that make this method less desirable for the present study:

- The exposure time had to be around 90 μs end the particles, moving at a relatively high velocity, are seen on the captured images as short streaks instead of well-defined dots.
- The image captured by the camera is the intense light reflecting off the particle. The irregular surface and shape generate unpredictable reflections, which do not depend only on the size, and can produce glare, saturating the sensor.

6.3.3.2 Illumination from the back

The experience accumulated when developing the method described in Section 5.4 is translated here. The illumination of the stream of particles comes from behind, as shown in the schematic of Figure 6.5b. The strong LED spotlight was fitted with a simple diffuser, which generates a relatively uniform white background.

In this setup the particles appear as dark spots against the white background, as exemplified by Figure 6.5d. The size of the spot does not depend on the particle's reflectivity anymore, but only on the projected shadow. The image is not saturated anywhere and, by carefully selecting the exposure, it uses the whole dynamic range of the sensor.

- With the posterior illumination, it was possible to reduce the exposure time to 16 μs, which eliminated the streaks deriving from the particle's movement.
- Cropping the image recorded by the sensor at a resolution of 844×1304 px, the high-speed video was recorded at 4490 fps, corresponding to a frame time of 0.2227 ms/frame.

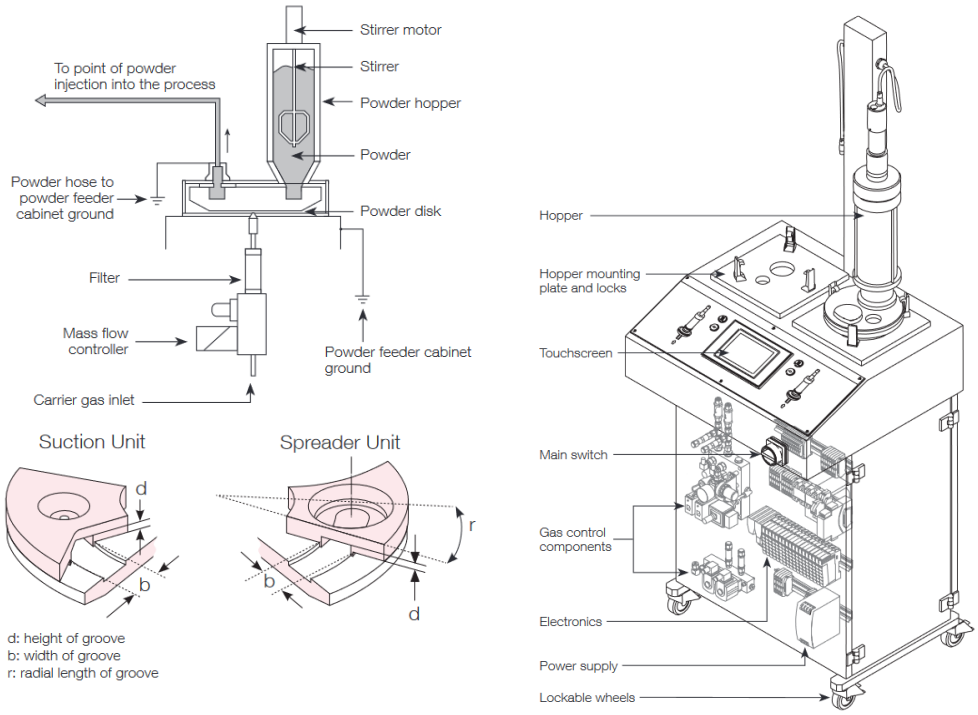

Figure 6.4: Operation principle of the disk powder feeder, and the Teflon components sliding on the disk. General construction of the Metco 150 powder feeder [79].

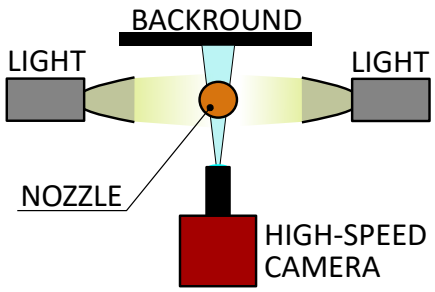

(a) Side illumination setup

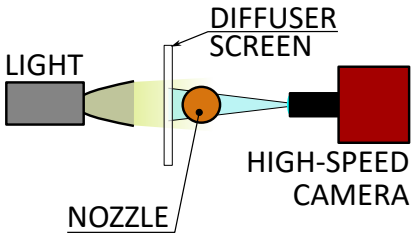

(b) Back illumination setup

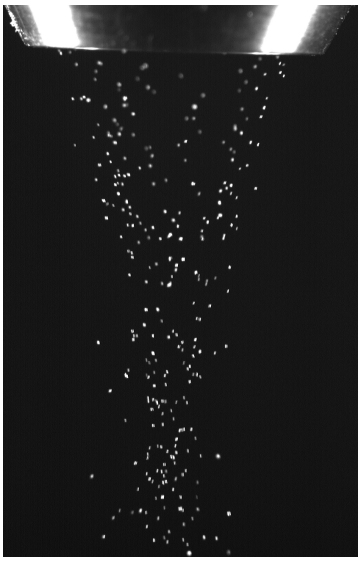

(c) Side illumination result: 3530 fps, 3× gain, 90 μs exposure

(d) Back illumination result: 4490 fps, 3× gain, 16 μs exposure

Figure 6.5: Setup and raw result of the two camera configurations used in the UPV experiment.

6.3.4 **Particle Tracking**

The particles were tracked with the approach described in Section 5.5, using in the image processing software Fiji/ImageJ [107].

The videos recorded by the AOS camera were saved as `*.mp4` compressed videos, requiring the use of the additional FFMPEG library.

The sequence of images was then pre-processed using a script, which performs:

Calibration: sets the properties of the image stack based on the framerate and dimensions of the video.

Pre-processing: the stack is converted to an 8-bit format, and a Z-projection (median) is computed to create a background image. This background is subtracted from the original stack to enhance the visibility of particles.

Thresholding: the resulting image stack is converted to a binary mask.

The TrackMate plugin was used once again [124], with the code developed and reported in Section 5.5.1. This allowed to track the rapid particle flow, as well as determining relevant metrics on the particle characteristics. The tracked flow is exemplified in Figure 6.6, which reports the same conditions, but with only the tracks 10 frames backwards in time, and all the recorded tracks fading over time.

Each recording was approximately 0.07 s long, containing around 5 000 tracks, 100 000 edges, 125 000 spots (depending on the flowrate). Thanks to the good image quality, virtually all particles were recognized and tracked. The particle tracking data is loaded into Matlab, allowing the post-processing of the recordings.

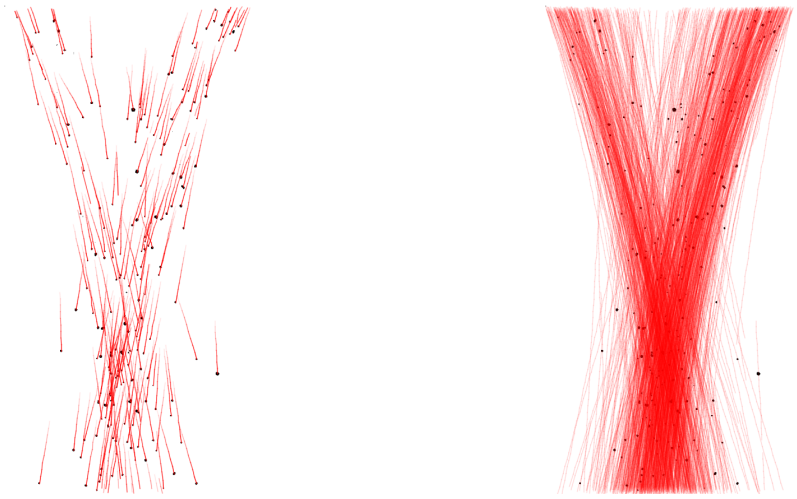

(a) (b)

Figure 6.6: Particle Tracking results. (a) Tracks representing 10 timesteps backward in time. (b) All full-length recorded tracks.

6.4 Results of the Continuous Coaxial Nozzle Experimental Study

The information coming from the Particle Tracking is analyzed, with the primary objective to observe the irregularity in the mass flowrate. This discussion is based on the results of the condition number 5 of Table 6.1, since it is closest to the usual process conditions used in the machine:

Powder Flow: 4.5 g/min

Carrier Gas Flow Rate: 3 L/min

Shielding Gas Flow Rate: 15 L/min

Ferreira et al. analyzed gas and powder streams using optical methods, such as laser sheets, to visualize the flow characteristics [34]. In contrast, the current study does not require laser sheets, as particle tracking provides a more granular and dynamic understanding by tracking individual particles. This approach allows for a more precise analysis of particle behavior and distribution, enhancing the overall understanding of the LMD process.

6.4.1 Particle Size Distribution

By using the backside illumination, the particles can actually be observed without much glare. It must be noted that the lens is not telecentric and, as discussed in Section 5.4.2, a telecentric lens would be the ideal solution in this case.

Small artifacts are barely noticeable towards the lower end of the distribution. The smallest particles are affected by the relatively large pixel size (around 15 μm), but the overall effect can be neglected in this case. This would be more of a concern for finer powders, requiring higher magnification and/or image resolution.

Figure 6.7 presents the PSD of the experimental observation. The Rosin-Rammler fit is also reported for further use. It must be noted that this distribution is normalized to the number of particles, as opposed to the mass: the script used is able to provide both, which is useful in different cases. The PSD is very similar to the one obtained in Section 5.6, and is in line with the expected.

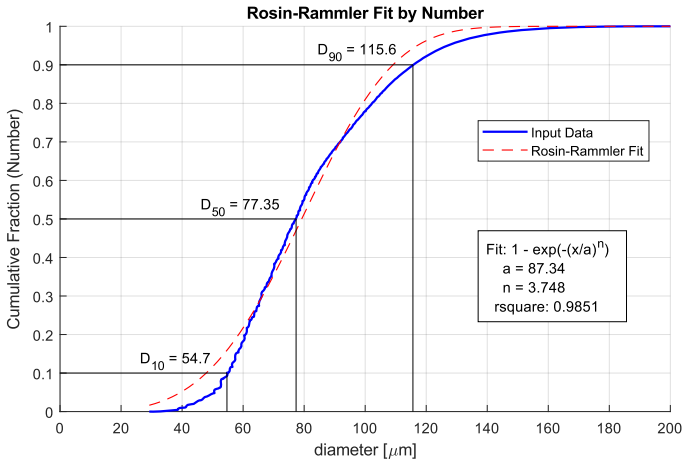

Figure 6.7: Particle Size Distribution (PSD) measured by the Particle Tracking (PT) algorithm in the nozzle experiments.

6.4.2 Particle locations and Standoff distance

In Laser Metal Deposition (LMD), the standoff distance is the ideal distance between the nozzle and the workpiece. This distance is critical as it significantly impacts the efficiency and quality of the deposition process. An optimal standoff

distance ensures that the powder particles are delivered precisely to the melt pool, leading to uniform layer deposition and minimal material waste. Conversely, an incorrect standoff distance can result in poor deposition quality, irregular layer thickness, and increased porosity.

The determination of the standoff distance involves analyzing the powder stream's spatial distribution as it exits the nozzle. Typically, the standoff distance is defined as the average distance from the nozzle exit where the powder particles are most concentrated. This concentration is usually measured as the minimum width of the stream that contains a significant percentage (commonly 90%) of the particles. Accurate determination of this distance is essential for process optimization and achieving high-quality builds.

Understanding the spatial distribution of particles is crucial for optimizing the Laser Metal Deposition (LMD) process. Figure 6.8 presents a side view of the particle distribution analysis, cumulative over the recorded time. The percentiles of the particle distribution are highlighted and analyzed to determine the standoff distance. This distance is critical for understanding the deposition process, representing the average distance from the nozzle exit where the particles are most concentrated. The standoff distance is identified as the minimum width of the stream that contains 90% of the particles, which is determined to be 16 mm from the nozzle exit.

The heatmap represents what would be seen using a long exposure image, similar to the method employed by [92], as shown in Figure 6.2a. However, the heatmap presented here offers a more rigorous representation because it is normalized as a Probability Density Function (PDF). Darker colors indicate regions with a higher particle density, providing a clearer visualization of particle distribution. The two horizontal lines denote a 1 mm thick slice around the standoff distance, highlighting the area of highest particle concentration.

Figure 6.9 presents the Probability Density Function (PDF) of the particle distribution across the horizontal ruler at the standoff distance of 16 mm from the nozzle exit. This histogram provides significant insights into the spatial distribution and concentration of particles within the deposition area. The red lines indicate the 50th percentile (median) at ± 1.28 mm, representing the central concentration of particles. The blue lines indicate the 90th percentile at ± 3.16 mm,

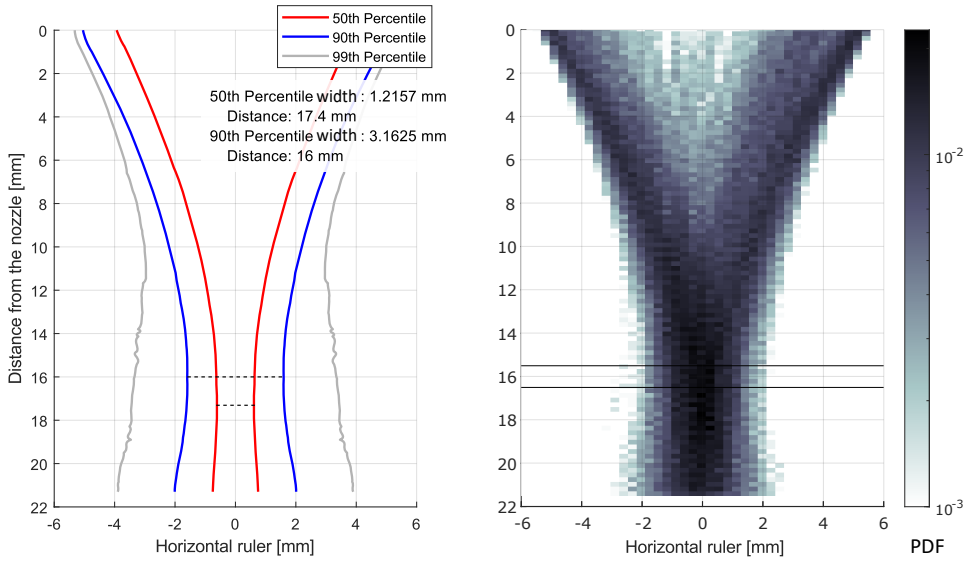

Figure 6.8: Side view of the particle distribution analysis, averaged over time. Percentiles of the distribution are highlighted and analyzed to find the standoff distance. The probability density of the particle distribution is shown, with darker colors indicating higher particle density. The horizontal lines denote a 1 mm thick slice around the standoff distance (Case 5 in Table 6.1).

illustrating the region that contains the majority of particles (90%). The gray lines indicate the 99th percentile at ±6.64 mm, highlighting the outer limits of particle dispersion.

The stream width is the distance encompassing 90% of the particle distribution (between the blue lines in Figure 6.9), and it directly influences the width of the material deposition trace. In this study, the spot diameter at the standoff distance is found to be 3.16 mm. The shape of this distribution might be expected to match the shape of the deposited trace, but the effect of the surface tension of the molten pool is definitely relevant, flattening the resulting trace. The width of the melt pool itself should match the width of the stream, directly affecting particle catchment. Knowing the exact distribution across the width of teh stream, it is possible to make an informed decision over the amount of powder catchment to accept.

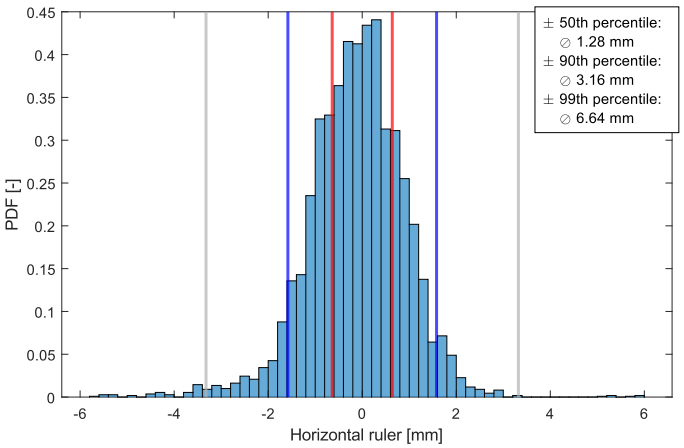

Figure 6.9: Probability Density Function (PDF) of the particle distribution across the horizontal ruler at the standoff distance of 16 mm from the nozzle exit. The red lines indicate the 50th percentile, the blue lines indicate the 90th percentile, and the gray lines indicate the 99th percentile. These figures are of Case 5 in Table 6.1.

6.4.3 **Particle Velocities**

The particle velocities can be determined in several ways. In this case, we consider a 1 mm thick slice around the standoff distance estimated in Figure 6.8. In this interval and over the whole recording time, the average velocity is $\overline{v} = 1.896$ m/s, with a standard deviation of $\sigma_v = 0.237$ m/s. From Figure 6.10, it is also evident that the velocity is fairly uniform over time.

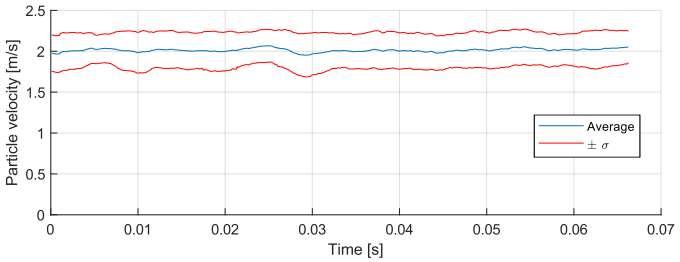

Figure 6.10: Particle velocity over time, averaged in a 1 mm thick slice around the standoff distance 16 mm from the nozzle (Case 5 in Table 6.1).

There is notable acceleration when particles exit the nozzle, and this is evident when selecting different locations along the stream. Figure 6.11 shows the median particle velocities along the stream, and it is evident that they accelerate along

the stream. Through a heatmap and the percentiles, the diagram also shows the distribution of the velocities.

The acceleration, given two velocities (v_1 and v_2) and two positions (z_1 and z_2), assuming constant acceleration, can be calculated using the kinematic equations:

$$\begin{aligned} v_2 &= v_1 + at \\ \Delta z &= v_1 t + \frac{1}{2} a t^2 \end{aligned} \tag{6.1}$$

where:

- v_2 is the final velocity,
- v_1 is the initial velocity,
- a is the acceleration,
- $\Delta z = z_2 - z_1$ is the displacement,
- t is the time.

The third kinematic equation relates these quantities without involving time directly:

$$v_2^2 = v_1^2 + 2a(z_2 - z_1) \tag{6.2}$$

Rearranging Equation 6.2 for acceleration (a):

$$a = \frac{v_2^2 - v_1^2}{2(z_2 - z_1)} \tag{6.3}$$

This results in the graph of Figure 6.12, and the average value between the nozzle exit and a distance of $\Delta D = 20$ mm is $\overline{a} = 67.65$ m/s^2.This high acceleration value is only partially explained by the gravitational effect. The gas jet at the nozzle exit continues to expand and pushes the particles, which are now unburdened by impacts with the internal walls.

6.4.4 **Mass Flowrate Estimation**

Accurate estimation of the mass flowrate is essential for calibrating and optimizing the Laser Metal Deposition (LMD) process. This estimation ensures consistent material deposition, which directly impacts the quality and reliability of the final

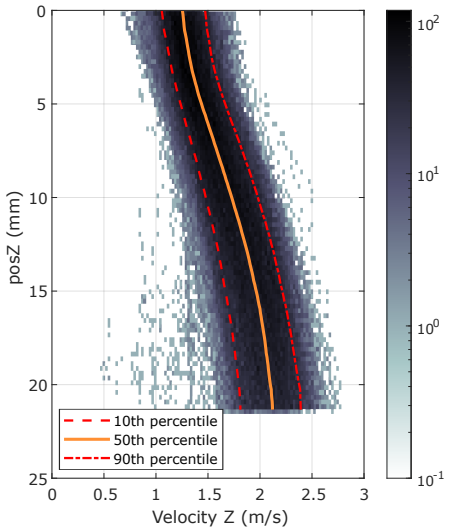

Figure 6.11

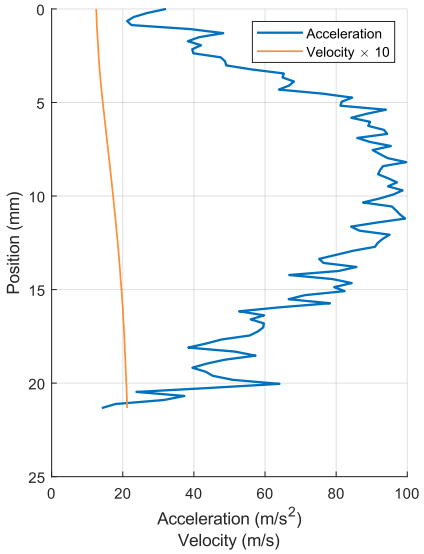

Figure 6.12

Figure 6.13: (a) Particle vertical velocities along the stream, with percentiles. (b) Median acceleration.

product. In this study, the mass flowrate is estimated by calculating the product of particle mass and velocity within a 1 mm slice around the standoff distance. This slice was chosen as it provides a representative sample of the particle flow at the critical standoff distance.

The average flowrate is found to be highly accurate, significantly surpassing the precision of traditional metering devices, which were calibrated by measuring the total mass of delivered powder over time using a scale and a container. At each discrete frame k, the mass flowrate $\dot{m}_k$ is calculated using the following formula:

$$\dot{m}_k = \sum_{i=1}^{N} \frac{m_i \cdot v_i}{\Delta z} \tag{6.4}$$

where m_i is the mass of particle i, v_i is the velocity of particle i, and Δz is the slice thickness converted to meters.

To smooth the mass flowrate data over time, a moving average filter is applied. The smoothed mass flowrate $\dot{m}_{\text{smoothed}}$ is then calculated as:

$$\dot{m}_{\text{smoothed}} = \frac{1}{w} \sum_{j=0}^{w-1} \dot{m}_{k-j} \tag{6.5}$$

where w is the window size in points and $\dot{m}_{k-j}$ are the mass flowrate values within the window.

The average mass flowrate $\overline{\dot{m}}$ and the root mean square (RMS) deviation $\sigma_{\dot{m}}$ are given by:

$$\overline{\dot{m}} = \frac{1}{T} \sum_{k=1}^{T} \dot{m}_k \tag{6.6}$$

$$\sigma_{\dot{m}} = \sqrt{\frac{1}{T} \sum_{k=1}^{T} (\dot{m}_k - \overline{\dot{m}})^2} \tag{6.7}$$

where T is the total number of time points. The average mass flowrate over the entire recording period is found to be 3.906 g/min, demonstrating the method's precision and reliability.

6.4.5 **Flow irregularities**

Flow irregularity is an important aspect to consider as it affects the consistency and quality of the material deposition in the LMD process. The mass flowrate over time is also discussed in Section 5.6.3, for the pneumatic conveying in a thin pipe.

The mass flowrate of the powder exiting the nozzle is recorded and presented in Figure 6.14. The value is plotted over time, using a moving average window of 2 ms. The flow irregularity over time is 16%, similar to the results in 5.6.3, with the same averaging time window.

The average value of the mass flowrate is substantially higher than the expected, but the procedure used to measure it is robust. The higher value is recorded in a brief time, and it is possibly caused by the dislodging of accumulated powder in the delivery system. This result presents an interesting improvement opportunity: the presented method can be implemented in a fast and reliable measurement system, with substantial improvement in the process. Further discussion is presented in Section 7.2.

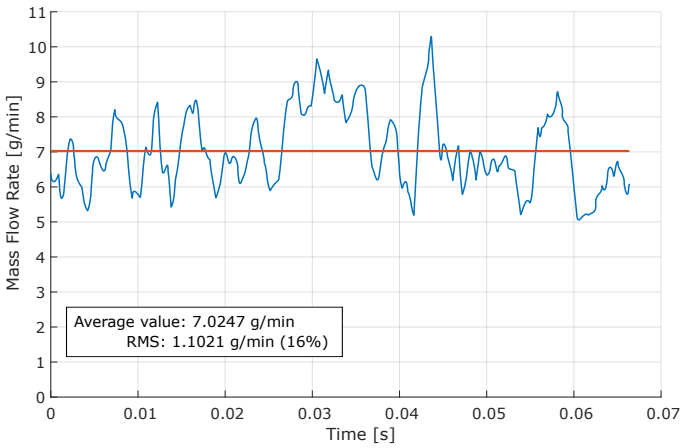

Figure 6.14: Mass flow rate over time. Case 5 in Table 6.1.

The flow irregularities are calculated to better understand the dynamic behavior of the mass flowrate. The RMS deviation provides a measure of the variability in the flowrate, which is critical for process optimization. By identifying and understanding these irregularities, adjustments can be made to the LMD process to minimize their impact, thereby enhancing the overall efficiency and quality of the deposition process.

6.4.5.1 **Effect of the printing speed**

Flowrate irregularities introduce a level of noise to the average mass flowrate, which diminishes when considering large quantities of powder or extended time periods. During machine calibration, the standard method involves measuring the mass of powder delivered by the nozzle over a set duration, typically several seconds to a minute, as documented by Tabernero et al. [120] and illustrated in Figure 6.15.

Higher print rates and detailed printing are more susceptible to flowrate irregularities. A smaller melt pool is more sensitive to rapid flow oscillations due to its limited size. The control system maintains the linear velocity of the print relatively constant along the trajectory. Variations in printing speeds are often employed to compensate for accumulated errors in deposited thickness across multiple layers [103].

By adjusting the moving average window of the recorded flow, we can observe

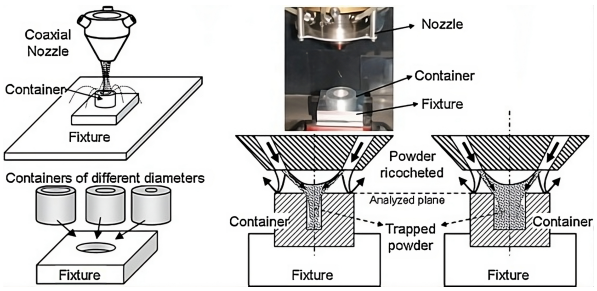

Figure 6.15: Measurement of the mass flowrate using cups of different diameters [120].

that the intensity of flow irregularity (RMS %) increases with a smaller window, which corresponds to faster printing speeds, down to 1 ms. This relationship is depicted in Figure 6.16.

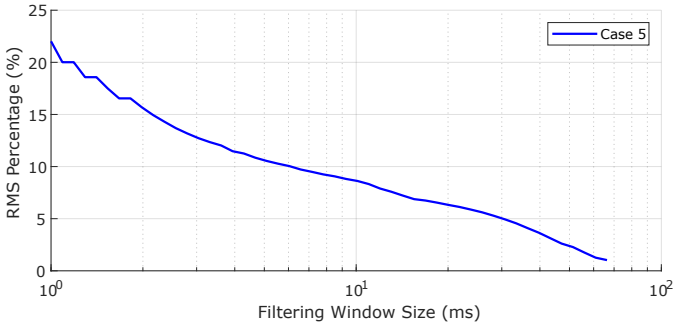

Figure 6.16: RMS percentage of flow irregularity across different moving average window sizes. Case 5 in Table 6.1.

6.4.6 **Taguchi analysis**

A comprehensive Taguchi analysis is essential for gaining a better understanding of the effects of various process parameters. Future work should focus on establishing a standardized framework and procedures that companies can adopt to calibrate these parameters effectively. By systematically varying these parameters through the Taguchi method, deeper insights can be obtained into their impact on mass flowrate, particle distribution, and overall process efficiency.

Table 6.2 presents the stream size and standoff distance (in mm) for each case in the UPV experiment. The values consider the minimum of either the 50th or 90th percentile of the distribution from the nozzle, as shown in Figure 6.8. The

case numbers reference the parameters in Table 6.1.

Additionally, Table 6.3 shows the mass flowrate and particle velocity parameters for each case in the UPV experiment, calculated in Section 6.4.4. The case numbers reference the parameters in Table 6.1.

Furthermore, exploring other Design of Experiments (DOE) methods may be appropriate and could potentially offer more efficient optimization procedures. These methods can help in identifying the most influential factors and their optimal settings more quickly and accurately. Implementing these optimization procedures will enable companies to fine-tune their Laser Metal Deposition (LMD) processes, ensuring consistent, high-quality production outcomes and enhancing overall process reliability.

Case	Width_50	Standoff_50	Width_90	Standoff_90
1	1.06	15.8	2.76	14.7
2	1.06	13.8	2.80	12.9
3	1.06	12.3	2.96	12.0
4	1.04	15.0	2.66	13.8
5	1.22	17.4	3.16	16.0
6	1.27	16.8	3.27	15.3
7	1.28	18.9	3.22	18.0
8	1.24	14.1	3.11	13.6
9	1.21	14.4	3.25	12.6

Table 6.2: Stream size and standoff distance (in mm) for each case in the UPV experiment, considering the minimum of either the 50th or 90th percentile of the distribution from the nozzle, as shown in Figure 6.8. The case numbers reference the parameters in Table 6.1.

6.5 Simulaiton of the Continuous Coaxial Nozzle

6.5.1 Geometry and Mesh Generation

The fluid domain of the continuous nozzle used in the simulation is provided by the UPV, who have manufactured the nozzle used in the work reported in Section 6.3. The nozzle geometry, as shown in Figure 6.17a, is sectioned to provide a clear view of its internal structure.

The space between the internal cone and external walls constitutes the channel through which the powder flows. The distributor, formed by a series of vertical channels, is visible in the middle of the figure. Its role is to distribute the powder

Case	Mass flowrate [g/min]		Velocity [m/s]	
	avg	RMS	avg	stdev
1	2.591	0.5867 (22.64%)	1.457	0.1187 (8.15%)
2	1.653	0.4315 (26.11%)	1.513	0.1373 (9.08%)
3	1.748	0.3403 (19.47%)	2.011	0.2241 (11.14%)
4	4.552	0.7211 (15.84%)	1.468	0.1435 (9.78%)
5	7.025	1.1021 (15.69%)	2.013	0.2194 (10.90%)
6	7.442	1.0651 (14.31%)	2.022	0.2220 (10.98%)
7	3.646	0.7975 (21.87%)	2.032	0.2143 (10.55%)
8	6.410	1.0765 (16.79%)	1.615	0.1551 (9.60%)
9	5.849	1.1439 (19.56%)	2.134	0.2314 (10.84%)

Table 6.3: Mass flowrate and particle velocity parameters for each case in the UPV experiment, as calculated in Section 6.4.4. The case numbers reference the parameters in Table 6.1.

and eliminate the twirling motion around the axis. The high-power laser used to melt the material passes through the central channel, which is protected by a continuous stream of shielding gas (Argon). The focusing lens of the laser is fixed at the top of the channel.

Creating the computational mesh for the nozzle simulation involved using the polyhedral meshing model in Simcenter STAR-CCM+. Polyhedral meshes offer a balanced solution for complex mesh generation problems, providing efficiency and ease of construction with fewer cells compared to tetrahedral meshes.

The mesh must balance detail and computational efficiency, ensuring that critical regions, such as the nozzle exit, are sufficiently refined to capture important flow characteristics. Using the provided geometry of the fluid domain, the mesh was generated using the advanced tools in STAR-CCM+. Gradual refinement levels were defined in the critical regions:

- in the small distributor channels;
- in the small space between the cone walls;
- at the exit of the nozzle, where the flow transitions from a constrained to an open domain.

Figure 6.18a provides an overview of the simulated nozzle's mesh, while Figure 6.18b offers a detailed view of the refined mesh at the nozzle exit.

The volume of the cells, in principle, cannot be smaller than the largest Lagrangian particles. This is to avoid situations where one particle center resides in a small cell, causing the volume of solid to be greater than the cell volume, result-

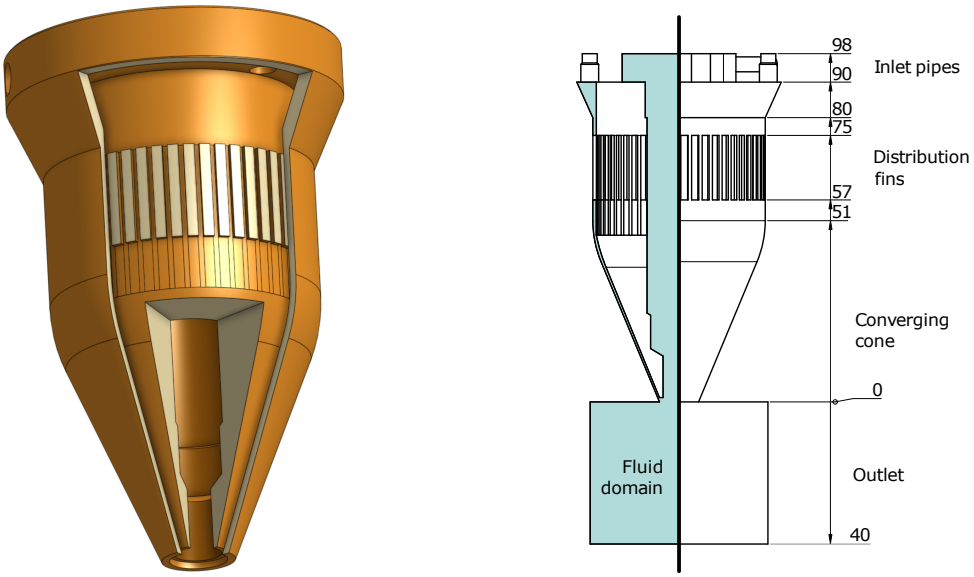

(a) (b)

Figure 6.17: (a) Sectioned view of the geometry of the simulated nozzle. (b) Annotated draft with partial section of the fluid domain geometry.

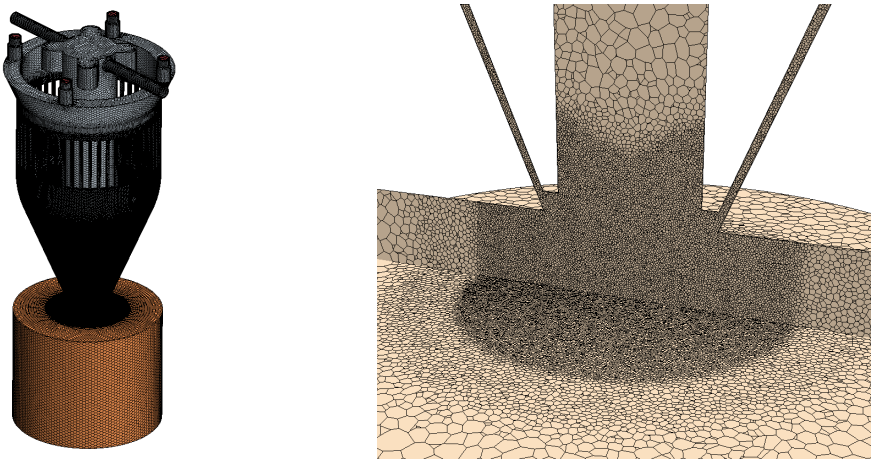

(a) (b)

Figure 6.18: (a) Overview of the simulated nozzle's mesh. (b) Detailed view of the refined mesh at the nozzle exit.

ing in a numerical error. STAR-CCM+, the software used in these simulations, has smoothing features that allow for particles larger than the mesh size, but the level of refinement achieved was sufficient to correctly represent the fluid flow without necessarily resorting to more advanced features. For this same reason, the mesh does not present refinement layers at the wall boundaries.

To maximize the level of detail for the constrained cell volume, the mesh uses polyhedral elements. The advanced element formulation goes beyond what is possible with tetrahedral elements in terms of adaptability, and its convex angles avoid issues arising from highly distorted tetrahedral elements, where small angles introduce approximation errors. Even with the added computational cost due to the more complex element formulation, polyhedral meshes reach convergence faster and with fewer cells than tetrahedral elements, or even hexahedral mesh elements in some cases. According to Thomas et al. (2022), the polyhedral mesh is an excellent alternative to the highly regarded hexahedral mesh style for predicting upper airway aerosol transport and deposition [123].

The computational mesh for the continuous nozzle simulation consists of a total of 4 102 881 cells, with 4 085 818 being polyhedral cells, alongside a small number of tetrahedral, hexahedral, wedge, and pyramid cells, necessary to adapt to the geometry. The checks indicate that all face validity metrics are perfect, ensuring a high-quality mesh. The containing prism for the mesh is $57.5 \times 57.5 \times 138$ mm in the x, y, and z directions respectively, with the origin placed exactly at the center of the nozzle's bottom face. The volume of the cells ranges from 1.09×10^{-14} m^3 to 3.50×10^{-9} m^3. For comparison, a spherical particle with a diameter of 100 μm (or 1.00×10^{-4} m) has a slightly smaller volume of approximately 5.24×10^{-15} m^3.

6.5.2 **Simulation Setup**

The simulation employs a coupled CFD-DEM (Computational Fluid Dynamics - Discrete Element Method) model, thoroughly described in Chapter 2. In this chapter, the CFD-DEM coupled simulation is performed using Star-CCM+, which implements enhanced stability features and advanced meshing capabilities, which are particularly advantageous for simulating the intricate nozzle geometries and flow dynamics inherent in the LMD process. Despite the change in software, the

fundamental CFD-DEM coupling approach remains consistent with Chapter 5, ensuring comparability of results and methodologies.

The Lagrangian Multiphase Model in Star-CCM+ tracks the discrete phase particles across the domain. By also selecting DEM module, the latter handles the interactions between particles, applying the contact models discussed in Section 2.1.3 as opposed to binary impacts only. This advanced treatment allowed the inclusion of a custom implementation of the JKR contact model, reported in Appendix B. The coupling between the particles and the flow is accounted for using the Schiller-Naumann drag model, along with the Sommerfeld particle lift model [112]. The volume source smoothing method is employed in the coupling to ensure numerical stability, with the Cell Cluster method and a cluster length of 350 µm being used. This length provides an optimal balance between smoothing the source terms and maintaining the accuracy of local interactions, given the particle size distribution between 40 and 180 µm. Gravity is included in the simulation, significantly influencing the powder distribution and deposition process.

It must be noted that the software StarCCM identifies as "two-way coupling" the solver modeling the exchange of momentum (and other properties) between the Eulerian and Lagrangian frame. This must not be confused with the definition given in Section 2.3, according to which the simulation here presented would effectively be a four-way coupled simulation.

Two species are considered in the simulation: environmental air present in the outlet and the overall domain, and Argon introduced through the inlets. The Multi-Component Gas model is utilized to account for the interactions between these gases, ensuring a realistic representation of the gas dynamics.

The k-Omega SST model is used to capture the turbulence effects within the nozzle and surrounding domain. Ostolaza et al. validated experimentally that this model is the most appropriate for this kind of simulation [92]. These models are chosen for their accuracy in predicting flow separation and reattachment, which are critical for the complex flow patterns observed in the nozzle. Additionally, an All y+ Wall Treatment is used to model the near-wall regions accurately, which is crucial given the high-speed flows and small geometries involved. The Reynolds-Averaged Navier-Stokes (RANS) equations are solved using the PISO Unsteady

method.

The domain is first initialized as a steady state without the particles, focusing solely on the two gases. This steady-state initialization ensures that the gas flow field reaches a stable condition before introducing the discrete particles. After achieving a steady state, the simulation transitions to the PISO stepping method, incorporating the particles into the flow field for a detailed time-dependent analysis.

Two species are considered in the simulation: environmental air present in the outlet and the overall domain, and Argon introduced through the inlets. The Multi-Component Gas model is utilized to account for the interactions between these gases, ensuring a realistic representation of the gas dynamics. The domain is initialized with environmental air, and the inlets are set with Argon at the specified flow rates. The two species can then mix, with the model able to determine the air concentration using the Schmidt Number, which is important to assess the oxygen contamination of the melt pool. The combined gas properties are determined using a mass-weighted mixture model. For the two gases, the properties are for the standard conditions of temperature (20°C) and pressure (1 atm). The properties are as follows:

- **Argon:** Density 1.63388 kg/m^3, Viscosity 2.27682×10^{-5} Pa $\cdot$ s, Molecular Weight 39.948 kg/kmol.
- **Air:** Density 1.18415 kg/m^3, Viscosity 1.85508×10^{-5} Pa $\cdot$ s, Molecular Weight 28.9664 kg/kmol.

The time-stepping method used in the simulation involves a primary timestep of 10^{-4} s, with the Lagrangian solver automatically performing up to 10^3 substeps to maintain the local Courant number below $Co \leq 0.35$. Contacts are resolved by the DEM solver, with the timestep being a fraction (1/5) of the Rayleigh time, as discussed in Section 2.1.1. Solver settings include the SIMPLE scheme for pressure-velocity coupling and second-order upwind discretization for momentum, turbulence, and species equations. Relaxation factors are set to standard values to ensure stable convergence.

The simulation is executed on a workstation utilizing 14 cores, with each timestep requiring approximately 40 s. Given that the total physical simulation time is about 2 s, the total computation time amounts to over 220 hours.

6.5.3 **Boundary Conditions**

The conditions used in the simulation are based on condition number 5 of the Taguchi array presented in Table 6.1. As the gas exits the nozzle, it flows into the bottom cylindrical domain, whose boundaries are set as a pressure outlet. This ensures the condition of free external flow in atmospheric conditions, with the standard atmospheric pressure of 1 atm = 101 325 Pa as a reference. The flow on the boundary is not prevented from reversing; if backflow occurs, it is managed using the environmental backflow pressure setting, which subtracts the dynamic head at the boundary to discourage backflow. The backflow direction is controlled using the boundary-normal method, assuming that any incoming flow enters the simulation along a vector orthogonal to the boundary surface in the specified reference frame. This configuration helps to accurately represent the realistic environmental conditions into which the fluid exits the nozzle, ensuring that the boundary conditions do not artificially constrain the flow and allowing for the possibility of recirculation if it occurs naturally in the simulation.

The walls of the domain have a no-slip boundary condition, ensuring that the velocity of the fluid at the walls is zero relative to the wall. Additionally, the k-Omega SST model is used for turbulence modeling near the walls.

A velocity inlet is specified for the lens shielding gas, which enters the domain through two pipes at the top, as seen in Figure 6.18a. The same velocity is applied to both pipes, calculated by dividing the volumetric flow rate of 15 L/min over the two 4.2 mm diameter pipes. The volumetric flow rate is converted to a velocity using the cross-sectional area of the pipes. This ensures a consistent and controlled inflow of shielding gas, protecting the lens and maintaining the integrity of the laser operation.

The pneumatic conveying inlets, also located at the top of the same figure, are velocity inlets. The powder is injected uniformly from the top surface using a ”Random Injection” method, with a velocity matching the inlet velocity. The gas flow rate of 3 L/min is divided over the area of the four 4.2 mm diameter pipes. The powder injector operates with a constant mass flow rate of 4.5 g/min, matching the particle diameters determined experimentally using the Rosin-Rammler distribution shown in Figure 6.7.

6.6 Results of the Continuous Coaxial Nozzle Computational Study

6.6.1 Particle Locations and Standoff Distance

The simulation results provide detailed insights into the spatial distribution of particles and their behavior as they exit the nozzle. Figure 6.19 presents a side view of the particle distribution analysis, averaged over the simulation time. The percentiles of the particle distribution are highlighted and analyzed to determine the standoff distance. This distance represents the average distance from the nozzle exit where the particles are most concentrated. As in 6.4.2, the standoff distance is identified as the minimum diameter that contains 90% of the particles, which is determined to be 10.2 mm from the nozzle exit. This distance is notably lower than the experimental one, and the reason is linked to the lower particle velocity calculated through the simulation, discussed in 6.4.3. At lower velocities, the particle paths cross closer to the nozzle.

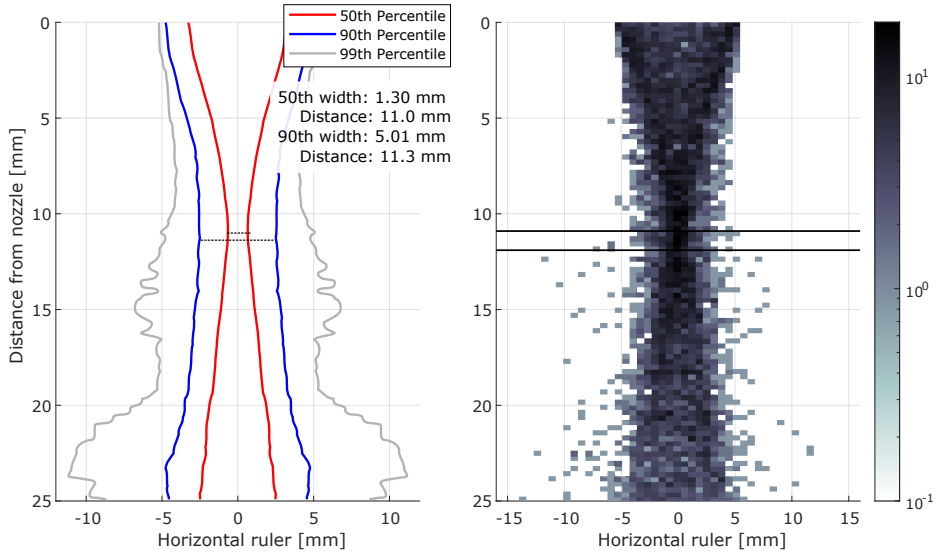

Figure 6.19: Side view of the particle distribution analysis from the simulation, averaged over time. Percentiles of the distribution are highlighted and analyzed to find the standoff distance. The probability density of the particle distribution is shown, with darker colors indicating higher particle density. The horizontal lines denote a 1 mm thick slice around the standoff distance.

The spatial distribution of particles at the standoff distance is represented in Figure 6.20. This histogram illustrates the spatial distribution and concentration of particles within the deposition area. The red lines indicate the 50th percentile (median), highlighting the central concentration of particles. The blue lines indicate the 90th percentile, which is considered the spot width. The gray lines indicate the 99th percentile, delineating the outer limits of particle dispersion. By using the simulation data, it is possible to compare the spot width determined here with what is visible through the experimental setup, as discussed in Section 6.4.2.

6.6.1.1 **Geometrical consideration on the stream width**

Due to the geometrical projection of the particle positions, the width of the distribution changes significantly when using the radial distance versus the linear distance of the particles from the nozzle's axis. The linear distance is actually easier to observe, as shown in Section 6.4, requiring only one point of view. The stream width is also more relevant since the trace deposition progresses in one direction. For these reasons, the suggested metric is the stream width rather than the diameter, as it can be easily observed by tracking particles only from one point of view. The histogram in Figure 6.20 shows both the distribution considering the radial distance (made symmetric by conserving the x-position sign) and the linear distribution, using only the X coordinate.

6.6.2 **Particle Velocity within the Nozzle**

The inlet pipes at the top of the nozzle are quite short, which means the velocity direction remains similar to the injection condition. Particles quickly encounter the first conical wall, causing the large scattering seen in Figure 6.21. In this section, particles redistribute and flow through the distribution fins. Within the converging nozzle, the velocity vectors align. Most acceleration occurs at and after the exit. Consequently, particle velocities within the nozzle are relatively low and uniform but are significantly affected by the large gradient in gas velocity at the nozzle exit.

The simulation provides velocity information for all particles, both within and outside the nozzle, accumulated over 0.2 seconds.

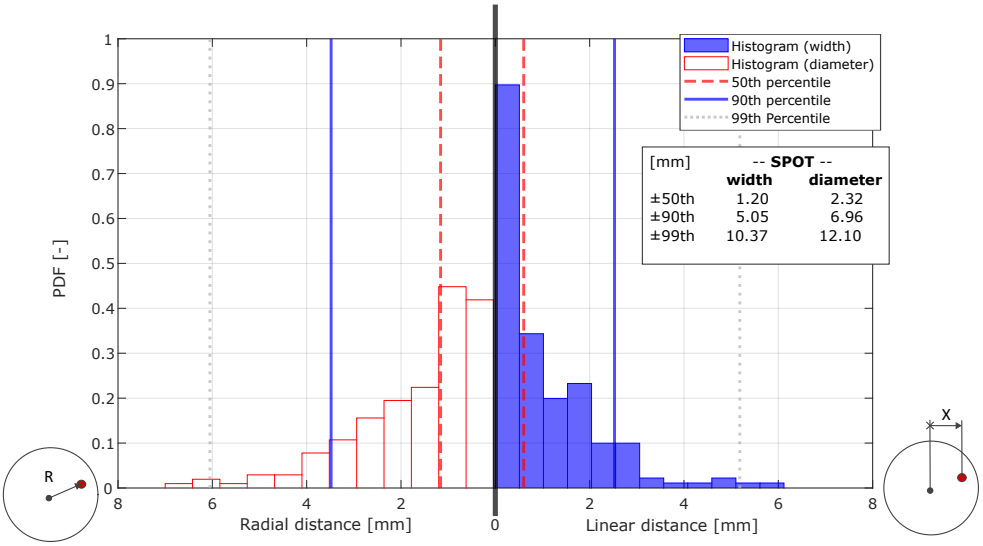

Figure 6.20: Probability Density Function (PDF) of the particle distribution across the horizontal ruler at the standoff distance of 16 mm from the nozzle exit. The red dashed lines indicate the 50th percentile, the blue solid lines indicate the 90th percentile, and the gray dotted lines indicate the 99th percentile.

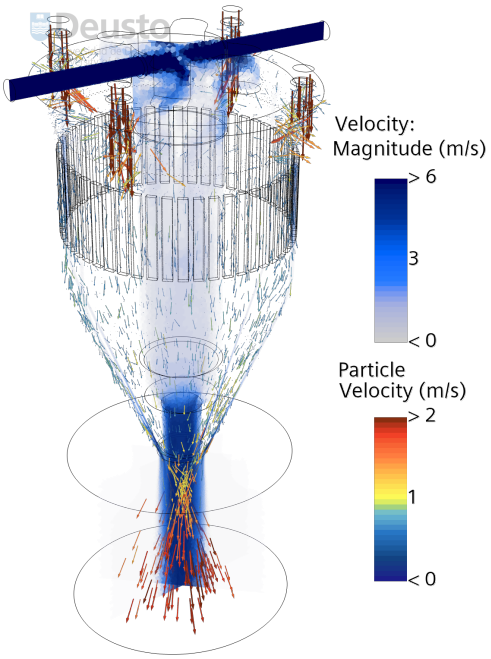

Figure 6.21: Particle velocity vectors and fluid velocity in the nozzle simulation.

Figure 6.22a shows the analysis of particle velocities in the vertical direction along the Z axis within the nozzle. The heatmap also shows the number of particles along the nozzle's height. At the top, a large velocity dispersion is visible due to rebounds, but it remains fairly narrow along the entire nozzle.

6.6.2.1 **Acceleration**

Analysis of the acceleration in Figure 6.22b reveals some interesting patterns. The most notable acceleration zone is just around the nozzle, where the gas is compressed into a thinner section and must accelerate due to the Bernoulli effect. This results in a large acceleration, up to about 52.8 m/s^2. This value closely matches the value determined experimentaly in Section 6.4.3, validating the simulation and confirming that the drag model used is adequate to represent this phenomenon. Nonetheless, this preliminary result opens the way to further investigation on the calibration of the drag coefficient using this technique.

Despite many rebounds at the top, the median acceleration tends to cancel out.

A large acceleration peak is visible at $z = -70$ mm, near the entrance of the distribution fins. This acceleration indicates an energy exchange from the accelerating fluid to the particles. This acquired velocity is then lost at the exit of the channels within the fins, as indicated by the large negative peak in the acceleration diagram.

6.6.3 **Powder Mass Flowrate**

Similarly to Section 6.4.4, the mass flowrate at each timestep is evaluated by the sum of the particles' mass multiplied by the respective vertical velocity. In this case, this is done directly in the software, and the values are recorded every 0.5 ms of simulated time. The mass flowrate of the powder exiting the nozzle in steady conditions is reported in Figure 6.23. The average value is slightly lower than expected, probably due to some particle accumulation at the top of the distribution fins, which is also hinted by the heatmap of Figure 6.22a.

The irregularity in the powder mass flowrate, smoothed via a moving average with a window of 2 ms, is 19%, which is consistent with the experimental results.

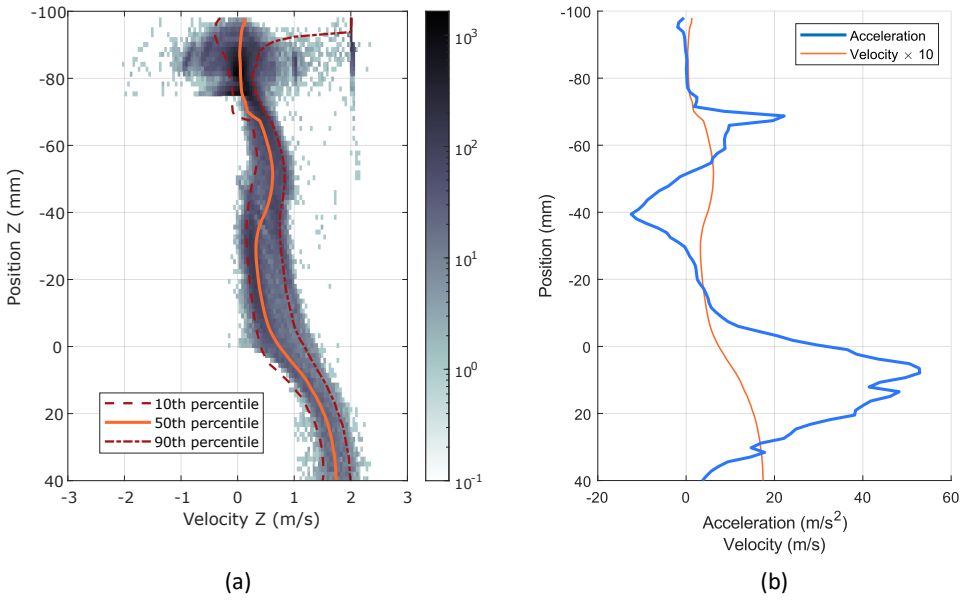

Figure 6.22: Particle vertical velocities along the nozzle, with percentiles. Median acceleration.

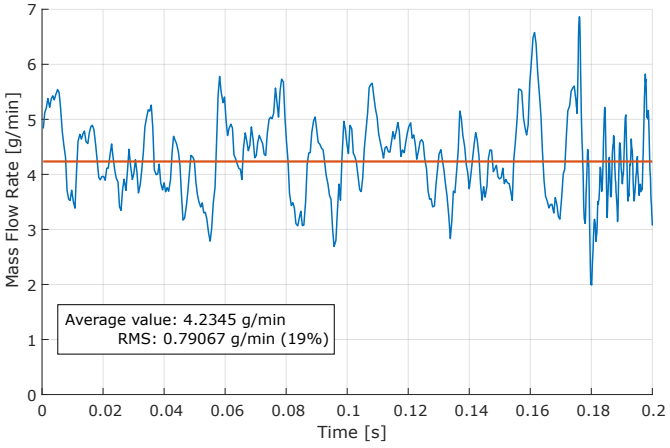

Figure 6.23: Mass flowrate over time for the simulated case

6.7 Comparison between Experiment and Simulation

6.7.1 Particle Size Distribution

The experimental Particle Size Distribution (PSD) was utilized in the simulation to ensure consistency and accuracy in comparing particle behavior between both methods. By using the backside illumination technique, particles were observed with minimal glare, as detailed in Section 6.4. The experimental PSD, normalized to the number of particles, closely aligns with the expected distribution and the one obtained this work, presented in Sections 5.6.1 and 6.4.1.

Figure 6.7 presents the PSD of the experimental observations, showing a Rosin-Rammler fit that provides a useful model for further analysis. This distribution was essential for the simulation, as it served as the basis for understanding the flow characteristics and particle behavior within the nozzle.

6.7.2 Standoff Distance

The standoff distance is a critical parameter in the Laser Metal Deposition (LMD) process, impacting deposition efficiency and quality.

As discussed in Section 6.4.2, the experimental standoff distance, based on particle distribution analysis, was found to be 16 mm from the nozzle exit (Figure 6.8).

The simulation results indicated a shorter standoff distance of 10.2 mm from the nozzle exit (Figure 6.19).

The shorter simulated standoff distance suggests the need for refining the drag conditions and incorporating gas expansion effects. Despite these discrepancies, the simulation provides a reasonable approximation of the experimental conditions, highlighting areas for further improvement in modeling the drag coefficient and gas dynamics to better match experimental observations.

6.7.3 Particle Velocities

Particle velocities in the simulation are slightly slower than those observed experimentally. However, the overall behavior matches well. This discrepancy could be due to uncertainties in the flowrate measurement and the fact that gas expansion is not accounted for in the simulation. The underestimation of particle velocities at the exit of the nozzle could also imply the necessity of simulating

these flow conditions with a compressible model, which however requires even more extensive validation.

6.7.4 Mass Flowrate and Flow Irregularities

The mass flowrate measured experimentally was found to be higher than expected, primarily due to the limited knowledge of the powder delivery method. This discrepancy suggests areas for improvement in the powder metering setup to achieve more accurate measurements and more uniform and repeatable powder delivery.

The RMS values of flow irregularities were found to be quite similar between the experiment and simulation, indicating that the simulation can effectively predict the presence of flow irregularities. As shown in Section 6.4.5, the experimental mass flowrate variability was 16% over time, using a 2 ms moving average window (refer to Figure 6.14).

Similarly, the simulation results exhibited an irregularity in the powder mass flowrate of 19%, smoothed with a 2 ms moving average (refer to Figure 6.23). This close agreement suggests that the CFD-DEM approach is capable of capturing the dynamic behavior of the mass flowrate with a reasonable degree of accuracy.

6.8 Chapter Summary

This chapter presents a comprehensive study of the Continuous Coaxial Nozzle within the Laser Metal Deposition (LMD) process, integrating both experimental and computational approaches to explore the influence of key process parameters on powder flow dynamics.

Experimentally, a Taguchi Orthogonal Array (L9) was employed to systematically vary and assess the effects of powder flow rate, carrier gas flow rate, and shielding gas flow rate. Although the Taguchi method facilitated an efficient exploration of the parameter space, the scope of this work focused on directly comparing the individual experimental cases rather than conducting a full Taguchi analysis. High-speed particle tracking yielded a Particle Size Distribution (PSD) consistent with expected Rosin-Rammler characteristics, validating the reliability of the experimental setup. The standoff distance, a critical parameter for deposition quality, was analyzed through particle distribution, revealing a stand-

off distance of 16 mm. Additionally, particle velocities averaged $\overline{v} = 1.896$ m/s with minimal temporal variation, and the mass flowrate was accurately measured at $\overline{\dot{m}} = 3.906$ g/min, exhibiting flow irregularities of 16%. These findings demonstrate the precision of the experimental methodology and underscore the significance of controlled parameter settings in achieving consistent deposition outcomes.

On the computational side, CFD-DEM simulations were conducted using a refined polyhedral mesh to accurately capture the intricate flow patterns and particle interactions within the nozzle. The simulations successfully reproduced flow irregularities, recording a 19% variation in mass flowrate, which closely aligns with experimental observations. However, discrepancies were noted in the standoff distance and mass flowrate values, with simulations indicating a shorter standoff distance of 10.2 mm and a lower mass flowrate compared to experimental data. These differences highlight the need for further refinement in the simulation model, particularly in calibrating drag coefficients and incorporating gas expansion effects to enhance accuracy.

A key outcome of this study is the establishment of a methodology for determining the optimal standoff distance through both experimental measurements and computational simulations. Although a single optimal distance was not identified, the groundwork laid by this research provides a robust framework for future investigations aimed at optimizing standoff distance to enhance deposition quality and process reliability.

The alignment between experimental and simulation results in capturing flow irregularities validates the efficacy of the CFD-DEM coupling approach in modeling dynamic powder flow behavior. Nonetheless, the observed deviations in standoff distance and mass flowrate emphasize the necessity for ongoing calibration and validation to fully reconcile computational predictions with empirical measurements.

In summary, this study advances the understanding of powder flow dynamics in Continuous Coaxial Nozzles by integrating experimental data with robust simulation models. The methodologies developed herein offer valuable insights for optimizing nozzle designs and process parameters, thereby contributing to improved deposition quality and enhanced reliability of the LMD process. Future

work will focus on refining the simulation models and expanding the experimental framework to establish definitive guidelines for determining optimal standoff distances, ultimately facilitating the consistent and high-quality production of metal deposits.

CHAPTER

7

Conclusions

Each chapter of this thesis presents its own conclusions based on the detailed studies conducted. This final chapter synthesizes the overall findings, highlighting the key outcomes and insights derived from the integrated experimental and computational approaches used throughout the research. The following sections summarize the research outcomes, models and calibration efforts, advancements in high-speed imaging, comprehensive studies on pneumatic conveying, and the analysis of the LMD nozzle.

7.1 Research Outcomes

The primary aim of this study was to analyze and enhance the pneumatic powder delivery system for Laser Metal Deposition (LMD). This section evaluates the level of completion of the objectives outlined in 1.3.

Objective 1: The structure of the pneumatic conveying system for LMD was thoroughly analyzed, from the powder dosing system to the nozzle. The most appropriate simulation models were selected, including a comparison of various existing models. Multiphase simulations in confined domains were carried out, and periodic and transient flow phenomena were investigated. High-speed imaging techniques were employed for experimental investigation, corroborating the simulation results. The main DEM parameters for calibration were determined, also by proposing a novel characterization technique for Adhesive Energy. This

objective was fully achieved, providing a robust understanding of the pneumatic conveying system's structure.

Objective 2: The effects of process parameters on the LMD system performance were investigated. This was achieved through a combined use of simulation tools and experimental investigation. The experimental procedure is clearly outlined, providing powerful insights for future investigations. This objective was substantially achieved, yielding significant insights into process parameter effects on LMD performance.

Objective 3: The sustainability improvements of LMD were evaluated. The research demonstrated significant areas of improvement in the powder delivery in the LMD process. When addressed, these improvements increase capabilities in flexibility, precision, manufacturing speed, accessibility, and repair capabilities, aligning with Sustainable Development Goal 9 (SDG 9). Additionally, the research shows that waste reduction can be achieved through better material use, supporting SDG 12. This objective was partially achieved, highlighting notable areas to be addressed for sustainability improvements in the LMD process.

7.1.1 Models and Calibration

The analysis of the pneumatic conveying system involved selecting and evaluating appropriate simulation models. A significant part of this process was calibrating Discrete Element Method (DEM) parameters, focusing in Chapter 4 on an innovative technique for characterizing Adhesive Energy, the Kinetic Adhesion Test (KAT).

The Adhesive Energy values determined with this test were used to perform a simulation on the same procedure using a DEM model. By employing the corresponding JKR contact model formulation, the simulation was able to reproduce the particle detachment observed in the experiment. The critical particle diameter, or the diameter above which particles detach, was determined within the margin of error of the experimental measurements. These results showcased the KAT's capability to accurately measure the Adhesive Energy, revealing the impact of variables such as particle size, material composition, and surface texture on adhesion strength. The theory of the KAT is based on the JKR model and provides a robust framework for assessing particle adhesion.

In addition to the theoretical foundation of the technique, the chapter details the design, assembly, and operation of the KAT device. The work includes recommendations for future research to further refine the methodology and explore its broader applications in granular matter research. All the information is available in open-source repositories, enhancing the understanding of surface adhesion phenomena in granular materials.

7.1.2 **High-speed Imaging**

Advanced imaging techniques were employed to capture and analyze flow phenomena within the pneumatic conveying system, as described in Chapter 5. Following the successful validation of these techniques, they were also applied in Chapter 6 to study the powder flow exiting the nozzle, under both controlled and realistic operating conditions.

High-speed cameras were instrumental in visualizing particle dynamics, allowing for detailed analysis of multiphase flow in confined domains as well as in real-world scenarios, such as the nozzle environment. The use of high-speed imaging provided crucial insights into particle trajectories and transient behaviors within the powder flow.

The particle trajectories were analyzed using open-source software, to which a contribution was made as part of this work. This development, along with the setup of the experimental system, represents a significant advancement over the existing characterization techniques currently used in industry, offering greater accuracy and precision in particle flow analysis.

The experimental results were compared against multiphase CFD-DEM simulations, focusing on both periodic and transient flow phenomena. The calibrated simulations demonstrated strong agreement with the experimental findings, capturing the flow irregularities with a deviation of only a few percentage points. This consistency between the experimental data and simulations confirms that the CFD-DEM model can effectively capture the complex flow interactions within the system, providing a reliable tool for further investigation and optimization of pneumatic conveying systems.

7.1.3 **Studies on the Pneumatic Conveying**

In Chapter 5, this work investigated pneumatic conveying methods used in the Laser Metal Deposition (LMD) process, highlighting the significance of efficient powder delivery for achieving high deposition quality. The chapter offered an in-depth analysis of metallic powder flow in narrow pipes, with a focus on understanding flow dynamics within the system. Experiments and simulations were conducted under conditions replicating those found in LMD, enabling meaningful comparisons and validation of the results.

A major finding of this study was the identification of self-induced flow irregularities, a phenomenon observed in both the experimental data and CFD-DEM simulations. These irregularities, appearing as fluctuations in mass flow rate, exhibited a single-digit percentage of consistency between the experimental outcomes and simulations, reinforcing the reliability of the simulation model. Furthermore, key flow characteristics, such as particle velocity distributions and pressure drops along the pipe, supported the model's accuracy. The ability of the simulations to replicate these behaviors precisely contributes significantly to the understanding of pneumatic conveying in LMD processes.

While these results offer a robust foundation for applying CFD-DEM to pneumatic conveying studies, they also reveal areas for further enhancement. The comparison between simulated and experimental data marks an initial step toward developing a novel calibration method, aimed at refining the simulation model for better predictive accuracy. However, this calibration approach remains in its preliminary phase, and additional work is required to fully realize its potential. Specifically, parameters such as drag coefficients, adhesive energy, and particle-fluid interactions will need iterative optimization to achieve a comprehensive calibration process.

Moreover, while this study used moving average filters for processing experimental data, more advanced filtering techniques—such as wavelet analysis—should be considered in future research to better capture and interpret noise and periodic patterns in the flow. This would provide deeper insights into flow dynamics, particularly in identifying and quantifying flow irregularities.

Although this work outlines a promising direction for calibration, it is essential to emphasize that the novel calibration setup is still under development. While

the current method served as a validation step, future efforts will concentrate on refining this calibration process through iterative adjustments to parameters like adhesive energy and drag coefficients, as discussed in Section 7.2.6.

7.1.4 **Study on the LMD Nozzle**

This work presents a comprehensive study on the Laser Metal Deposition (LMD) nozzle, focusing on its design, performance, and optimization. The investigation, reported in Chapter 6, included both experimental and simulation approaches to understand the influence of nozzle geometry on the deposition process.

The experimental setup for testing these nozzles is meticulously described, providing a clear understanding of the methodologies employed. The setup shows good potential in improving the understanding of the powder flow in LMD, and was used to collect data over a set of parameters using a Taguchi Orthogonal Array.

Experimental and numerical results are in good agreement, confirming the presence and magnitude of mass flow rate irregularities. The experimental and computational results aid in determining the standoff distance, or the optimal distance between nozzle and substrate, with a substantial improvement in the level of detail achieved compared to existing methods, wiht significant improvement in determining the particle distribution across the stream of powder. This result can contribute both to avoid material waste and improve the uniformity and predictability of the deposition.

In-depth observations of the complex flow highlighted notable areas for improvement in the pneumatic conveying systems for LMD, specifically in accounting for the effects of flow irregularities and mass flow rate control. Detailed experimental procedures were established, offering a comprehensive framework for future research. These procedures validated the initial hypothesis regarding flow irregularities in both pipe and nozzle simulations and experiments, paving the way for more refined investigations.

The research outcomes provide a foundation for future studies and practical applications in the characterization and control of the mass flow rate in pneumatic conveying of metallic powders for AM applications.

7.2 Next Steps

Future research in this study should focus on several strategic initiatives to enhance the understanding and optimization of the Laser Metal Deposition (LMD) process. These initiatives aim to improve process quality, reduce waste, and align with the Sustainable Development Goals (SDGs), particularly SDG 9 on industry, innovation, and infrastructure, and SDG 12 on responsible consumption and production.

7.2.1 Designing Stand-Alone Calibration Setups

Precise calibration of the powder delivery system is essential for maintaining consistent and accurate mass flow rate measurements in industrial LMD machines. A dedicated calibration setup would enhance the reliability and performance of these machines, ensuring that the deposition process is both predictable and controllable. Improved calibration translates directly to higher process quality, reducing material waste by minimizing over-deposition and under-deposition, thus supporting sustainable industrial practices aligned with SDG 9 and SDG 12.

This calibration method can determine the Particle Size Distribution (PSD), standoff distance, average flow rate, spot diameter, and flow irregularity more efficiently than existing methods that require multiple devices and setups. This approach will optimize the LMD process, improving both efficiency and quality. Stakeholders, including machine designers and process specialists, will find this procedure valuable for optimizing the precision and efficiency of the deposition process and the entire powder delivery system.

7.2.2 Implementing Telecentric Lenses

Implementing telecentric lenses in the calibration device is essential for analyzing particle flow. Telecentric lenses minimize optical distortions, allowing for more accurate measurements of particle sizes and velocities. Improved measurement accuracy will enable a more precise characterization of particle distribution and flow dynamics, leading to significant advancements in optimizing the LMD process and ensuring uniform and consistent particle deposition.

7.2.3 **Implementing 3D Flow Reconstruction**

Exploring advanced setups, such as implementing a second point of view, is a promising direction. Using a second camera or a mirror to obtain dual perspectives could enable 3D flow reconstruction, providing a detailed understanding of particle trajectories. This dual perspective facilitates the identification of particle shape and orientation, crucial for understanding the deposition process and enhancing the quality of the final product. While this approach may involve higher costs and more complex setups, the potential benefits in process optimization and product quality could be substantial.

Studies, such as those by Brown et al. and Du et al., demonstrate the effectiveness of using multiple 2D images to achieve accurate 3D particle shape characterization, highlighting the potential of such techniques in industrial applications.

7.2.4 **AI-Driven Process Optimization**

Collecting precise data from calibration devices can support the development of AI systems for LMD process optimization. High-resolution data on mass flow rate, particle size distribution, and flow dynamics can train machine learning models to predict optimal process parameters, identify potential issues early, and suggest real-time adjustments. Integrating AI-driven optimization can make the LMD process more adaptive and intelligent, consistently achieving high-quality standards.

7.2.5 **Real-Time Monitoring and Control**

Developing real-time monitoring systems for LMD processes could provide immediate feedback and adjustments during manufacturing. This requires the design of reliable actuators and robust data acquisition systems. Real-time monitoring would enable the detection of anomalies and the implementation of corrective actions on-the-fly, thus enhancing the overall reliability and quality of the LMD process.

7.2.6 **Refinement of Simulation Models**

The comparison between experimental data and CFD-DEM simulations presented in Chapter 5 opens up a potential path for a novel calibration setup, though this is still in its early stages. Current simulations provide valuable insights, but further refinement of key parameters, such as the drag coefficient and fluid-particle interaction terms, is necessary for more accurate results.

The calibration process discussed in Section 2.2 served as a verification step, ensuring that the model reasonably represents physical phenomena. For instance, the particle size distribution (PSD) was measured and integrated into the simulations. However, a more precise calibration approach, using an iterative parameter optimization method, would involve fine-tuning these parameters through a systematic comparison of experimental results with simulation outcomes.

Future work should focus on enhancing this calibration process, particularly by improving the robustness of the experimental setup and applying more sophisticated techniques, such as automated optimization algorithms.

7.2.7 **Optimization of Nozzle Geometry**

Optimizing the current nozzle design for better performance is a critical next step. This involves exploring various nozzle geometries through both simulations and experiments to identify designs that minimize particle scattering and maximize deposition precision. Typically, LMD equipment operates in chambers filled with argon at very low oxygen concentrations, adding complexity and cost while limiting the maximum size of the manufactured parts. Studies on improving the coverage of protection gas by providing an additional stream around the main nozzle have shown performance improvements but also increased argon gas usage. Future research should focus on optimizing nozzle design to balance performance with cost-effectiveness and resource efficiency.

7.2.8 **Investigation of Multi-Material Deposition**

Expanding the study to multi-material deposition processes could unlock new applications for LMD. Simulating and experimenting with different material combinations will provide insights into the challenges and potential solutions for achieving uniform multi-material layers. This topic already garners scientific interest,

and this work sets the stage for studying the delivery, dosing, and mixing of powders in multi-material systems.

7.2.9 Implementing a Schlieren Setup

To better visualize the expanding and mixing flow at the exit of the nozzle, a schlieren setup can be highly effective. Schlieren imaging allows for the visualization of changes in the refractive index of air, which can indicate variations in density and flow patterns. Previous studies have demonstrated the use of schlieren photography to study the gas flow of 3D-printed LMD nozzles, revealing crucial insights into material loss due to overspray and the impact of nozzle design on powder stream quality.

Further research can leverage this technique to gain a deeper understanding of the flow dynamics at the nozzle exit, optimizing nozzle designs to minimize material loss and improve deposition quality. Additionally, existing studies have utilized schlieren imaging to study gas flow in welding and additive manufacturing processes, highlighting the potential of schlieren setups to provide detailed visualizations of flow interactions, aiding in the development of more efficient and precise LMD processes.

The application of schlieren imaging in LMD can significantly enhance the ability to visualize and understand complex flow dynamics, leading to more informed design decisions and process optimizations.

7.3 Contributions

7.3.1 Publications

Publishing is a cornerstone of scientific research. The journal publications supporting this thesis are:

10/2024 **Optical Particle Tracking in the Pneumatic Conveying of Metal Powders through a Thin Capillary Pipe**
MDPI Technologies – DOI: 10.3390/technologies12100191

02/2024 **Comparison of CFD-DEM and MP-PIC in the Simulation of Metal Powder Conveying for Laser Metal Deposition**
OpenFOAM Journal – DOI: 10.51560/ofj.v4.91

01/2024 **Estimation of Mesoscale Surface Energy in the Kinetic Adhesion Test**
Powder Technology – DOI: 10.1016/j.powtec.2024.119426

06/2023 **Kinetic Adhesion Test to Determine Particle Surface Energy**
HardwareX – DOI: 10.1016/j.ohx.2023.e00437

7.3.2 Conferences

Participating in international conferences post-2020 pandemic was especially enriching, offering valuable interactions with peers and fostering a deeper understanding of my research topic. Key conferences attended include:

09/2024 **11th International Conference on Conveying and Handling of Particulate Solids (CHoPS)** – Edinburgh, UK
Presentation: *CFD-DEM Simulation Validation of Metal Powder Conveying in Thin Pipes*

05/2023 **VII Congreso Nacional III Congreso Iberoamericano de Pulvimetalurgia (CEIPM)** – San Sebastián, ES
Presentation: *Kinetic Adhesion Test to determine Adhesive Energy*

12/2022 **19th UK Travelling Workshop: GeoMechanics: from Micro to Macro (GM3)** – Imperial College London, UK
Presentation: *Platform development for the determination of powders' adhesive contact properties*

07/2022 **17th OpenFOAM Workshop** – University of Cambridge, UK
Presentation: *MP-PIC Calibration Using CFD-DEM for Multiphase Gas-Metal Powder Flows in Additive Manufacturing*

07/2022 **10th International Conference on Conveying and Handling of Particulate Solids (CHoPS)** – Salerno, IT
Presentation: *Benchmark of different discrete particle models for the simulation of pneumatic conveying of additive manufacturing metallic powders*

7.3.3 **Mobility 1 - Newcastle**

During my stay at Newcastle University (16th September 2022 - 21st December 2022), under the supervision of Dr. Sadegh Nadimi, I worked on the JKR contact model and measuring the Adhesive Energy parameter Γ (Chapter 4). This included theoretical modeling and practical testing of the Kinetic Adhesion Test apparatus. Additional skills acquired included electron microscopy (SEM), optical microscopy, image processing, and x-ray tomography.

7.3.4 **Mobility 2 - Trento**

During my stay at the University of Trento (November-December 2023), I collaborated with Prof. Luigi Fraccarollo on exploring pneumatic conveying phenomena. This involved developing a test bench and capturing particle motion using a high-speed camera. This work is detailed in Section 5.4.

References

[1] Dong-Gyu Ahn. Direct metal additive manufacturing processes and their sustainable applications for green technology: A review. *International Journal of Precision Engineering and Manufacturing-Green Technology*, 3(4):381–395, October 2016. 13

[2] Jun Ai, Jian-Fei Chen, J. Michael Rotter, and Jin Y. Ooi. Assessment of rolling resistance models in discrete element simulations. *Powder Technology*, 206(3):269–282, January 2011. 54, 55

[3] Maarten Alderliesten. Mean particle diameters. part VII. the rosin-rammler size distribution: Physical and mathematical properties and relationships to moment-ratio defined mean particle diameters. *Particle & Particle Systems Characterization*, 30(3):244–257, mar 2013. 222

[4] Mohammadreza Alizadeh, Maryam Asachi, Mojtaba Ghadiri, Andrew Bayly, and Ali Hassanpour. A methodology for calibration of DEM input parameters in simulation of segregation of powder mixtures, a special focus on adhesion. *Powder Technology*, 339:789–800, November 2018. 70

[5] Yassin Alkassar, Vijay K. Agarwal, Niranjana Behera, Mark G. Jones, and R. K. Pandey. Transient characteristics of fine powder flows within fluidized dense phase pneumatic conveying systems. *Powder Technology*, 343:629–643, 2 2019. 11, 100

[6] Vasileios Angelidakis, Sadegh Nadimi, Mohamed Garum, and Ali Hassanpour. Nano-scale characterisation of particulate iron pyrite morphology in shale. *Particle & Particle Systems Characterization*, n/a:2200120, oct 2022. 73

[7] Vasileios Angelidakis, Sadegh Nadimi, Masahide Otsubo, and Stefano Utili. CLUMP: A code library to generate universal multi-sphere particles. *SoftwareX*, 15:100735, July 2021. 23

[8] Vasileios Angelidakis, Sadegh Nadimi, and Stefano Utili. SHape analyser for particle engineering (SHAPE): Seamless characterisation and simplification of particle morphology from imaging data. *Computer Physics Communications*, 265:107983, August 2021. 22

[9] Sergiy Antonyuk, Jürgen Tomas, Stefan Heinrich, and Lothar Mörl. Breakage behaviour of spherical granulates by compression. *Chemical Engineering Science*, 60(14):4031–4044, July 2005. xii, 51

[10] J. I. Arrizubieta, I. Tabernero, J. Exequiel Ruiz, A. Lamikiz, S. Martinez, and E. Ukar. Continuous Coaxial Nozzle Design for LMD based on Numerical Simulation. *Physics Procedia*, 56:429–438, January 2014. 23

[11] Utkarsh Ayachit. *The ParaView guide*. Kitware Inc., full color version edition, 2015. 137

[12] Stefano Baraldo, Alessandro Roncoroni, Filippo Palo, and Anna Valente. Multi-physics based methodology for evaluating powder feeding quality for Laser Metal Deposition. *Procedia CIRP*, 107:623–628, January 2022. 100

[13] L. Benvenuti, C. Kloss, and S. Pirker. Identification of DEM simulation parameters by artificial neural networks and bulk experiments. *Powder Technology*, 291:456–465, apr 2016. 38

[14] bp. bp energy outlook 2023. Technical report, British Petroleum (bp), 2023. 1

[15] N.V. Brilliantov and T. PÃ¶schel. Rolling friction of a viscous sphere on a hard plane. *Europhysics Letters*, 42(5):511–516, 1998. 55

[16] G. Calvert, M. Ghadiri, and R. Tweedie. Aerodynamic dispersion of cohesive powders: A review of understanding and technology. *Advanced Powder Technology*, 20(1):4–16, jan 2009. 72, 79

[17] Arati Chokshi, A. G. G. M. Tielens, and D. Hollenbach. Dust coagulation. *The Astrophysical Journal*, 407:806, apr 1993. 61, 63, 64, 72

[18] Sanjib C. Chowdhury and John W. Gillespie. Strain-rate dependent mode i cohesive traction laws for glass fiber-epoxy interphase using molecular dynamics simulations. *Composites Part B: Engineering*, 237:109877, May 2022. 85, 87

[19] Marius Chyasnavichyus, Seth L. Young, and Vladimir V. Tsukruk. Probing of polymer surfaces in the viscoelastic regime. *Langmuir*, 30(35):10566–10582, February 2014. xiii, 62

[20] C.J. Coetzee. Review: Calibration of the discrete element method. *Powder Technology*, 310:104–142, apr 2017. 37

[21] Colin Thornton. *Granular Dynamics, Contact Mechanics and Particle System Simulations : A DEM study*. Springer-Verlag GmbH, September 2015. xxi, 11, 29, 53, 61, 72, 85, 86, 100, 107, 109

[22] R. Courant, K. Friedrichs, and H. Lewy. On the partial difference equations of mathematical physics. *IBM Journal of Research and Development*, 11(2):215–234, mar 1967. 30

[23] Clayton T. Crowe, John D. Schwarzkopf, Martin Sommerfeld, and Yutaka Tsuji. *Multiphase Flows with Droplets and Particles*. Taylor and Francis Ltd., Boca Raton, FL, 2 edition, August 2011. xii, 45, 104

[24] P. A. Cundall and O. D. L. Strack. A discrete numerical model for granular assemblies. *Géotechnique*, 29(1):47–65, mar 1979. 35, 52

[25] Sasan Dadbakhsh, Liang Hao, and Choon Kong. Surface finish improvement of LMD samples using laser polishing. *Virtual and Physical Prototyping*, 5:215–221, December 2010. 100

[26] B. V Derjaguin, V. M Muller, and Yu. P Toporov. Effect of contact deformations on the adhesion of particles. *Journal of Colloid and Interface Science*, 53(2):314–326, November 1975. 59

[27] Alberto Di Renzo, Erasmo Napolitano, and Francesco Di Maio. Coarse-grain dem modelling in fluidized bed simulation: A review. *Processes*, 9(2):279, February 2021. 41

[28] Freeman J. Dyson. Search for artificial stellar sources of infrared radiation. *Science*, 131(3414):1667–1668, June 1960. 2

[29] K. E. Easterling and A. R. Thölén. Surface energy and adhesion at metal contacts. *Acta Metallurgica*, 20(8):1001–1008, August 1972. 78

[30] Sina Ebnesajjad. 3 - surface tension and its measurement. In Sina Ebnesajjad, editor, *Handbook of Adhesives and Surface Preparation*, Plastics Design Library, pages 21–30. William Andrew Publishing, Oxford, January 2011. 71

[31] S. Elghobashi. On predicting particle-laden turbulent flows. *Applied Scientific Research*, 52(4):309–329, June 1994. 41

[32] Behrad Esgandari, Stefanie Rauchenzauner, Christoph Goniva, Paul Kieckhefen, and Simon Schneiderbauer. A comprehensive comparison of two-fluid model, discrete element method and experiments for the simulation of single- and multiple-spout fluidized beds. *Chemical Engineering Science*, 267:118357, March 2023. 42

[33] Nicolas Estrada, Emilien Azéma, Farhang Radjai, and Alfredo Taboada. Identification of rolling resistance as a shape parameter in sheared granular media. *Physical Review E*, 84(1):011306, jul 2011. 56

[34] Elise Ferreira, Morgan Dal, Christophe Colin, Guillaume Marion, Cyril Gorny, Damien Courapied, Jason Guy, and Patrice Peyre. Experimental and numerical analysis of gas/powder flow for different LMD nozzles. *Metals*, 10(5):667, May 2020. 160

[35] Stephanie Fraley, John Zalewski, Mike Oom, and Ben Terrien. Design of Experiments via Taguchi Methods - Orthogonal Arrays, March 2023. 154

[36] Alessandro Freddi and Mario Salmon. *Introduction to the Taguchi Method*, pages 159–180. Springer International Publishing, July 2018. 154

[37] H. Purseyand Edward Crisp Bullard G. F. Miller. On the partition of energy between elastic waves in a semi-infinite solid. *Proceedings of the Royal Society of London. Series A. Mathematical and Physical Sciences*, 233(1192):55–69, dec 1955. Raileigh wave energy partition. 28

[38] Jiali Gao, Chengzu Wu, Xudong Liang, Yunbo Hao, and Kai Zhao. Numerical simulation and experimental investigation of the influence of process parameters on gas-powder flow in laser metal deposition. *Optics & Laser Technology*, 125:106009, May 2020. xviii, 151, 155

[39] Mojtaba Ghadiri, Mehrdad Pasha, Wenguang Nan, Colin Hare, Vincenzino Vivacqua, Umair Zafar, Saeid Nezamabadi, Alejandro Lopez, Massih Pasha, and Sadegh Nadimi. Cohesive powder flow: Trends and challenges in characterisation and analysis. *KONA Powder and Particle Journal*, 37(0):3–18, jan 2020. 70

[40] I. Gibson. *Additive manufacturing technologies rapid prototyping to direct digital manufacturing*. Springer, 2010. Chapter 9 - beam methods. 4

[41] Dimitri Gidaspow. *Multiphase flow and fluidization : continuum and kinetic theory descriptions*. Academic Press, Boston, 1994. 45, 111, 114

[42] John R. Grace, Xiaotao Bi, and Naoko Ellis. *Essentials of Fluidization Technology*. Wiley-VCH Verlag GmbH, 2020. xii, 39, 40

[43] D. S. Grierson, E. E. Flater, and R. W. Carpick. Accounting for the JKR–DMT transition in adhesion and friction measurements with atomic force microscopy. *Journal of Adhesion Science and Technology*, 19(3–5):291–311, January 2005. xiii, 62

[44] Alan Arnold Griffith and Geoffrey Ingram Taylor. VI. the phenomena of rupture and flow in solids. *Philosophical Transactions of the Royal Society of London. Series A, Containing Papers of a Mathematical or Physical Character*, 221(582-593):163–198, January 1921. 62, 78

[45] Ahmet Guner, Prveen Bidare, Amaia Jimenez, Stefan Dimov, and Khamis Essa. Nozzle designs in powder-based direct laser deposition: A review. *International Journal of Precision Engineering and Manufacturing*, 23(9):1077–1094, aug 2022. 151

[46] Coşkun Hamzaçebi. Taguchi method as a robust design tool. In *Quality Control - Intelligent Manufacturing, Robust Design and Charts*, chapter 7. IntechOpen, March 2021. 154

[47] Kevin J. Hanley, Catherine O'Sullivan, Jorge C. Oliveira, Kevin Cronin, and Edmond P. Byrne. Application of Taguchi methods to DEM calibration of bonded agglomerates. *Powder Technology*, 210(3):230–240, July 2011. 35, 38, 154

[48] Heinrich Hertz. Ueber die berührung fester elastischer körper. *Journal für die reine und angewandte Mathematik*, 92:156–171, 1882. 27, 33, 50, 52, 59, 71, 82

[49] Ko Higashitani, Hisao Makino, and Shuji Matsusaka. *Powder technology handbook*. CRC Press, Taylor & Francis Group, 2020. x, 7, 8, 70, 100

[50] Honeywell International Inc. Honeywell trustability™SSC pressure sensors. 126

[51] Y. Hoshino, N. Kutsuwada, Y. Watanabe, and H. Izawa. Measurement of van der waals force of toner adhesion employing a linearly increasing electric field and determining the toner jumping voltage. *Particulate Science and Technology*, 14(3):267–277, jul 1996. 71

[52] J. Hærvig, U. Kleinhans, C. Wieland, H. Spliethoff, A. L. Jensen, K. Sørensen, and T. J. Condra. On the adhesive JKR contact and rolling models for reduced particle stiffness discrete element simulations. *Powder Technology*, 319:472–482, September 2017. 29

[53] Martin Isoz, Martin Kotouč Šourek, Ondřej Studeník, and Petr Kočí. Hybrid fictitious domain-immersed boundary solver coupled with discrete element method for simulations of flows laden with arbitrarily-shaped particles. *Computers & Fluids*, 244:105538, August 2022. 40

[54] Jacob N. Israelachvili. *Intermolecular and surface forces*. Academic Press, 2011. xii, 57, 58, 59, 70

[55] Khuloud Jaqaman, Dinah Loerke, Marcel Mettlen, Hirotaka Kuwata, Sergio Grinstein, Sandra L Schmid, and Gaudenz Danuser. Robust single-particle tracking in live-cell time-lapse sequences. *Nature Methods*, 5(8):695–702, July 2008. 132

[56] M.J. Jiang, H.-S. Yu, and D. Harris. A novel discrete model for granular material incorporating rolling resistance. *Computers and Geotechnics*, 32(5):340–357, jul 2005. 55, 56

[57] K. L. Johnson and J. A. Greenwood. An adhesion map for the contact of elastic spheres. *Journal of Colloid and Interface Science*, 192(2):326–333, August 1997. xiii, 58, 59, 60, 63

[58] K. L. Johnson, A. K. Kendalland, and D. Roberts. Surface energy and the contact of elastic solids. *Proceedings of the Royal Society of London. A. Mathematical and Physical Sciences*, 324(1558):301–313, sep 1971. xiii, 59, 61, 63, 64, 71, 72, 76, 78, 80, 85

[59] K.L. Johnson and H.M. Pollock. The role of adhesion in the impact of elastic spheres. *Journal of Adhesion Science and Technology*, 8(11):1323–1332, jan 1994. xiii, 64, 65, 66, 71, 76

[60] Nikolai Semyonovich Kardashev. Transmission of information by extraterrestrial civilizations. *Soviet Astronomy*, 8:217, October 1964. Provided by the SAO/NASA Astrophysics Data System. 1

[61] Kevin Kendall. Cracks at adhesive interfaces. *Journal of Adhesion Science and Technology*, 8(11):1271–1284, jan 1994. 60, 61, 72, 85

[62] Shunto Kinugasa, Shuya Tanoue, Yasuhiro Shimada, and Shuji Matsusaka. Detailed analysis of particle–substrate interaction based on a centrifugal method. *Advanced Powder Technology*, 33(11):103793, November 2022. 61, 72

[63] G. E. Klinzing, F. Rizk, R. Marcus, and L. S. Leung. *Pneumatic Conveying of Solids: A Theoretical and Practical Approach.* SPRINGER NATURE, Dordrecht, 3 edition, July 2010. 8, 11, 100

[64] George E. Klinzing. Historical review of pneumatic conveying. *KONA Powder and Particle Journal*, 35:150–159, 2018. 97, 98

[65] S. B. Kuang, K. Li, R. P. Zou, R. H. Pan, and A. B. Yu. Application of periodic boundary conditions to CFD-DEM simulation of gas–solid flow

in pneumatic conveying. *Chemical Engineering Science*, 93:214–228, April 2013. 104

[66] Shibo Kuang, Mengmeng Zhou, and Aibing Yu. CFD-DEM modelling and simulation of pneumatic conveying: A review. *Powder Technology*, 365:186–207, April 2020. 42, 98

[67] J. Kussin and M. Sommerfeld. Experimental studies on particle behaviour and turbulence modification in horizontal channel flow with different wall roughness. *Experiments in Fluids*, 33(1):143–159, July 2002. 104

[68] B.E. Launder and D.B. Spalding. The numerical computation of turbulent flows. *Computer Methods in Applied Mechanics and Engineering*, 3(2):269–289, March 1974. 43

[69] A. Levy. *Handbook of conveying and handling of particulate solids*. Elsevier, Amsterdam New York, 2001. 8, 100

[70] Fei Li, Feifei Song, Sofiane Benyahia, Wei Wang, and Jinghai Li. MP-PIC simulation of CFB riser with EMMS-based drag model. *Chemical Engineering Science*, 82:104–113, September 2012. 102

[71] Li Qun Li, Jiandong Wang, Panpan Lin, and Han Liu. Microstructure and mechanical properties of functionally graded tic p /ti6al4v composite fabricated by laser melting deposition. *Ceramics International*, 43, September 2017. 7

[72] Liqun Li, Yichen Huang, Chunyu Zou, and Wang Tao. Numerical Study on Powder Stream Characteristics of Coaxial Laser Metal Deposition Nozzle. *Crystals*, 11(3):282, March 2021. 101, 102

[73] Alejandro López, Matthew T. Stickland, and William M. Dempster. CFD study of fluid flow changes with erosion. *Computer Physics Communications*, 227:27–41, June 2018. 8

[74] G. Lu, J. R. Third, and C. R. Müller. Discrete element models for non-spherical particle systems: From theoretical developments to applications. *Chemical Engineering Science*, 127:425–465, May 2015. 22

[75] Retief Lubbe, Wen-Jie Xu, Daniel N. Wilke, Patrick Pizette, and Nicolin Govender. Analysis of parallel spatial partitioning algorithms for GPU based DEM. *Computers and Geotechnics*, 125:103708, sep 2020. 31

[76] Sadaf Maramizonouz and Sadegh Nadimi. Drag force acting on ellipsoidal particles with different shape characteristics. *Powder Technology*, 412:117964, September 2022. 47

[77] Daniel Maugis. Adhesion of spheres: The JKR-DMT transition using a dugdale model. *Journal of Colloid and Interface Science*, 150(1):243–269, April 1992. 60

[78] F. R. Menter. Two-equation eddy-viscosity turbulence models for engineering applications. *AIAA Journal*, 32(8):1598–1605, August 1994. 43

[79] Metco Joining & Cladding. Twin 150-lc powder feeder. xviii, 154, 157

[80] Maksim Mezhericher, Tamir Brosh, and Avi Levy. Modeling of particle pneumatic conveying using DEM and DPM methods. *Particulate Science and Technology*, 29(2):197–208, mar 2011. 23, 100, 101

[81] David Mills. *Handbook of pneumatic conveying engineering*. Marcel Dekker, New York, 2004. 8, 100

[82] R. D. Mindlin. Compliance of elastic bodies in contact. *Journal of Applied Mechanics*, 16(3):259–268, sep 1949. 52, 82

[83] R. D. Mindlin and H. Deresiewicz. Elastic spheres in contact under varying oblique forces. *Journal of Applied Mechanics*, 20(3):327–344, sep 1953. 52, 82

[84] Pouya Moghimian, Thomas Poirié, Mahdi Habibnejad-Korayem, Javier Arreguin Zavala, Jens Kroeger, Frédéric Marion, and Frédéric Larouche. Metal powders in additive manufacturing: A review on reusability and recyclability of common titanium, nickel and aluminum alloys. *Additive Manufacturing*, 43:102017, July 2021. xi, 34, 36

[85] F. Moukalled, L. Mangani, and M. Darwish. *The Finite Volume Method in Computational Fluid Dynamics*. Springer-Verlag GmbH, August 2015. 35

[86] Mauro Murer, Valentina Furlan, Giovanni Formica, Simone Morganti, Barbara Previtali, and Ferdinando Auricchio. Numerical simulation of particles flow in laser metal deposition technology comparing eulerian-eulerian and lagrangian-eulerian approaches. *Journal of Manufacturing Processes*, 68:186–197, August 2021. 11, 23, 42, 100, 101, 104

[87] Wenguang Nan, Mehrdad Pasha, Tina Bonakdar, Alejandro Lopez, Umair Zafar, Sadegh Nadimi, and Mojtaba Ghadiri. Jamming during particle spreading in additive manufacturing. *Powder Technology*, 338:253–262, October 2018. 7, 69, 78, 107

[88] National Aeronautics and Space Administration (NASA). OSIRIS-REx: Origins, spectral interpretation, resource identification, and security – regolith explorer. 2

[89] NightHawkInLight. Test multiple variables at once to optimize anything, October 2023. 154

[90] Masanobu Oda and Kazuyoshi Iwashita. Study on couple stress and shear band development in granular media based on numerical simulation analyses. *International Journal of Engineering Science*, 38(15):1713–1740, oct 2000. 56

[91] Kyle Odum, Masakazu Soshi, and Kazuo Yamazaki. Measurement and analysis of impact dynamics suitable for modelling pneumatic transport of metallic powder flow through a directed energy deposition nozzle. *Advanced Powder Technology*, 33(3):103515, March 2022. 155

[92] Marta Ostolaza, Aizpea Urresti, Jon Iñaki Arrizubieta, Aitzol Lamikiz, and Mikel Ortiz. Cfd simulation for the modelling of the powder flow on continuous coaxial nozzles in the laser ded process. *Procedia CIRP*, 111:282–286, 2022. 12th CIRP Conference on Photonic Technologies [LANE 2022]. xviii, 150, 151, 155, 162, 174

[93] Lorenzo Pedrolli. Kinetic adhesion test apparatus to determine powder's adhesive surface energy, 2022. 73, 88

[94] Lorenzo Pedrolli, Beatriz Achiaga Menor, Inger Martinez de Arenaza, and Alejandro López. Comparison of cfd-dem and mp-pic in the simulation of metal powder conveying for laser metal deposition. *OpenFOAM® Journal*, 4:26–40, February 2024. 97

[95] Lorenzo Pedrolli, Sadegh Nadimi, Beatriz Achiaga, and Alejandro López. Estimation of mesoscale surface energy in the kinetic adhesion test. *Powder Technology*, 435:119426, February 2024. 69, 227

[96] Lorenzo Pedrolli, Sadegh Nadimi, Sadaf Maramizonouz, Beatriz Achiaga Menor, and Alejandro López. Kinetic adhesion test to determine particle surface energy. *HardwareX*, 14:e00437, jun 2023. xiii, 69, 73, 74, 88, 227

[97] P. G. C. Petean and M. L. Aguiar. Determining the adhesion force between particles and rough surfaces. *Powder Technology*, 274:67–76, April 2015. 61, 72

[98] Gabriele Piscopo, Eleonora Atzeni, Abdollah Saboori, and Alessandro Salmi. An overview of the process mechanisms in the laser powder directed energy deposition. *Applied Sciences*, 13(1):117, dec 2022. 151

[99] Thorsten Pöschel. *Computational granular dynamics*. Springer-Verlag, 2005. 30, 31, 41

[100] Alfio Quarteroni, Riccardo Sacco, Fausto Saleri, and Paola Gervasio. *Matematica Numerica*. Springer, 2014. 26

[101] Joachim Raedler and Erich Sackmann. On the measurement of weak repulsive and frictional colloidal forces by reflection interference contrast microscopy. *Langmuir*, 8(3):848–853, March 1992. 80

[102] C. V. Raman. On some applications of hertz's theory of impact. *Physical Review*, 15(4):277–284, apr 1920. 27, 86

[103] Daniel Regulin and Raffaele Barucci. A benchmark of approaches for closed loop control of melt pool shape in ded. *The International Journal of Advanced Manufacturing Technology*, 126(1–2):829–843, February 2023. 168

[104] P. G. Saffman. The lift on a small sphere in a slow shear flow. *Journal of Fluid Mechanics*, 22(2):385–400, June 1965. 46

[105] Carl Sagan. *Carl Sagan's cosmic connection.* Cambridge Univ. Press, Cambridge [u.a.], 2000. Includes index. 1

[106] D. M. Schaefer, M. Carpenter, B. Gady, R. Reifenberger, L. P. DeMejo, and D. S. Rimai. Surface roughness and its influence on particle adhesion using atomic force techniques. In *Fundamentals of Adhesion and Interfaces*, pages 35–48. De Gruyter, dec 1995. 70

[107] Johannes Schindelin, Ignacio Arganda-Carreras, Erwin Frise, Verena Kaynig, Mark Longair, Tobias Pietzsch, Stephan Preibisch, Curtis Rueden, Stephan Saalfeld, Benjamin Schmid, Jean-Yves Tinevez, Daniel James White, Volker Hartenstein, Kevin Eliceiri, Pavel Tomancak, and Albert Cardona. Fiji: an open-source platform for biological-image analysis. *Nature Methods*, 9(7):676–682, July 2012. 73, 131, 159, 216

[108] Christiane Schulz. The many names of laser deposition welding. 5

[109] Jonathan P. K. Seville and Chuan-Yu Wu. *Particle Technology and Engineering.* Elsevier Science and Technology Books, Kidlington, Oxford, UK, 2016. x, xi, 8, 22, 34

[110] Yasuhiro Shimada, Motohiro Tsubota, and Shuji Matsusaka. Measurement of particle adhesion force and effective contact radius via centrifuge equipped with horizontal and vertical substrates. *Powder Technology*, 397:117103, January 2022. 61, 72, 76

[111] Nimisha Shukla and Kimberly H. Henthorn. Effect of relative particle size on large particle detachment from a microchannel. *Microfluidics and Nanofluidics*, 6(4):521–527, jul 2008. 71

[112] Siemens Digital Industries Software. *Simcenter STAR-CCM+ User Guide v. 2023.1*, Siemens 2021. 47, 174

[113] Ambrish Singh, Sajan Kapil, and Manas Das. A comprehensive review of the methods and mechanisms for powder feedstock handling in directed energy deposition. *Additive Manufacturing*, 35:101388, October 2020. x, 5, 9, 10, 70, 99

[114] Jack Smith. Review and viability of a dyson swarm as a form of dyson sphere. *Physica Scripta*, 97(12):122001, November 2022. 2

[115] D. M. Snider. An Incompressible Three-Dimensional Multiphase Particle-in-Cell Model for Dense Particle Flows. *Journal of Computational Physics*, 170(2):523–549, July 2001. 102

[116] M. Sommerfeld. Analysis of collision effects for turbulent gas-particle flow in a horizontal channel: Part I. Particle transport. *International Journal of Multiphase Flow*, 29(4):675–699, April 2003. 101

[117] Martin Sommerfeld. Numerical methods for dispersed multiphase flows. In *Advances in Mathematical Fluid Mechanics*, pages 327–396. Springer International Publishing, July 2017. xii, 21, 40, 42

[118] Zifeng Song, Qingzhan Li, Fei Li, Yanpei Chen, Atta Ullah, Sheng Chen, and Wei Wang. MP-PIC simulation of dilute-phase pneumatic conveying in a horizontal pipe. *Powder Technology*, 410:117894, September 2022. 101

[119] B. Spinewine, H. Capart, M. Larcher, and Y. Zech. Three-dimensional voronoï imaging methods for the measurement of near-wall particulate flows. *Experiments in Fluids*, 34(2):227–241, February 2003. xvi, 134, 135

[120] I. Tabernero, A. Lamikiz, E. Ukar, L. N. López de Lacalle, C. Angulo, and G. Urbikain. Numerical simulation and experimental validation of powder flux distribution in coaxial laser cladding. *Journal of Materials Processing Technology*, 210(15):2125–2134, November 2010. xix, 150, 155, 168, 169

[121] D. Tabor. Surface forces and surface interactions. In Milton Kerker, Albert C. Zettlemoyer, and Robert L. Rowell, editors, *Plenary and Invited Lectures*, pages 3–14. Elsevier, January 1977. 59

[122] The OpenFOAM Foundation. Openfoam v9 user guide. 45, 46, 53, 102

[123] Morgan L. Thomas and P. Worth Longest. Evaluation of the polyhedral mesh style for predicting aerosol deposition in representative models of the conducting airways. *Journal of Aerosol Science*, 159:105851, January 2022. 173

[124] Jean-Yves Tinevez, Nick Perry, Johannes Schindelin, Genevieve M. Hoopes, Gregory D. Reynolds, Emmanuel Laplantine, Sebastian Y. Bednarek, Spencer L. Shorte, and Kevin W. Eliceiri. Trackmate: An open and extensible platform for single-particle tracking. *Methods*, 115:80–90, February 2017. 132, 133, 138, 159

[125] Jürgen Tomas. Adhesion of ultrafine particles - a micromechanical approach. *Chemical Engineering Science*, 62(7):1997–2010, April 2007. 58

[126] Yutadka Tsuji, T. Tanaka, and T. Ishida. Lagrangian numerical simulation of plug flow of cohesionless particles in a horizontal pipe. *Powder Technology*, 71(3):239–250, sep 1992. xii, 53, 54, 82, 107, 108, 109

[127] Avinash Vaidheeswaran, Aytekin Gel, Mary Ann Clarke, and William A. Rogers. Assessment of model parameters in MFiX particle-in-cell approach. *Advanced Powder Technology*, 32(8):2962–2977, August 2021. 102

[128] Franck Varenne. *Models and Simulations in the Historical Emergence of the Science of Complexity*, pages 3–21. Springer Berlin Heidelberg, 2009. 34

[129] Various. ESA technology strategy. Technical report, European Space Agency (ESA), 2022. 3

[130] P. Aarne Vesilind. The Rosin-Rammler particle size distribution. *Resource Recovery and Conservation*, 5(3):275–277, September 1980. 222

[131] Vincenzino Vivacqua, Alejandro López, Robert Hammond, and Mojtaba Ghadiri. DEM analysis of the effect of particle shape, cohesion and strain rate on powder rheometry. *Powder Technology*, 342:653–663, jan 2019. 7

[132] Johannes Waschke, Tilo Pompe, David Rettke, Stephan Schmidt, and Mario Hlawitschka. Radial profile detection of multiple spherical particles in contact with interacting surfaces. *PLOS ONE*, 14:e0214815, April 2019. 80

[133] Kimiaki Washino, Ei L. Chan, and Toshitsugu Tanaka. DEM with attraction forces using reduced particle stiffness. *Powder Technology*, 325:202–208, February 2018. 29, 109

[134] David R. Williams. Sun fact sheet. NASA Goddard Space Flight Center, July 2013. Accessed on 16/07/2024. 1

[135] J.R. Williams and R. O'Connor. A linear complexity intersection algorithm for discrete element simulation of arbitrary geometries. *Engineering Computations*, 12(2):185–201, feb 1995. 30

[136] Changhua Xie, Huaqing Ma, and Yongzhi Zhao. Investigation of modeling non-spherical particles by using spherical discrete element model with rolling friction. *Engineering Analysis with Boundary Elements*, 105:207–220, aug 2019. 56

[137] Fei Yan and Akira Rinoshika. Particle fluctuation velocity of a horizontal self-excited pneumatic conveying near the minimum pressure drop. *Powder Technology*, 241:115–125, jun 2013. 8, 11

[138] Z. Yan, S. K. Wilkinson, E. H. Stitt, and M. Marigo. Discrete element modelling (DEM) input parameters: understanding their impact on model predictions using statistical analysis. *Computational Particle Mechanics*, 2(3):283–299, September 2015. 29, 109

[139] U. Zafar, C. Hare, A. Hassanpour, and M. Ghadiri. Drop test: A new method to measure the particle adhesion force. *Powder Technology*, 264:236–241, sep 2014. xiv, xxi, 61, 72, 85, 86, 87, 92

[140] Srdja Zekovic, Rajeev Dwivedi, and Radovan Kovacevic. Numerical simulation and experimental investigation of gas–powder flow from radially symmetrical nozzles in laser-based direct metal deposition. *International Journal of Machine Tools and Manufacture*, 47(1):112–123, January 2007. 11, 100

[141] Hemin Zhao and Yongzhi Zhao. CFD–DEM simulation of pneumatic conveying in a horizontal channel. *International Journal of Multiphase Flow*, 118:64–74, September 2019. 100

[142] Wenqi Zhong, Aibing Yu, Xuejiao Liu, Zhenbo Tong, and Hao Zhang. DEM/CFD-DEM modelling of non-spherical particulate systems: Theoretical developments and applications. *Powder Technology*, 302:108–152, November 2016. 22

[143] Fubao Zhou, Shengyong Hu, Yingke Liu, Chun Liu, and Tongqiang Xia. CFD–DEM simulation of the pneumatic conveying of fine particles through a horizontal slit. *Particuology*, 16:196–205, October 2014. 11, 100

[144] Qian Zhou, Wen-Jie Xu, and Guang-Yu Liu. A contact detection algorithm for triangle boundary in GPU-based DEM and its application in a large-scale landslide. *Computers and Geotechnics*, 138:104371, October 2021. 31

[145] Y.C. Zhou, B.D. Wright, R.Y. Yang, B.H. Xu, and A.B. Yu. Rolling friction in the dynamic simulation of sandpile formation. *Physica A: Statistical Mechanics and its Applications*, 269(2-4):536–553, jul 1999. 55

APPENDIX

A

Determining the Particle Size Distribution (PSD) and other shape parameters

This part of the investigation is instrumental to the correct use of the KAT, reported in Section 4.3. The powder samples are imaged either using an optical or Scanning Electron Microscope (SEM). In both cases, at the same level of magnification and digitized image resolution, it is possible to reach the same level of precision. The advantage of using SEM over optical only resides in the ability to reach much higher magnification, therefore resolving finer particles. With appropriate instruments and techniques, there should be no difference in the measurement accuracy, determined only by the pixel size. Example images are reported in Figure A.1, which give an idea in the difference in clarity obtainable with the two methods.

The particles have been deposited onto a strip of carbon conductive tape. As can be seen in Figure A.1b, the composition of the tape has the side effect of providing a good contrast with the particles. Probably the powder distribution is the one critical step in the preparation. Metal powders can have a relatively high cohesion, making it likely to find overlapping particles. They can be easily recognized by the human eye, but the software might have more of a hard time to correctly interpret the grayscale tonalities.

The sample was prepared without the aid of specific distribution tools. A high shear stress when depositing the powder using a gas carrier might encourage the particles to distribute with a larger spacing. Commercial characterization tools include a specific particle dispersion module (for instance: Morphologi 4).

The images have been taken with the intention to include in the order of

around a hundred particles. The measurement in Figure A.1b has a pixel size of 1.655 μm. This leads to a number of pixels per particle diameter between 27 and 60 for the expected size range $45 \div 100$ μm.

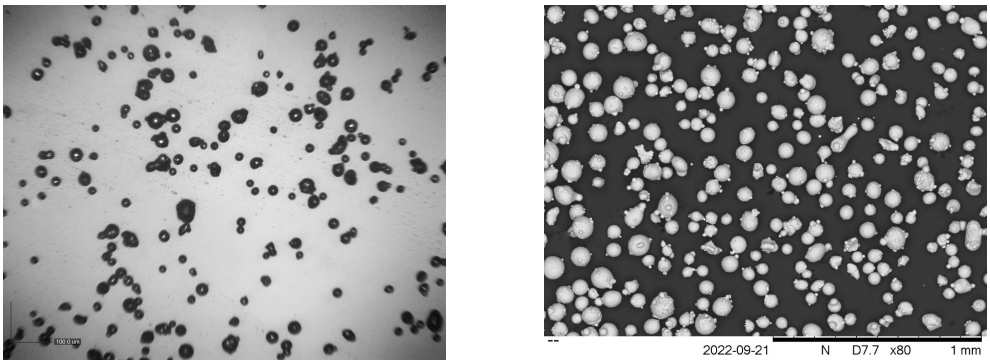

(a) (b)

Figure A.1: Comparison of 316L Stainless Steel powder granules captured through different imaging techniques: (a) Optical Microscopy and (b) Scanning Electron Microscopy. Note that this comparison is biased due to the available optical microscope, which was of lower quality compared to the SEM (Hitachi TM3030). Better results can be expected with higher-quality optical microscopy equipment.

A.1 **Image segmentation procedure**

Image segmentation is a crucial step in the field of image analysis, allowing for the partitioning of an image into meaningful and distinct regions. Relevant to this work is the segmentation of 2D images obtained from scanning electron microscopy (SEM) using Fiji / ImageJ [107]. The objective it to automatically recognize the particles in the image, subdividing it, and extracting the relative metrics, in particular the equivalent diameter.

The grayscale images acquired from SEM, similar to the one in Figure A.1b, are TIFF format, with a resolution of 1280x1100, and a intensity depth of 8bit. A calibration bar is present at the bottom of the image, which allows to adjust the image scale for accurate analysis.

The image scale has to be adjusted according to the scale bar:

- Using the line tool, trace the length of the calibration bar
- *Analyze >Set Scale*

    - *Distance in pixels* should be according to the line just traced
    - *Known distance* and *Unit of length* are according to the calibration bar

From this point on, the actual analysis takes place. First, determine the grayscale threshold:

- *Image >Adjust >Threshold*
    - Check that the particles are correctly identified, check whether the background is dark. The highlighted areas will become the analyzed areas.
    - *Set* only saves the setting
    - *Apply* transforms the image into the B/W mask (see Figure A.2), necessary for most plugins
- *Rectangle*
    - Select the area to perform the analysis on
- *Analyze >Set Measurement*
    - Allows choosing which shape parameters are calculated
    - Allows selecting scientific notation and the number of decimal places. This is better than the default fixed decimals (12345.123 becomes 1.234e4; and 0.001 becomes 1.234e-3).
- *Analyze >Analyze Particles*
    - *Exclude on edges*; *include holes*
    - *Show >overlay*; displays a numbered mask to identify how the particles have actually been segmented
    - Display results

At his point the basic procedure is complete, and the results can be saved as a `.csv` file. The filenames should be the same as the image it has been taken from, for consistency, and it should be consistent with Matlab's file naming rules (do not begin with a number, do not contain characters like "-+*.", etc. The character "_" is allowed. The suggested way to organize the files is in folders describing the

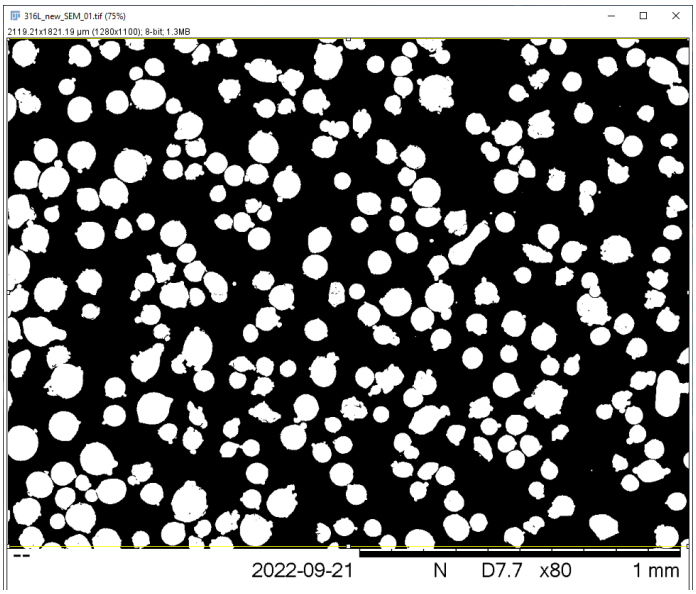

Figure A.2: Black and White mask of Figure A.1b, used to determine the PSD of the 316L stainless steel powder sample.

case (`./SEM/_images/SS316L/newPowder/`) and number the images with two (or more) digits integers (`imageName_01.tif`).

The result can be affected by the presence of connected particles, when they shouldn't be. Most of them can be treated as outliers, but an accurate filtering can allow us to preserve more information.

Process >Filters >Median

- Should eliminate over- and under-exposed edges in irregular particles

Process >Binary >Watershed

- The filter called Watershed can determine the presence of bridges between two particles, using an erosion of the particle boundaries of different strength and identifying those borders which open during this process
- Some particles with irregular shape can be erroneously divided

A.2 Analysis and plot

The extracted data can be collected in Matlab using multiple csv files reads. Once this is achieved, the various metrics can be analyzed. The function `importSEMdata_lp` imports the data and combines it in a single Table dataset.

Listing A.1: Matlab function to import the image segmentation data generated using ImageJ.

```
function [impSEMdata,imported] = importSEMdata_lp(filesBaseFolder,filesBaseName,
    maxNfiles_I)
%importSEMdata_lp imports the csv files generated with ImajeJ / Fiji from
%multiple files and collects them in a single table. "imported" tells which
%data has actually been imported. base name and folder change depending on
%the case. The intended sructure is:
%   filesBaseFolder = "./316L/New_powder/SEM_images/";
%   filesBaseName   = "316L_new_SEM";

    if nargin > 2
        maxNfiles = maxNfiles_I;
    else
        maxNfiles = 20;
    end

    imported_0 = [];

    % Import the data
    for k=1:maxNfiles
        if exist(sprintf("%s%s_%02d.csv",filesBaseFolder,filesBaseName,k)) == 2
            impSEMdata_k = readtable(sprintf("%s%s_%02d.csv",filesBaseFolder,
                filesBaseName,k),"VariableNamingRule","preserve");
            if k>1
                impSEMdata_0 = [impSEMdata_0;impSEMdata_k];
            else
                impSEMdata_0 = impSEMdata_k;
            end
            clear impSEMdata_k
            imported_0=[imported_0;k];
        end
    end
    impSEMdata = impSEMdata_0;
    imported = imported_0;
end
```

Once the dataset is loaded, it can be analyzed. The Script A.1:

- Loads the data using the function `importSEMdata_lp` (only if it hasn't been loaded yet)
- Calculates the equivalent diameter as $d_{eq} = \frac{4 \cdot \text{Area}}{\text{Perimeter}}$ (or $d_{eq} = \sqrt{\frac{4 \cdot \text{Area}}{\pi}}$ since the result might be slightly different in irregular particles).
- Using d_{eq}, estimates the volume and mass of each particle
- Creates groups according to d_{eq} to plot the metrics as histograms
- Calculates the mass and numeric fraction of the group, providing dimensionless quantities
- Plots the values

The resulting plots are combined in Figure A.3. The size distribution graphs

show also the influence of the fine speckles of powder on the numeric size distribution. The fines can also be seen on the graph “Roundness by equivalent diameter”. Given the image resolution it is very possible that they are outliers, which can be eliminated.

Listing A.2: Matlab script to generate the particle groups by equivalent diameter d_eq, and plot the results.

```
CleanRun = false;

if (exist("SEMdata") == 0 || CleanRun)
    clear all
    [SEMdata,imported] = importSEMdata_lp("./316L/New_powder/SEM_images/","316
        L_new_SEM");
end
clear CleanRun


caseName = "SS316L new";

rho = 7890; % density, kg/m^3

% Calculate equivalent diameter in two different ways
SEMdata.d_eq = 4.*(SEMdata.Area ./ SEMdata.("Perim."));
%SEMdata.d_eq = sqrt((4 .* SEMdata.Area) ./ pi);

rho_g_um3 = rho * 1e-15; % density, g/um^3
x = 4/3 * pi * rho_g_um3;
SEMdata.m_eq = x .* (SEMdata.d_eq).^3;

m_tot = sum(SEMdata.m_eq);
n_tot = size(SEMdata,1);
% Compute group summary
mass_group = groupsummary(SEMdata,"d_eq",15,["sum","median"],["d_eq","m_eq"]);
mass_group.frac_m = mass_group.sum_m_eq ./ m_tot;
mass_group.frac_n = mass_group.GroupCount ./ n_tot;

% Create bar graph of size distribution by mass
figure
h1 = bar(mass_group.disc_d_eq,mass_group.frac_m);
    % Add xlabel, ylabel, title
    xlabel("Equivalent diameter d_{eq} [\mum]")
    ylabel("Mass fraction")
    title(strcat("Size distribution by mass (",caseName,")"))

% Create bar graph of size distribution by count
figure
h2 = bar(mass_group.disc_d_eq,mass_group.frac_n);
    % Add xlabel, ylabel, title
    xlabel("Equivalent diameter d_{eq} [\mum]")
    ylabel("Count fraction")
    title(strcat("Size distribution by particle count (",caseName,")"))

% Create bar graph of roundness by equivalent diameter
figure
h3 = plot(SEMdata.d_eq,SEMdata.Round,'.');
    % Add xlabel, ylabel, title
    xlabel("Equivalent diameter d_{eq} [\mum]")
    ylabel("Roundness")
    title(strcat("Roundness by equivalent diameter (",caseName,")"))
    xlim([0 100])

figure
h4 = plot(SEMdata.("Circ."),SEMdata.Skew,'.');
    % Add xlabel, ylabel, title
    xlabel("Circularity")
    ylabel("Skew")
```

```
    title(strcat("Skew by Circularity (",caseName,")"))
```

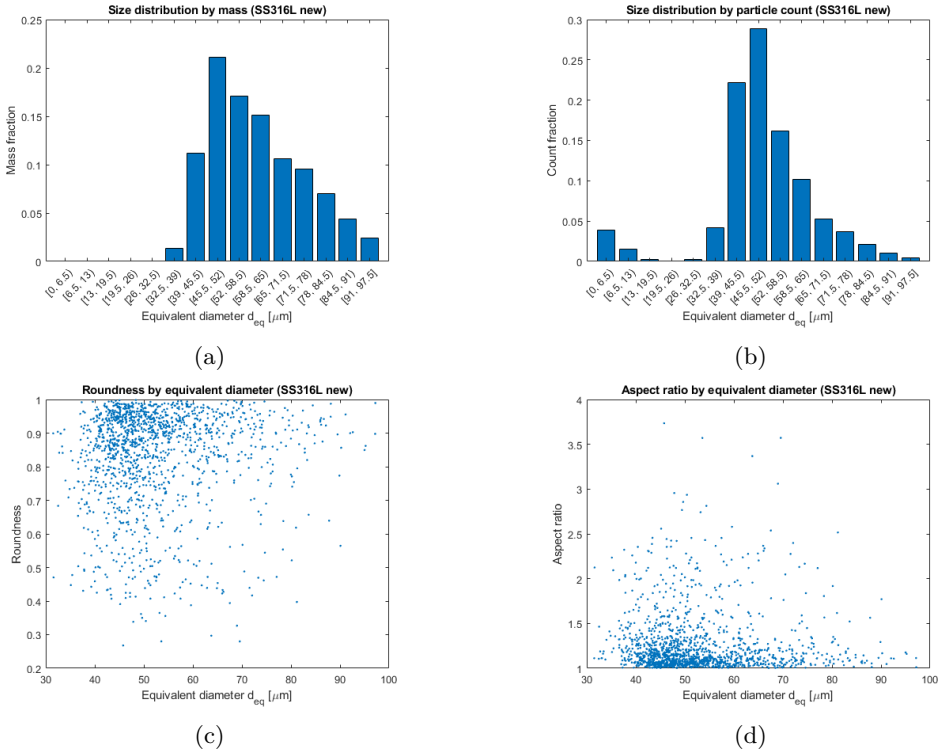

Figure A.3: Graphs from Script A.2, representing PSD using the histograms by mass (a) and by numerosity (b). Also, an example of additional metrics like roundness (c) and aspect ratio (d).

A.3 **Rosin-Rammler distribution**

The particle size distribution (PSD) is a fundamental characteristic in the field of powder technology. To generate particles within a DEM framework, one must define a size distribution within a specified range, $d_{min} < d < d_{max}$. Several distribution models can be utilized:

Fixed size or all particles have the same diameter.

Uniform distribution according to which the sizes are equally likely within the interval.

Normal distribution is characterized by particle sizes that cluster around a mean value following a Gaussian curve.

Rosin-Rammler distribution usually shown as a cumulative curve, it is closely related to the Weibull distribution, but its original field of application was specifically for powders [3].

Other models are be used to more closely represent the PSD: Weibull, Lorgnormal, or even polynomial fits or lookup tables.

A number of analytical and semi-empirical equations have been used over the years to represent the PSD of granular solids, and there is no absolutely "correct" model. Introduced by Rosin and Rammler in 1933, the Rosin-Rammler equation [130] is widely accepted thanks to its relative simplicity and generality, as it can be applied to a wide range of different scenarios. The cumulative fraction of material by weight for particles below a certain size is mathematically defined as:

$$Y = 1 - \exp\left(-\left(\frac{x}{x_0}\right)^n\right) \tag{A.1}$$

where, Y denotes the cumulative weight fraction of particles smaller than size x; n is the uniformity constant, and x_0 represents the characteristic particle size. The latter is the size below which 63.2% of the particle mass is finer, a value derived from the exponential function's nature where $1 - \frac{1}{e} \approx 0.632$. The higher n is, the tighter is the distribution.

The characterization of PSD via sieving—partitioning the powder into size-defined fractions and weighing them to establish a mass distribution is The original method used to fit the Rosin-Rammler distribution. In use since ancient times, **sieving** is a straightforward yet crucial step in understanding particle sizes. It involves separating a powder sample into layers based on particle size through a set of sieves with different mesh sizes, arranged from larger to smaller. The powder is prepared to flow easily and then added to the top sieve. With the help of a mechanical shaker, particles are sifted through the stack, each sieve catching particles that are too large to pass through its mesh, thus sorting them by size. After the shaking, the amount of powder on each sieve is weighed. These weights give a profile of the sample's particle size distribution, which is especially useful for simulations that need to mimic how a group of particles will behave in real-world scenarios.

The values of x_0 and n can be fit to the size distribution by mass obtained by sieving the sample. In this work, however, the parameters are fit on the cumulative curve determined using the the information from the microscopy images' analysis. The Script A.3 generates the cumulative curve by mass using the data from Script A.2, and fits Equation A.1. Figure A.4 shows the result of the fit operation, and the experimental data and the model differ only slightly. To increase the resolution it should be possible to use the experimental curve almost directly using a lookup table, but most codes standardise this step to reduce the need for input parameters. The parameters reported in Figure A.4 are then used to generate the PSD in the DEM codes.

Listing A.3: Matlab script to generate and fit the cumulative PSD to the Rosin-Rammler model, and plot the results.

```
function RosinRammlerFit(diameters, plotPercentiles, useVolume)
% RosinRammlerFit Fits a Rosin-Rammler distribution to the given diameters.
%
%   RosinRammlerFit(DIAMETERS) fits a Rosin-Rammler distribution to the
%   given array of DIAMETERS, assuming number-based distribution if no
%   volume-based calculation is specified. The diameters should be in
%   micrometers (um).
%
%   RosinRammlerFit(DIAMETERS, PLOTPERCENTILES, USEVOLUME) optionally plots
%   the 10th, 50th, and 90th percentiles of the original data if
%   PLOTPERCENTILES is true. If USEVOLUME is true, calculates by volume.
%
%   The function generates a plot comparing the input data and the fit data
%   using a cumulative curve, and includes an annotation with the fit
%   formula and parameter values.
%
%   Example:
%       diameters = [10, 20, 30, 40, 50]; % in um
%       RosinRammlerFit(diameters, true, true);
%
%   Inputs:
%       diameters - Array of particle diameters in micrometers (um).
%       plotPercentiles - (Optional) Boolean to plot the 10th, 50th, and
%                         90th percentiles of the original data.
%       useVolume - (Optional) Boolean to calculate the distribution by
%                   volume.
%
%   Outputs:
%       A plot of the cumulative distribution and the Rosin-Rammler fit.
%
%   Author: Lorenzo Pedrolli
%   Date: 2024-07-05

    if nargin < 2
        plotPercentiles = false; % Default to not plotting percentiles
    end

    if nargin < 3
        useVolume = false; % Default to not using volume calculation
    end

    % Sort the diameters
    diameters_sorted = sort(diameters);

    % Calculate the cumulative distribution
    if useVolume
```

```
    % Calculate by volume
    volumes = (pi/6) * (diameters_sorted .* 1e-6).^3; % Convert diameters to
        meters for volume calculation
    v_tot = sum(volumes);
    m_cumul = cumsum(volumes) / v_tot;
    method = 'Volume';
else
    % Calculate by number
    m_cumul = (1:length(diameters_sorted))' / length(diameters_sorted);
    method = 'Number';
end

% Prepare data for fitting
[xData, yData] = prepareCurveData(diameters_sorted, m_cumul);

% Set up fittype and options
ft = fittype('1-exp(-(x/a)^n)', 'independent', 'x', 'dependent', 'y');
opts = fitoptions('Method', 'NonlinearLeastSquares');
opts.Display = 'Off';
opts.Lower = [0 0];
opts.StartPoint = [mean(diameters_sorted) 1];

% Fit model to data
[fitresult, gof] = fit(xData, yData, ft, opts);

% Generate the plot
figure;
hold on;
plot(diameters_sorted, m_cumul, 'b-', 'DisplayName', 'Input Data');

% Generate fit data for the plot
fit_x = linspace(min(diameters_sorted), max(diameters_sorted), 100);
fit_y = feval(fitresult, fit_x);
plot(fit_x, fit_y, 'r--', 'DisplayName', 'Rosin-Rammler Fit');

xlabel('diameter [\mum]');
ylabel(['Cumulative Fraction (' method ')']);
title(['Rosin-Rammler Fit by ' method]);
ylim([0, 1]);
legend('show');
grid on;

% Add annotation with fit formula and parameters
conf = confint(fitresult);
annotation_text = sprintf(['Fit: 1 - exp(-(x/a)^n)\n' ...
                           '     a = %.4g\n' ...
                           '     n = %.4g\n' ...
                           '  rsquare: %.4g'], ...
                           fitresult.a, fitresult.n, gof.rsquare);
annotation('textbox', [0.62, 0.2, 0.3, 0.2], 'String', annotation_text, ...
           'FitBoxToText', 'on', 'BackgroundColor', 'white');

if plotPercentiles
    percentiles = [10, 50, 90];
    % Calculate the cumulative distribution for the percentiles
    if useVolume
        % Calculate by volume
            % volumes = (pi/6) * (sorted_diameters .* 1e-6).^3;
            % sorted_volumes = sort(volumes);
        volumes_sorted = (pi/6) * diameters_sorted.^3; % um^3
        cumulative_volumes = cumsum(volumes_sorted) / sum(volumes_sorted);
        percentile_values = interp1(cumulative_volumes, diameters_sorted,
            percentiles/100);
    else
        % Calculate by number
        percentile_values = prctile(diameters_sorted, percentiles);
    end

    for i = 1:length(percentiles)
        x_val = percentile_values(i);
```

```
            y_val = percentiles(i)/100;

            % Plot the percentile lines without including them in the legend
            plot([x_val x_val], [0 y_val], 'k-', 'HandleVisibility', 'off');
            plot([0 x_val], [y_val y_val], 'k-', 'HandleVisibility', 'off');
            text(x_val - 5, y_val, sprintf('D_{%d} = %.4g', percentiles(i), x_val)
                , ...
                'VerticalAlignment', 'bottom', 'HorizontalAlignment', 'right');
        end
    end

    % Display fit parameters
    disp('Fit Parameters:');
    disp(fitresult);
    disp('Goodness of Fit:');
    disp(gof);
end
```

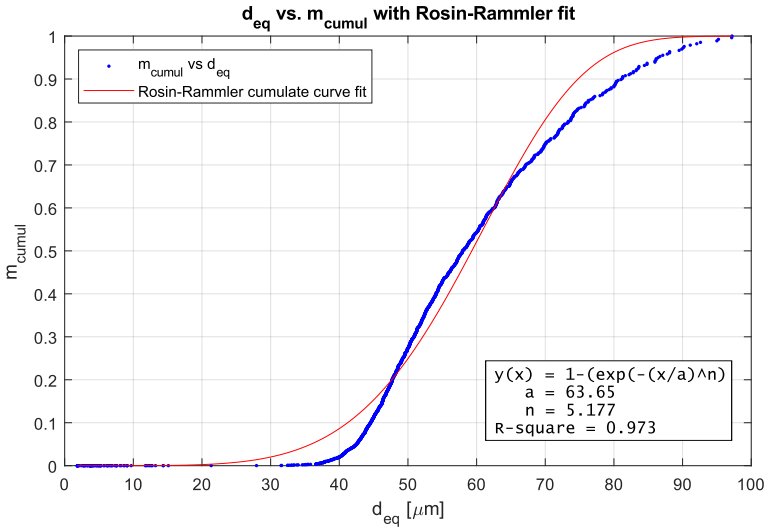

Figure A.4: Result of the fit operation of the Rosin-Rammler model on the experimental measurements taken by several SEM images on a 316L metallic powder sample, visible in Figure A.1b. This figure is the result of Script A.3.

APPENDIX

B

JKR model implementation in StarCCM+

The JKR contact model throughly used in this work, described in Section 3.3.2, is not included in StarCCM+. Therefore, it was necessary to code it as a Field Function, a way to define custom mathematical expressions in StarCCM+.

The model takes the parameter Γ_{12}, the adhesive energy, which can be determined by the KAT test presented in Chapter 4 [96, 95]. Using the custom JKR model for the normal direction meant that the tangential Mindlin model needed to be rewritten as well. The parameter μ is the contact friction (constant, same value for static and dynamic). The model uses the contact radius value $a = \sqrt{\frac{4 \cdot \mathrm{ContactArea}}{\pi}}$, as opposed to the overlap. This is more convenient since StarCCM+ provides the ContactArea, making the model valid for all allowed particle shapes (cylinders, pills, hyperquadrics, polyhedrals).

By working in this way, the particle overlap is overestimated sa, per the JKR model, particles would detach at a distance from the surface. This however is not possible due to the software limitation, for which the contact can be evaluated exclusively with an actual overlap. Given the relatively disperse phase of the cases analyzed in this work this limitation can be ignored, as the overlap is orders of magnitude smaller than the actual particle diameter, even when considering a reduced elastic modulus. However, it must be accounted for in dense phase, for which the packing factor would be affected.

B.1 Defining Reduced Modulus and Radius

The reduced modulus of elasticity (E^*) and the reduced radius (R^*), and by extension the reduced tangential modulus (G^*) and mass (m^*), are defined as

follows:

```
Estar = 1 / (((1 - pow(${ContactPoissonRatio0}, 2)) / ${ContactYoungsModulus0
    }) +
            ((1 - pow(${ContactPoissonRatio1}, 2)) / ${ContactYoungsModulus1})
                )
Rstar = 1 / (1 / ${ContactPhysicalRadius0} + 1 / ${ContactPhysicalRadius1})
mstar = min(${ContactContactMass0}, ${ContactContactMass1})
Gstar = 1 / (((2 * (1 + ${ContactPoissonRatio0}) * (2 - ${ContactPoissonRatio0
    })) / ${ContactYoungsModulus0}) +
            ((2 * (1 + ${ContactPoissonRatio1}) * (2 - ${ContactPoissonRatio1
                })) / ${ContactYoungsModulus1}))
```

B.2 Initial Contact Radius Calculation

The initial contact radius a_0 is calculated as:

```
a0 = pow((0.5 * 9 * 3.14159 * ${Gamma_12} * pow(${Rstar}, 2) / ${Estar}), 1 /
    3)
```

B.3 Normal Contact Force Calculation

The value of the JKR force changes depending on whether the particles are entering or leaving the contact:

```
FN_JKR_val = -(4 * ${Estar} * pow(${a}, 3) / (3 * ${Rstar}) -
             sqrt(8 * 3.14159 * ${Gamma_12} * ${Estar} * pow(${a}, 3))) * $${
                 ContactNormal}

FN_JKR = alternateValue(mag($${ContactForce}), 0) > 0 ?
        ($${FN_JKR_val}) :
        (${a} < pow((2 / 3), (2 / 3)) * ${a0_JKR} ?
          (dot($${ContactRelativeVelocity}, $${ContactNormal}) > 0 ? [0, 0, 0]
               : $${FN_JKR_val})
          : $${FN_JKR_val}) +
        (5 / 3 * ${dc_beta} * sqrt(${damping_Sn} * ${mstar}) * dot($${
            ContactRelativeVelocity}, $${ContactNormal})) * $${ContactNormal}
```

B.4 Damping Calculation

Damping is calculated as:

```
damping_Sn = 2 * ${Estar} * sqrt(${Rstar} * mag($${ContactNormalOverlap}))
dc_beta = log(${restitutionCoeff_e}) / sqrt(pow(log(${restitutionCoeff_e}), 2)
     + pow(3.1415927, 2))
```

B.5 Tangential Contact Force Calculation

In the tangential direction, the Mindlin model is implemented as:

```
FT_Mindlin = - ${damping_St} * $${ContactTangentialOverlap} +
            2 * sqrt(5 / 6) * ${dc_beta} * sqrt(${damping_St} * min(${
                ContactContactMass0}, ${ContactContactMass1})) *
            ($${ContactRelativeVelocity} - dot($${ContactRelativeVelocity}, $$
                {ContactNormal}) * $${ContactNormal})

FT_cont = min(mag($${FT_Mindlin}), ${contactFric_mu} * mag($${FN_JKR})) * unit
    ($${FT_Mindlin})
```

B.6 **Total Contact Force Calculation**

Finally, the total contact force is calculated as:

```
contact_Force_JKR = $${FN_JKR} + $${FT}
```

Declaration

This project has received funding from the European Union's Horizon 2020 research and innovation programme under the Marie Skłodowska-Curie grant agreement No. 847624. In addition, a number of institutions back and co-finance this project.

I hereby declare that I have produced this work without unauthorized assistance from third parties and without using aids other than those specified. Ideas and content directly or indirectly taken from other sources have been appropriately identified as such. This work has not been previously presented in identical or similar form to any examination board.

Tools of Generative Artificial Intelligence (GAI) have been used for text reviewing, grammar correction, and paraphrasing purposes. No information was derived directly and exclusively from GAI tools without appropriate references. Parts of original code and scripts have been iteratively reworked with the aid of GAI tools. The use of GAI adhered to professional ethics.

The dissertation work was conducted from 2021 to 2024 under the supervision of Alejandro Lopez and Beatriz Achiaga at the University of Deusto.

This dissertation was completed in Bilbao in November 2024